
THEORY OF CRYSTAL
STRUCTURE

Generalized Crystallography of Diamond-Like Structures.

1. Finite Projective Planes and Specific Clusters of Diamond-Like Structures Determined by These Planes

A. L. Talis

Institute of Synthesis of Mineral Raw Materials, Aleksandrov, Moscow oblast, Russia

e-mail: ofi@vniisims.elcom.ru

Received March 20, 2001; in final form, March 6, 2002

Abstract—It is shown that the adequate mapping of the symmetry of determined crystalline and noncrystalline diamond-like structures requires a change in the Euclidean basis of the structural crystallography to a more general basis of projective (algebraic) geometry. It is established that the incidence graphs of specific subconfigurations of a finite projective plane $PG(2, q)$ with $q = 2, 3, 4$ are isomorphic to the graphs of specific clusters of diamond-like structures. The clusters thus determined are invariant with respect to the groups of projective geometry that have orthogonal groups as subgroups and, in fact, are set by the subtables of the incidence tables $PG(2, q)$ with $q = 2, 3, 4$. As an example, the *a priori* derivation of clusters, which are not traditional crystallographic objects, is considered, namely, the parallelohedron of the diamond structure, the combination of two Bernal polyhedra $Z8$ and clusters containing icosahedra. © 2002 MAIK “Nauka/Interperiodica”.

INTRODUCTION

The importance of determined diamond-like structures for fundamental crystallography and their application can hardly be overestimated. Diamond-like structures are formed in high-pressure crystalline phases, crystals with linear defects, thin films, nanomaterials, etc., whose structure types are determined by a tetrahedrally coordinated graph consisting of a set of vertices and edges. For several decades, the *a priori* derivation of the structure types of crystals was based on the empirical and intuitive construction of such graphs, and only in 1999, the efforts of mathematicians (a group headed by A. Dress) and crystallographers (A. Mackay) were crowned with the determination of all the crystalline tetrahedrally coordinated combinatorially and topologically different graphs of the divisions of the three-dimensional Euclidean space E^3 into convex polyhedra with vertices of one, two, or three different types [1]. In fact, the mathematical apparatus used in [1] is based on the algebraic constructions, which are more general than discrete groups of motion in E^3 . Thus, the adequate mapping of the symmetry of a crystalline structure (to say nothing of the determined noncrystalline structures) cannot be made in terms of the classical crystallography limited by space groups defined in E^3 .

Lifting the main restrictions of classical crystallography requires a transition to E^n at $n > 3$ and to non-Euclidean geometries. The most important examples here are the studies of quasicrystals [2–4], regular divisions of three-dimensional Riemann and Lobachevski

spaces, S^3 and H^3 [5, 6], the theory of stratified spaces [7], and the lattices of roots [8]. However, up to now, no mathematical apparatus for adequate mapping of the symmetry of the determined (not only crystal) diamond-like structures has been developed within all the mentioned extensions of classical crystallography, either because the mathematical basis was developed insufficiently or, on the contrary, because the most complicated mathematical apparatus was confirmed only by a few rather abstract two-dimensional examples.

We believe that the necessary mathematical apparatus for the adequate mapping of the symmetry of a diamond-like structure should be similar to that of the space groups and represented in the form of a clear but mathematically rigorous basis. The results obtained in our earlier studies [2, 9–11] show that all these requirements are met by the projective (in a wider sense, algebraic) geometry whose joint scheme includes Euclidean, Lobachevski, and Riemannian geometries and deals with the objects whose consideration in E^3 uniquely determines diamond-like structures [12].

The aim of the present study is to construct the generalized crystallography of diamond-like structures as a specific structural application of algebraic geometry, which includes, as the limiting cases, also the corresponding sections of classical crystallography.

The construction of the generalized crystallography of diamond-like structures allows one to derive *a priori* defined diamond-like structures and determine possible phase transitions in these structures. The criterion of the

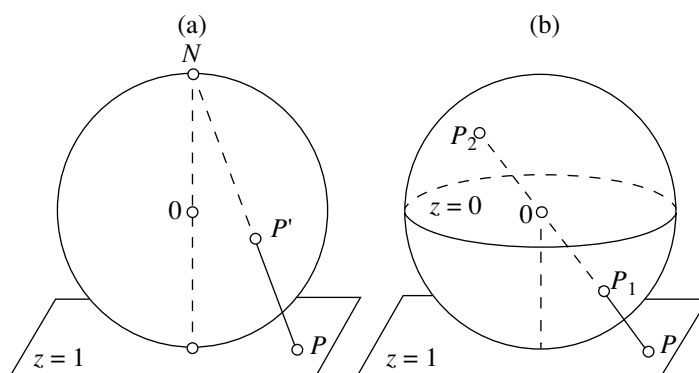


Fig. 1. Projection of a sphere onto Euclidean and projective planes. (a) The sphere S^2 is uniquely projected from the North pole N onto the plane E^2 and (b) a pair of points lying on the opposite ends of the diameter of the sphere S^2 are projected from the center of the sphere onto one point of the projective plane $PG(2, K)$.

correctness of this generalized crystallography is the independent reproduction of the results obtained in [1, 3–6, 13–17] within the framework of this generalized theory. The inefficiency of the synthesis and the study of crystals without the use of classical crystallography leads to the conclusion that the application of the generalized crystallography of diamond-like structures in these studies and the synthesis of the determined diamond-like structures would facilitate the efforts of chemists, physicists, and scientists working in materials and other sciences in their labor-consuming empirical and intuitive structural constructions. In virtue of the tetrahedral coordination the characteristic of zeolites, silicates, gas hydrates, fullerites, etc., certain sections of the generalized crystallography of diamond-like structures can also be successfully used in the studies of these materials [17]. For mathematicians, the generalized crystallography of diamond-like structures can be an interesting example of mathematical applications.

The present article is of an introductory nature and considers examples that clearly show that, at least, for diamond-like structures, the Euclidean basis of the structural crystallography should be substituted by a more general basis of projective (algebraic) geometry. We consider the examples of clusters of diamond-like structures whose symmetry can be adequately mapped only at the level of the groups of projective geometry including the orthogonal groups as their subgroups. In many instances, mathematical rigor was often sacrificed for the sake of a clearer representation, and provided the reader with numerous illustrations that allowed a direct comparison of the constructions of the projective geometry with the clusters of the diamond-like structure uniquely defined by these structures. In other words, to show the great possibilities of the generalized crystallography of diamond-like structures one should not necessarily read the whole article; it is sufficient to get acquainted with the figures showing that the real and hypothetical clusters of diamond-like struc-

tures are uniquely defined by certain mathematical constructions represented in tabulated form.

DEFINITIONS AND TERMINOLOGY

A projective plane $PG(2, K)$ consists of a Euclidean plane $E^2 = EG(2, K)$ and one added point at the infinity for each pencil of straight lines parallel in E^2 . The model of $PG(2, K)$ is shown in Fig 1b.

The straight line in the general position in E^3 passing through the center of a sphere does not lie in the plane $z = 0$, and, thus, intersects the plane $z = 1$ only at one point. The straight lines lying in the plane $z = 0$ do not intersect the plane $z = 1$, and, therefore, they correspond not to the points from E^2 , but to the pencils of parallel straight lines from E^2 . The structure containing n points P_1, P_2, \dots, P_n and n straight lines l_1, l_2, \dots, l_n in which each point is intersected by the $q + 1$ “straight line” ($n = q^2 + q + 1$) consisting of $q + 1$ points is called a finite projective plane $PG(2, q)$ of order q (Fig. 2a). The plane $PG(2, q)$ is uniquely defined by its incidence table in the form of a square $n \times n$ table in which the columns P_1, P_2, \dots, P_n are called the points, and the rows l_1, l_2, \dots, l_n , the straight lines. The incidence of the point P_j and the straight line l_i in this table are defined by placing a black circle into the cell ij ; the empty cell signifies the absence of incidence (Fig. 2). For $PG(2, q)$, the incidence table ($IT(q)$) can be constructed using the summation and multiplication tables of the Galois field $GF(q)$, of order q [8, 18, 19].

The set of m points and n straight lines (planes) in which f straight lines (planes) pass through each point and d points lie on each straight line (plane) is called a configuration. The configuration is denoted as (m_f, n_d) ; if $m = n$, the configuration is self-dual and is denoted as n_d (Figs. 2a and 3a). The configuration is defined by its incidence table ($IT(m_f, n_d)$) consisting of m rows and n columns and containing $m \cdot f = n \cdot d$ incidence signs. The configuration can be implemented in various (finite or infinite) spaces; if it is implemented on a certain pro-

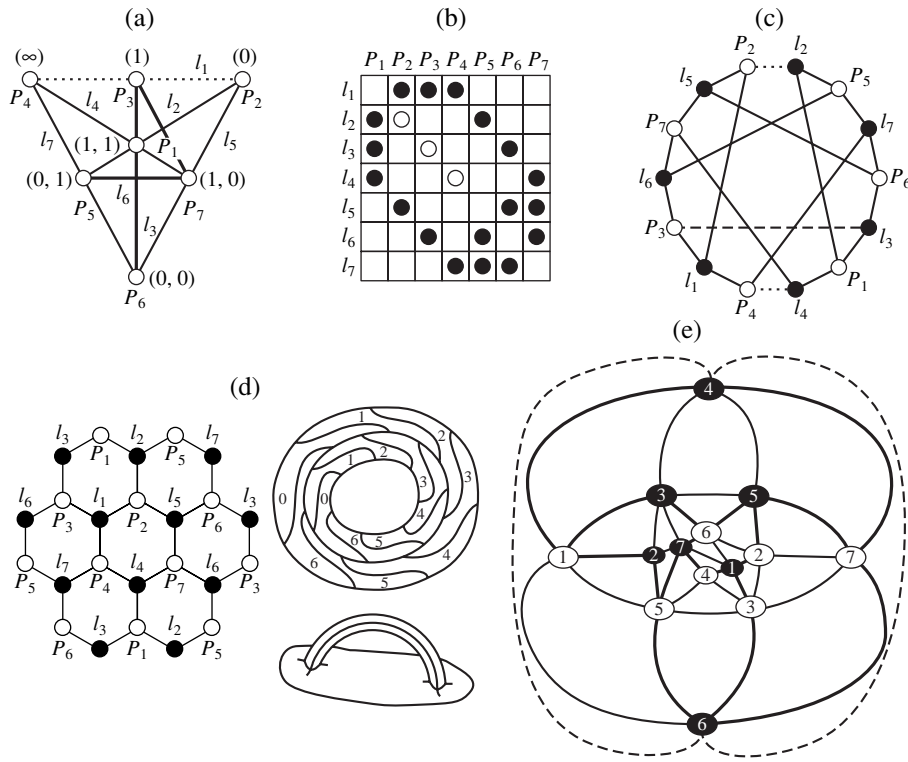


Fig. 2. Finite projective plane $PG(2, 2)$. (a) A graphical model of the finite projective plane $PG(2, 2)$; (b) the incidence table $PG(2, 2)$; (c) the incidence graph of subconfiguration $\{7_3\}^3$; (d) the incidence graph $PG(2, 2)$ as a regular bichromatic map $\{6, 3\}_{2,1}$ on a torus and its representation by a sphere with a handle in the shape of a bent triangular prism; (e) the stereographic projection of a 14-vertex division of a sphere into hexacycles obtained as a result of the removal of the torus handle; triangulation of a sphere is indicated by thin lines, the hexacycles consisting of four triangles are indicated by solid lines.

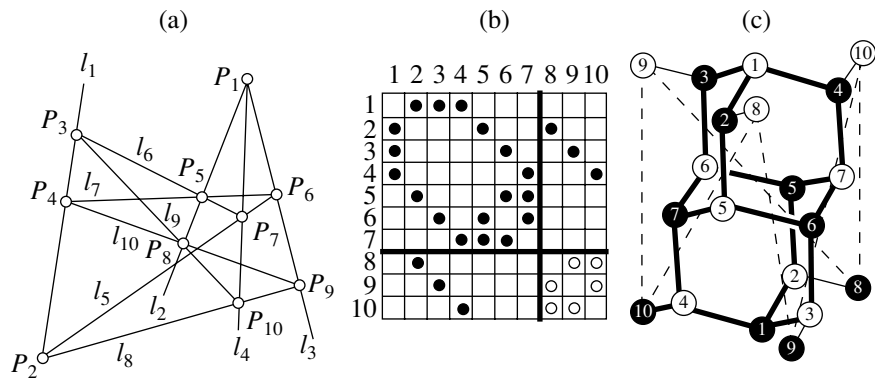


Fig. 3. Self-dual Arguesian configuration 10_3 . (a) The Arguesian configuration 10_3 . The triangles P_5, P_6, P_7 and P_8, P_9, P_{10} possess a center of perspective, P_1 , and the axis of perspective, $l_1 = \{P_2, P_3, P_4\}$; (b) incidence table 10_3 ; and (c) a 20-vertex diamond cluster determined by the subconfiguration $\{10_3\}^6$; the “nondiamond bonds” in the cluster are shown by dashed lines.

jective plane, it should be geometric, i.e., incidence table $IT(m_f, n_d)$ should have at least one empty cell in each of its subtable 2×2 (Figs. 2b and 3b). If the addition of several incidence signs to the $IT(m_f, n_d)$ does not change the geometric configuration, the configuration is extended [18, 19].

The automorphism or the one-to-one mapping of $PG(2, q)$ onto itself is such a transformation in which

the images of three points belong to one straight line then and only then, if these points themselves belong to one straight line. These automorphisms are called collineations and, in the general case, are determined by the reversible 3×3 matrices of the linear-fractional transformations. All the permutations of the set consisting of n elements form the complete group of permutations S_n of the order $n!$. The set of all the collineations $PG(2, q)$ makes the subgroup $P^{col}(2, q)$ of the group S_n ;

the order is $P^{\text{col}}(2, q) = m(q^2 + q + 1)(q + 1)q^3(q + 1)^2$, where $q = p^m$ and p is a prime number [18, 19].

The separation of the subgroups of the symmetry group S_n with $n = q^2 + q + 1$ implemented by $PG(2, q)$ is also possible within the framework of the graph theory. Each graph edge connects two different points; two points are connected by only one edge; if k edges are converged at a vertex, this vertex is of the power k . If all the vertices of the graph are of the same power k , then the graph is a regular graph of the power k . The path of the shortest graph cycle is called its girth, and the cycle passing through each point of the graph is called the Hamiltonian path. (The graph with the Hamiltonian path is the Hamilton graph.) If the set of the graph vertices can be divided into two nonintersecting subsets (of black and white points) in such a way that any edge would connect the points of different subsets (white and black), then the graph is called bichromatic. The regular graph of power k and girth l with the minimum number of vertices n is denoted as $\Gamma(n, k, l)$ [18].

If one brings into coincidence the points P_1, P_2, \dots, P_n and the straight lines l_1, l_2, \dots, l_n of the finite projective plane $PG(2, q)$ to the white and black vertices of the graph and connects by the edges those and only those pairs of white and black points for which the intersection of the corresponding row l_i and column P_j contains the incidence sign, then the incidence graph $PG(2, q)$ consisting of $2(q^2 + q + 1)$ vertices and $(q + 1)(q^2 + q + 1)$ edges is formed. The incidence graph $PG(2, q)$ is a regular bichromatic Hamilton graph of power $q + 1$ and girth 6 with the minimum possible order [18]. The incidence graph $PG(2, 2)$ or a Levi graph of the self-dual configuration 7_3 is shown in Fig. 2c.

GRAPH OF A DIAMOND CLUSTER AS AN IRREGULAR BICHROMATIC

MAP $\{6, 3\}_{q,1}^3$

Let $\Gamma(N_0, k, 6)$, $N_0 \leq 2(q^2 + q + 1)$, and $k \leq q + 1$ be the maximum regular subgraph of the incidence graph $\Gamma(2(q^2 + q + 1), q + 1, 6)$ of the finite projective plane $PG(2, q)$ that can be represented in the form of a regular map $\{6, k\}_r$ on the surface S . In accordance with parity or odd parity r , the surface S is either orientable (a sphere with handles) or nonorientable (a sphere with crossed caps). The symbol $\{6, k\}_r$ signifies that the map is composed of hexagons, with k hexagons converging at each vertex. The map is obtained from the primitive mosaics $\{6, k\}$ by identifying those pairs of its vertices which are separated by r steps along Petrie's polygon—a zigzag of h edges in which any two (and not three successive) sides belong to one face [18–21]. In each oriented map, one can single out handles [19, 21, 22]. Thus, in a regular map on a torus, one can single out a handle in the shape of a bent k -gonal prism (Fig. 2d) which complements this sphere to a torus [19]. The

removal of this handle (i.e., of k edges in the regular map on the torus) results in the formation of an irregular map on the remaining sphere.

Among the subconfigurations of the plane $PG(2, q)$, one can find configurations whose incidence graphs can be represented only by irregular maps providing such a division of the sphere that the number of hexagons at each vertex would be different. In particular, such an irregular map $\{6, 3\}_{b,c}^3$ is obtained from the regular map $\{6, 3\}_{b,c}$ on a torus, which contains, upon the removal of $k = 3$ edges (Figs. 2d, 2e), $N_2 = b^2 + bc + c^2$ hexacycles, $N_1 = 3N_2$ edges, and $N_0 = 2N_2$ vertices. The irregular map $\{6, 3\}_{b,c}^3$ possesses the following Eulerian characteristic typical of a sphere [19, 21, 22]:

$$\chi(\{6, 3\}_{b,c}^3) = 2N_2 - 3(N_2 - 1) + (N_2 - 1) = 2, \quad (1)$$

where $2N_2$, $3(N_2 - 1)$, and $(N_2 - 1)$ are the numbers of vertices, edges, and hexacycles of the map $\{6, 3\}_{b,c}^3$ (Fig. 2e).

An fcc lattice coincides with the root lattice D_3 , and, therefore, the diamond structure as a combination of two fcc lattices can be denoted as D_3^+ [8] and is a regular bichromatic graph $\Gamma(D_3^+)$ of power 4 and girth 6. The edges of this graph do not intersect each other and, therefore, the general subgraph $\Gamma(D_3^+)$ and $\Gamma(2(q^2 + q + 1), q + 1, 6)$ (in the combinatorial–topological sense, i.e., with no regard for the metric relationships) should coincide with the irregular map $\{6, 3\}_{q,1}^3$ determined by Eq. (1). A diamond is an object of Euclidean geometry, whereas $PG(2, q)$ is an object of finite projective geometry, and, therefore, a diamond cluster with the graph

$$(\Gamma(2(q^2 + q + 1), q + 1, 6) \cap \Gamma(D_3^+)) = \{6, 3\}_{q,1}^3 \quad (2)$$

is an object of finite projective geometry that is considered in Euclidean geometry. *A priori*, the number of bonds at the cluster vertex at $q = 2, 3$ does not exceed four, and, therefore, taking into account Eq. (2), one can state that diamond clusters with the graphs $\{6, 3\}_{q,1}^3$, $q = 2, 3$, possess additional super-Euclidean symmetry in E^3 that remains from $PG(2, q)$ and that the adequate mapping of this additional symmetry is possible only at the level of collineation and correlation groups [19, 20].

PARALLELOHEDRON GRAPH OF DIAMOND

$\{6, 3\}_{2,1}^3$ AS AN INCIDENCE GRAPH OF SUBCONFIGURATION $\{7_3\}^3$

Now, consider the transition from Fano's configuration 7_3 or $PG(2, 2)$ to its self-dual subconfiguration $\{7_3\}^3$ formed upon the removal of three edges from the

incidence graph $PG(2, 2)$. Ideal points 0, 1, and ∞ in Fig. 2a compose an ideal straight line; 0 and Euclidean points (0,0), (1,0) and (0,1), (1,1) form two straight lines of the first family; ∞ and Euclidean points (0,0), (0, 1) and (1,0), (1,1) form two straight lines of the second family; and 1 and Euclidean points (1,0), (0,1) and (1,1), (0,0) form two “straight lines” of the diagonal family. According to the axiomatics of $PG(2, q)$, the straight lines of each family are parallel and converge at the points of the ideal straight line which lie at infinity. Since three points are located on each line, the straight line consists of two segments to each of which there correspond individual edges of the incidence graph (Fig. 2c) and an individual incidence sign in the incidence table (Fig. 2b). The graph edges shown by dashed lines and the incidence signs indicated by empty circles indicate the absence of the corresponding segments of straight lines and the transition to a subgraph of the incidence graph or a subtable of the incidence table. Thus, to the subconfigurations $\{7_3\}^3$ there corresponds the removal of the segments between the points P_1 and P_2 , P_3 , P_4 on the straight lines l_2 , l_3 , and l_4 (Fig. 2a), the incidence graph without 3 dashed edges (Fig. 2c), and the incidence table without 3 empty circles (Fig. 2b). However, in this case the parallel lines l_2 and l_5 , l_4 , and l_7 , and l_3 and l_6 do not intersect (at the ideal points P_2 , P_4 , and P_3), which signifies the transition from projective to Euclidean geometry, where the parallel lines are intersected. In other words, the transition from 7_3 to $\{7_3\}^3$ is the transition to the Euclidean representation $PG(2, 2)$,

If 7_3 is mapped onto itself by the collineation and correlation group $PGL_2(7)$ of order 336 [19, 21], then $\{7_3\}^3$ is mapped onto itself by the isomorphic group of loaded collineations $PGL_2^W(7)$. Within the framework of the apparatus of the color W -symmetry groups [23, 24], $PGL_2^W(7)$ is the junior group and, therefore, by virtue of Eq. (2), we have

$$\begin{aligned} PGL_2(7) &\longleftrightarrow PGL_2^W(7) \\ \supset PGL_2(7) \cap PGL_2^W(7) &= \bar{3}m, \end{aligned} \tag{3}$$

where the orthogonal group $\bar{3}m$ is its symmetry subgroup, which, in the general case, is not a normal subgroup. Relationships (3) specify the well-known statement that the finite groups of sphere motion are the subgroups of the group of linear-fractional transformations [25]. If the intersection $PGL_2(7) \cap PGL_2^W(7)$ was the normal subgroup of index 2, then $PGL_2^W(7)$ would be a Shubnikov antisymmetry group [23, 24]. Thus, to the transition from 7_3 to $\{7_3\}^3$ there corresponds the transition from $PGL_2(7)$ to the isomorphic group $PGL_2^W(7)$ specifying the principle accord-

ing to which the symmetry does not disappear; indeed, in the transition from $PG(2, 2)$ in E^3 , the symmetry does not disappear but only changes its form [23].

The Arguesian configuration 10_3 (a pair of triangles perspective with respect to the center and the axis of perspective, Fig. 3a) is a subconfiguration $PG(2, 3)=13_4$ not containing $PG(2, 2)$, but probably containing its subconfigurations. Any Arguesian projective plane (i.e., the plane where the Desargues theorem is valid) is a plane of translations in which any pair of points can be related by a translation [26].

The incidence table 10_3 defines a 20-vertex diamond cluster (Figs. 3b, 3c) divided into two diagonal blocks, $(1-7) \times (1-7)$ and $(8-10) \times (8-10)$, and two nondiagonal blocks, $(8-10) \times (1-7)$ and $(1-7) \times (8-10)$, symmetric with respect to the diagonal. The diagonal block is an incidence table of the subconfiguration $\{7_3\}^3$ (Fig. 2b) and defines a 14-vertex diamond cluster with the graph $\{6, 3\}_{2,1}^3$ (Figs. 2c, 2e) indicated by solid lines in Fig. 3c. For the first time, this cluster was separated from the diamond structure in [13]. It is a diamond parallelohedron described in detail in [10, 11] and defined by the specifying relationships (2) as

$$\begin{aligned} \{6, 3\}_{2,1}^3 &= \Gamma(7_3) \cap \Gamma(D_3^+) = \Gamma(7_3) \cap \Gamma(10_3) \\ &= \Gamma(7_3 \cap 10_3) = \Gamma(\{7_3\}^3), \end{aligned} \tag{4}$$

which provide its formation in E^3 under the condition of equality of the edges (without their intersection) and the angles formed by these edges. Indeed, the fact that $\{7_3\}^3$ belongs to 10_3 (defining the plane of translations) and the existence of nonintersecting parallel lines (unlike 7_3) in $\{7_3\}^3$ signifies the possible division of the diamond structure D_3^+ into translationally equivalent parallelohedra with the graphs $\{6, 3\}_{2,1}^3$.

The blocks $(8-10) \times (1-7)$ and $(1-7) \times (8-10)$ correspond to six singly coordinated vertices complementing each doubly coordinated vertex in $\{6, 3\}_{2,1}^3$ to a triply coordinated one. To the connection of these six vertices into a hexacycle there corresponds the block $(8-10) \times (8-10)$ (Fig. 3b), but the edges of this hexacycle (dashed lines in Fig. 3c) do not correspond to the bonds of the diamond structure, and, therefore, a 20-vertex diamond cluster with 24 bonds is defined by incidence table $\{10_3\}^6$, i.e., by incidence table 10_3 without six empty circles.

GRAPHS OF SPECIFIC CLUSTERS
OF DIAMOND-LIKE STRUCTURES AS
INCIDENCE GRAPHS OF
SUBCONFIGURATIONS $PG(2, 3)$

The finite projective plane $PG(2, 3)$ contains self-dual Möbius–Cantor configuration 8_3 whose incidence

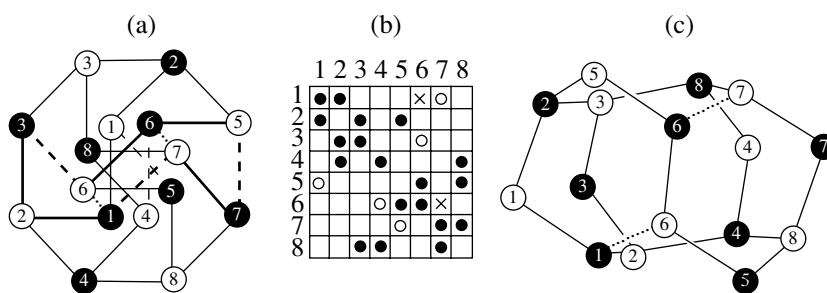


Fig. 4. (a) The graph $\{8\} + \{8/3\}$ with two edges, 6-1' and 7'-6', not belonging to this graph (the primed numerals enumerate the black vertices), which divide the octagon shown by solid lines into three triangles; (b) the incidence table 8_3 ; (c) a 16-vertex cluster 2Z8 determined by the incidence table of the subconfiguration $\{8_3\}^{5-2}$, which is the combination of two (black and white) Bernal polyhedra Z8 related by a twofold axis passing normally to the middle of edge 6-6'.

graph is a bichromatic graph $\{8\} + \{8/3\}$ of power 3 and girth 6 (Fig. 4a) coinciding with the regular map $\{4 + 4, 3\}$ [20] consisting of $N_2 = 6$ octagons on a sphere S_2 with two handles. The Eulerian characteristic χ of this map with $N_0 = 16$ vertices and $N_1 = 24$ edges equals $2 - 2p = -2$, where $p = 2$ is the number of handles on the surface S_p (the sphere S_0 with p handles) [19, 21, 22].

Dividing each octagon in $\{4 + 4, 3\}$ by two edges into three tetragons, one obtains $6 \times 3 = 18$ tetragons separated by $24 + 6 \times 2 = 36$ edges on S_2 . The map $\{4 + 4, 3\}$ divided into tetragons is denoted as $\{\widetilde{4 + 4}, 3\}$. The removal of the handle in the map $\{4, 4\}_{b,c}$ on the torus S_1 reduces the number of edges by four, and the number of tetragons by 2 [12]. Thus, the removal of two handles of S_2 divided into tetragons should result in the formation of the map $\{\widetilde{4 + 4}, 3\}^8$ on the sphere S_0 divided into tetragons, where the numbers of edges and tetragons are less by 8 and 4, respectively, than on $\{\widetilde{4 + 4}, 3\}$. The removal of the edge shared by two tetragons results in the formation of a hexagon, which allows one to pass from the sphere division into tetragons to its division into hexacycles. Thus, the division of octagons into tetragons on $\{4 + 4, 3\}^8$, the removal of two handles of $\{\widetilde{4 + 4}, 3\}$, and the connection of tetragons into hexacycles on $\{\widetilde{4 + 4}, 3\}^8$ yields the graph $\Gamma(2Z8)$ defining the irregular division of the sphere into hexacycles and containing 16 vertices, 21 edges, and 7 hexacycles (Fig. 4c),

$$\begin{aligned} \chi(\{4 + 4, 3\}) &= \chi(\{\widetilde{4 + 4}, 3\}:) \\ &: 16 - 24 + 6 = -2 = 16 - 36 + 18, \\ \chi(\{\widetilde{4 + 4}, 3\}^8) &= \chi(\Gamma(2Z8):) \end{aligned} \quad (5)$$

$$16 - (36 - 8) + (18 - 4) = 2 = 16 - (28 - 7) + 14/2,$$

where -2 and $+2$ are the Eulerian characteristics of S_2 and S_0 .

Of the total twelve edges dividing the octagons into tetragons on $\{\widetilde{4 + 4}, 3\}$ and not belonging to the graph $\{8\} + \{8/3\}$, the $\Gamma(2Z8)$ retains only two edges, 6-1' and 7-6' (where the primed numerals enumerate the black vertices), with the corresponding incidence signs not belonging to the incidence table 8_3 being denoted by crosses (Fig. 4b). The edges 6-1' and 7-6' belong to the map $\{\widetilde{4 + 4}, 3\}$, and, therefore, the incidence table of the subconfiguration $\{8_3\}^{5-2}$, formed upon the removal of five empty circles from the incidence table 8_3 and the introduction of two crosses, will be geometric. In other words, the removal of empty circles allows one to introduce the crosses into the incidence table 8_3 without the formation in this table of forbidden rectangles of incidence signs corresponding to the cycles of four edges (Fig. 4b). The graph $\Gamma(2Z8)$ defined by the incidence table $\{8_3\}^{5-2}$ is a graph of the combination of two Bernal polyhedra Z8 (black and white) [15] related by a twofold axis (Fig. 4c). Thus, a Bernal polyhedron Z8 can be obtained from the graph $\Gamma(2Z8)$ defined by Eq. (5) under the condition that the edges are equal but not intersecting and the angles between the edges in this graph are also equal.

For all (ideal) diamond-like structures, the second coordination sphere consists of combined four centered tetrahedra, and therefore the diamond-like structures have different torsion angles determined by the rotation of triads of atoms from the second coordination sphere. If these 12 vertices form an Archimedean cuboctahedron, the diamond-like structure is a diamond ($\theta = 60^\circ$); if they form a hexagonal cuboctahedron, then the diamond-like structure is lonsdaleite ($\theta = 60^\circ, 0^\circ$); if both these 12-vertex polyhedra are formed, the diamond-like structure is a polysynthetic twin [14]. If four triads of the Archimedean cuboctahedron are synchronously rotated by an angle of ψ , the cuboctahedron is rearranged into the oblique icosahedron described by the symmetry group 23, whereas the torsion angle θ becomes equal to $60^\circ - \psi$. The variation of the distances from the vertex of an oblique icosahedron to the remaining 11 vertices as functions of the angle $\theta = 60^\circ - \psi$ was

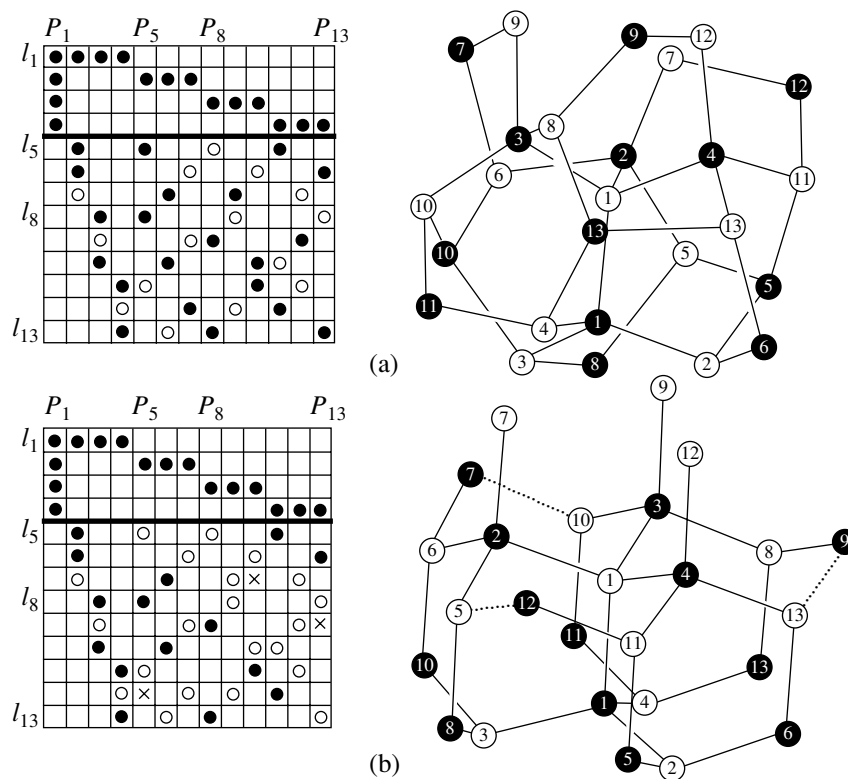


Fig. 5. Incidence table of a finite projective plane $PG(2, 3)$ and the determination of specific 26-atom clusters of diamond-like structures with the aid of the table subtables. (a) Without the incidence signs shown by empty circles, the incidence table $PG(2, 3)$ determines the cluster of the diamond-like structure in which the white vertices 2–13 form an icosahedron; (b) without empty circles but with crosses, the incidence table $PG(2, 3)$ determines a 26-vertex cluster in lonsdaleite in which 12 white vertices 2–13 form a hexagonal cuboctahedron of the second coordination sphere. The subtable separated by a solid line 4×13 of the incidence table of $PG(2, 3)$ determines the 17-vertex association of four sharing-vertex centered tetrahedra.

considered in [16] and it was shown that, at $\psi = 22^\circ$, 24° ($\theta = 37.76^\circ$), the oblique icosahedron is the closest to an icosahedron. Obviously, the appropriate generalized crystallography of diamond-like structures should provide an adequate description of diamond-like structures so that all the specific clusters can be derived within the framework of this theory.

In all the diamond-like structures, a 17-vertex polyhedron of the second coordination sphere is defined by incidence table 4×13 , which is the subtable of $PG(2, 3) = 13_4$ (Fig. 5a). Thus, the maximum subconfiguration $PG(2, 3)$, whose incidence graph defines a specific cluster of the diamond-like structure, should be obtained from a certain regular 26-vertex map. Such a map is the $\{6, 3\}_{3,1}$ map on a torus with 39 edges and 13 hexacycles. Removing the handle from this map (as in the above-described removal of the handle in $\{6, 3\}_{2,1}$), we arrive at the irregular division of a sphere into $13 - 1 = 12$ hexagons separated by $39 - 3 = 36$ edges. In the subtable 4×13 of the incidence table $PG(2, 3)$, the point P_1 is tetrahedrally coordinated. Thus, the incidence table of the subconfiguration to be determined should contain $36 + 1 = 37$ incidence signs, and the sign in the first column of the first row should correspond to the internal 37th edge of the cluster in the diamond-like struc-

ture. Thus, singling out the subtable 4×13 in the incidence table $PG(2, 3)$, and rejecting in the remaining part (9×13) of this table the incidence signs, we arrive at the incidence table which is a subconfiguration of $PG(2, 3)$ determining a certain specific cluster of the diamond-like structure built by hexacycles. The condition necessary for the assembly of this cluster from hexacycles (i.e. the condition of the absence of dangling bonds and singly coordinated vertices) requires that not more than two incidence signs (empty circles) be removed from each row (column) of the subtable 9×13 . There is only one subconfiguration satisfying all the above conditions $\{13_4\}^{15}$ of the plane $PG(2, 3)$ that uniquely defines the 26-atomic cluster of the diamond-like structure containing an icosahedron formed by the vertices of the second coordination sphere of the cluster center (Fig. 5a).

In addition to subconfiguration $\{13_4\}^{15}$, one can also single out in the plane $PG(2, 3)$ some other subconfigurations that also define a specific 26-atom clusters in the diamond-like structure [11]. Thus, the 26-atom cluster in lonsdaleite (Fig. 5b) is determined by the subconfiguration $\{13_4\}^{21-3}$ of $PG(2, 3)$ formed upon the removal of 21 (empty circles) and the addition of 3

(crosses) incidence signs in the incidence table 13_4 . Thus, it is possible to single out in $PG(2, 3)$ the subconfigurations that would provide the divisions of a sphere into 26-vertex hexacycles, which uniquely define specific clusters of the diamond-like structure. Among all these subconfigurations, there is only one maximum configuration, $\{13_4\}^{15}$, which can be completely included into the incidence table $PG(2, 3)$ by rejecting the minimum number of the incidence signs. The cluster of the diamond-like structure determined by this subconfiguration contains an icosahedron formed by the vertices of the second coordination sphere of the cluster center. Obviously, this is the solution of the problem stated in [16] but at a higher level of the generalized crystallography of diamond-like structures.

FINITE PROJECTIVE PLANE OF $PG(2, 4)$ AND CLUSTERS DEFINED BY THIS PLANE

By virtue of the tetrahedral coordination characteristic of the diamond-like structure, a subgraph of the incidence graph $PG(2, q)$ $q > 3$ can define the cluster of the diamond-like structure only upon the removal of at least $q - 3$ edges from each vertex. The total number of the removed edges drastically increases with an increase in q , and, therefore, there should exist a certain maximum value of q appropriate for the generalized crystallography of diamond-like structures. We determine this q value as a result of a rather qualitative consideration which will be strengthened in our further studies.

Like the separation of specific subconfiguration $\{13_4\}^{15}$ in $PG(2, 3)$ determining a 26-atom cluster of the diamond-like structure (Fig. 5a), we can reject 49 incidence signs in the incidence table $PG(2, 4)$ and single out the configuration defining a 40-atom cluster of the diamond-like structure containing two icosahedra (of white and black atoms) with the centers at points 1 and 6' (Fig. 6a). Complementing this cluster with three white and three black atoms (I, II, III, and I', II', III'), we arrive at a 46-atom combination of four icosahedra (with the centers at points 4', 1, 6', and 14) along the common threefold axis. The location on this axis of atoms 5' and 18, whose bonds with atoms 5, 9, 13 and 9', 18', 21' do not correspond to the incidence signs of the incidence table $PG(2, 4)$, allows one to obtain a 48-atom cluster of the diamond-like structure (Fig. 6a) defined by the subconfiguration of the unique combinatorial object, MOG (magic octad generator) [8]. The MOG generalizes $PG(2, 4)$ and is defined by the table 6×4 (Fig. 6b), whose points I, II, and III correspond to atoms I, II, and III, and the point ∞ , to atom 18 in Fig. 6a.

The incidence table $PG(2, 4)$ with 52 incidence signs removed also defines a 40-atom cluster of the diamond-like structure containing two icosahedra of white and black atoms (with centers at points 1 and 4') (Fig. 6c). Complementing this cluster with six black

atoms ($\hat{1}-\hat{6}$) not corresponding to the rows of the incidence table $PG(2, 4)$ and white atom 18, whose bonds with atoms 9', 18', and 21' do not correspond to the incidence signs of the incidence table $PG(2, 4)$, we arrive at a 47-atom cluster of the diamond-like structure (Fig. 6c). The white atoms of this cluster form a centered cube with an inscribed ideal icosahedron whose deformation yields the unit cell of the Frank–Kasper phase A15 described by the sp. gr. $Pm\bar{3}n$ [4, 27]. Black atoms form a 26-atom combination of four icosahedra (with the centers at points 1', 2', 3', and 4') which belongs to the Frank–Kasper phase C15 described by the sp. gr. $Fd\bar{3}m$ [27]. On the whole, this 47-atomic cluster, defined by the subconfiguration $PG(2, 4)$, can be enclosed into the unit cell of a hypothetical diamond-like structure [4] described by the sp. gr. $P\bar{4}3n = Pm\bar{3}n \cap Fd\bar{3}m$. The removal of other combinations of not less than 52 incidence signs from the incidence table $PG(2, 4)$ allows one to determine other energetically advantageous clusters of the diamond-like structure [11].

The subconfiguration $PG(2, 4)$ defining the most symmetric cluster of the diamond-like structure (Fig. 6a) contains the maximum number (56) of the incidence signs of $PG(2, 4)$. The minimum specific subconfiguration of $PG(2, 4)$ is the extended Arguesian configuration 10_3^3 , whose incidence table contains three more incidence signs than the incidence table of the Arguesian configuration 10_3 (Fig. 3) and can be enclosed only in the incidence table $PG(2, 4)$ [18]. A cluster of the diamond-like structure determined by 10_3^3 (20 vertices and 24 edges) is contained in the clusters of the diamond-like structure defined by the subconfigurations of $PG(2, 4)$ (Figs. 6a, 6c) that can be considered as different variants of its growth. Comparing the data obtained with the earlier results, one can draw the conclusion that the specific subconfigurations $PG(2, q)$, $q = 2, 3, 4$ determine the specific clusters of the diamond-like structure according to the same algorithm.

Since it is impossible to divide E^3 into ideal icosahedra, the clusters with icosahedral order can only be of relatively small dimensions [5] and are energetically favorable only to a certain extent that is determined by the possibility of dividing E^3 . Thus, the enclosure of the unit cell of the crystalline diamond-like structure [4] in the cluster defined by $PG(2, 4)$ (Fig. 6c) signifies that this 47-atom cluster is the maximum possible one. In other words, the clusters of the diamond-like structure determined by $PG(2, q)$, $q \geq 5$ are either energetically disadvantageous or are the combinations of the clusters defined by $PG(2, q)$, $q \leq 4$. Within the framework of algebraic geometry, the limited character of $PG(2, 4)$ in the generalized crystallography of diamond-like struc-

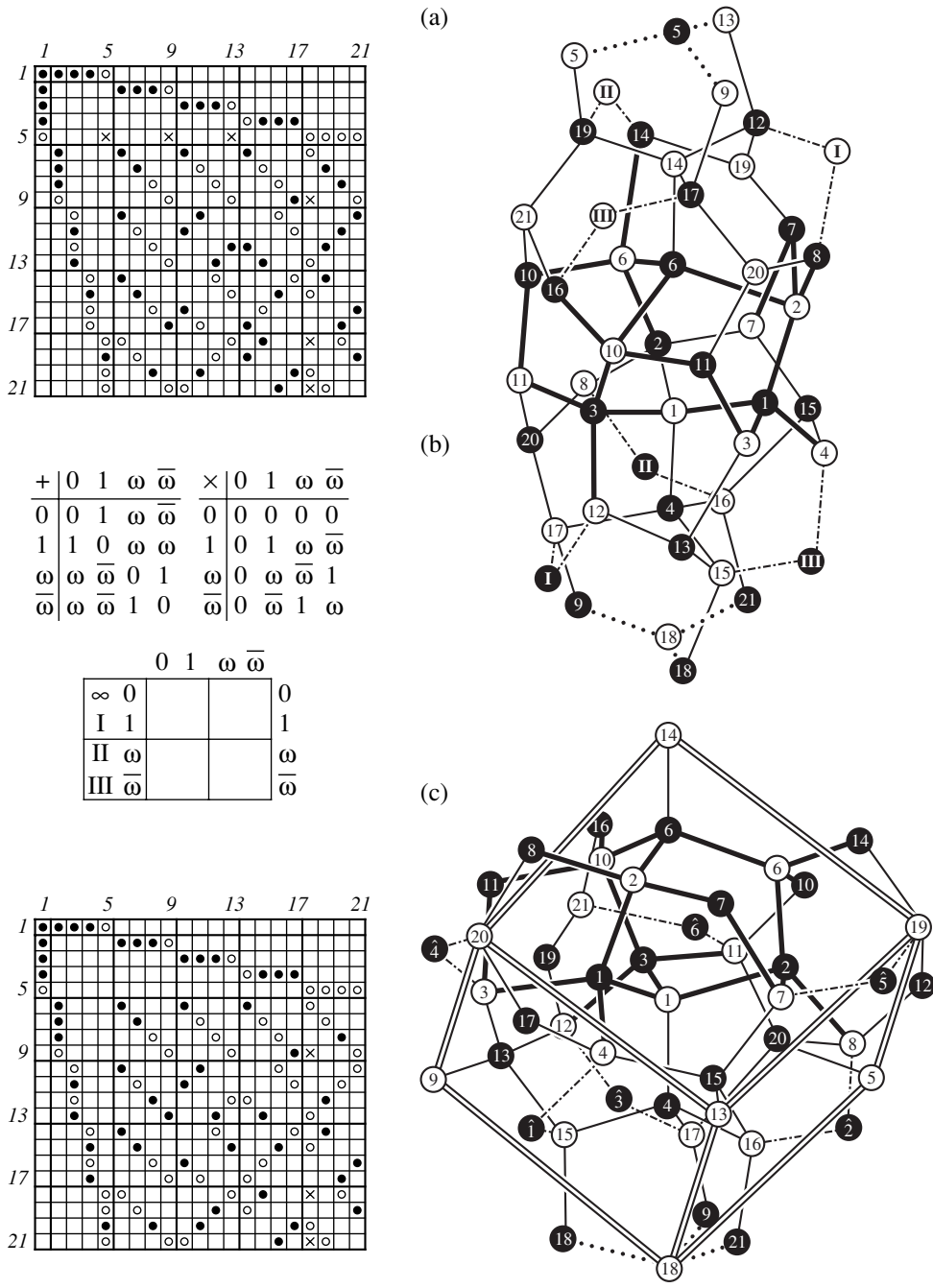


Fig. 6. The incidence table $PG(2, 4)$, its extension to the MOG (the magic octad generator) and the specific clusters of the diamond-like structure thus determined. (a) A 40-vertex cluster of the diamond-like structure which, together with vertices I, II, III and I', II', III' corresponding to the roman points of MOG , is the combination of four icosahedra with the centers at points 14, 6', 1, and 4'; (b) summation (+) and multiplication (x) tables of the Galois field, $GF(4) = \{0, 1, \omega, \bar{\omega}\}$, $\omega = \frac{1}{2}(i\sqrt{3} - 1)$, and MOG as an extension of $PG(2, 4)$; (c) a 40-vertex cluster of the diamond-like structure whose 20 white vertices together with vertex 18 are isomorphic to the unit cell of the Frank–Casper phase A15. Together with 6 black vertices $\hat{1}-\hat{6}$, twenty black vertices of this cluster form a 26-vertex Pauling polyhedron of the Frank–Kasper phase C15. A 20-vertex cluster of the diamond-like structure determined by the extended Arguesian configuration 10_3^3 is shown by solid lines.

tures follows from its enclosure in the MOG (Fig. 6b), which, in the final analysis, is determined by the limiting lattice E_8 , a root lattice in the simplest specific Lie algebra e_8 [8, 21, 25].

CONCLUSION

The separation of diamond-like structures, the Frank–Kasper phases, the Bernal structures, gas hydrates, etc. into a specific class of diamond-like

structures [1–6] indicates the failure of the adequate mapping of their symmetry within the framework of classical crystallography. The main result obtained in this study is the determination of the specific clusters of diamond-like structures as the Euclidean implementations of the incidence graphs of specific subconfigurations $PG(2, q)$, $q = 2, 3, 4$ uniquely determined by their incidence tables. Somewhat prematurely, we indicate here that the number of specific subconfigurations $PG(2, q)$, $q = 2, 3, 4$ is relatively small, and, therefore, like the simple forms, all the possible clusters of the diamond-like structures can *a priori* be enumerated. The symmetry of these clusters (including super-Euclidean symmetry) is adequately mapped within the framework of the generalized crystallography of diamond-like structures, which is an extension of some sections of the algebraic geometry to the structural level. The concrete results obtained in this study can be formulated as follows:

(1) The diamond structure, being a combination of two fcc lattices, is a regular bichromatic graph of power 4 and girth 6 and, therefore, the subconfigurations $PG(2, q)$, $q = 2, 3, 4$ (which have incidence graph as a regular bichromatic graph of power $q + 1$ and girth 6) define the graphs of specific clusters of the diamond-like structure.

(2) The specific clusters of the diamond-like structure, being the objects of the higher (projective) geometry considered in the lower (Euclidean) geometry [12], possess supersymmetry with respect to the latter geometry, which can adequately be reflected only within the framework of the generalized crystallography of diamond-like structures. For instance, the cluster $\{6, 3\}_{2,1}^3$ determined by the subconfiguration $\{7_3\}^3$ of the finite projective plane $PG(2, 2)$ is a diamond parallelohedron described by a linear-fractional symmetry group $PGL_2^W(7)$ of order 336 containing the orthogonal subgroup $\bar{3}m$ of order 12.

(3) The mathematical apparatus of the generalized crystallography of diamond-like structures allows one to determine *a priori* the specific clusters of the real and hypothetical diamond-like structures, which are not traditional crystallographic objects. For instance, the cluster of the diamond-like structure combining two Bernal polyhedra Z8 and the cluster of the diamond-like structure containing the icosahedron in the second coordination sphere are determined by the subconfigurations $PG(2, 3)$, whereas the cluster of the diamond-like structure combining the clusters of two Frank—Kasper phases (the unit cell A15 and a Pauling 26-atom cluster C15) is determined by the subconfiguration $PG(2, 4)$.

ACKNOWLEDGMENTS

The author is grateful to V.A. Koptsik, N.A. Bul'enkov, L.I. Tsinober, M.I. Samoilovich, V.S. Kraposhin, and M.I. Mironov for their constant and stimulating many-year interest in his studies over many years and to V.E. Dmitrienko for fruitful discussion of the results and valuable remarks.

REFERENCES

- O. Delgado Friedrichs, A. W. M. Dress, D. H. Huson, *et al.*, *Nature* **400**, 644 (1999).
- L. Danzer, Z. Popadopoulos, and A. Talis, *Int. J. Mod. Phys. B* **7**, 1379 (1993).
- V. E. Dmitrienko, M. Kleman, and F. Mauri, *Phys. Rev. B* **60**, 9383 (1999).
- V. E. Dmitrienko and M. Kleman, *Kristallografiya* **46**, 591 (2001) [*Crystallogr. Rep.* **46**, 527 (2001)].
- R. Mosseri, D. P. Di Vincenzo, T. F. Sadoc, and M. H. Brodsky, *Phys. Rev. B* **32**, 3974 (1985).
- M. Kleman, *Adv. Phys.* **38**, 605 (1989).
- V. V. Manzhur, Preprint No. 9-93 (L'vov, 1993).
- J. H. Conway and N. J. A. Sloane, *Sphere Packings, Lattices, and Groups* (Springer-Verlag, New York, 1988; Mir, Moscow, 1990), Vols. 1, 2.
- A. L. Talis and V. A. Koptsik, *Kristallografiya* **35** (6), 1347 (1990) [*Sov. Phys. Crystallogr.* **35**, 794 (1990)].
- A. L. Talis, in *Proceedings of the IV International Conference "Crystals: Growth, Properties, Real Structure, Application"* (VNIISIMS, Aleksandrov, 1999), p. 219.
- A. L. Talis, *Sint. Miner.* **3**, 321 (2000).
- N. V. Efimov, *Higher Geometry* (Nauka, Moscow, 1978).
- N. A. Bul'enkov, *Dokl. Akad. Nauk SSSR* **284**, 1392 (1985).
- R. V. Galiulin, *Crystallographic Geometry* (Nauka, Moscow, 1984).
- J. Bernal, *Kristallografiya* **7**, 507 (1962) [*Sov. Phys. Crystallogr.* **7**, 410 (1962)].
- Y. Ishii, *Acta Crystallogr., Sect. A: Found. Crystallogr.* **44**, 987 (1988).
- V. S. Kraposhin, A. L. Talis, and M. N. Pankova, *Metall. Obrab. Met.*, No. 8, 23 (1999).
- F. Karteszi, *Introduction to Finite Geometries* (Akademiai Kiado, Budapest, 1976; Nauka, Moscow, 1980).
- H. S. M. Coxeter, *Introduction to Geometry* (Wiley, New York, 1961; Nauka, Moscow, 1966).
- H. S. M. Coxeter, *Bull. Am. Math. Soc.* **56**, 413 (1950).
- H. S. M. Coxeter and W. O. J. Moser, *Generations and Relations for Discrete Groups* (Springer-Verlag, New York, 1972; Nauka, Moscow, 1980).
- G. Ringel, *Map Color Theorem* (Springer-Verlag, New York, 1974; Mir, Moscow, 1977).
- V. A. Koptsik, in *Problems of Modern Crystallography*, Ed. by B. K. Vainshtein and A. A. Chernov (Nauka, Moscow, 1975), p. 42.
- V. A. Koptsik, *Group-Theoretical Methods in Physics* (Nauka, Moscow, 1986), Vol. 1, p. 368.
- I. R. Shafarevich, *Basic Concepts in Algebra* (Izhevskaya Respublikanskaya Tipografiya, Izhevsk, 1999).
- J. Lelong-Ferrand, *Les fondements de la geometrie* (Presses univ. de France, Paris, 1985; Mir, Moscow, 1989).
- L. Pauling, in *Aperiodicity and Order*, Vol. 3: *Extended Icosahedral Structures*, Ed. by M. V. Jaric and D. Gratias (Academic, Boston, 1988), p. 137.

Translated by L. Man

DIFFRACTION AND SCATTERING OF IONIZING RADIATION

Approximation of Local Reflection in Meridional Schemes of Bragg Focusing

L. N. Gyngazov and S. I. Tyutyunnikov

Joint Institute of Nuclear Research, Dubna, Moscow oblast, 141980 Russia

e-mail: post@jinr.dubna.ru

Received November 29, 2001

Abstract—The wave amplitudes in the vicinity of the focus in monochromatic focusing are calculated in the approximation where each point of the surface of a weakly bent single crystal reflects an X-ray wave as a planar crystal, while the reflection coefficient is a coordinate function of the deviation from the exact Bragg condition. These amplitudes are calculated for all the meridional diffraction geometries (those for plane and spherical waves and the Johann and aberration-free schemes). For all these schemes, the quantitative characteristic of the process of polychromatic focusing—the intensity integrated over the pass band—is introduced and calculated. The analytical expressions of polyprofiles necessary for the consideration of these schemes are also derived. © 2002 MAIK “Nauka/Interperiodica”.

INTRODUCTION

When one describes the properties of X-ray image obtained in the focus of a Bragg spectrometer with a weakly bent crystal, some useful results can be obtained in the approximation of local reflection [1]. In this case, it is assumed that each point of the surface of a bent crystal reflects an incident X-ray wave as a planar crystal with the reflection coefficient being the function of only the deviation from the exact Bragg angle. Since the reflection vector $\mathbf{h}(x)$ for a bent crystal becomes the function of the coordinate measured along the crystal surface (Fig. 1), the amplitude of the wave diffracted at the symmetric reflection has the form

$$E_h(x, y) = \exp i\varphi(x, y) D[(\chi_0 - \alpha(x))/\chi], \quad (1)$$

$$\alpha(x) = [\mathbf{k}(x) + \mathbf{h}(x)]^2/k^2 - 1.$$

In the general case, the direction of the vector $\mathbf{k}(x)$ of the incident wave is assumed to be varying. In Eq. (1), $\varphi(x, y)$ is the phase of the incident wave, χ and χ_0 are the X-ray susceptibilities of the given reflection, and the y -axis coincides with the generatrix of the cylindrically bent crystal, whereas the function

$$D(\eta) = \begin{cases} i\eta + (1 - \eta^2)^{1/2}, & |\eta| < 1 \\ i[\eta - \text{sgn}(\eta)(\eta^2 - 1)^{1/2}], & |\eta| > 1 \end{cases}$$

is the Darwin amplitude of the diffraction reflection of a monochromatic wave from an ideal thick crystal. Using the value of the amplitude at the crystal surface given by Eq. (1), one can obtain the field of the reflected

wave using the Huygens–Fresnel principle [2],

$$E(\xi, z) = iks \int E_h(x, y) \times \exp ikr(x, y, \xi, z)/r(x, y, \xi, z) dx dy / (2\pi), \quad (2)$$

where $r(x, y, \xi, z)$ is the distance from the crystal point with the coordinates (x, y) to the point of observation (ξ, z) and s is the sine of the diffraction angle. Later, we shall show that, irrespectively of the reflection scheme, the integral in Eq. (2) will have a maximum—the focal image of the radiation source. The behavior of the wave amplitude in the vicinity of the focus can be described

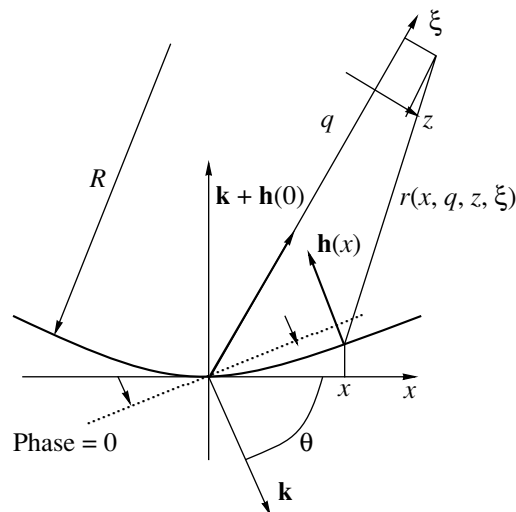


Fig. 1. Typical scheme of meridional focusing. The amplitude of the reflected wave is set in the ray coordinates with the origin being located at the focus, the ξ -axis coinciding with the $\mathbf{k} + \mathbf{h}(0)$ direction, and the z -axis being normal to it. The reflection vector h is the function of the coordinate x .

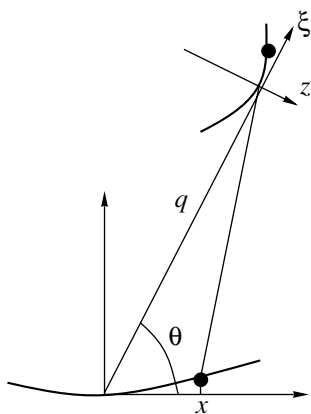


Fig. 2. Dispersion curve and polyprofile set in the ray coordinate system (ξ, z) of the central beam.

in the system of ray coordinates with the origin at the focus point, with the ξ -axis coinciding with the direction $\mathbf{k} + \mathbf{h}$ and the z -axis being normal to it. (Fig. 1). The condition of the applicability of the local approximation is given below.

Now, consider the geometry of meridional focusing. The diffraction plane of a cylindrically bent crystal coincides with the bending plane. We distinguish between two types of focusing. *Focusing of a monochromatic wave* in which a wave with fixed k is reflected from the surface region within which the Darwin amplitude in Eq. (1) has a non-zero value. In this case, one focus is formed, and the squared modulus of Eq. (2) determines the spatial intensity distribution in the vicinity of this focus. *Polychromatic focusing* is considered as a reflection of the radiation with a white spectrum. Each ray from the pass band has its individual energy [3] and is reflected with the formation of a focus by the monochromatic mechanism. The waves from the spectral band reflected by a bent crystal form the *polychromatic (dispersion) curve*, a set of monofoci of the diffracted waves. This curve is an envelope of the system of reflected rays from the pass band. The intensity of the focused band—the *polyfocus profile*—is concentrated in the vicinity of the dispersion curve. The dispersion curve and the profile function are set in the ray coordinates (ξ, z) of the *central ray* (Fig. 2). The “color” of the X-ray intensity maximum varies along the polychromatic curve.

Below, we study the spatial behavior of the wave amplitude in monochromatic focusing and the wave intensity in polychromatic focusing for all the meridional reflection schemes, namely, those of plane and spherical waves and the Johann [4] and aberration-free schemes. Each of these schemes is characterized by a specific form of the function $\alpha(x)$, the function of a monochromatic amplitude, the shape of the dispersion curve, and the polyfocus profile, which is determined as the sum of monoprofiles of the pass band with due

regard for the varying position of the profile maximum on the dispersion curve.

PLANE WAVE

In the scheme of a plane wave, the deviation has the form $\alpha(x) = -4csx/R$. The focus is located at a distance of $q = Rs/2$ along the direction of the diffracted wave, and the amplitude in the vicinity of the focus has the form

$$E(\xi, z) = \chi/(2c)(\pi kR/(2s))^{1/2} \times H[k\chi^2\xi/(8s^2c^2), k\chi z/(2cs)],$$

$$H(x, y) = \int_{-\infty}^{\infty} D(t) \exp[-i(xt^2 + yt)] dt / (2\pi) \quad (3)$$

$$= \begin{cases} J_1(y)\theta(y)/y, & x = 0 \\ \exp(-ix/2)[J_0(x/2) + iJ_1(x/2)]/4, & y = 0. \end{cases}$$

Hereafter, $J_\nu(z)$ is the Bessel function and c is the cosine of the diffraction angle. It can be shown [5] that the dispersion curve in this case is a parabola $2\xi^2 + 3Rcz = 0$ and the polychromatic intensity in the vicinity of this curve is described by the equation

$$I(\xi, z) = 2/(3cl) \int_{-3cl/4}^{3cl/4} |E(\xi - t, z - 4\xi t/(3cR) - 2t^2/(3cR))|^2 dt, \quad (4)$$

where the amplitude E is given by Eq. (3) and l is the crystal length in the scattering plane. The squared modulus of the function $H(x, y)$ and the profile described by Eq. (4) are shown in Figs. 3 and 4. Since the amplitude with respect to the variable ξ in Eq. (3) decreases more slowly (by a factor of $1/\chi$) than in the transverse direction, the variation in the first argument of the integrand in Eq. (4) can be ignored. Then, using Eq. (3) and performing integration, we can rewrite Eq. (4) in the region determined by the following inequalities (Fig. 5):

$$3cRz + 2\xi^2 > 0, \quad Rz < \pm\xi l + 3cl^2/8 \quad (5)$$

and the polyprofile in the form

$$I(\xi, z) = \pi\chi R/(8c^2l)[kR\chi/(3s)]^{1/2} \times \Psi_1(k\chi[z + 2\xi^2/(3cR)]/(2cs)),$$

$$\Psi_1(u) = 4u^{1/2} \int_0^1 J_1^2(u[1-x^2]) / (u[1-x^2])^2 dx \quad (6)$$

$$= u^{-3/2} \{1 - {}_2F_3(1/2, -1/2; 1/4, -1/4, 2; -u^2)\},$$

where ${}_mF_n(\alpha_1, \dots, \alpha_m; \beta_1, \dots, \beta_n; z)$ is the generalized hypergeometrical function [6]. The region described by inequalities (5), where the polyprofile is expressed ana-

lytically, is, in fact, the working space of the energy-dispersive exposure; in this region, the specimen in the absorption experiment is located in the vicinity of the dispersion curve.

For monochromatic focusing, we calculated the amplitudes without using the approximation of a weak bending (local reflection) [2]. In this case, the amplitude has the integrated form (3), where the Darwin amplitude is substituted by the expression

$$R_v(\eta) = (iv)^{1/2} D_{-iv-1}[-i(iv)^{1/2}\eta] / D_{-iv}[-i(iv)^{1/2}\eta]. \quad (7)$$

Here, $D_\mu(z)$ is the function of a parabolic cylinder, $v = kR\chi^2\beta$, and β is a certain function of elastic constants of the crystal. For a weak bending ($v \gg 1$), the following transition is known to take place [7]:

$$\lim_{v \rightarrow \infty} R_v(\eta) = D(\eta);$$

i.e., at $R \gg 1/(k\chi^2)$, we pass to the region of the local approximation, which adequately describes the image of a very distant X-ray source created by reflection from a weakly bent crystal. This speculation justifies the approximation of the local reflection. Using Eq. (1), we can obtain the amplitudes in other geometries of meridional focusing.

SPHERICAL WAVE

If the source-crystal p and crystal-image q distances are different, the monoamplitude is described by an expression similar to Eq. (3),

$$E(\xi, z) = \frac{\chi}{4cq} \frac{2q - Rs}{Rs - q} (\pi kR/s)^{1/2} \times H\left(\frac{k\chi^2 R^2 \xi}{32c^2 (Rs - q)^2}, \frac{k\chi Rz}{4c(Rs - q)}\right),$$

with the term indicating the position of the focus under the condition that $1/p + 1/q = 2/Rs$. Then, the dispersion curve is again a parabola,

$$8cR(1 - \gamma^2)(1 + \gamma)z + 3\xi^2 = 0, \quad \gamma = q/p,$$

whose minimum curvature is attained if $p = 3q$. The polychromatic profile in this scheme is described by the relationship similar to Eq. (4).

JOHANN SCHEME

The condition $p \rightarrow q = Rs$ provides the imaging of a point source into a point. For such a scattering geometry, the deviation from the Bragg condition has the form

$$\alpha(x) = -4cs(1/R - s/p)x - 2c^2 x^2/R^2, \quad (8)$$

and the amplitude in the monochromatic focus is

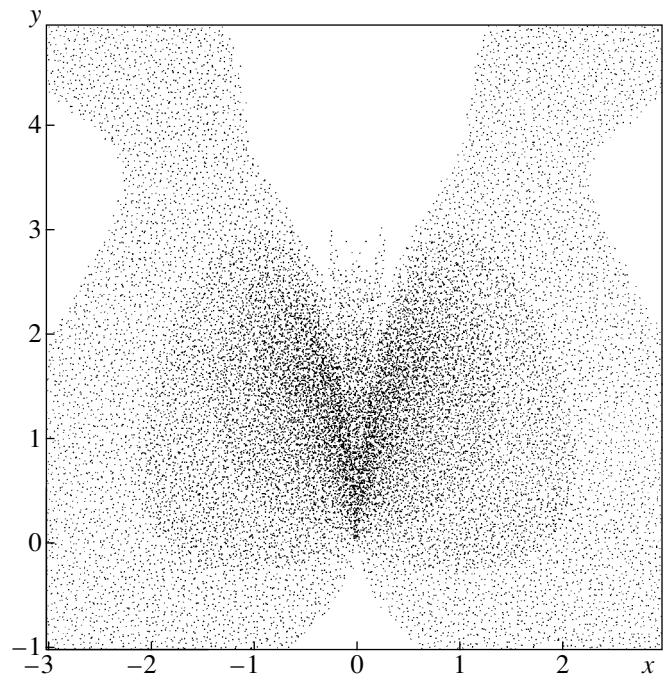


Fig. 3. Microprofile function (view from above), which describes the focusing schemes of a plane and spherical ($p \neq q$) waves and the aberration-free scheme ($p \neq ae$).

expressed as

$$E(\xi, z) = (\pi\chi k/(2sR))^{1/2} / cK[k\chi\xi/(4c^2), k(\chi/2)^{1/2}z/c, (2/\chi)^{1/2}(p/R - s)], K(\xi, z, t) = \int_{-\infty}^{\infty} D(x^2 + 2tx) \exp i(\lambda x^4 - \xi x^2 - zx) dx / (2\pi), \quad (9)$$

$$\lambda = kR\chi^2 / (16sc^4).$$

Since $kR\chi^2 \gg 1$, then, at $p = Rs$, the E can be approximately written as

$$E(\xi, z) = (2\pi)^{1/2} (k/(sR^3))^{1/4} [\Pi(x, y) + \lambda^{-1/2} \partial \Pi(x, y) / \partial x], x = (ks/R)^{1/2} \xi, \quad y = (4sk^3/R)^{1/4} z, \quad (10)$$

$$\Pi(x, y) = \int_{-\infty}^{\infty} \exp i(t^4 - xt^2 - yt) dt / (2\pi).$$

The latter expression is, in fact, the Piercey function [8] showing “longitudinal behavior”

$$\Pi(z, 0) = e^{-iz^2/8 + i\pi/8} \begin{cases} (z/2)^{1/2} [J_{-1/4}(z^2/8) + e^{-i\pi/4} J_{1/4}(z^2/8)] / 4, & z > 0 \\ |z|^{1/2} H_{-1/4}^{(1)}(z^2/8) / 4, & z < 0, \end{cases} \quad (11)$$

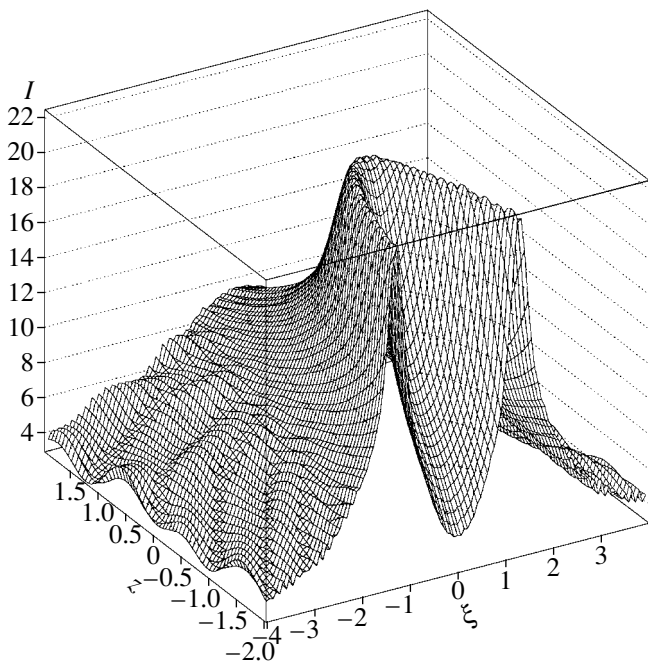


Fig. 4. Profile of a polychromatic focus for the parabolic dispersion curve.

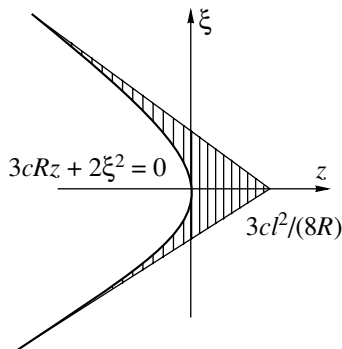


Fig. 5. Region of determination of the polychromatic intensity (6), the part of the polyfocus within which all the rays of the pass band propagate.

where $H_v^{(1)}(z)$ is the Hankel function. In the transverse direction, the Piercey function is determined, based on Eq. (11), as

$$\begin{aligned}
 &4\pi\Pi(0, 4y) \\
 &= 4\pi \sum_{m=0}^{\infty} (-i16y^2)^m / (2m)! \partial^m \Pi(z, 0) / \partial z^m |_{z=0} \\
 &= e^{i\pi/8} \Gamma(1/4) [{}_0F_2(1/2, 3/4; iy^4) \\
 &- (1+i)y^2 \Gamma^2(1/4) {}_0F_2(5/2, 3/4; iy^4) / (3\pi)].
 \end{aligned}$$

The first term in (10) describes the amplitude in the vicinity of the caustic if a wave of the optical frequency is reflected from a bent interface [9]. For the X-ray range, the focus has a smaller size because of the short-

ened wavelength. Moreover, Eq. (10) includes the correction for the nonoptical X-ray diffraction mechanism of reflection from a weakly bent interface. Using Eq. (11), one can also obtain the longitudinal monochromatic profile at $\xi > 0$ with the same accuracy,

$$\begin{aligned}
 |E(\xi, 0, 0)|^2 &= \pi/(8R)(2k/(sR))^{1/2} h[ks\xi^2/(8R)], \\
 h(u)u^{-1/2} &= J_{1/4}^2(u) + J_{-1/4}^2(u) + 2^{1/2} J_{1/4}(u)J_{-1/4}(u) \\
 &- (u/\lambda)^{1/2} [J_{3/4}(u) - J_{-3/4}(u)][J_{1/4}(u) + 2^{1/2} J_{-1/4}(u)].
 \end{aligned} \tag{12}$$

At the intermediate values of the argument t , the following approximate expression is obtained for the function $K(0, 0, t)$ that describes the amplitude at the maximum:

$$K(0, 0, t) = \int_{-\infty}^{\infty} D(u) \exp i\lambda u^4 / (16t^4) du / (4\pi t).$$

Moreover, $K(0, 0, t) = 1/(4t)$ at $t \gg \lambda^{1/4}$.

Constructing the envelope for the system of specularly reflected rays from the source, we arrive at the parametric form of the dispersion curve

$$\xi = 3c^2 x^2 / (Rs), \quad z = -2c^2 x^3 / (R^2 s), \tag{13}$$

whereas summing up the profiles of the reflected rays of the pass band with due regard for the positions of all the maxima on this curve, we arrive at the intensity distribution in the polyfocus

$$\begin{aligned}
 &I(\xi, z) \\
 &= 1/(2b) \int_{-b}^b |\Pi(x - 3c^2 s^{-1/2} t^2 / 2, y + xt - c^2 t^3 / 2)|^2 dt, \tag{14} \\
 &b = l[kR/(4s)]^{1/4} / R,
 \end{aligned}$$

where x, y are taken from Eq. (10). The monochromatic intensity obtained with the use of Eq. (10) is shown in Fig. 6.

ABERRATION-FREE SCHEME

The previous scheme cannot provide rigorous "point to point" imaging—with the varying energy of the fixed source, the monofocus is displaced along the curve described by Eq. (13). If a crystal is bent along the ellipse arc and the pointlike source is located in one of its foci, the image of the source coincides with another focus of the ellipse irrespectively of the radiation energy. In the kinematic approximation, this scheme is characterized by the following relationships (Fig. 7):

$$p + q = 2a, \quad p = a + ex, \quad r = ae, \quad 0 < c < e, \tag{15}$$

where e and a are the eccentricity and the semimajor axis of the ellipse. In all cases where $p \neq ae$, the ampli-

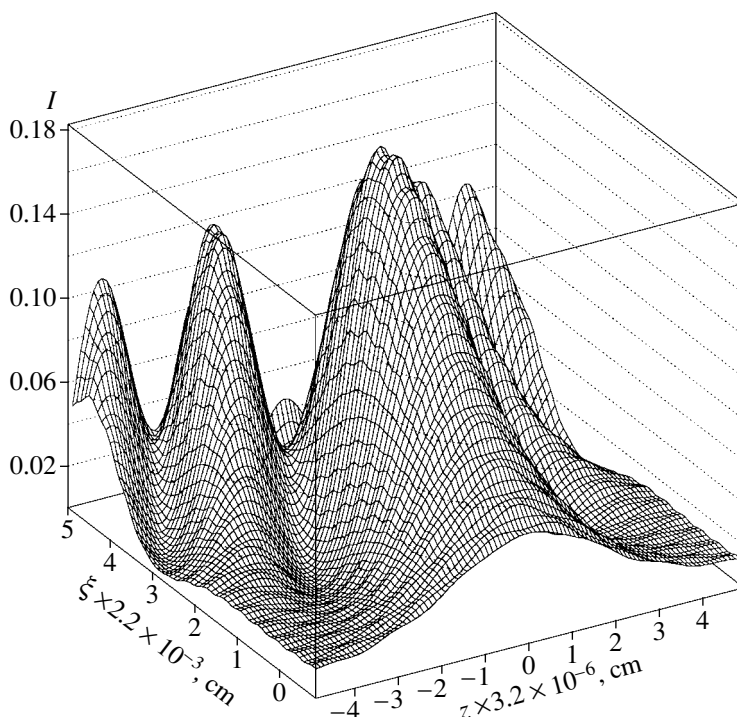


Fig. 6. Intensity in monochromatic focusing in the Johann reflection geometry.

tude of the monofocus is described in terms of the function $H(x, y)$ from (3),

$$E(\xi, z) = \frac{\chi}{4e^2 x} \left(\frac{\pi k a (1 + ex)}{2(1 - e^2)} \right)^{1/2} H(A_1 k \chi^2 \xi, A_2 k \chi z),$$

$$A_1 = \frac{(1 - x^2)(1 - e^2 x^2)(1 + ex)^2}{32e^3(1 + e)(1 - e^2)x^2}, \quad (16)$$

$$A_2 = \frac{1 + ex}{4e^2(1 - e^2)x},$$

where the coordinate x is given in units of a . The polyfocus of the aberration-free scheme is *pointlike (dispersion free)*. In this case, the spatial distribution of polyintensity has the form

$$I(\xi, z) = \frac{\pi k \chi^2 a^2}{32e^4 x^2 l} \left(\frac{1 - e^2 x^2}{1 - e^2} \right)^{3/2} \times \int_{-b}^b |H(0, A_2 k \chi [z(1 - t^2)^{1/2} - \xi t])|^2 dt, \quad (17)$$

$$b = l(1 - e^2)^{1/2} (1 - e^2 x^2)^{-1/2} / [2a(1 - ex)].$$

This function is shown in graphical form in Fig. 8. Calculating Eq. (17) in a way similar to that used for calculating Eq. (4), we obtain for a not too small value of ξ

$$I(\xi, z) = \frac{\pi k \chi a^2 (1 - ex)}{64e^2 x l \xi} \left(\frac{1 - e^2 x^2}{1 - e^2} \right)^{-1/2} \times \begin{cases} \Psi_2(z_+) - \Psi_2(z_-), & z > b|\xi| \\ \pm \Psi_2(z_{\pm}), & |z| < \pm b\xi \\ 0, & z < b|\xi|, \end{cases} \quad (18)$$

where

$$z_{\pm} = (1 + ex)k\chi[z \pm \xi b] / [4e^2(1 - e^2)x],$$

$$\Psi_2(u) = u {}_1F_2(1/2; 2, 3; -u^2).$$

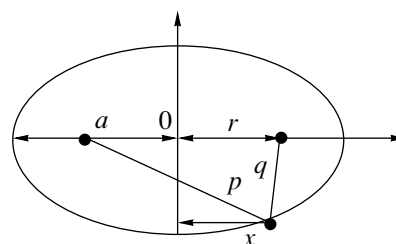


Fig. 7. Kinematics of aberration-free meridional focusing. The foci of the ellipse are the loci of the points of the source and its image.

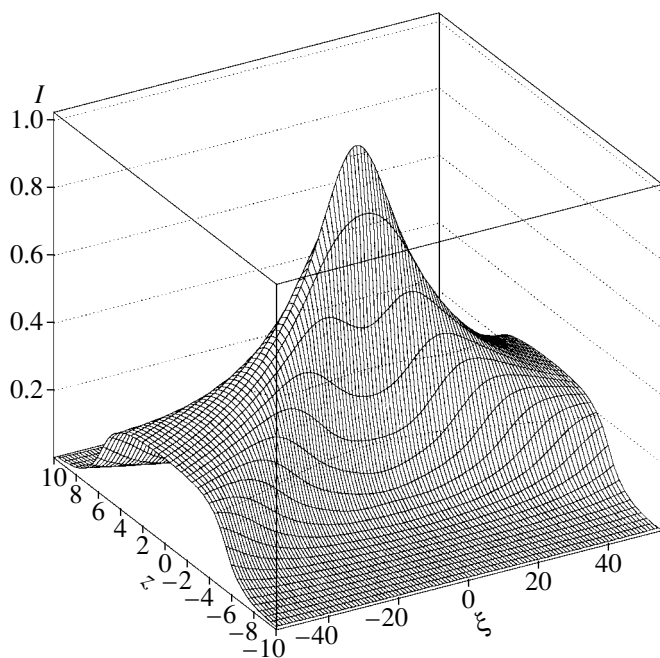


Fig. 8. Polychromatic intensity at the point (absent) dispersion.

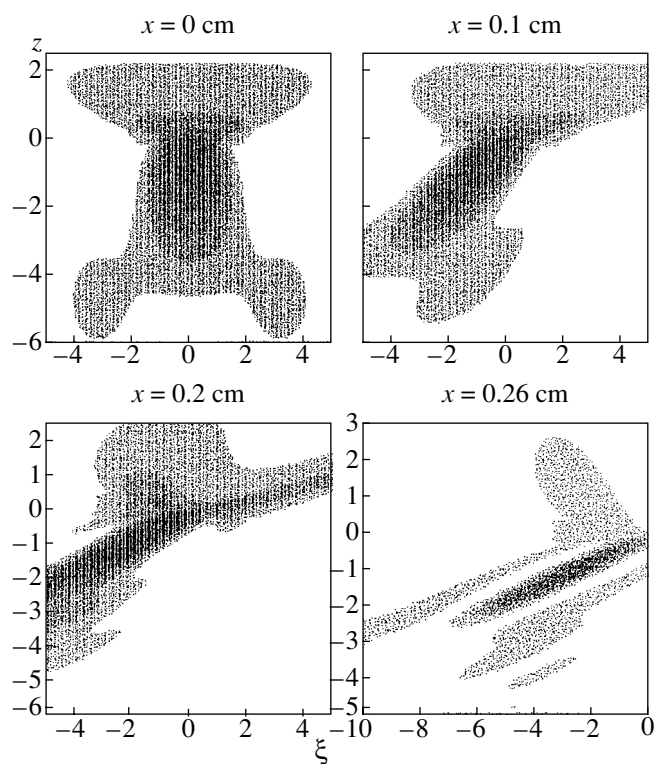


Fig. 9. Function of monochromatic intensity in aberration-free focusing at the minimum angle and different deviations from the condition $p = q$ (in cm).

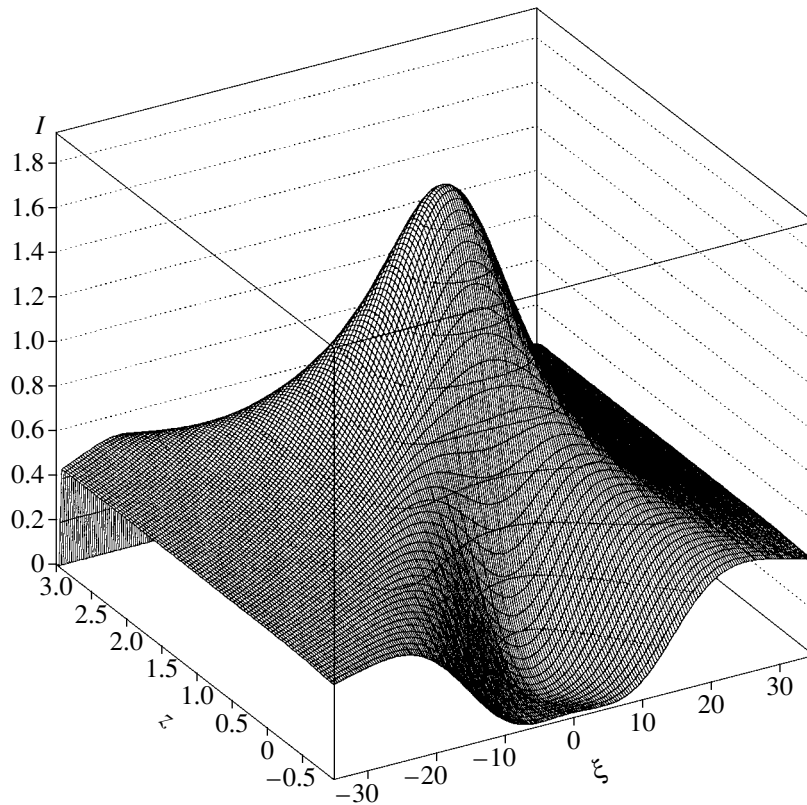


Fig. 10. Function of the polyprofile in the dispersion-free scheme at the minimum diffraction angle.

At small values of ξ and $b^2 \ll 1$, the polyprofile ($u = A_2 k \chi z$) equals

$$I(\xi, z) = \frac{\pi k a \chi^2 (1 + e x) J_1(u)}{192 e^4 x^2 (1 - e^2) u^2}$$

$$\times \{3J_1(u) + b^2 u J_2(u) + b^2 \xi^2 [J_1(u) - J_2(u) + J_3(u)]\}.$$

In the particular case of aberration-free monofocusing at the minimum diffraction angle ($p = q = ae$), we obtain, as in the Johann scheme, the quadratic deviation $\alpha(x) = -2e^2(1 - e^2)(x/a)^2$. For the amplitude, we have

$$E(\xi, z, x) = (\pi k a \chi)^{1/2} / (2e) L[k \chi \xi / (4e^2), \quad (19)$$

$$(\chi/2)^{1/2} k z / e, 2e(2(1 - e^2)/\chi)^{1/2} x/a],$$

$$L(\xi, z, t)$$

$$= \int_{-\infty}^{\infty} D(x^2 + 2tx) \exp -i(\xi x^2 + zx) dx / (2\pi), \quad (20)$$

whereas the argument x in Eq. (19) describes the deviation from the conditions $p = q$ in units of the coordinate. For the maximum of the amplitude (the function of this deviation), we obtain

$$3\pi L(0, 0, t) = \begin{cases} i(1 + t^2)^{-3/2} [1 + (1 - t^4)(3 + 2t^2)] \\ + 2^{1/2} [Q_1(t^2) + iQ_1(-t^2)], \\ |t| < 1 \\ 2^{1/2} Q_2(2^{1/2} [1 + t^2]^{-1/2}), \quad |t| > 1, \end{cases}$$

$$Q_1(u) = (1 - u)K(2^{-1/2} [1 + u]^{1/2})$$

$$+ 2uE(2^{-1/2} [1 + u]^{1/2}),$$

$$Q_2(u) = 4(E(u) - (1 - u^2)K(u))/u^3,$$

where $K(k)$ and $E(k)$ are the complete first- and second-order elliptic integrals. The pointlike polychromatic focus, based on Eq. (19) for the amplitude, has the following intensity distribution

$$I(\xi, z) = \pi 2^{-1/2} k a^2 \chi^{3/2} / [8e^3 (1 - e^2)^{1/2} l] \times \int_{-b}^b |L[0, k(\chi/2)^{1/2} z/e - k \chi \xi t / (4e^2), t]|^2 dt, \quad (21)$$

$$b = e[2(1 - e^2)/\chi]^{1/2} l/a.$$

The squared modulus of the function described by Eq. (20) and the function described by Eq. (21) are shown in graphical form in Figs. 9 and 10, respectively.

CONCLUSIONS

The case of meridional focusing is typical of X-ray spectral devices in which the beam incident onto the

crystal is characterized by a narrow collimation along the direction parallel to the generatrix of the cylindrically bent surface. The focal distances and the radius of crystal bending are usually selected to be rather large. Under the condition $kR\chi^2 \gg 1$, each point of the surface reflects with the reflection coefficient characteristic of a planar crystal and which is a function of the coordinate of this point. In this study, we obtained quantitative expressions for the amplitudes of the reflected wave in the vicinity of the focus for four different schemes of meridional focusing—those of plane and spherical waves and in the Johann and the aberration-free schemes. The first two schemes are described by the parabolic dispersion curves, the Johann scheme corresponds to the semicubic dispersion curve, and the aberration-free scattering geometry, to the point curve. We also constructed the functions of semiprofiles for the focusing of a white beam.

The polychromatic mode is discussed in connection with the fact that the focusing of the pass band is a particular property of an X-ray optical system based on a bent crystal and also in connection with its use in energy-dispersive spectral devices. To characterize the first aspect, we introduced and then calculated the intensity integrated over the pass band for all the reflective configurations. As to the second aspect, we can state that there always exists a certain neighborhood of the dispersion curve within which all the rays of the pass band propagate. The dimensions of this exposure region and the localization of the intensity within this region determines the minimum diameter of the specimen and the efficiency of the instrument in the experiments in energy-dispersive spectrometry.

The amplitude in monofocusing by the Johann scheme differs from the amplitude in the optical case by the correction described by Eq. (12), whereas for all the other focusing geometries, the X-ray amplitudes are the functions that are essentially different from the amplitudes in the vicinity of the optic caustics in the same scattering geometries. In the local approximation, the amplitudes in Bragg focusing are certain integral transformations of the Darwin amplitude. One more distinction of the focusing of waves from the wavelength ranges considered above is the fact that the optical white light yields a white caustic, whereas the X-ray white spectrum is dispersed into geometrically the same caustic, with the pass-band monofoci being distributed along this caustic in accordance with their "colors."

REFERENCES

1. V. V. Skadorov and S. I. Tyutyunnikov, Preprint No. P14-99-80, OIYaI (Joint Inst. for Nuclear Research, Dubna, 1999).
2. K. T. Gabrielyan, F. N. Chukhovskii, and Z. G. Pinsker, Zh. Tekh. Fiz. **50**, 3 (1980) [Sov. Phys. Tech. Phys. **25**, 1 (1980)].

3. L. N. Gyngazov and S. I. Tiutiunnikov, Preprint No. E14-97-332, OIYaI (Joint Inst. for Nuclear Research, Dubna, 1997).
4. V. A. Bryzgunov, Zh. Tekh. Fiz. **70** (1), 49 (2000) [Tech. Phys. **45**, 46 (2000)].
5. L. N. Gyngazov and S. I. Tyutyunnikov, Poverkhnost, No. 6, 66 (2001).
6. *Higher Transcendental Functions (Bateman Manuscript Project)*, Ed. by A. Erdelyi (McGraw-Hill, New York, 1953; Nauka, Moscow, 1965), Vol. 1.
7. F. N. Chukhovskii, K. T. Gabrielyan, and P. V. Pet-rashen', Acta Crystallogr., Sect. A: Cryst. Phys., Diffr., Theor. Gen. Crystallogr. **34**, 610 (1978).
8. T. Piercey, Philos. Mag. **37**, 311 (1946).
9. Yu. A. Kravtsov and Yu. I. Orlov, Usp. Fiz. Nauk **141**, 591 (1983) [Sov. Phys. Usp. **26**, 1038 (1983)].

Translated by L. Man

**STRUCTURES
OF INORGANIC COMPOUNDS**

Crystallochemical Characteristics of Alkali Calcium Silicates from Charoitites

I. V. Rozhdestvenskaya and L. V. Nikishova

*Department of Geology, St. Petersburg State University,
Universitetskaya nab. 7/9, St. Petersburg, 199034 Russia
e-mail: olga@of3102.spb.edu*

Received December 13, 2001

Abstract—The characteristic features of the crystal structures of alkali calcium silicates from various deposits are considered. The structures of these minerals, which were established by single-crystal X-ray diffraction methods, are described as the combinations of large construction modules, including the alternating layers of alkali cations and tubular silicate radicals (in canasite, frankamenite, miserite, and agrellite) and bent ribbons linked through hydrogen bonds in the layers (in tinaksite and tokkoite). The incorporation of impurities and the different ways of ordering them have different effects on the structures of these minerals and give rise to the formation of superstructures accompanied by a change of the space group (frankamenite–canasite), leading, in turn, to different mutual arrangements of the layers of silicate tubes and the formation of pseudopolytypes (agrellites), structure deformation, and changes in the unit-cell parameters (tinaksite–tokkoite). © 2002 MAIK “Nauka/Interperiodica”.

INTRODUCTION

Alkali calcium silicates, which contain tubular radicals such as tinaksite, tokkoite, frankamenite, and agrellite-Sr, with the structures that have been established in recent years, are exotic minerals among widespread silicates (Table 1) [1–9]. All these minerals were found at the Murun massif (Yakutia), unique not only because of the discovery there of a very beautiful mineral charoite at the Sirenevyy Kamen’ deposit, but also because of ultrapotassium specialization. Many unusual rocks found in this massif are used as ornamental raw materials, of which charoitites are the most well-known ones [10].

Close concretions, intergrowth, and gradual transformations of these minerals into other minerals are indicative of their constitutional relation and metasomatic genesis. The studies of these minerals demonstrated that, despite different compositions and structures, they can be considered from a unified standpoint within the framework of modern modular theory [11, 12] as layered structures consisting of alternating large construction modules.

Silicon, calcium, alkali metals (potassium and sodium), oxygen, fluorine, and hydroxy groups are the major components of these minerals. The ratio between the fluorine atoms and the hydroxy groups determines the fine characteristics of their structures, which involve silicon–oxygen radicals as the major components found exclusively in these minerals. The radicals form either tubes or bent ribbons with broad channels along two crystallographic axes. Silicate radicals are located between the walls of the Ca- and Ca,Na-polyhedra.

ALKALI CALCIUM SILICATES WITH TUBULAR [Si₁₂O₃₀]¹²⁻ RADICALS

The presence of the tubular radicals [Si₁₂O₃₀]¹²⁻ is common to several minerals—frankamenite, canasite, and miserite (Table 2).

The crystal structures of frankamenite [1] and canasite [2] may be considered as a set of infinite zigzag layers (walls) formed by the Ca,Na-octahedra (Figs. 1, 2) and linked via layers of the one-dimensionally infinite silicon–oxygen radicals [Si₁₂O₃₀]¹²⁻.

The minimum structure fragment containing one silicate tube and a minimum number of independent octahedra of the zigzag wall linked with this tube can be chosen as the unit cell. Then, the choice of the directions of the crystallographic axes and unit-cell parameters is apparent. This minimum fragment is exemplified by the unit cell of frankamenite (sp. gr. *P1*) (Fig. 2).

Monoclinic canasite with the same structural motif is characterized by the ordered arrangement of the octahedral cations dictating an alternative choice of crystallographic axes (Fig. 2). The unit-cell volume of the canasite structure is doubled compared to that of frankamenite (Table 2). The monoclinic unit cell of canasite is related to the triclinic unit cell of frankamenite by the following transformation matrix: $a_{tr} = (1/2a_m + b_m)$; $b_{tr} = c_m$; $c_{tr} = -b_m$ [1].

Like the frankamenite and canasite structures, the miserite structure [3, 4] contains the tubular silicate radical [Si₁₂O₃₀]¹²⁻ (Fig. 3). The tubes are linked to form layers located between the octahedral walls that have a structure that is more complicated than the walls

Table 1. Crystallochemical formulas and localities of the minerals

Mineral name	Crystallochemical formula	Locality, reference
Frankamenite	$K_3Na_3Ca_5[Si_{12}O_{30}](OH)F_3 \cdot H_2O$	Murun massif, Yakutia, [1]
Canasite	$K_3Na_3Ca_5[Si_{12}O_{30}](OH, O)_{2.5}F_{1.5}$	Khibiny massif, the Kola Peninsula, [2]
Miserite	$K_3Ca_{10}(Ca, M^{3+})_2[Si_{12}O_{30}][Si_2O_7]_2(O, F, OH)_2 \cdot H_2O$, where $M^{3+} = Y, REE, Fe$	Quebec, Canada, [3]; Dara-i-Pioz, Pamirs, [4]
Agrellite-Sr	$Na_2(Ca, Sr)_4[Si_8O_{20}]F$	Murun massif, Yakutia, [5]
Agrellite-RE	$Na_2(Ca, REE)_4[Si_8O_{20}]F$	Quebec, Canada, [6]
Tokkoite	$K_2Ca_4[Si_7O_{18}(OH)](F, OH)$	Murun massif, Yakutia, [7]
Tinaksite	$K_2Ca_2NaTi[Si_7O_{18}(OH)]O$	Murun massif, Yakutia, [8]
Charoite	$(K, Na)_5(Ca, Ba, Sr)_8[Si_{12}O_{30}][Si_2O_7][Si_4O_9](F, OH)_2 \cdot nH_2O$	Murun massif, Yakutia, [9]

Table 2. Crystallographic data for minerals with tubular radical $[Si_{12}O_{30}]^{12-}$

Data	Frankamenite	Canasite	Miserite
$a, \text{\AA}$	10.094(3)	18.836(4)	10.120(3)
$b, \text{\AA}$	12.692(3)	7.244(1)	16.077(3)
$c, \text{\AA}$	7.240(1)	12.636(2)	7.378(2)
α, deg	90.00(2)	90.0	96.62(2)
β, deg	111.02(2)	111.76(2)	111.15(2)
γ, deg	110.20(2)	90.0	76.33(2)
$V, \text{\AA}^3$	804.5(7)	1601.3(8)	1087.4(5)
Z	1	2	1
Sp. gr.	$P1$	Cm	$P\bar{1}$

in the frankamenite and canasite structures. The unit cell is the minimum structure fragment and contains one silicate tube.

The octahedral wall of frankamenite may be conceived as a layer composed of four edge-sharing octahedral columns (Fig. 2). The structure of the walls was described in detail elsewhere [1, 2].

The octahedral positions in the frankamenite structure are filled differently than in canasite, despite the fact that in both structures the positions are occupied predominantly by Ca^{2+} and Na^+ cations. Of the eight positions in the triclinic structure of frankamenite, one position ($M1$) is completely occupied by Na^+ cations and one more position ($M2$), by Ca^{2+} cations (Fig. 2, Table 3). These octahedral positions alternate in one of the octahedral columns along the z -axis. In all other columns, the octahedral positions are isomorphously occupied by Ca^{2+} and Na^+ cations. The $M3$ and $M4$ positions are occupied by approximately equal numbers of these cations, whereas the $M5$ – $M8$ positions are filled with by Ca^{2+} and Na^+ cations in a ratio of approximately 2 : 1. The composition of the octahedral wall is $Na_{3.14}Ca_{4.86}$ [1].

The monoclinic structure of canasite contains only six independent octahedral positions. The ordered

Table 3. Distribution of Na and Ca atoms in the frankamenite and canasite structures

Position	Frankamenite	Canasite
$M1$	Na	Na
$M2$	Ca	Ca
$M3$	$Na_{0.52}Ca_{0.48}$	Ca
$M4$	$Na_{0.46}Ca_{0.54}$	$Na_{0.44}Ca_{0.43}R_{0.13}^1$
$M5$	$Na_{0.30}Ca_{0.70}$	Ca
$M6$	$Na_{0.31}Ca_{0.69}$	Na
$M7$	$Na_{0.27}Ca_{0.73}$	$Na_{0.44}Ca_{0.43}R_{0.13}^1$
$M8$	$Na_{0.28}Ca_{0.72}$	Ca

Note: $R = Fe, Mn, Mg, Al, Ti$.

arrangement of the cations in these positions is more obvious. One of the octahedral positions in each of two vertex-sharing columns ($M1, M2$ and $M3, M6$) is occupied by the Ca^{2+} cations, and the other position is occupied by the Na^+ cations. In the adjacent vertex-sharing columns, two calcium octahedra and two sodium octahedra alternate (Fig. 2). The octahedra on the opposite sides of the columns are filled differently (Table 3). Hence, the cationic composition of the sides of the octahedral wall are nonequivalent. The general atomic composition of the octahedral positions in the canasite structure is $Na_{2.96}Ca_{4.69}R_{0.38}$ (where $R = Fe, Mn, Mg, Al, Ti$) and is similar to the composition of the octahedral positions in the frankamenite structure. However, the octahedral positions in the canasite structure are occupied in a more ordered way, which results in a doubling of the a parameter and a change in the space group (Table 2).

In the miserite structure, the octahedral walls are two times thicker than in the frankamenite and canasite structures, because they are formed by two zigzag layers of edge-sharing octahedra and seven-vertex polyhedra (Fig. 3). The isolated silicate diortho groups $[Si_2O_7]^{6-}$ are located between these layers and alternate with vacancies along the z -axis. Generally, five of the

six octahedral positions are occupied mainly by Ca^{2+} cations, whereas one position is filled with a large number of trivalent Y^{3+} and REE^{3+} cations (Fig. 3).

Belov proposed [13] to consider a $[\text{Si}_{12}\text{O}_{30}]^{12-}$ silicate radical as a one-dimensionally infinite tube formed due to the condensation of four wollastonite chains or two xonotlite ribbons (Fig. 1). However, comparing the Si–O–Si angles in the silicate radical in the minerals considered in our works with the analogous angles in wollastonite and pectolite, we concluded that the tube of the $[\text{Si}_{12}\text{O}_{30}]^{12-}$ silicate radical should be treated as a combination of four pectolite chains. This is all the more true if one takes into account the mixed Ca,Na composition of the octahedral walls in the frankamenite and canasite structures [1, 2].

Positions of the K^+ cations and H_2O molecules. The vertex-sharing tetrahedra of the silicate tube form eight-, six-, and four-membered windows. The eight-membered windows inside the silicate tube are occupied by potassium atoms. The charges of these cations are compensated not only with six oxygen atoms located inside the same tube, but also with three oxygen atoms of the adjacent tube, thus linking the radicals in the layer (Figs. 1, 3). The centers of the silicate radicals are occupied by alternating potassium atoms and H_2O molecules separated by half a translation along the tube axis.

Special positions of the anions. In this group of minerals, F^- , OH^- , and O^{2-} anions not bonded to the silicate radical take part in the formation of octahedral walls. Although these anions were not distinguished by the X-ray diffraction methods, some assumptions can be made on their distribution over the positions with due regard for the sums of valence strength obtained in the calculations of the local valence balance by the method suggested by Pyatenko [14].

The charges of F^- , OH^- , and O^{2-} anions in the positions within the octahedral walls are compensated with $\sim 1/6$ of the charges of each of the four cations of the coordination spheres about these anions. Consequently, the compensation of the charge of the F^- anion requires that two Na^+ and two Ca^{2+} cations should be included into its coordination sphere, one Na^+ and three Ca^{2+} cations are necessary for the compensation of the charge of an OH^- anion, and four Ca^{2+} cations are required in the case of O^{2-} .

Hence, the distribution of cations over the octahedral positions correlates with the distribution of anions over the positions within the octahedral wall that are not bonded to the silicate radical. The proposed cation and anion distribution agrees well with the results of calculations of the valence strengths V_a and the total charge of the Z cations in four octahedral positions (Tables 3, 4).

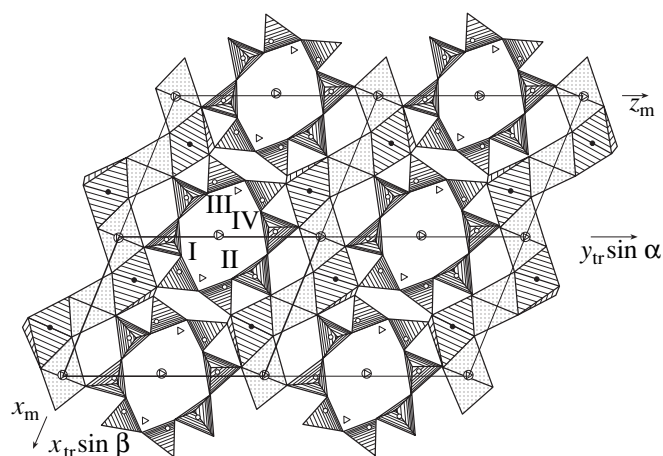


Fig. 1. Frankamenite and canasite structures projected along the elongation axis. The triclinic unit cell is shown by bold lines.

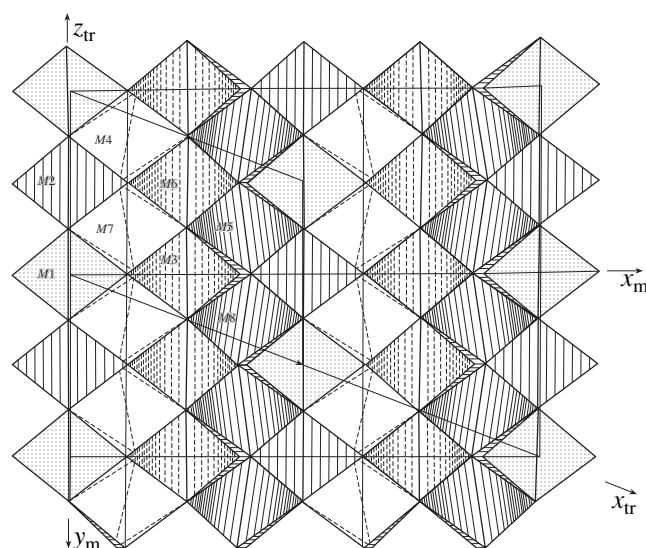
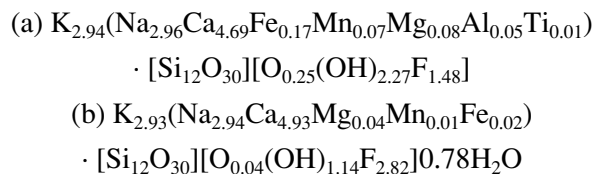


Fig. 2. Octahedral wall in the frankamenite and canasite structures. The columns of the octahedra are hatched. In both structures, the M1 and M2 octahedra are occupied by the Na^+ and Ca^{2+} cations, respectively, and the other octahedra have different compositions. The chosen axes in the monoclinic and triclinic unit cells are shown; the common origin of coordinates is located in the M1 position.

A comparison of the crystallochemical formulas of (a) canasite from the Khibiny massif and (b) frankamenite from the Murun massif:



reveals the difference in the amount of F^- and OH^- for virtually identical cationic composition. The presence

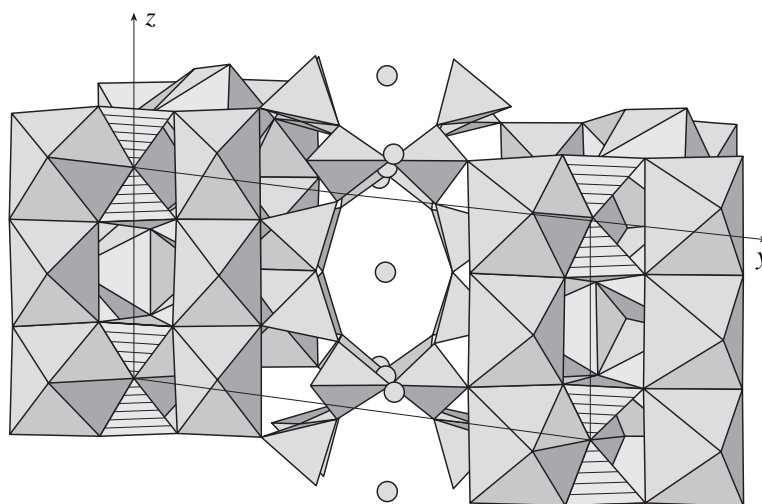
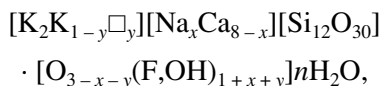


Fig. 3. Miserite structure projected onto the yz -plane; Si_2O_7 diortho groups are hatched.

of OH^- groups in the positions within the octahedral wall in canasite leads to the stabilization of the structure via hydrogen bonds with tubular radicals, whereas the incorporation of F^- anions into these positions in frankamenite impairs the stability of the structure. In addition, the mode of the distribution of cations over the octahedral positions is indicative of the presence of a larger number of mixed (Ca,Na) positions in the frankamenite structure, which gives rise to microtwinning and deteriorates the quality of single crystals.

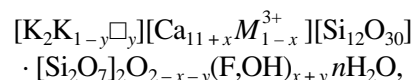
The general structural formula of canasite and frankamenite may be written as follows:



where $0 \leq x \leq 3$, $0 \leq y \leq 1$, \square are vacancies in the K^+ cationic positions located on the axis of the silicate radical, $n \leq 1.0$.

In miserites, whose crystal structures involve trivalent cations compensating for an excessive negative charge of the anionic radical, the REE content is gener-

ally not higher than one atomic unit per formula. As a rule, the K^+ content in the structure is lower than three atomic units per formula, which suggests that some oxygen atoms of the anionic radical are replaced by the OH^- groups. The structural formula of miserite may be represented as follows:



where $0 \leq x \leq 1$, $0 \leq y \leq 1$, \square are vacancies in the K^+ cationic positions located on the axis of the silicate radical, $n \leq 1.0$.

STRUCTURAL FEATURES OF AGRELLITES

Strontium and rare-earth agrellites (Table 1) have close unit-cell parameters (Table 5). These minerals differ primarily in their chemical compositions. Thus, calcium atoms are partly replaced by strontium and rare-earth atoms in the agrellite-Sr and agrellite-RE structures, respectively. However, this seemingly insign-

Table 4. Octahedra coordinating the special anionic positions, the total charges of the cations (Z), and the sums of the valence strength of anions (V_a)

Anionic position	Cationic position*	Canasite			Frankamenite		
		anions	Z	V_a^2	anions	Z	V_a^{**}
F1	$M1, M3, M4, M7$	F, OH	6.12	1.27	F	5.91	1.04
F2	$M2, M4, M6, M7$	F, OH	6.12	1.18	F, OH	6.97	1.17
F3	$M2, M3, M5, M8$	O, OH	8.00	1.33	F, OH	6.89	1.17
F4	$M1, M5, M6, M8$	F	6.00	1.01	F	5.95	1.04

* Occupancies of octahedra by the Ca^{2+} and Na^+ cations are indicated in Table 3.

** Calculated according to Pyatenko (1972).

nificant change in composition leads to substantial differences in their structures.

In the crystal structure of agrellite, the walls of the Ca-polyhedra (octahedra and seven-vertex polyhedra), which are parallel to the (010) plane, are linked to each other through silicate tubes of the composition $[\text{Si}_8\text{O}_{20}]^{8-}$ along the z -axis (Fig. 4). The eight-membered boat-like windows of the tubes are occupied by the Na^+ cations. Each unit cell contains two layers of Ca-polyhedra and two silicate-sodium layers [5, 6]. The agrellite-*RE* structure is characterized by the presence of a C -pseudo-centered cell, which is well seen from the coordinates of all atoms, except for the F atoms. As a consequence of the violation of the C -centered arrangement by fluorine atoms, two types of coordination polyhedra (octahedra and seven-vertex polyhedra) are formed about the Ca atoms. All the atoms, except for F, and also silicate tubes and pairs of the Ca-polyhedra related by the pseudotranslation $[1/2 \ 1/2 \ 0]$ were denoted by A and B in the original study [6]. In a similar way, only F atoms violate the centered packing of the agrellite-Sr structure, whereas Ca atoms are arranged so as to satisfy both the C - and I -centered arrangements [5].

These agrellite species differ primarily because of the arrangement of silicate tubes and alkali cations bonded to these tubes. The mutual arrangement of the A and B silicate layers can be characterized by the vector equal to half a diagonal in the (001) plane (conditionally, the C -centered packing) in the agrellite-*RE* structure and by the vector equal to half a body diagonal of the unit cell (conditionally, the I -centered packing) in the agrellite-Sr structure. In other words, the arrangements of the octahedral walls and the A silicate tubes are the same in both structures, whereas B silicate tubes and Na^+ cations bonded to these tubes are shifted by half a translation along the c -axis in the agrellite-Sr structure in comparison with their arrangement in the agrellite-*RE* structure (Fig. 5) [5].

The $[\text{Si}_8\text{O}_{20}]^{8-}$ silicate radical can be considered as a tube consisting of two chains related by a center of symmetry, with each chain being formed by the four-membered rings of vertex-sharing Si-tetrahedra [5, 6]. The tube has four-, six-, and eight-membered windows (Fig. 5).

Characteristic features of Ca-walls. Calcium polyhedra are formed by terminal oxygen atoms of the silicate tubes and F atoms. The cations in the Ca2A and Ca1B positions have an octahedral environment. The sharing-edge octahedra alternate along the z -axis to form chains. The coordination environment about the cations in the Ca1A and Ca2B positions are seven-vertex polyhedra also linked into chains along the z -axis. Chains of the octahedra and seven-vertex polyhedra share vertices and edges to form a wall parallel to the (010) plane. There are two polyhedra in each chain per c -period of the unit cell. The A and B silicate tubes are

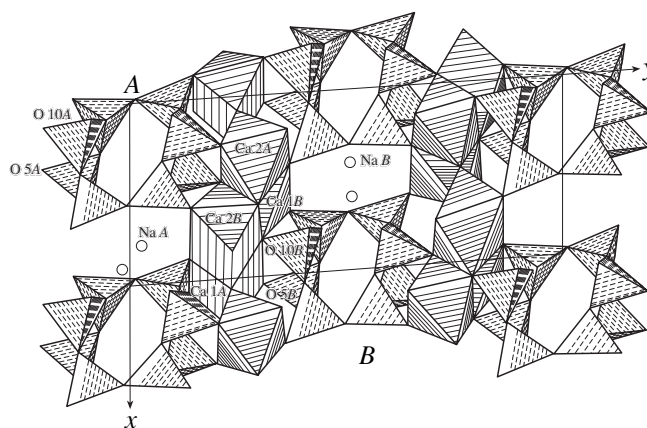


Fig. 4. Agrellite-Sr structure projected onto the (001) plane.

bonded to the lateral edges of these polyhedra formed by the oxygen atoms alternating along the z -axis.

In both structures under consideration, the major impurity atoms (Sr and *REE*) are located in the Ca1A polyhedra (Table 6). Other positions in the agrellite-*RE* structure incorporate only insignificant amounts of rare-earth elements. In the agrellite-Sr structure, the Ca2B position is occupied by Ca atoms, and the Ca1B and Ca2A positions are isomorphously occupied by Ca and Na atoms. Hence, these structures have a different

Table 5. Crystallographic data for agrellites, sp. gr. $P\bar{1}$

Data	Agrellite-Sr*	Agrellite- <i>RE</i> **
a , Å	7.788(4)	7.759(2)
b , Å	18.941(2)	18.946(3)
c , Å	6.995(4)	6.986(1)
α , deg	90.17(9)	89.88(2)
β , deg	116.78(8)	116.65(2)
γ , deg	94.16(4)	94.32(2)
V , Å ³	918.0(3)	914.7(4)
Z	4	4

* Crystallochemical formula of agrellite-Sr:
 $(\text{Na}_{0.94}\text{K}_{0.03})(\text{Ca}_{1.75}\text{Sr}_{0.16})[\text{Si}_4\text{O}_{10}][\text{F}_{0.78}(\text{O}, \text{OH})_{0.22}] \cdot 0.24\text{H}_2\text{O}$.

** Crystallochemical formula of agrellite-*RE*:
 $(\text{Na}_{1.01}\text{K}_{0.02})(\text{Ca}_{1.82}\text{REE}_{0.12}\text{M}_{0.04})[\text{Si}_{3.90}\text{Al}_{0.01}\text{O}_{9.92}][\text{F}_{0.93}(\text{OH})_{0.18}]$.

Table 6. Occupancies of the cationic positions in the agrellite structures

Polyhedron	Agrellite-Sr	Agrellite- <i>RE</i>
Ca2A	$\text{Ca}_{0.90}\text{Na}_{0.10}$	$\text{Ca}_{0.993}\text{REE}_{0.007}$
Ca1A	$\text{Ca}_{0.70}\text{Sr}_{0.30}$	$\text{Ca}_{0.853}\text{REE}_{0.147}$
Ca1B	$\text{Ca}_{0.86}\text{Na}_{0.14}$	$\text{Ca}_{0.978}\text{REE}_{0.022}$
Ca2B	$\text{Ca}_{1.0}$	$\text{Ca}_{0.985}\text{REE}_{0.015}$

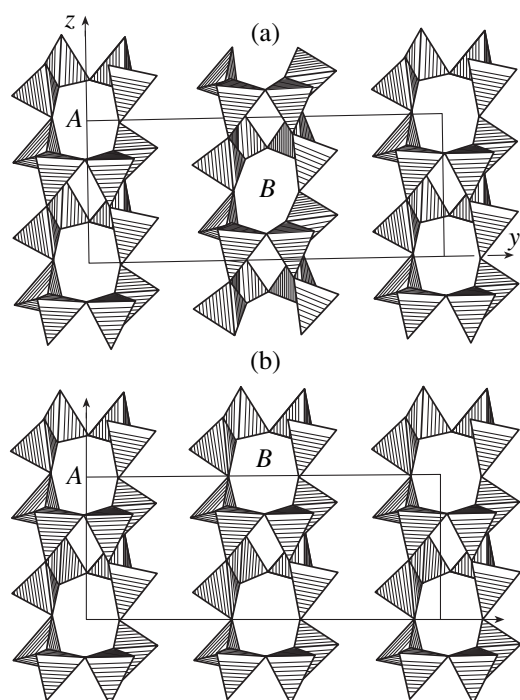


Fig. 5. Mutual arrangement of the A and B silicate tubes in the (a) agrellite-Sr and (b) agrellite-RE structures projected onto the (100) plane. In both structures, the B tube is shifted by $a/2$ with respect to the A tube.

order of cations in the two adjacent Ca-walls, which results in the doubling of the unit-cell parameter b .

Characteristic features of the junction of Ca-walls and Si radicals. The role of the geometric factor. It is of interest to compare the lengths of the O5–O10 edges adjacent to four-membered rings and the lengths of the corresponding edges between the rings in the A and B tubes. In both structures, the O5–O10 edges adjacent to the four-membered rings of the A and B tubes are larger than the O5–O10 edges between the rings. In the agrellite-RE structure, the O5B–O10B edge of the Ca1A-seven-vertex polyhedron containing the largest amount of rare-earth elements is the shortest one (3.356 Å) and is located between the four-membered rings. In the agrellite-Sr structure, the O5A–O10A edges of the Ca2A and Ca1B octahedra isomorphously occupied by the Ca and Na atoms have close lengths (3.51 and 3.49 Å,

respectively). These edges are adjacent to the A silicate tube. The longest O5B–O10B edge (3.75 Å) belongs to the Ca1A-seven-vertex polyhedron occupied by the Sr and Ca atoms, and it borders on the four-membered ring of the B tube.

The attachment of four-membered rings of the vlasovite chain to the longer edges of Ca-polyhedra accounts for the difference in the mutual arrangement of the A and B silicate radicals in the agrellite-Sr and agrellite-RE structures (Fig. 5). Consequently, in terms of the arrangement of silicate radicals, these structures can be considered as polytypes with geometric factors (the lengths of the O5–O10 edges in the Ca-polyhedra) playing an important role in the formation of these polytypes.

The choice of unit cells in structures containing the $[\text{Si}_8\text{O}_{20}]^{8-}$ tubular radical and the description of the agrellite polytypes. The silicate tubes and the Na^+ cations bonded to these tubes form corrugated layers (T) alternating with the cationic layers (K) parallel to the (010) plane (Fig. 6a). In the case of the identical compositions of the positions in the cationic layers, the unit cell of agrellite can be chosen as the minimum structure fragment (the a_{\min} and b_{\min} parameters) consisting of one silicate tube and one cationic layer. In Fig. 6b, this fragment is shown by dashed lines. This fragment was taken as a unit cell in the structures of litidionite $\text{K}_2\text{Na}_2\text{Cu}_2(\text{Si}_8\text{O}_{20})$ and fenaksite $\text{K}_2\text{Na}_2\text{Fe}_2(\text{Si}_8\text{O}_{20})$ (different notation of the axes) [15].

This structure may be considered as a one-layer polytype with the triclinic unit cell $A(a_{\min}b_{\min}c)$ or 1A (the Gard notation [16]). In the case of the ordered arrangement of cations in each second layer, the unit cell is doubled (the parameters $a_2, b_2 = 2b_{\min}, c$). In Fig. 6b, this unit cell is shown by dashed lines and contains two layers of tubes and two layers of cations. However, the pseudo-centered triclinic unit cell with angles close to 90° (the parameters a, b, c) can be chosen proceeding from crystallochemical considerations, which does not change the character of layer alternation.

In the latter case, the agrellite-RE structure can be regarded as a two-layer triclinic polytype with the C-pseudo-centered cell. In the agrellite-Sr structure, the unit-cell axes are chosen as in the agrellite-RE structure, but each second silicate layer is shifted by half a translation along the z -axis compared to the positions of

Table 7. Crystallographic data for tokkoite and tinaksite, sp. gr. $P\bar{1}$

Data	Tokkoite*	Tinaksite**	Data	Tokkoite*	Tinaksite**
a , Å	10.438(3)	10.361(2)	β , deg	99.75(2)	99.22(2)
b , Å	12.511(3)	12.153(2)	γ , deg	92.89(2)	92.83(2)
c , Å	7.112(2)	7.044(2)	V , Å ³	914.2(4)	874.2(7)
α , deg	89.92(2)	90.79(2)	Z	2	2

* Crystallochemical formula of tokkoite: $\text{K}_{1.85}(\text{Ca}_{0.87}\text{Ti}_{0.13})(\text{Ca}_{0.85}\text{Na}_{0.15})(\text{Ca}_{1.71}\text{Fe}_{0.15}\text{Mn}_{0.08}\text{Mg}_{0.06})[\text{Si}_7\text{O}_{18}(\text{OH})][\text{F}_{0.61}(\text{OH})_{0.39}]$.

** Crystallochemical formula of tinaksite: $\text{K}_{2.06}(\text{Ti}_{0.95}\text{Fe}_{0.05})(\text{Na}_{1.0})(\text{Ca}_{1.87}\text{Fe}_{0.06}\text{Mn}_{0.11}\text{Mg}_{0.02})[\text{Si}_7\text{O}_{18}(\text{OH})]\text{O}_{1.02}$.

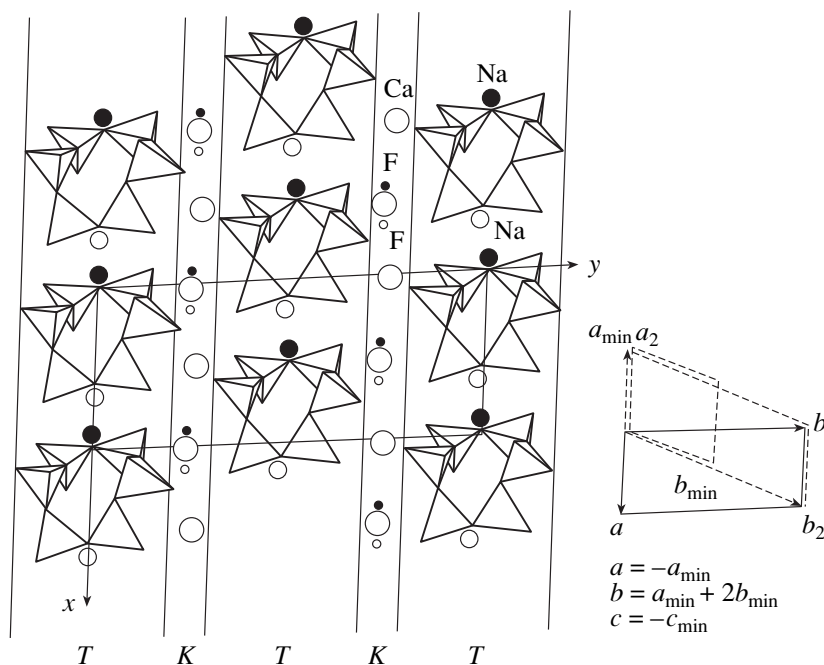


Fig. 6. Schematic representations of (a) the structures and (b) relations between the axes of the minimum fragment, the doubled unit cell, and the pseudo-centered unit cell of the agrellite structure. Solid and empty circles represent the atomic positions at the heights $\pm z$. The sections of the tubular silicate radicals are represented by tetrahedra.

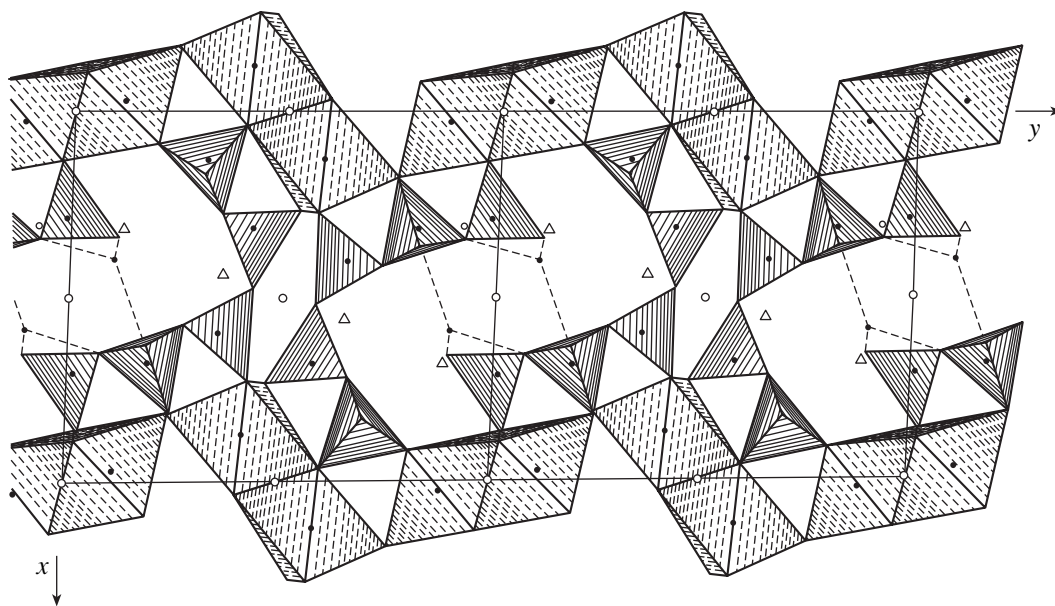


Fig. 7. Tokkoite and tinaksite structures projected onto the *xy*-plane. Hydrogen bonds are indicated by dashed lines.

the analogous layer in the agrellite-*RE* structure. Hence, the agrellite-*Sr* structure can be considered as a two-layer triclinic polytype with an *I*-pseudo-centered cell. As was mentioned above, the pseudo-centered packing is associated with the fact that F atoms in both structures violate the centered arrangement.

Following the recommendations of [16], one can attribute the identical modified Gard symbols *Aabc* to these polytypes. However, taking into account the dif-

ference in the arrangements of the silicate layers in these polytypes, the agrellite-*RE* and agrellite-*Sr* structures can be denoted as agrellite- $2A_C$ and agrellite- $2A_I$, respectively, where the coefficient 2 indicates the two-layer polytype, *A* signifies the triclinic system, and the *C* and *I* indices indicate the *C*- and *I*-pseudo-centered packings, respectively.

The above-mentioned structural features of the agrellite polytypes clearly manifest themselves in the

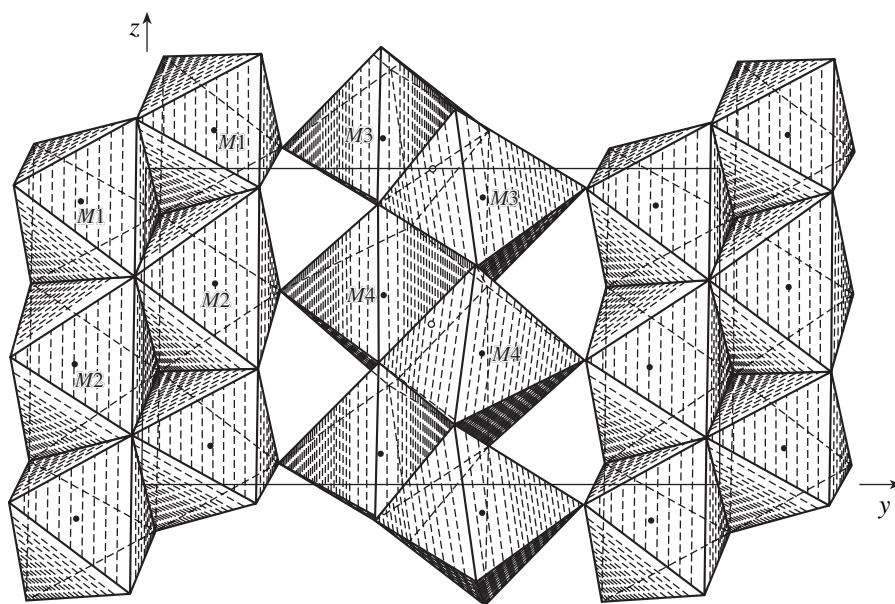


Fig. 8. Corrugated octahedral wall containing columns of the $M1$ -, $M2$ -, $M3$ -, and $M4$ -octahedra.

X-ray powder diffraction patterns. Thus, the stronger general-type reflections correspond to the C -pseudo-centered packing ($h + k = 2n$) and to the I -pseudo-centered packing ($h + k + l = 2n$) of the agrellite- RE and agrellite- Sr structures, respectively [17].

MINERALS WITH THE $[\text{Si}_7\text{O}_{18}(\text{OH})]^{9-}$ SILICATE RADICAL

A $[\text{Si}_7\text{O}_{18}(\text{OH})]^{9-}$ silicate radical exists in the structures of isostructural minerals tokkoite [17, 18] and tinaksite [8, 19, 20] (Tables 1, 7).

Numerous chemical analyses of the specimens from the rocks of the Murun massif did not reveal any minerals with intermediate compositions. The observed insignificant replacement of titanium and calcium by other elements in the tinaksite and tokkoite structures, respectively, shows the limited isomorphism between these isostructural minerals (Table 8). The incorporation of a small Ti^{4+} cation into one of four octahedral positions in the tinaksite structure leads to a decrease in all the unit-cell parameters in comparison with those of tokkoite (Table 7).

Table 8. Occupancies of the octahedral positions in the tokkoite and tinaksite structures

Position	Tokkoite	Tinaksite
$M1$	$\text{Ca}_{0.87}\text{Ti}_{0.13}$	$\text{Ti}_{0.95}\text{Fe}_{0.05}$
$M2$	$\text{Ca}_{0.85}\text{Na}_{0.15}$	$\text{Na}_{1.0}$
$M3$	$\text{Ca}_{0.79}\text{Fe}_{0.15}\text{Mg}_{0.06}$	$\text{Ca}_{0.95}\text{Fe}_{0.06}$
$M4$	$\text{Ca}_{0.92}\text{Mn}_{0.08}$	$\text{Ca}_{0.92}\text{Mn}_{0.11}\text{Mg}_{0.02}$

In the crystal structures of tokkoite and tinaksite, the layers of corrugated octahedral walls parallel to the (100) plane alternate with layers of silicon–oxygen radicals (Fig. 7) [7, 8, 19, 20].

The $[\text{Si}_7\text{O}_{18}(\text{OH})]^{9-}$ silicate radical. Unlike the above-considered radicals, this radical exists as a bent ribbon rather than as a closed tube. The $[\text{Si}_7\text{O}_{18}(\text{OH})]^{9-}$ silicate radical is unique because one of its terminal anions is not bonded to the octahedral wall but is “suspended” in a Z -like cavity formed by two radicals (Fig. 7). This anionic position is occupied by an OH^- group involved in hydrogen bonding between two silicon–oxygen radicals. The ribbon may form as a result of condensation of two wollastonite chains with an additional tetrahedron or of wollastonite and vlasovite chains. Condensation of these chains gives rise to the formation of eight- and four-membered windows. The silicate radical is bent to form a semiring in such a way that the vlasovite chain is linked to one octahedral wall via the terminal oxygen atoms, whereas the wollastonite chain is attached to another octahedral wall (Fig. 7). There are three tetrahedra bonded to the lateral edges of two octahedra per c -period along the elongation axis of the crystals.

Octahedral walls in the tinaksite and tokkoite structures are formed by two infinite ribbons along the [001] direction. These ribbons consist of edge-sharing columns of octahedra related by a center of symmetry. The ribbons share vertices, so that the octahedral wall formed is corrugated (Fig. 8).

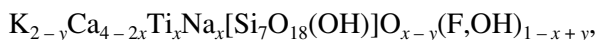
The ribbons in the tinaksite structure have different compositions. In one of these ribbons, the Ti - and Na -octahedra ($M1$ and $M2$, respectively) alternate. In

another ribbon, both octahedra (*M3* and *M4*) are occupied mainly by Ca^{2+} cations (Table 8). In the tokkoite structure, all four octahedral positions are occupied mainly by Ca^{2+} cations, whereas a small amount of Ti^{4+} and Na^+ cations are also in the *M1* and *M2* positions (as mentioned above, the Ti^{4+} and Na^+ cations prevail in these positions of the tinaksite structure). The fact that one of the four octahedral positions is favorable for incorporating smaller cations, whereas another position is occupied predominantly by larger cations, is not accidental and, apparently, is associated with the mode of the attachment of the wollastonite chain to the octahedral wall (Fig. 8). The vertical diortho group $[\text{Si}_2\text{O}_7]^{6-}$ with the largest Si–O–Si angle borders on the vertical edge of the largest *M2* octahedron, whereas the vertical edge of the smallest octahedron is parallel to the vertical edge of the tetrahedron linking diortho groups [7, 8].

The K^+ cation and the hydrogen atom of the (OH)⁻ group are located in large zigzag channels between the silicate radicals. As in the case of the $(\text{Si}_{12}\text{O}_{30})^{12-}$ radicals, the tinaksite and tokkoite structures have two positions suitable for K^+ cations (Fig. 7). One of these positions is in the eight-membered window at the bend of the silicate radical. The K^+ cation in this position is also bonded not only to the oxygen atoms of the ribbon containing the above silicon-radical bend but also to three oxygen atoms of the adjacent ribbon. Another position is located approximately at half the height between the terminal OH⁻ groups.

Like the canasite and frankamenite structures, the structures of the group of minerals under consideration contain a special anionic position within the octahedral wall which is not bonded to the silicate radical (Fig. 8). Its composition corresponds to the compositions of the three surrounding octahedra.

Obviously, the mineral tokkoite is isostructural to tinaksite. These minerals are the end members of the tokkoite–tinaksite series with the replacements in the cationic and anionic positions proceeding according to the scheme $2\text{Ca}^{2+} + (\text{F}, \text{OH})^- \leftarrow \text{Ti}^{4+} + \text{Na}^+ + \text{O}^{2-}$, so that the general formula of the minerals of this series may be written as follows:



$$\text{where } 0 \leq x \leq 1, 0 \leq y \leq 1.$$

CONCLUSIONS

The comparison of the crystallochemical characteristics of rarely occurring alkali calcium silicates discovered in the Murun charoite deposit with those of analogous minerals from other deposits shows that they possess unique features. First, they contain a large amount of fluorine and hydroxy groups in the positions that are not incorporated into the silicate radical. The ratio between the F^- , OH^- , and O^{2-} anions in these positions

correlates with the cationic order within the polyhedral walls. Second, the structures of these minerals generally contain no trivalent cations. Third, the position and role of the K^+ cation in the structures of these minerals differ from those of the Na^+ cations. The K^+ cations link the tubes to form silicate layers, due to which these minerals can be considered as layered structures. The Na^+ cation acts as a partner of the Ca^{2+} cation in the polyhedral walls.

In spite of insignificant variations in the chemical composition, the character of the impurity distribution influences the fine structural characteristics of this mineral group. Thus, the distribution of Na^+ and Ca^{2+} cations (order–disorder) determines the choice of the unit cell and the symmetry of the structure (frankamenite–canasite). The ordered incorporation of particular-type cations into one of the positions in the structure gives rise to the formation of pseudopolytypes (agrellites-*RE* and -*Sr*).

It should also be noted that the selected large construction modules in the form of polyhedral walls and layers of silicate radicals in the minerals under study does not result in prognostic constructions, because the shift of the silicate radicals along the polyhedral walls is always limited by the shift by half a translation along the elongation axis (the period *c* is about 7 Å). Moreover, polysomatic reactions of pyriboles are readily controlled by chemical means, namely, by constructing linear combinations of compositions (for example, $P + M = PM$, amphiboles; $PMMPMMP$, jimthompsonite; etc.) or by combining the modules of the olivine and brucite structures for a series of silicates of the forsterite–humite group [10, 11], in the case under consideration, those reactions cannot be designed with sufficient confidence. This is the fundamental characteristic of the crystal chemistry of silicates with large cations (in our case, Ca^{2+} and Na^+), in which the size effect plays a decisive role in the complication of the structural motifs. Instead of the pyroxene chain (the period along the elongation axis is ~5 Å), the silicate radical of these minerals consists of the pyroxenoid chains typical of the wollastonite $\text{Ca}_3[\text{Si}_3\text{O}_9]$ and pectolite $\text{Ca}_2\text{Na}[\text{Si}_3\text{O}_8]\text{OH}$ (period ~7 Å) structures.

In conclusion, it should be noted that although the charoite structure is still unknown, there is no doubt that this mineral belongs to the alkali calcium silicates with tubular radicals and that its structure consists of construction modules analogous to those considered above.

ACKNOWLEDGMENTS

This study was supported by the Russian Foundation for Basic Research, project no. 01-05-64952.

REFERENCES

1. I. V. Rozhdestvenskaya, L. V. Nikishova, and K. A. Lazebnik, *Miner. Mag.* **60**, 897 (1996).
2. I. V. Rozhdestvenskaya, L. V. Nikishova, I. I. Bannova, and Yu. D. Lazebnik, *Mineral. Zh.* **10** (4), 31 (1988).
3. J. D. Scott, *Can. Mineral.* **14**, 515 (1976).
4. I. V. Rozhdestvenskaya, L. V. Nikishova, I. I. Bannova, and M. D. Evdokimov, in *Proceedings of the III National Conference on Application of X-ray and Synchrotron Radiations, Neutrons and Electrons for Materials Research, Moscow, 2001*, p. 136.
5. S. Ghose and Ch. Wan, *Am. Mineral.* **64**, 563 (1979).
6. I. V. Rozhdestvenskaya and L. V. Nikishova, *Kristallografiya* **43** (4), 637 (1998) [*Crystallogr. Rep.* **43**, 589 (1998)].
7. I. V. Rozhdestvenskaya, L. V. Nikishova, Yu. D. Lazebnik, and K. A. Lazebnik, *Z. Kristallogr.* **189**, 195 (1989).
8. I. V. Rozhdestvenskaya, L. V. Nikishova, and K. A. Lazebnik, *Mineral. Zh.* **13** (4), 3 (1991).
9. L. V. Nikishova, K. A. Lazebnik, and Yu. D. Lazebnik, in *Crystal Chemistry and Structural Typomorphism of Minerals* (Nauka, Leningrad, 1985), p. 100.
10. A. A. Konev, E. I. Vorob'ev, and K. A. Lazebnik, *Mineralogy of Murunskii Alkaline Massif* (Sib. Otd. Ross. Akad. Nauk, Nauchno-Izd. Tsentr Ob'edin. Inst. Geologii, Geofiziki Mineralogii, Novosibirsk, 1996).
11. B. B. Zvyagin, *Kristallografiya* **38** (1), 98 (1993) [*Crystallogr. Rep.* **38**, 54 (1993)].
12. J. Ferraris, *Polysomatism as an Instrument for Establishment of Relation between the Properties and Structure of Crystals*, Ed. by O. E. Gorchakova (VINITI, Moscow, 1999).
13. N. V. Belov, *Essais on Structural Mineralogy* (Nedra, Moscow, 1976).
14. Yu. A. Pyatenko, *Kristallografiya* **17** (4), 773 (1972) [*Sov. Phys. Crystallogr.* **17**, 677 (1972)].
15. *Minerals: Handbook*, Ed. by F. V. Chukhrov (Nauka, Moscow, 1981), Vol. 3, issue 3.
16. A. Guinier, G. B. Bokij, K. Boll-Dornberger, *et al.*, *Acta Crystallogr., Sect. A: Found. Crystallogr.* **40** (4), 399 (1984).
17. I. V. Rozhdestvenskaya, L. V. Nikishova, and K. A. Lazebnik, *Zap. Vseross. Mineral. O-va.* **127** (1), 89 (1998).
18. K. A. Lazebnik, L. V. Nikishova, and Yu. D. Lazebnik, *Mineral. Zh.* **8**, 85 (1986).
19. G. Bissert, *Acta Crystallogr., Sect. B: Struct. Crystallogr. Cryst. Chem.* **36**, 259 (1980).
20. A. A. Petrunina, V. V. Ilyukhin, and N. V. Belov, in *Constitution and Properties of Minerals* (Naukova Dumka, Kiev, 1973), Vol. 7, p. 10.

Translated by T. Safonova

STRUCTURES OF INORGANIC COMPOUNDS

Analysis of the Structure of an Amorphous Sediment Obtained upon Decomposition of Potassium Oxofluoroniobate in Water

K. B. Aleĭnikova*, E. N. Zinchenko*, A. V. Arakcheeva**, and V. V. Grinevich**

* Voronezh State University, Universitetskaya pl. 1, Voronezh, 394893 Russia

** Baikov Institute of Metallurgy, Russian Academy of Sciences,
Leninskii pr. 49, Moscow, 117334 Russia

e-mail: arakchee@ultra.imet.ac.ru

Received December 24, 2001

Abstract—An amorphous sediment was prepared by the decomposition of potassium oxofluoroniobate $K_{2-x}Nb_4O_3(O, F)_3F$ in water. For this sediment, the atomic radial distribution function was analyzed with the use of a fragment model, which allows one to interpret expanded coordination spheres as being formed by first several strongest diffusion maxima. These spheres carry the most reliable information on the structure. It is shown that the amorphous sediment consists of the randomly packed $Nb(O, F)_6$ -octahedra with interatomic distances close to those observed in the ordered region in the $N-Nb_2O_5$ structure. During decomposition in water, the initial $K_{2-x}Nb_4O_3(O, F)_3F$ phase loses KF-layers, whereas Nb_6 clusters with metal bonds are destroyed.
© 2002 MAIK “Nauka/Interperiodica”.

INTRODUCTION

New niobium-containing phases of the general formula $[Nb_4O_3(O, F)_2][K_{1-x}(F, O)]_n$, where $n = 1, 2$, or 3 , were first prepared by electrolysis of a salt melt with the composition $K_2NbOF_5 + (KF + NaF + LiF)$ and analyzed elsewhere [1, 2]. Single-crystal studies showed that these phases have composite structures consisting of alternating $nK(F, O)$ layer blocks with the NaCl structure and the layer fragments of niobium monoxide (Fig. 1). In different phases, the number (n) of the KF-type layers incorporated into niobium oxide varies from one to three [2]. Crystals taken out of an electrolytic bath are contaminated with alkali fluorides and so they are washed for one to three hours in an HCl solution. Being kept in this solution over a longer period of time, the phase $K_{2-x}Nb_4O_3(O, F)_3F$ corresponding to $n = 2$ proved to be unstable and completely decomposed to form an amorphous sediment. Earlier [2], it was proposed that the amorphous phase consisting of disordered blocks of NbO oxide remained after “washing-off” KF blocks from the structure. To test the validity of this assumption, we analyzed the experimental atomic radial distribution function (ARDF) for the amorphous sediment based on the fragment model [3], which allows us to interpret multicomponent amorphous compounds in the ordered region.

EXPERIMENTAL

The experimental X-ray scattering curve from an amorphous sediment was measured on a DRON-3M diffractometer (CuK_α radiation, graphite monochromator) in the range of θ -angles from 2.5° to 50° at a step

of 0.025° . Although the exact chemical composition of the sediment was unknown, it was indicated [2] that the transformation into the amorphous state was accompanied by a substantial decrease in the potassium and fluorine content in comparison with their content in the initial crystal. The intensity curve $I(s)$, where $s = 4\pi\sin\theta/\lambda$, revealed the presence of a small amount of the modified crystalline phase corresponding to $n = 3$. Processing the experimental curve, we excluded from consideration the weak diffraction lines attributed to this phase. The experimental data were corrected for polarization and then were processed by the Nabitovich–Stetsiv method [4]. The starting value of the normalization factor k and the relative scattering powers of the atoms K_i were determined according to the well-known equations [5]. The Nabitovich–Stetsiv method enables one to find the interference function $i(s)$ directly from the experimental curve without using the analytical functions to account for the background and incoherent scattering. As a result, no additional errors are introduced into the calculations of $i(s)$, which makes it possible to obtain reliable results even using rather crude experimental data. The interference function was calculated according to the formula

$$i(s) = \frac{1}{j} \left(\frac{kI_c(s)}{\sum f_i^2(s)} - \frac{kI_c(s)}{\sum f_i^2(s)} \right).$$

The summation was carried out over the formula composition; $I_c(s)$ is the average line or the average intensity which would be obtained under similar conditions of X-ray scattering on the same system of independent atoms. The average line was extrapolated when opti-

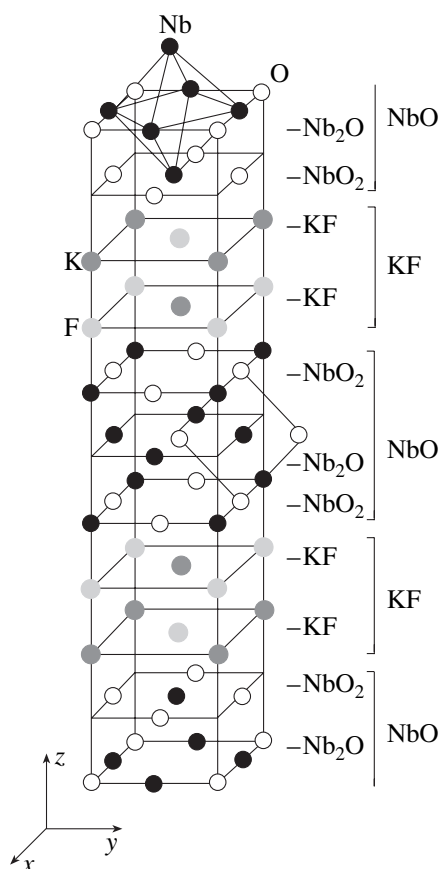


Fig. 1. Idealized model of the $K_{2-x}Nb_4O_3(O, F)_3F$ structure. The Nb_6 -cluster is shown by thick lines at the top of the figure.

mizing of the background curve. The normalization factor j was chosen in the range between j_{\min} and j_{\max} ,

$$\left(\frac{I_c(s) - I_e(s)}{\sum f_i^2(s)} \right)_{\max} < j < \left(\frac{I_c(s)}{\sum f_i^2(s)} \right)_{\min},$$

so that the atomic radial distribution function had no high negative values. In this case, the coefficient j was close to its maximum value.

The radial distribution function was calculated by the formula proposed in [5],

$$4\pi r^2 u(r) = 4\pi r^2 \frac{d}{Mm_H} (\sum K_i)^2 + \frac{2r}{\pi} \sum K_i^2 \int_0^{s_{\max}} si(s) \sin(sr) \exp(-\alpha^2 s^2) ds,$$

where d is the density of the amorphous material (it was taken to be not higher than 0.8 of the initial-crystal density), M is the molar weight of one formula unit, $s_{\max} = 6.24 \text{ \AA}^{-1}$, and $\Delta s = 0.01 \text{ \AA}^{-1}$. The atomic radial distribution function was calculated in the range $0 < r < 10 \text{ \AA}$ at a step $\Delta r = 0.04 \text{ \AA}$. The maxima were localized more

precisely at a step decreased to 0.01 \AA . Six maxima were clearly seen in the experimental radial distribution function in the range $0\text{--}10 \text{ \AA}$. These maxima correspond to the coordination spheres with the average interatomic distances of 2.07, 4.05, 5.4, 6.6, 7.71, and 9.01 \AA (curve 1 in Fig. 2). It is also evident that the second maximum is doubled.

RESULTS AND DISCUSSION

The experimental atomic radial distribution function was interpreted based on the fragment model in the ordered region. The fragment model proposed earlier [3] allowed us to analyze the multicomponent amorphous compounds and is one of models based on the crystal structures of chemical analogues. Within the framework of this model, the structure of an amorphous material is represented as a mosaic consisting of structural fragments of the crystalline phases, whose formation does not contradict the elemental composition of the compound under study. The use of this model is advantageous because the arrangement of the atoms in the crystal always corresponds to the deepest energy minimum of the system in comparison with that of any random packing. The most probable interatomic distances and angles in the amorphous phase retain values close to the analogous characteristics of a particular crystalline phase. Hence, the fragment model allows the interpretation of the average coordination spheres making the major contribution to the several first strongest diffuse maxima of the intensity curve.

The model radial distribution functions for the structure fragments were constructed using complete structure data on the corresponding analogues and the method of atom–atom correlation functions developed by Warren [6]. The model atomic radial distribution functions were calculated by the formula

$$4\pi r^2 u(r) = \frac{2r}{\pi} \sum_i \sum_j \frac{2N_{ij}}{r_{ij}} K_i K_j \times \int_0^{s_{\max}} \sin(sr) \sin(sr_{ij}) \exp\left(-\left(\alpha^2 + \frac{\sigma_{ij}^2}{2}\right) s^2\right) ds.$$

Here, r_{ij} are the interatomic distances calculated from the structure data for the chosen compound and sorted according to their types, Nb–O, Nb–F, Nb–Nb, etc.; $2N_{ij}$ is the number of interatomic distances r_{ij} of a given type per formula unit; α is the attenuation coefficient generally equal to the thermal factor; and σ_{ij} is the dispersion of the bonds of the same type, having close lengths and related by the Gaussian function. When combining the bonds, the following condition was fulfilled: $\alpha^2 \gg \sigma_{ij}^2$. Physically, the model radial distribution function for a structure fragment is a spherically symmetrical Patterson function of its crystal analogue. To interpret reliably the coordination spheres with the radii ranging from 3 to 9 \AA , the model radial distribution

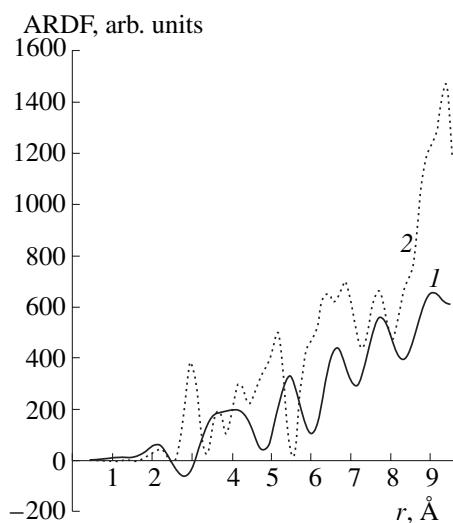


Fig. 2. (1) Experimental atomic radial distribution function and (2) the ARDF model for the crystalline $K_{2-x}Nb_4O_3(O, F)_3F$ specimen.

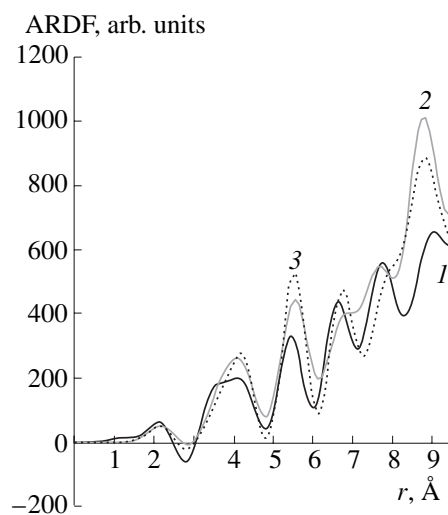


Fig. 3. (1) Experimental atomic radial distribution function and (2) the ARDF model for the (2) $N-Nb_2O_5$ and (3) Nb_3O_7F crystal structures.

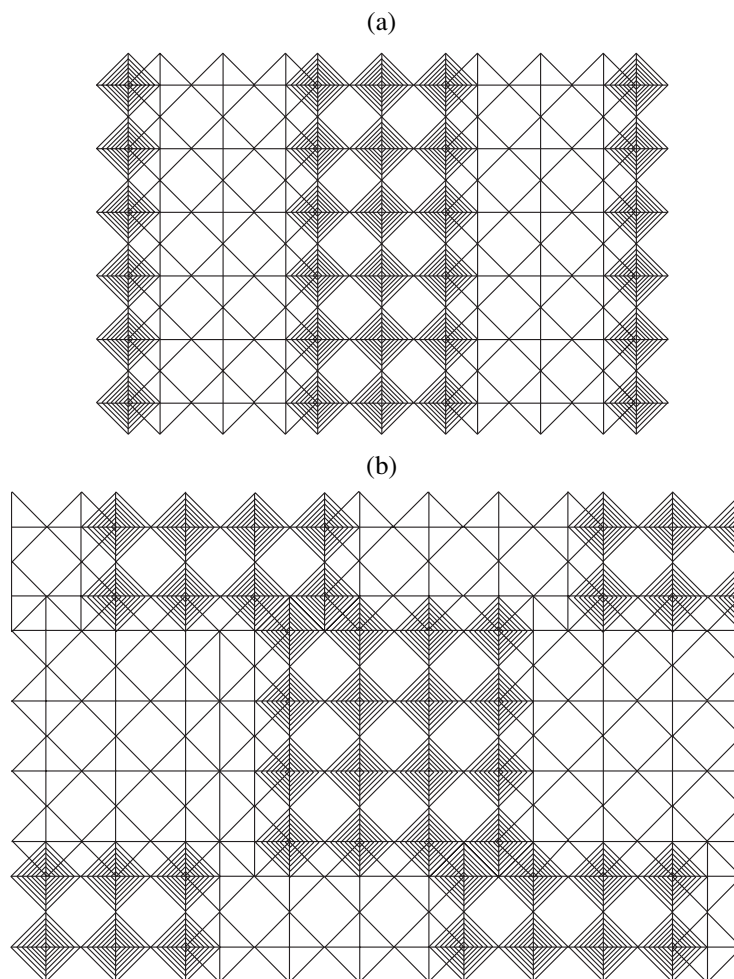


Fig. 4. Schematic representations of the (a) Nb_3O_7F and (b) $N-Nb_2O_5$ structures. The vertex-sharing NbO_6 -octahedra linked into blocks that have an ReO_3 -type structure are shown. The adjacent blocks sharing the octahedron edges are located at different heights and are hatched.

function was calculated up to 15 Å; i.e., the model consisted of more than 6000 atoms.

To find out whether the amorphous sediment is an ultradispersed phase of the starting potassium oxofluoroniobate or not, the model radial distribution function for the crystal analogue $K_{2-x}Nb_4O_3(O, F)_3F$ was constructed (Fig. 2, curve 2). The model function had a maximum at $r = 2.92$ Å corresponding to the Nb–Nb interatomic distance along the edge of the octahedral Nb_6 -cluster (Fig. 1), whereas the experimental radial distribution function has a deep minimum in this region. This indicates that the octahedral Nb_6 -clusters with the metal bonds were destroyed upon the decomposition of the initial phase in an aqueous solution of HCl and argues against the assumption that the amorphous sediment consists of randomly packed layers of NbO oxide typical of the initial crystal.

To reveal the structures whose fragments were present in the amorphous phase, we calculated the model radial distribution functions for 37 crystalline analogues containing the Nb, K, F, and O atoms in different ratios, for example, $K_2NbO_2F_5(H_2O)$, K_2NbO_3F , $K_3(NbF_5O)(HF_2)$, etc. Most of the model radial distribution functions were inconsistent with the experimental data. Many of these curves had maxima in the region of 2.8–3.0 Å resulting from the interatomic Nb–Nb, K–F, and K–O distances, whereas the experimental curve had a deep minimum in this region. Some model curves, for example, those constructed for the Nb_4O_5 , $NbKF_6$, etc. structures, show a maximum between 4 and 5 Å, which also corresponds to a deep minimum in the experimental curve. In some cases, the positions of the minima in the model curves coincide with the positions of the maxima in the experimental curve. All these models were excluded from subsequent consideration.

The models constructed for the $NbK_{0.3}F_3$ [7], $N-Nb_2O_5$ [8], and Nb_3O_7F [9] (Fig. 3) structures best fitted the experimental curve. It is unlikely that the amorphous phase contained structure fragments of the $NbK_{0.3}F_3$ crystal, because the K and F content in the sediment was decreased upon the decomposition of $K_{2-x}Nb_4O_3(O, F)_3F$ in water. Hence, this curve is not shown in Fig. 3. Both Nb_3O_7F and $N-Nb_2O_5$ crystal structures (Fig. 4) consist of the vertex-sharing distorted $Nb(O, F)_6$ -octahedra, linked into blocks with the ReO_3 -type structure [10]. The blocks of these structures have different sizes and are differently packed. It can be assumed that the amorphous phase under study is composed of the vertex-sharing $Nb(O, F)_6$ -octahedra, which form a disordered packing, but the interatomic Nb–Nb and Nb–O distances corresponding to the crystalline phases are retained. It should be mentioned that of all the Nb_2O_5 polymorphs, only a needle-like *N* modifica-

tion appeared to be a crystal analogue, with the model radial distribution function being consistent with the experimental data.

CONCLUSIONS

The results obtained lead to the following conclusions. The assumption [2] that the KF-type layers are a “weak link” of the $K_{2-x}Nb_4O_3(O, F)_3F$ structure is confirmed. These layers are “washed-out” upon prolonged storage in an aqueous solution of hydrochloric acid. The layer fragments of the niobium monoxide are destroyed because of the rupture of the metal bonds in the NbO_6 -octahedra. The amorphous phase consists of randomly arranged NbO_6 -octahedra with the interatomic distances typical of the *N-Nb*₂O₅ structure in the whole ordered region. The structure feature common to the starting phase and the amorphous sediment is the presence of the NbO_4 -squares. As was assumed in the earlier study [11] of low-valence niobium oxides, these squares, apparently, are the most stable atom associates in the Nb–O system.

REFERENCES

1. A. V. Arakcheeva, V. V. Grinevich, G. U. Lubman, and E. G. Polyakov, *Kristallografiya* **43** (3), 433 (1998) [*Crystallogr. Rep.* **43**, 395 (1998)].
2. A. V. Arakcheeva, V. V. Grinevich, E. G. Polyakov, and S. A. Kuznetsov, in *Refractory Metals in Molten Salts: Their Chemistry, Electrochemistry, and Technology*, Ed. by D. H. Kerridge and E. G. Polyakov (Kluwer, Dordrecht, 1998), NATO ASI Series, Partnership Sub-series, High Technology, Vol. 53, p. 143.
3. K. B. Aleĭnikova, M. V. Lesovoĭ, and Yu. N. Perin, *Dokl. Akad. Nauk* **329** (3), 308 (1993).
4. I. D. Nabitovich, Ya. I. Stetsiv, and Ya. V. Voloshchuk, *Kristallografiya* **12** (4), 584 (1967) [*Sov. Phys. Crystallogr.* **12**, 513 (1967)].
5. B. K. Vainshtein, *Kristallografiya* **2** (1), 29 (1957) [*Sov. Phys. Crystallogr.* **2**, 24 (1957)].
6. B. E. Warren, *Kristallografiya* **16** (6), 1264 (1971) [*Sov. Phys. Crystallogr.* **16**, 1106 (1971)].
7. R. Masse, S. Aleonard, and M. T. Averbuch-Pouchot, *J. Solid State Chem.* **53**, 136 (1984).
8. S. Andersson, *Z. Anorg. Allg. Chem.* **351**, 106 (1967).
9. S. Andersson, *Acta Chem. Scand.* **18**, 2339 (1964).
10. A. Wells, *Structural Inorganic Chemistry* (Clarendon, Oxford, 1984; Mir, Moscow, 1987), Vol. 2.
11. A. V. Arakcheeva, *Kristallografiya* **37** (3), 589 (1992) [*Sov. Phys. Crystallogr.* **37**, 306 (1992)].

Translated by T. Safonova

STRUCTURES
OF INORGANIC COMPOUNDS

Incorporation of Alkali Impurities into Single Crystals
of Barium Metaborate β -BaB₂O₄

A. E. Kokh*, N. G. Kononova*, P. P. Fedorov**, V. S. Boyarkov**,
R. M. Zakalyukin**, and V. A. Chubarenko**†

* Institute of Mineralogy and Petrography, Siberian Division, Russian Academy of Sciences,
Universitetskii pr. 3, Novosibirsk, 630090 Russia

** Shubnikov Institute of Crystallography, Russian Academy of Sciences,
Leninskii pr. 59, Moscow, 117333 Russia

Received September 3, 2001

Abstract—The impurities in single crystals of the low-temperature β modification of BaB₂O₄ grown from flux in the BaB₂O₄–Na₂O system have been studied. The β -BaB₂O₄ compound was examined by X-ray powder diffraction analysis. The appearance of scattering centers in the crystals correlates with the high content of sodium whose critical concentration is about 0.021 wt %. The effective distribution coefficient of sodium is $2.5\text{--}4.4 \times 10^{-3}$. The conditions for constitutional supercooling at the crystallization front are considered. © 2002 MAIK “Nauka/Interperiodica”.

Barium metaborate, BaB₂O₄, is known to have two polymorphs—a high-temperature α polymorph stable above 925°C and crystallizing in the sp. gr. $R\bar{3}c$ and a low-temperature β modification crystallizing in the noncentrosymmetric sp. gr. $R3c$. The crystals of the β -BaB₂O₄ modification (BBO) are widely used in nonlinear optics for the transformation of the laser frequency in the visible and UV regions. In spite of the fact that the growth conditions of these crystals and their properties have been repeatedly studied [1–11], a number of questions remained unsolved. The scattering in some β -BaB₂O₄ crystals and variations in their transmission spectra are still unclear. In the crystals grown under unfavorable conditions, the loss in crystallization-front stability, the formation of a porous substructure, and the incorporation of inclusions are observed [4, 5, 8].

The typical mechanism of the formation of a cellular substructure involves constitutional supercooling [4], which can result in the formation of solid solutions. The unstable BBO composition is indirectly indicated by small but significant variations in the unit-cell parameters of single crystals observed in different studies—from $a = 12.547(6)$ Å, $c = 12.736(9)$ Å [2] to $a = 12.5000(3)$ Å, $c = 12.6875(9)$ Å [12]. However, no systematic studies of possible nonstoichiometry postulated in [13], the types of point defects, and the incorporation of impurities and their distribution coefficients in the BBO crystals have been done as yet. The BBO crystals are usually grown from flux in the BaO–B₂O₃–Na₂O system, and sodium is a natural impurity inherited from the flux. Moreover, additional impurities present in the

starting reagents can also be incorporated into the crystals. Below, we examine the incorporation of such impurities into the BBO crystals.

EXPERIMENTAL

The BBO crystals were grown from flux in the BaB₂O₄–Na₂O system containing 20 mol % of Na₂O [10]. The starting reagents were BaCO₃, Na₂CO₃, and B₂O₃ oxides of special purity grade. Barium metaborate BaB₂O₄ was synthesized by sintering thoroughly premixed reagents at 700°C. The synthesis was performed until the complete removal of CO₂ and H₂O, which took from 5 to 16 h depending on the weight of the initial charge. The crystals were grown by the modified Czochralski method on [001]-oriented seeding crystals. The rates of the lowering of temperature, rotation, and pulling were 0.5–3 K/day, 1–7 rpm, and 0.2–0.7 mm/day, respectively. The length of the synthesized crystals ranged within 25–30 mm and had up to 50% of the useful volume suitable for preparation of nonlinear optical elements.

The X-ray phase analysis was made on an HZG-4 diffractometer (CuK α radiation) with the Si external standard. The X-ray data were processed using the Profit and Powder 2 (Moscow State University) program packages. The theoretical X-ray pattern was modeled using the Powder Cell 1.8 program (Berlin).

Microprobe analysis of the impurity content made in a JXA-8600S scanning electron microscope–microanalyzer (25 kV voltage, 10^{–8} A current). The standards were purchased from Microanalysis Consultants LTD (jadeite with 10.94 wt % of Na and orthoclase with 9.46 wt % of K). The specimens were coated with

† Deceased.

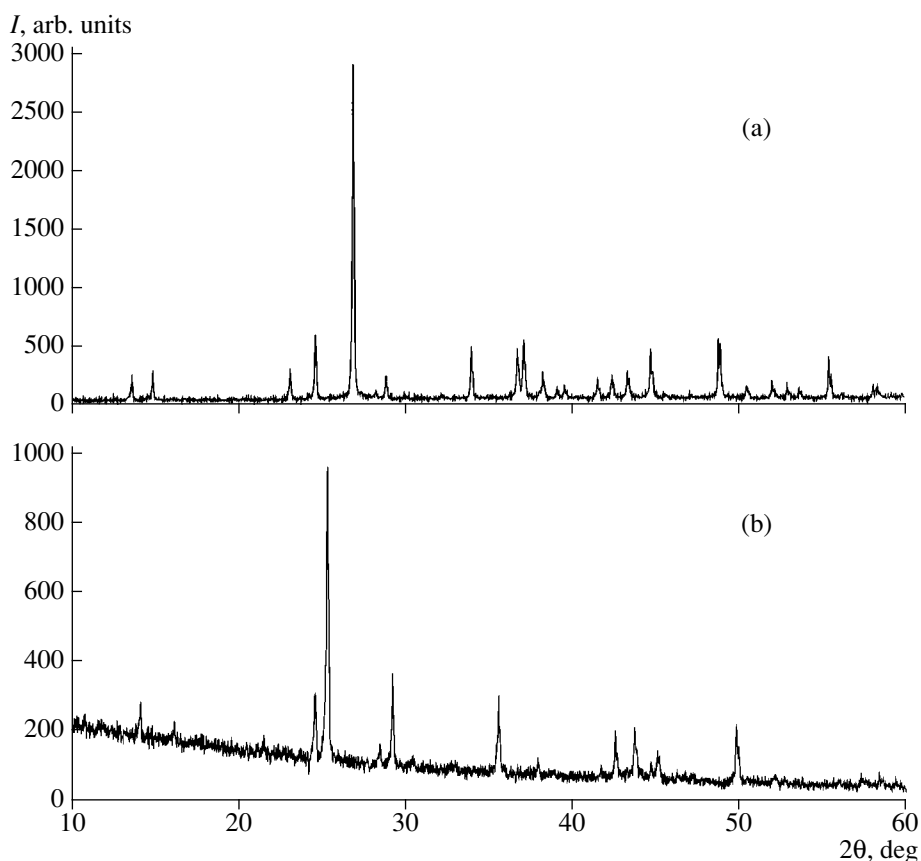


Fig. 1. X-ray powder diffraction patterns ($\lambda = \text{CuK}\alpha$) for (a) α - BaB_2O_4 and (b) β - BaB_2O_4 .

an aluminum conducting coating. In addition, the presence of Na and K impurities was checked by atomic emission spectroscopy on a Z-8000 Hitachi spectrometer (the relative standard deviation $S \leq 0.05$).

RESULTS AND DISCUSSION

The experimental X-ray diffraction pattern of β - BaB_2O_4 is shown in Fig. 1 together with the X-ray diffraction pattern of the α modification. The results of indexing of the X-ray pattern are given in Table 1. We failed to find a reliable X-ray diffraction pattern of this compound in the literature. The interplanar distances of the low-temperature modification, β - BaB_2O_4 (without indexing), were first reported in [14]. In [13], this modification was mistakenly assigned the monoclinic sp. gr. $C2/c$ (within which the diffraction pattern was indexed). More recently, it was demonstrated [12, 15, 16] that the crystal structure of this compound is described by the trigonal sp. gr. $R3c$ (no. 161), despite the fact that the X-ray pattern was also indexed within the monoclinic system [17]. The reference JCPDS card (no. 38-0722) includes an incomplete set of observed reflections. Some weak reflections were assigned wrong indices in [18, 19]; some reflections remained unindexed [20].

Microprobe analysis of the crystal exhibiting strong scattering (crystal no. 5-5, Table 2) revealed only two impurities—sodium and potassium. The quantitative measurements using 5 points gave a very high impurity content (1.068 ± 0.165 wt % of Na and 0.281 ± 0.78 wt % of K). It was assumed that under the conditions of the X-ray diffraction (the electric-field intensity of the order of 10^5 V/cm), Na and K atoms diffuse and they are accumulation at the sample surface. Earlier [21], sodium diffusion and its accumulation into surface clusters were observed in the electron microscopy study of the SiO_2 -Si structures under conditions of thermal-field stress. To confirm this assumption, the presence of impurities was analyzed under electron-beam defocusing. With an increase in the dimensions of the surface under study up to $20 \times 20 \mu\text{m}$, we obtained 0.462 ± 0.121 and 0.210 ± 0.064 wt % of Na and K, respectively, whereas at the dimensions $50 \times 50 \mu\text{m}$, we obtained 0.418 ± 0.086 and 0.192 ± 0.045 wt % of Na and K, respectively. The subsequent analysis of the impurity content was made by atomic emission spectroscopy. The results of this analysis are given in Table 2.

As is seen from Table 2, the appearance of the scattering centers correlates with a high Na content in the crystals. The critical concentration is 0.021 wt %. The effective distribution coefficients k_{eff} (Table 2) were cal-

Table 1. Indexing of X-ray diffraction patterns of β -BaB₂O₄. Parameters of the trigonal unit cell: $a = 12.527(3)$ Å, $c = 12.722(4)$ Å, $V = 1728.8(9)$ Å³

2θ , deg	d , Å	$Q = 10^4/d^2$, Å ⁻²	I/I_0 , %	h	k	l	Q_{calcd}	ΔQ
14.140	6.2581	255.34	16	1	1	0	254.91	0.43
16.164	5.4787	333.15	8	1	0	2	332.12	1.03
21.531	4.1236	588.08	4	2	0	2	587.03	1.05
22.813	3.8947	659.24	1	2	1	1	656.55	2.69
24.613	3.6138	765.72	18	3	0	0	764.72	1.01
25.350	3.5104	811.50	100	1	1	3	811.00	0.49
28.499	3.1293	1021.19	12	2	2	0	1019.62	1.56
29.248	3.0508	1074.42	41	0	1	4	1073.59	0.83
30.452	2.9329	1162.53	11	3	1	1	1166.38	-3.85
33.030	2.7096	1362.01	1	3	1	2	1351.75	10.26
35.614	2.5187	1576.33	40	2	2	3	1575.72	0.61
37.978	2.3672	1784.56	9	4	1	0	1784.34	0.21
38.911	2.3126	1869.82	1	2	3	2	1861.56	8.26
41.778	2.1602	2142.95	1	2	1	5	2139.49	3.46
42.609	2.1200	2224.99	20	0	0	6	2224.39	0.60
43.761	2.0668	2341.01	38	4	1	3	2340.44	0.57
44.712	2.0251	2438.41	3	4	2	1	2440.91	-2.50
45.107	2.0082	2479.63	9	1	1	6	2479.29	0.33
49.819	1.8288	2989.98	25	3	0	6	2989.11	0.87
52.034	1.7560	3243.03	2	2	2	6	3244.01	-0.98
56.006	1.6405	3715.76	1	6	1	1	3715.44	0.32
57.225	1.6084	3865.56	3	5	2	3	3869.88	-4.32
58.350	1.5801	4005.26	7	4	1	6	4008.73	-3.47

Table 2. Impurity content in the BBO crystals and the initial reagents

Specimen	Na, wt %	k_{eff} Na	K, wt %	Note
Na ₂ CO ₃			0.0015	Reagent of special purity grade 5-4
BaB ₂ O ₄	0.016		0.016	Synthesized
Crystal 5-5	0.160	3.3×10^{-2}	0.018	With scattering
Crystal 29-3	0.021	4.4×10^{-3}	0.018	Without scattering*
Crystal 29-7	0.022	4.6×10^{-3}	0.012	Traces of scattering
Crystal 26-13	0.012	2.5×10^{-3}	0.011	Without scattering

* Several percent of K₂O in the melt.

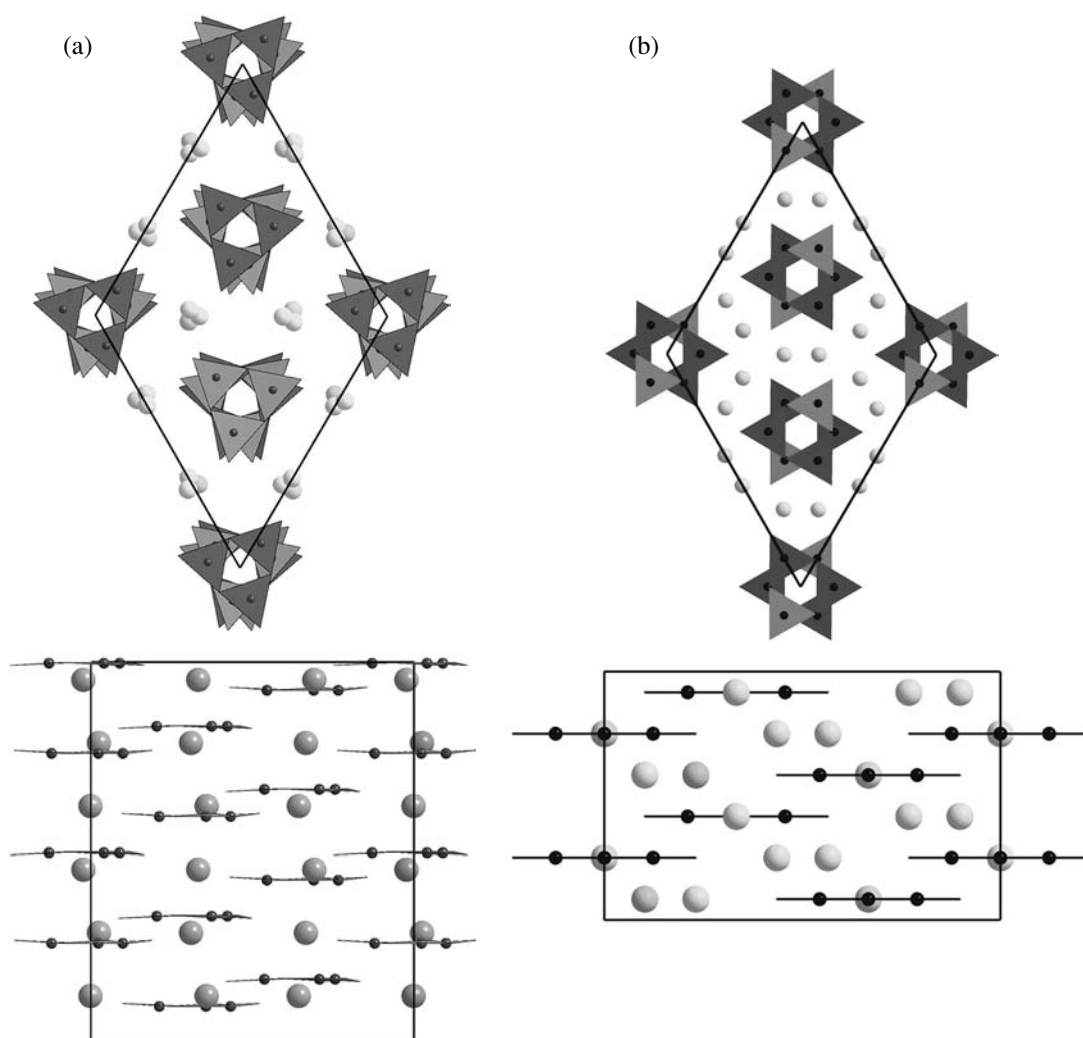


Fig. 2. (a) β -BaB₂O₄ (trigonal system, sp. gr. $R3c$, $a = 12.500 \text{ \AA}$, $b = 12.69 \text{ \AA}$) [12] and (b) NaBO₂ (trigonal system, sp. gr. $R\bar{3}c$, $a = 11.875 \text{ \AA}$, $c = 6.4375 \text{ \AA}$) [22] structures; the projections along and normal to the c -axis. Small spheres represent boron atoms; large spheres denote (a) Ba and (b) Na atoms; BO₃ groups are shown by triangles.

culated at the Na concentration in the starting melt $C = 4.82 \text{ wt \%}$.

Crystallochemical analysis showed that alkali impurities can be incorporated into the β -BaB₂O₄ structure. As is seen from Fig. 2, the crystal structure of barium metaborate is similar to the structure of sodium metaborate (NaBO₂). Both structures have identical structure elements—ring [B₃O₆]³⁻ anions packed into layers normal to the c -axis of the trigonal lattice. The structures have different arrangements of cations. The number of Na ions electrostatically compensating the charge is twice as large as that of Ba ions. The corresponding parameters of the trigonal unit cells have rather close values (Fig. 2). This gives grounds to believe that the Ba \leftrightarrow 2Na heterovalent isomorphism with the incorporation of additional Na ions into the lattice is possible. Hence, the major type of intrinsic point defects in the β -BaB₂O₄ structure seems to be Frenkel defects with

the Ba ions being displaced from their ideal positions into interstitial sites. The close values of the unit-cell parameters can also result in the epitaxial growth of NaBO₂ on β -BaB₂O₄ crystals.

The metrics of β -BaB₂O₄ is even closer to the metrics of isostructural potassium metaborate. (For KBO₂, $a = 12.76 \text{ \AA}$, $c = 7.34 \text{ \AA}$ [23].) As follows from Table 2, the K content in the BBO crystals without scattering is approximately equal to the Na content, despite the fact that K is only an impurity of the starting reagents (in our case, Na₂CO₃). It can be concluded that the effective distribution coefficient k_{eff} of potassium is considerably higher than that of sodium. For crystals nos. 5-5, 29-7, and 26-13, this coefficient is of the order of unity. However, the purposeful introduction of K (in the form of carbonate) into the starting flux (crystal no. 29-13) led to neither a substantial increase in its concentration in the crystal nor the formation of scattering centers.

However, the effect produced by this impurity on the quality and properties of the BBO crystals calls for their further study.

Now, consider the results obtained in other studies on the impurity content in BBO crystals. Cheng *et al.* [3] evaluated the Na content at $0.01 \pm 0.005\%$, which is in agreement with the data reported by other Chinese researchers. In study [7], Na was not detected, and Sr was the major impurity (0.028%). According to [20], the Na content in the β -BaB₂O₄ crystals grown from flux and by the Czochralski method from the stoichiometric melt varied from 0.012 to 0.068%. The transparent crystals having no inclusions contained from 0.012 to 0.023 wt % of Na. At Na content exceeding 0.035 wt %, the crystals had inclusions that varied from semitransparent to milk-white, which is consistent with our results.

It was indicated [16] that a very large amount of Sr atoms (tens of percent), isovalently replacing the Ba atoms, can be isomorphously incorporated into the BBO lattice. Apparently, in our experiments, the concentrations of Sr impurities in the starting reagents were very low. The K atoms were readily incorporated into the BBO lattice [6] if the melt of potassium fluoride was used as the flux.

The low values of the Na distribution coefficient in the BBO structure are consistent with the high efficiency of purification from this impurity by the zone melting method [18]. On the other hand, this method was inefficient in purification from Sr impurities [24], which indicates that the distribution coefficient of Sr is close to unity.

Now, consider the distribution of the concentrations of the major components in the course of the BBO-crystal growth in more detail. Figure 3 presents the qualitative distribution of the component concentrations in the vicinity of the crystallization front in the steady-state growth of the BBO crystals from the Na₂O flux at a rate of R . Since only a small amount of Na atoms are incorporated into the crystal, they are pushed away by the growing crystal, and we observe a jump in the concentration at the crystallization front. As a result, the diffusive flux of Na ions from the crystallization front is directed to the melt. The reduced Ba and B concentrations in the melt in comparison with the concentrations in crystal give rise to the capture of these components in the crystal and the formation of a zone depleted of these components before the crystallization front and diffusive flows directed from the melt bulk to the crystallization front. An excessive accumulation of sodium must decrease the equilibrium liquidus temperature. The integrated curve is shown in Fig. 3c. The possible shift of the figurative point corresponding to real crystallization is displayed in the schematic phase diagram (Fig. 3d). According to our data [25], the BaB₂O₄-Na₂O section is unstable, but it passes in the immediate vicinity of the eutectic point in the BaB₂O₄-NaBO₂-NaBaBO₃ concentration triangle.

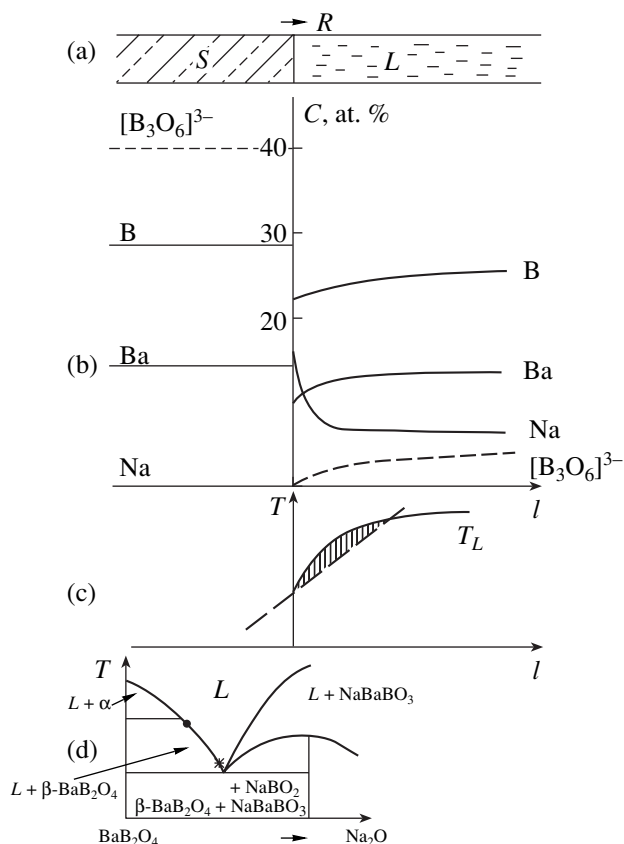


Fig. 3. Qualitative patterns of (a) the crystal–melt system at the steady-state directed crystallization at a rate of R ; (b) the distribution of the B, Ba, and Na concentrations and metaborate $[B_3O_6]^{3-}$ -rings; (c) the temperature of the beginning of the equilibrium crystallization of β -BaB₂O₄ (solid line) and the actual change in the temperature (dashed-and-dotted line), the region of constitutional supercooling is hatched in the vicinity of the crystallization front; (d) phase equilibria in the BaB₂O₄-Na₂O section according to [25].

A more detailed consideration should necessarily take into account different forms of boron presence in the melt. High-temperature Raman spectroscopic studies [26–28] showed that the metaborate $[B_3O_6]^{3-}$ -rings, the structural elements of the BBO crystal, are not typical of the BaB₂O₄ melt. Here, the polymer $[B_nO_{2n}]^{n-}$ -chains built by $[BO_3]$ -triangles prevail. Only in a supercooled melt is there a noticeable amount of $[BO_3]^{3-}$ -rings along with broken rings (chains of three-membered boron–oxygen chains with one B=O double bond per unit) and $[BO_4]^{5-}$ -tetrahedra. The molecular-dynamics calculations [29] showed that the introduction of Na₂O into the melt decreases the chain length and increases the proportion of the isolated $[BO_3]^{3-}$ -triangles, the two- $[B_2O_5]^{4-}$ fragments and the three-membered $[B_3O_7]^{5-}$ fragments, and the metaborate $[B_3O_6]^{3-}$ -rings. Nevertheless, it can be stated that it is the low concentration of the metaborate rings before the crystallization front that is the limiting factor in BBO-crystal growth.

The changes in the melt concentrations normal to the crystallization front because of independent diffusion in the steady-state process obeys the exponential law with the characteristic length R/D (the distance within which an excessive content is decreased by a factor of e), where D is the diffusion coefficient of the corresponding component [30]. Apparently, the sodium mobility is substantially higher than the mobility of Ba, and the mobility of B atoms diffusing as anionic complexes is lower by several orders of magnitude than the mobility of cations. The Coulomb interactions between these components of the melts and various chemical transformations between boron–oxygen anions give rise to cooperative processes and, also, cause substantial changes in the impurity distributions in the vicinity of the crystallization front. This melt should be considered to be multicomponent [31].

It should be noted that the steady-state growth of BBO-crystals from flux can be performed either by the Czochralski technique with melt replenishment [32] or by the floating-zone technique [33]. In our experiments based on the Kyropoulos method (slow cooling of the system), a nonsteady-state process occurs. During growth, Na ions are accumulated before the growth front. Once the supersaturation with sodium before the crystallization front reaches the critical value, the front becomes unstable, and the cellular structure is formed with the incorporation of impurities.

It is obvious that the simplest Tiller–Chalmers criterion for constitutional supercooling and stability of the crystallization front,

$$G/R < mC_0(1 - k)/Dk,$$

(where G is the temperature gradient at the crystallization front in liquid, R is the growth rate, m is the slope of the liquidus curve, C_0 is the solvent concentration in the solution, k is the distribution coefficient, and D is the diffusion coefficient of the solvent) cannot be applied to our case, although this criterion has been used, e.g., in [5]. The nonstationarity can be taken into account if one rewrites the criterion in the form

$$GD/R < m\Delta C,$$

(where ΔC is the jump in the concentration at the crystallization front [34]) whereas there is no way to take into account the multicomponent composition of the system.

Nevertheless, on the whole, the integrated curve of the increase in the temperature of the equilibrium crystallization (liquidus) in the direction from the crystallization front is similar to that observed for binary systems. In all cases, the stability of the crystallization front with respect to constitutional supercooling is favored predominantly by an increase in the temperature gradient at the crystallization front and a decrease in the growth rate. Because of the nonstationarity of the BBO growth, not only the control over thermal convection [8] but also the stirring of the melt are of particular importance [10, 11] for leveling the melt composition.

It can be seen from Fig. 3 that the equilibrium distribution coefficient k of sodium is lower than k_{eff} . According to the phase diagram of the BaO–B₂O₃–Na₂O system [25], an increase in the Na content before the crystallization front by a factor of 1.5 should give rise to crystallization of the second phase, NaBaBO₃. These melts are characterized by considerable supercooling, and, therefore, the actual sodium accumulation can be more pronounced. Apparently, it can be assumed that the equilibrium distribution coefficient k of sodium during BBO crystallization is about $(1-2) \times 10^{-3}$.

ACKNOWLEDGMENTS

We are grateful to Yu.V. Pisarevskii for valuable advice and encouragement in the course of this study.

REFERENCES

1. A. Jiang, F. Cheng, Q. Lin, *et al.*, *J. Cryst. Growth* **79**, 963 (1986).
2. D. Eimerl, L. Davis, S. Velsko, *et al.*, *J. Appl. Phys.* **62** (5), 1968 (1987).
3. L. K. Cheng, W. Bosenberg, and C. L. Tang, *J. Cryst. Growth* **89**, 553 (1988).
4. R. S. Feigelson, R. J. Raymakers, and R. K. Route, *J. Cryst. Growth* **97**, 352 (1989).
5. D. Y. Tang, W. R. Zeng, and Q. L. Zhao, *J. Cryst. Growth* **123**, 445 (1992).
6. A. B. Bykov, V. V. Dozmarov, and O. K. Mel'nikov, *Kristallografiya* **39** (4), 720 (1994) [*Crystallogr. Rep.* **39**, 651 (1994)].
7. Q. Tan, H. Mao, S. Lin, *et al.*, *J. Cryst. Growth* **141**, 393 (1994).
8. E. G. Tsvetkov and A. M. Yurkin, *Kristallografiya* **43** (6), 1142 (1998) [*Crystallogr. Rep.* **43**, 1080 (1998)].
9. R. Sole, V. Nikolov, M. C. Pujol, *et al.*, *J. Cryst. Growth* **207**, 104 (1999).
10. A. E. Kokh and N. G. Kononova, *J. Cryst. Growth* **198/199**, 161 (1999).
11. A. E. Kokh, N. G. Kononova, and P. W. Mokruchnikov, *J. Cryst. Growth* **216**, 359 (2000).
12. K. Ito, F. Marumo, M. Ohgaki, and K. Tanaka, *Rep. Res. Lab. Eng. Mater., Tokyo Inst. Technol.* **15**, 1 (1990).
13. K.-H. Hubner, *Neues Jahrb. Mineral., Monatsh.*, 335 (1969).
14. E. M. Levin and H. F. McMurdie, *J. Res. Natl. Bur. Stand.* **42**, 131 (1949).
15. R. Frohlich, *Z. Kristallogr.* **168**, 109 (1984).
16. J. Liebertz, *Z. Kristallogr.* **182**, 307 (1988).
17. K. L. Ovanesyan, A. G. Petrosyan, and G. O. Shirinyan, *Cryst. Res. Technol.* **24** (9), 859 (1989).
18. T. Katsumata, H. Ishijima, T. Sugano, *et al.*, *J. Cryst. Growth* **123**, 597 (1992).
19. L. I. Ivleva, I. G. Gordadze, Yu. S. Kuz'minov, *et al.*, *Izv. Akad. Nauk SSSR, Neorg. Mater.* **25** (5), 804 (1989).
20. S. C. Sabharwal, Sangeeta M. Goswami, *et al.*, *J. Mater. Sci.: Mater. Electron.* **11**, 325 (2000).

21. K. Ventsel, Yu. Dziziati, U. Muller, *et al.*, *Poverkhnost* **5**, 114 (1986).
22. M. Marezio, H. A. Plettinger, and W. H. Zachariasen, *Acta Crystallogr.* **16**, 594 (1963).
23. W. Schneider and G. B. Carpenter, *Acta Crystallogr., Sect. B: Struct. Crystallogr. Cryst. Chem.* **26**, 1189 (1970).
24. H. Kimura and R. S. Feigelson, *J. Alloys Compd.* **123**, 597 (1992).
25. A. E. Kokh, N. G. Kononova, P. P. Fedorov, *et al.*, *Technical Summary Digest of SPIE's LASE*, San Jose, 2002, p. 5.
26. Yu. K. Voron'ko, A. V. Gorbachev, A. B. Kudryavtsev, *et al.*, *Neorg. Mater.* **28** (8), 1713 (1992).
27. Yu. K. Voron'ko, A. V. Gorbachev, A. A. Sobol', and L. I. Tsymbal, *Neorg. Mater.* **30** (5), 646 (1994).
28. Yu. K. Voronko, A. V. Gorbachev, V. V. Osiko, *et al.*, *J. Phys. Chem. Solids* **54** (11), 1579 (1993).
29. Z. Cheng, Y. Lei, and D. Tang, *J. Cryst. Growth* **183**, 227 (1998).
30. B. Chalmers, *Principles of Solidification* (Wiley, New York, 1964; Metallurgiya, Moscow, 1968).
31. V. I. Tyurikov, E. G. Tsvetkov, and G. G. Khramenko, *Poverkhnost*, 2002, No. 5 (in press).
32. D. Perlov and M. Roth, *J. Cryst. Growth* **137**, 123 (1994).
33. R. O. Hengel and F. Fischer, *J. Cryst. Growth* **114**, 656 (1991).
34. P. P. Fedorov, *Neorg. Mater.* **37** (1), 95 (2001).

Translated by T. Safonova

STRUCTURES OF INORGANIC COMPOUNDS

Crystal Structure of New Synthetic Ca,Na,Li-Carbonate-Borate

N. A. Yamnova, Yu. K. Egorov-Tismenko, O. V. Dimitrova, and A. P. Kantor

Faculty of Geology, Moscow State University, Vorob'evy gory, Moscow, 119899 Russia

e-mail: natalia_yamnova@mail.ru

Received September 10, 2001; in final form, December 19, 2001

Abstract—In the process of studying the phase formation in the $\text{Li}_2\text{CO}_3\text{--CaO--B}_2\text{O}_3\text{--NaCl}$ system, new Ca,Na,Li-carbonate-borate has been synthesized under hydrothermal conditions. The crystal structure of carbonate-borate with the crystallochemical formula $\text{Ca}_4(\text{Ca}_{0.7}\text{Na}_{0.3})_3(\text{Na}_{0.7}\square_{0.3})\text{Li}_5[\text{B}_{12}^t\text{B}_{10}^\Delta\text{O}_{36}(\text{O},\text{OH})_6](\text{CO}_3)(\text{OH}) \cdot (\text{OH},\text{H}_2\text{O})$ was refined to $R_{\text{hkl}} = 0.0716$ by the least squares method in the isotropic approximation of atomic thermal vibrations without the preliminary knowledge of the chemical composition and the formula (sp. gr. $R\bar{3}$, $a_{\text{th}} = 13.05(2) \text{ \AA}$, $\alpha = 40.32(7)^\circ$, $V = 838(2) \text{ \AA}^3$, $a_h = 8.99(2)$, $c_h = 35.91(2) \text{ \AA}$, $V = 2513(2) \text{ \AA}^3$, $Z = 3$, $d_{\text{calcd}} = 2.62 \text{ g/cm}^3$, Syntex $\text{P}\bar{1}$ diffractometer, 3459 reflections, $2\theta\text{--}\theta$ method, λMo). The structure has a new boron–oxygen radical $[\text{B}_{12}^t\text{B}_{10}^\Delta\text{O}_{36}(\text{O},\text{OH})_6]_{\infty}^{15-}$, a double layer of nine-membered $[\text{B}_6^t\text{B}_3^\Delta\text{O}_{15}(\text{O},\text{OH})_3]^{7.5-}$ -rings bound by BO_3 -triangles, and twelve-membered $[\text{B}_6^t\text{B}_6^\Delta\text{O}_{19.5}(\text{O},\text{OH})_3]^{7.5-}$ rings. This allows one to relate this compound to megaborates with complex boron–oxygen radicals. The structure is built from two types of blocks consisting of Ca,Na,B- and Li,B-polyhedra alternating along the c -axis, which explains the perfect cleavage of the crystals along the (0001) plane. © 2002 MAIK “Nauka/Interperiodica”.

INTRODUCTION

The ever increasing attention paid to boron-containing compounds is associated with the possible practical application of their physical, in particular, ferroelectric, ferromagnetic, nonlinear optical, semiconductor, and other specific properties in various devices. The unusual crystal chemistry of these compounds is explained by the different coordination of boron atoms resulting in various structural rearrangements whose study allows a better understanding of the genesis of these compounds and the establishment of the relation between their composition, structure, and properties. At present, no Ca,Na,Li-carbonate-borates have been found in the group of well-studied carbonate-borates with mixed cationic composition such as gaudefroyite $\text{Ca}_4\text{Mn}[(\text{BO}_3)_3](\text{CO}_3)\text{O}_3$ [1], sakhaite $\text{Ca}_3\text{Mg}[\text{BO}_3]_2(\text{CO}_3) \cdot \text{H}_2\text{O}$ [2], carboborite $\text{Ca}_3\text{Mg}[\text{B}(\text{OH})_4]_2(\text{CO}_3)_2 \cdot 4\text{H}_2\text{O}$ [3], moydite $(\text{Y,REE})[\text{B}(\text{OH})_4](\text{CO}_3)$ [4], and borcarite $\text{Ca}_4\text{Mg}[\text{B}_4\text{O}_6(\text{OH})_6](\text{CO}_3)_2$ [5].

Below, we describe the structural investigation of new synthetic Ca,Na,Li carbonate-borate whose single crystals were synthesized while studying the phase formation in the $\text{Li}_2\text{CO}_3\text{--CaO--B}_2\text{O}_3\text{--NaCl}$ system. The mechanical mixture of the components (analytical-grade reagents) were placed into an autoclave preliminarily filled with water. The experiments were per-

formed in standard 4-cm³ Teflon-futerated autoclaves at $t = 250^\circ\text{C}$. The lower temperature was limited by the kinetics of the hydrothermal reactions, whereas the upper temperature, by the possibilities of the apparatus used. The filling coefficient of the autoclave was calculated so as to provide a constant pressure (100 atm). The duration of the experiment (18–20 days) was selected to ensure the completion of the reaction. The phase thus synthesized consisted of colorless transparent trigonal crystals with a plane prismatic habit. Some crystals attained a size of 0.5–1.0 mm.

EXPERIMENTAL: DETERMINATION AND REFINEMENT OF THE STRUCTURE MODEL

We studied a specially selected single crystal with the linear dimensions indicated in Table 1. The parameters and the symmetry of the trigonal unit cell were determined by the Laue method in a RKOP chamber and then were refined on an automated Syntex $\text{P}\bar{1}$ diffractometer. The intensities of 8443 experimental reflections were recorded on the same diffractometer. The main characteristics of the experimental data are listed in Table 1. In order to use the AREN complex of programs [6], the set of experimental reflections obtained in the rhombohedral setting was transformed

into the reflections in the hexagonal setting (the transition matrix $01\bar{1}/\bar{1}01/111$). The analysis of the transformed set of reflections indicated the diffraction class $\bar{3}$, and the extinction law $-h + k + l = 3n$ indicated two possible space groups— $R\bar{3}$ and $R3$. At the first stage of the study, the computations were made within the sp. gr. $R\bar{3}$ with the use of the averaged set of reflections ($R_{av} = 0.044$).

The insufficient amount of material did not allow us to obtain the powder diffraction pattern and to perform the quantitative chemical analysis, and, as a result, to correctly identify the compound. The qualitative X-ray spectral analysis made on a scanning CAMSCAN/4DV microscope with the LINK energy-dispersion attachment (analyst E.V. Guseva) and, independently, on a CAMECA SX-50 X-ray microanalyzer (analyst I.A. Bryzgalov) showed the presence of Ca atoms and a small amount of Na. The comparison of the habit of grown Ca,Na,Li-carbonate-borate crystals and their unit-cell metrics with the habit and unit-cell metrics of recently studied lead dodecaborate $Pb_6B_{12}O_{24}$ ($a_h = 11.436 \text{ \AA}$, $c_h = 17.385 \text{ \AA}$, sp. gr. $R\bar{3}$, $Z = 3$ [7]) allowed us to assume their structural similarity, and, therefore, the presence of 12 Ca atoms, 24 B atoms, and 48 O atoms in the double unit cell of this compound. The structural model was determined by the direct method. From 12 variants, we selected the E-synthesis with the minimum reliability factor, $R_{hkl} = 0.39$, which allowed us to analyze the coordination environment and heights of the maxima and, thus, to establish the positions of all the Ca atoms and some of the O and B atoms. The additional maxima determined by the method of successive approximations were identified with O, B, and Li atoms, with the possible presence of Li atoms assumed on the basis of the charge composition. The model found was refined by the least-squares method to $R_{hkl} = 0.1149$ in the isotropic approximation and to $R_{hkl} = 0.0862$ in the anisotropic approximation.

The high value of the isotropic thermal correction ($B_{iso} \approx 4.5 \text{ \AA}^2$) for one of the Ca-positions led to the assumption that it is filled with Na^+ -cations. The refinement of the occupancy of this position (with the use of the atomic scattering curve of Na) and also of the remaining Ca-positions showed that the former position is statistically filled by Na-cations (~70%), whereas one of the latter Ca-positions, Ca(2), is statistically filled by 70% Ca and 30% Na. The division of the anionic part of the structure into O^{2-} ions and OH^- hydroxyl groups was made based on the calculation of the local balance of valence strengths with due regard for the cation–oxygen distances [8] (Table 2). The presence of isolated CO_3 -groups was assumed upon the analysis of the average cation–oxygen distances slightly shorter in CO_3 -groups (1.302 \AA) than the value of 1.372 \AA in BO_3 -triangles. The presence of CO_3^{2-} -

Table 1. Main crystallographic characteristics and experimental data

System	Trigonal
Sp. gr.	$R3$
Z	3
a_{rh} , \AA	13.05(2)
α , deg	40.32(7)
V , \AA^3	838(2)
a_h , \AA	8.99(2)
c_h , \AA	35.91(2)
V , \AA^3	2513(2)
d_{calcd} , g/cm^3	2.62
μ , cm^{-1}	13.4
Linear dimensions of crystal, mm	$0.350 \times 0.350 \times 0.200$
Radiation, wavelength	Mo- K_{α} , 0.71069
Diffraction meter	Syntex P $\bar{1}$
Scanning mode	$2\theta : \theta$
Maximum $\sin\theta/\lambda$	1.08
Scanning rate, deg/min	4–24
Number of measured reflections ($I \geq 1.96 \sigma(I)$) within the half of the reciprocal space	8443
Number of reflections in the independent region	3459
Number of reflections used at the concluding stage of the least squares refinement	3281
Complex of computational programs used	AREN
Final reliability factor	
R_w	0.1018
R	0.0716
The weighting scheme in the least squares procedure	$w = 1/(A + F + BF^2)$ $A = 2F_{\text{min}}, B = 2/F_{\text{max}}$
The number of parameters to be refined	272

and OH^- -groups and also of H_2O molecules in Ca,Na,Li-carbonate-borate was confirmed by the IR-spectroscopy data. The IR spectrum was obtained by N.V. Chukanov on a Specord 75 IR spectrophotometer (Fig. 1) (pressing with KBr, polystyrene and gaseous-ammonia standards). The frequencies were measured with an accuracy of $\pm 1 \text{ cm}^{-1}$ at the Institute of Chemical Physics of the Russian Academy of Sciences

Table 2. Local balance of valence strengths at anions

Anion	Cation																Total
	Ca(1)	Ca(2)	Ca(3)	Na	Li(1)	Li(2)	Li(3)	C	B(1)	B(2)	B(3)	B(4)	B(5)	B(6)	B(7)	B(8)	
O(1)	0.271	–	–	0.114 ↓ × 3	–	–	–	–	–	0.690	–	0.939	–	–	–	–	2.014
(O,OH)(2)	–	–	–	0.119 ↓ × 3	–	–	–	–	–	0.766	–	–	–	–	–	0.859	1.744
O(3)	–	0.408	–	–	–	–	–	–	0.694	–	–	–	–	–	–	0.841	1.943
O(4)	0.161	–	–	–	–	0.184 ↓ × 3	–	–	–	–	–	0.995	0.644	–	–	–	1.984
O(5)	0.260	0.250	–	–	–	–	–	–	1.585	–	–	–	–	–	–	–	2.095
O(6)	–	–	0.170 ↓ × 3	–	–	0.149 ↓ × 3	–	–	–	–	0.975	–	0.667	–	–	–	1.961
O(7)	–	0.260	0.227 ↓ × 3	–	0.264	–	–	–	–	–	1.122	–	–	–	–	–	1.873
O(8)	0.271	–	–	–	–	–	0.162 ↓ × 3	–	–	–	–	–	0.834	0.724	–	–	1.991
O(9)	–	0.273	0.270 ↓ × 3	–	0.181	–	–	–	–	–	–	–	–	–	–	1.303	2.027
O(10)	–	–	–	–	–	–	–	–	–	–	–	1.068	–	0.762	–	–	1.830
O(11)	–	–	–	–	0.232	–	0.122 ↓ × 3	–	–	–	–	–	0.857	0.814	–	–	2.025
O(12)	0.260	–	–	–	–	–	–	–	–	0.766	–	–	–	–	1.003 ↓ × 3	–	2.029
O(13)	0.483	–	–	–	–	–	–	–	0.717	0.781	–	–	–	–	–	–	1.981
(OH)(14)	0.292 → × 3	–	–	–	–	–	0.149	–	–	–	–	–	–	–	–	–	1.025
(O,OH)(15)	–	–	–	–	–	–	–	–	–	–	0.901	–	–	0.701	–	–	1.602
O(16)	–	0.258	–	–	0.322	–	–	1.336 ↓ × 3	–	–	–	–	–	–	–	–	1.916
(OH,H ₂ O)(17)	–	0.250 → × 3	–	–	–	–	–	–	–	–	–	–	–	–	–	–	0.750
Total	1.998	1.699	2.001	0.699	0.999	0.999	1.001	4.008	2.996	3.003	2.998	3.002	3.002	3.001	3.009	3.003	

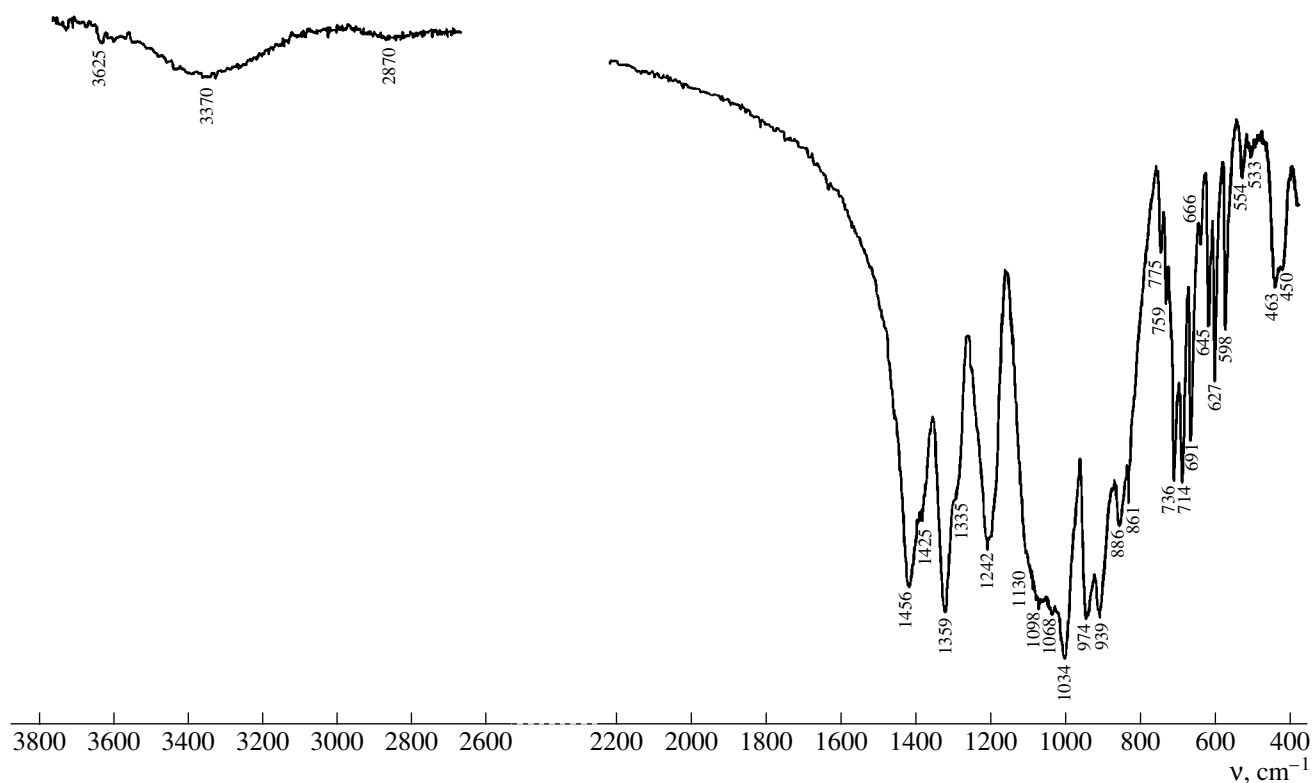


Fig. 1. The IR spectrum of synthetic Ca,Na,Li-carbonate-borate.

(Chernogolovka). An analysis of the absorption bands showed the presence of condensed radicals of B-tetrahedra ($1130\text{--}886\text{ cm}^{-1}$) and $[\text{BO}_3]^{3-}$ -radicals ($1359\text{--}1242\text{ cm}^{-1}$). We failed to identify the absorption bands of Li–O vibrations against the background of a large number of absorption bands due to deformation vibrations associated with the presence of BO_4 -tetrahedra. Four absorption bands in the vicinity of 2870 and 3370 cm^{-1} indicated the existence of strong hydrogen bonding in water molecules, whereas the absorption band in the vicinity of 3625 cm^{-1} indicated the existence of free OH^- -groups. The bright absorption bands in the vicinity of 861 and 1456 cm^{-1} in the IR spectrum confirmed our assumption regarding the presence of isolated $(\text{CO}_3)^{2-}$ groups. As a result, at the final stage of our study, we obtained the following structural and general formulas for the compound:

$$\text{Ca}_4(\text{Ca}_{0.7}\text{Na}_{0.3})_3(\text{Na}_{0.7}\square_{0.3})\text{Li}_5[\text{B}'_{12}\text{B}^{\Delta}_{10}\text{O}_{36}(\text{O},\text{OH})_6](\text{CO}_3) \cdot (\text{OH}) \cdot (\text{OH},\text{H}_2\text{O}) \text{ and } \text{Ca}_6\text{Na}_{(2-x)} \cdot \text{Li}_5[\text{B}'_{12}\text{B}^{\Delta}_{10}\text{O}_{36}(\text{O},\text{OH})_6](\text{CO}_3)(\text{OH})(\text{OH})_{(1-x)} \cdot x\text{H}_2\text{O}$$

($Z = 3$, $d_{\text{calcd}} = 2.62\text{ g/cm}^3$). With due regard for the statistical filling of the Ca(2) and Na positions, the refined extinction parameters, and the layer coefficients, the reliability factor was $R_{hkl} = 0.0716$. The concluding coordinates of the basis atoms are listed in Table 3.

DESCRIPTION OF THE STRUCTURE

The Ca(1) and Ca(2) atoms occupy the seven-vertex polyhedra with average Ca–O distances 2.412 and 2.429 \AA , respectively; the Ca(3) atom is located in ten-vertex polyhedron with average Ca–O distance 2.538 \AA , whereas the Na atom statistically occupies the trigonal prism with average Na–O distance 2.624 \AA . The Li(1) atom is located in a considerably distorted tetrahedron with Li–O distances ranging within $1.88\text{--}2.28\text{ \AA}$ and average Li–O distance 2.07 \AA , whereas the Li(2) atom is located in an octahedron with average Li–O distance 2.15 \AA and the Li(3) atom, in a seven-vertex polyhedron with the average Li–O distance 2.15 \AA . This coordination of the Li(3) atom is explained by its location in the plane of the tetrahedron face formed by the four closest ligands spaced $\sim 2.06\text{ \AA}$ from the anions. This explains the necessity of also including in the environment of the Li(3) atom three O^{2-} -ions from the second coordination sphere located at a distance of 2.27 \AA from Li(3). The unusual Li coordination (c.n. 5 and 6) was also observed earlier in the structure of synthetic Li-borate, $\text{Li}_3[\text{B}_5\text{O}_8(\text{OH})_2]$ [9]. Eight independent B atoms are characterized by tetrahedral and triangular coordination with the average cation–oxygen distances in the B(1)-, B(2)-, B(5)- and B(6)-tetrahedra equal to 1.481 , 1.474 , 1.473 , and 1.470 \AA and in the B(4)-, B(3)-, B(7)-, and B(8)-triangles, 1.374 , 1.373 , 1.361 , and 1.378 \AA , respectively. Carbon atoms center

Table 3. Coordinates of basis atoms and the equivalent thermal corrections

Atom	x/a	y/b	z/c	$B_{\text{iso}} (\text{\AA}^2)$
Ca(1)	0.7630(1)	0.7353(1)	0.9100(1)	0.76(2)
Ca(2)*	0.3231(1)	0.9182(1)	0.7009(1)	0.84(2)
Ca(3)	0.0000	0.0000	0.4067(6)	0.79(3)
Na*	0.0000	0.0000	0.2673(6)	2.2(3)
C	0.0000	0.0000	0.7275(3)	1.2(1)
B(1)	0.3558(5)	0.5099(5)	0.6378(1)	0.6(1)
B(2)	0.4211(5)	0.3938(5)	0.9375(1)	0.5(1)
B(3)	0.5907(6)	0.5791(6)	0.7830(1)	0.6(1)
B(4)	0.5877(6)	0.9862(6)	0.8708(1)	0.70(9)
B(5)	0.8434(6)	0.6730(6)	0.8262(1)	0.68(9)
B(6)	0.6672(6)	0.8293(6)	0.8257(1)	0.84(8)
B(7)	0.0000	0.0000	0.6048(8)	0.8(2)
B(8)	0.8834(7)	0.6111(6)	0.6705(1)	0.80(9)
Li(1)	0.295(2)	0.255(2)	0.7517(5)	2.1(3)
Li(2)	0.0000	0.0000	0.5009(9)	1.1(3)
Li(3)	0.0000	0.0000	0.8377(4)	1.78(3)
O(1)	0.4981(4)	0.9748(4)	0.9031(1)	0.80(7)
(O,OH)(2)	0.4867(4)	0.9591(5)	0.9691(1)	1.09(8)
O(3)	0.5827(4)	0.9504(4)	0.6714(1)	0.74(8)
O(4)	0.8567(4)	0.5646(4)	0.8567(1)	0.90(8)
O(5)	0.8553(3)	0.8342(3)	0.9727(1)	0.57(6)
O(6)	0.7167(4)	0.5529(4)	0.7981(1)	0.91(7)
O(7)	0.5059(4)	0.4892(4)	0.7524(1)	0.84(7)
O(8)	0.7752(5)	0.7701(5)	0.8441(1)	1.02(9)
O(9)	0.7888(3)	0.5770(5)	0.7009(1)	1.13(9)
O(10)	0.5573(5)	0.8359(4)	0.8551(1)	1.07(8)
O(11)	0.7733(5)	-0.0055(4)	0.8080(1)	1.08(8)
O(12)	0.7853(4)	0.5039(4)	0.9389(1)	0.88(7)
O(13)	0.2351(4)	0.2771(4)	0.9363(1)	0.67(6)
(OH)(14)	0.0000	0.0000	0.8955(1)	0.8(1)
(O,OH)(15)	0.5539(5)	0.7005(5)	0.7977(1)	1.04(8)
O(16)	0.8335(6)	0.9081(6)	0.7304(2)	2.13(7)
(OH,H ₂ O)(17)	0.0000	0.0000	0.0519(2)	0.7(1)

* The Ca(2) position is filled statistically with 0.7Ca + 0.3Na and the Na position is filled statistically with 0.7Na.

the isolated CO₃-triangles. In the hexagonal twice body-centered *R* cell of Ca,Na,Li-carbonate-borate with the unit-cell parameters $c = 35.91 \text{ \AA}$ (exceeding the *a*- and *b*-parameters by a factor of 3.5), one can single out two alternating fundamental building blocks

parallel to the basis plane (0001) [10]. One unit cell contains three pairs of blocks related by the *R*-translation (Fig. 2).

The first block consists of original Ca-B-clusters forming a double layer. Each cluster is formed by two

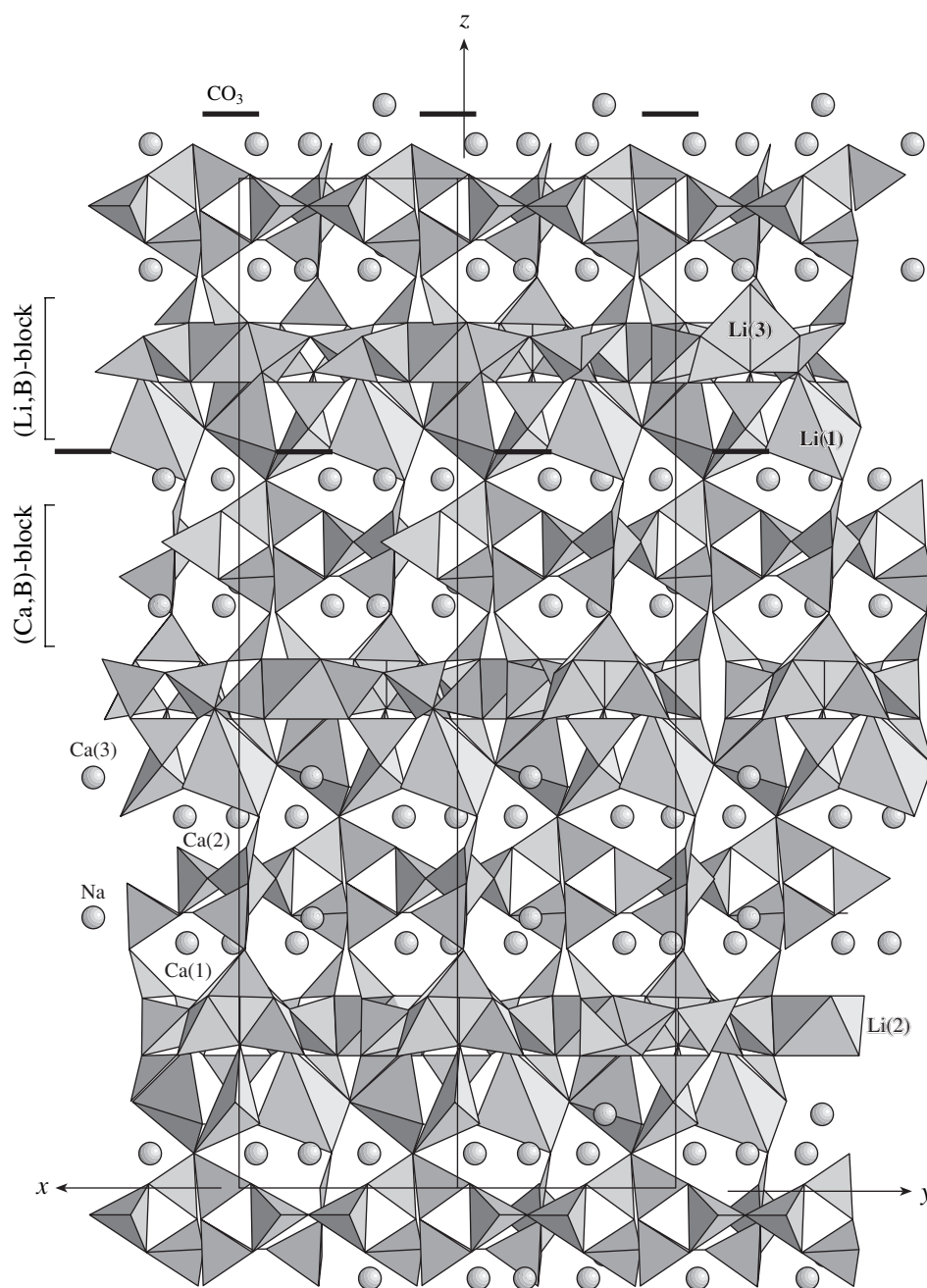


Fig. 2. The Ca,Na,Li-carbonate-borate structure projected onto the (110) plane. The Ca and Na atoms are denoted by spheres.

triads of seven-vertex Ca(1)- and Ca(2)-polyhedra “wound” around the threefold axis (Fig. 3a). The triads of Ca-polyhedra are located one under another and share the oxygen vertices; they are rigidly “cemented” by three-membered rings of B(1)-tetrahedra sharing edges with Ca-polyhedra. Moreover, the additional B(2)-tetrahedra and B(8)-triangles and the B(1) tetrahedron form a three-membered “inderite ring” (Fig. 3a). Three inderite rings form a ten-membered boron–oxygen anion described by the formula $[B'_6B_3^{\Delta}O_{15}(O,OH)_3]^{7.5-}$

(Fig. 3b). Some translationally identical B,O-anions (along the *a*- and *b*-axes) are connected by B(7) triangles parallel to the (0001) plane into the $\{[B'_6B_3^{\Delta}O_{15}(O,OH)_3] \cdot [B^{\Delta}O_{1.5}]\}_{\infty\infty}^{7.5-}$ layers (Fig. 4a). In turn, the Ca(1,2),B-clusters form a double layer via Ca(3)- and N-polyhedra (Fig. 3c). The lower triads of seven-vertex Ca(1)-polyhedra form the layer via trigonal Na-prisms sharing the O-vertices (Fig. 4a). In this case, Na-atoms are located along the threefold axes. Each Na-prism share the vertical edges with three B(2)-

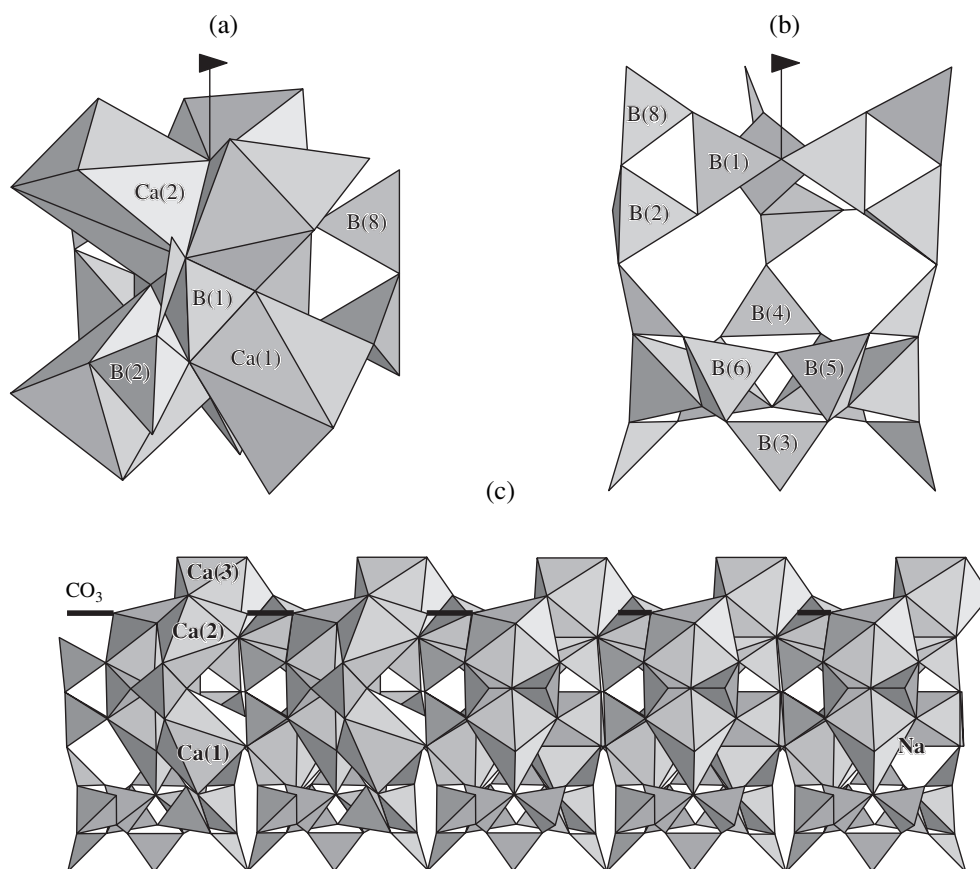


Fig. 3. Fragments of the Ca,Na,Li-carbonate-borate structure: (a) the clusters of seven-vertex Ca(1)- and Ca(2)-polyhedra bound to the nine-membered boron–oxygen anion consisting of three inderite rings; (b) boron–oxygen lantern consisting of nine- and twelve-membered boron–oxygen rings projected onto the (110) plane; and (c) a double layer of Ca,Na-polyhedra and its relation to a thick boron–oxygen layer.

tetrahedra of the inderite rings from three adjacent nine-membered B₉O₉-anions. The nine-vertex Ca(3)-polyhedra are located above the Na-prisms and form the layer of triads of seven-vertex Ca(2)-polyhedra and share edges with these polyhedra (Fig. 4b). Moreover, the triads of Ca(2) polyhedra share the O-vertices with the isolated CO₃-triangles “beaded” onto the axes 3. As a result, a two-layer Ca,Na,B-block is formed (Figs. 2 and 3c).

The second block has different chemical composition and is formed by B- and Li-polyhedra (Fig. 2). A six-membered ring is “wound” around the seven-vertex Li(3)-polyhedron composed by alternating B(5)- and B(6)-tetrahedra whose upper and lower parts are inlaid with B(3)- and B(4)-triangles. As a result, twelve-membered rings described by the formula $[B_6^t B_6^\Delta O_{19.5}(O,OH)_3]^{7.5-}$ are formed (Fig. 4c). These rings are similar to those found in the structures of new lead dodecaborate Pb₆B₁₂O₂₄ [7] with the anion described by the formula $[B_6^t B_6^\Delta O_{24}]^{12-}$ and Na-borate Na₈[B₁₂O₂₀(OH)₄] [11] with the anion described by the

formula $[B_{12}O_{20}(OH)_4]^{8-}$. However, in Pb- and Na-dodecaborates, the twelve-membered rings are isolated, whereas in Ca,Na,Li-carbonate-borate, they are bound to three B(2)-tetrahedra of the inderite rings located above (Fig. 3b). This leads to the formation of three-dimensional “lanterns,” with triads of Ca(1)-polyhedra of the first block being located inside these lanterns (Fig. 3c). The translationally identical boron–oxygen lanterns (along the *a*- and *b*-axes) are bound by B(7)-triangles to form rather thick (0001)-layers described by the formula $\{[B_6^t B_3^\Delta O_{15}(O,OH)_3] \cdot [B^\Delta O_{1.5}] \cdot [B_6^t B_6^\Delta O_{19.5}(O,OH)_3]\}_{\infty}^{15-} = [B_{12}^t B_{10}^\Delta O_{36}(O,OH)_6]_{\infty}^{15-}$, which, in turn, form the mixed B,Li-framework bound by the distorted Li(1)-tetrahedra and Li(2)-octahedra also located in the second block (Figs. 2, 4c). Thus, the Li-polyhedra play the role of binders and form the mixed B,Li-framework and bind the Ca,Na,B-blocks into the crystal structure. It is the presence of Li-interlayers that can explain the perfect cleavage along the (0001) plane of carbonate-borate.

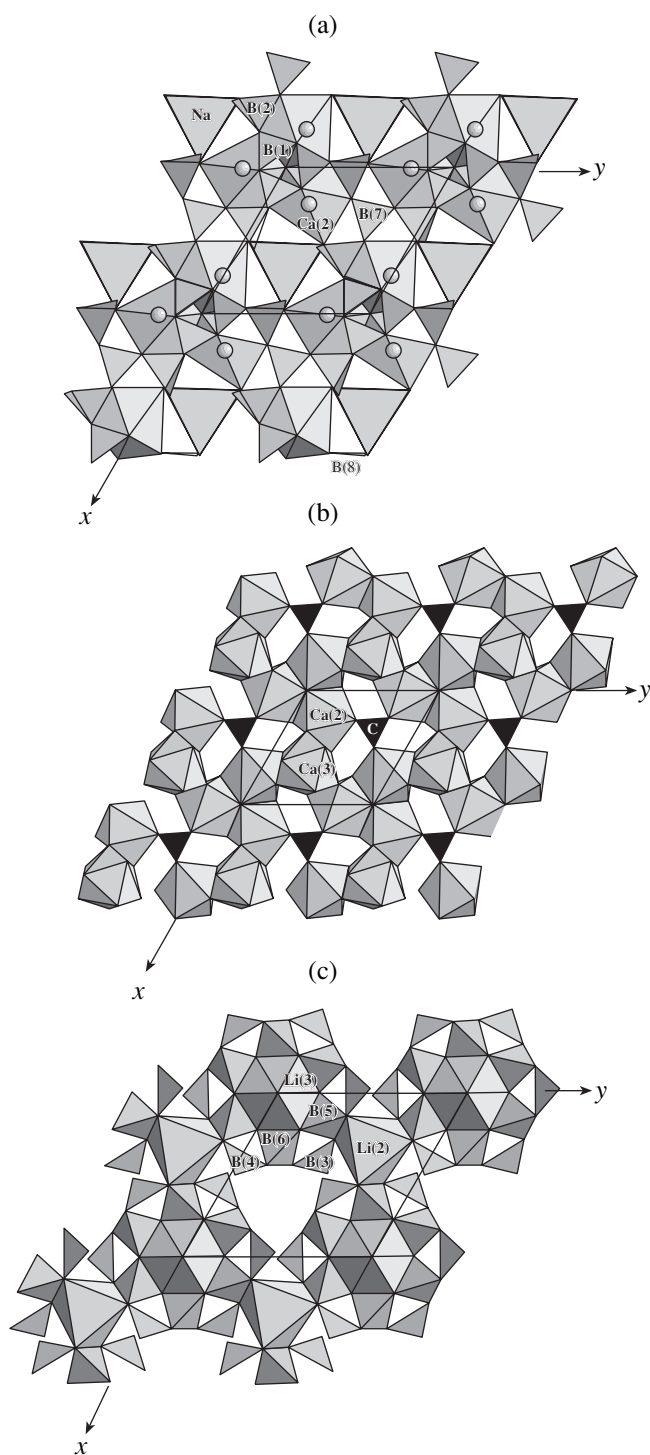


Fig. 4. Fragments of the Ca,Na,Li-carbonate-borate structure projected onto the (0001) plane: (a) a layer built by triads of seven-vertex Ca(1)-polyhedra and trigonal Na-prisms and nine-membered boron–oxygen rings [3B(1)^f, 3B(2)^f, and 3B(8)^Δ] connected via B(7) triangles; (b) a layer formed by triads of seven-vertex Ca(2)-polyhedra and nine-vertex Ca(3)-polyhedra and CO₃-triangles; (c) the combination of translationally related identical twelve-membered boron–oxygen rings [3B(5)^f, 3B(6)^f, 3B(3)^Δ, and 3B(4)^Δ], Li(2)-octahedra, and seven-vertex Li(3)-polyhedra.

CONCLUSIONS

The structure of Ca,Na,Li-carbonate-borate has no analogues among the well-known carbonate-borates and borates. The complexity of the crystal structure allows one to characterize this compound as megaborate (according to the Strunz classification, [12]) containing rather thick boron–oxygen layers. Until now, only two megaborates have been described whose complex boron–oxygen radicals can be compared with the complexes in the compound studied here—pringleite and its dimorphous modification ruitenbergitte, Ca₉[B₂₆O₃₄(OH)₂₄]Cl₄ · 13H₂O [13]. Their fundamental building blocks consist of twelve-membered rings of alternating B-tetrahedra and B-triangles, which, together with three-membered inderite rings, form a zeolite-like framework with voids filled with Ca, Cl, and H₂O molecules. The only difference between the two structures is how their fundamental building blocks are connected.

ACKNOWLEDGMENTS

The authors are grateful to E.L. Belokoneva for her help in the diffractometric experiment, N.V. Zubkova for her help in computations, and D.Yu. Pushcharovskii for valuable remarks and discussion of the results.

REFERENCES

- O. V. Yakubovich, M. A. Simonov, and N. V. Belov, *Kristallografiya* **20** (1), 152 (1975) [*Sov. Phys. Crystallogr.* **20**, 87 (1975)].
- O. V. Yakubovich, Yu. K. Egorov-Tismenko, M. A. Simonov, and N. V. Belov, *Dokl. Akad. Nauk SSSR* **239** (5), 1103 (1978) [*Sov. Phys. Dokl.* **23**, 225 (1978)].
- Z. Ma, N. Shi, J. Shen, and Z. Peng, *Bull. Mineral.* **104**, 578 (1981).
- J. D. Grice and T. S. Ercit, *Can. Mineral.* **24**, 675 (1986).
- P. C. Burns and F. C. Hawthorne, *Miner. Mag.* **59**, 297 (1995).
- V. I. Andrianov, *Kristallografiya* **32** (1), 228 (1987) [*Sov. Phys. Crystallogr.* **32**, 130 (1987)].
- E. L. Belokoneva, O. V. Dimitrova, and T. A. Korchemkina, *Zh. Neorg. Khim.* **44** (2), 187 (1999).
- Yu. A. Pyatenko, *Kristallografiya* **17** (4), 773 (1972) [*Sov. Phys. Crystallogr.* **17**, 677 (1972)].
- O. S. Bondareva, Yu. K. Egorov-Tismenko, M. A. Simonov, and N. V. Belov, *Dokl. Akad. Nauk SSSR* **243** (3), 641 (1978) [*Sov. Phys. Dokl.* **23**, 806 (1978)].
- F. C. Hawthorne, P. C. Burns, and J. D. Grice, *Rev. Mineral.* **33**, 41 (1996).
- S. Menchetti and C. Sabelli, *Acta Crystallogr., Sect. B: Struct. Crystallogr. Cryst. Chem.* **35**, 2488 (1979).
- H. Strunz, *Eur. J. Mineral.* **9**, 225 (1997).
- J. D. Grice, P. C. Burns, and F. C. Hawthorne, *Can. Mineral.* **32**, 1 (1994).

Translated by L. Man

STRUCTURES OF INORGANIC COMPOUNDS

Aluminum Fluoride Nanohydrate

A. B. Ilyukhin and S. P. Petrosyants

Kurnakov Institute of General and Inorganic Chemistry, Russian Academy of Sciences,
Leninskiĭ pr. 31, Moscow, 117907 Russia

e-mail: ilyukhin@igic.ras.ru

Received October 2, 2001

Abstract—The structure of $\text{AlF}_3 \cdot 9\text{H}_2\text{O}$ was established by the methods of X-ray diffraction analysis. The structure consists of isolated complex $\text{AlF}_3(\text{H}_2\text{O})_3$ molecules and molecules of crystal water linked via a network of $\text{Al-F}\cdots\text{HOH}$ and $\text{Al-OH}_2\cdots\text{OH}_2$ hydrogen bonds. © 2002 MAIK “Nauka/Interperiodica”.

Aluminum fluorides are important inorganic compounds. In $\text{AlF}_3 \cdot n\text{H}_2\text{O}$ ($n = 1$ or 3) and anionic aluminum fluorides, the octahedral AlF_6 fragments are linked to each other through bridging ligands to form chain, layer, or framework structures. As part of our current studies of aluminum fluorides [1, 2], we investigated the crystal structure of $\text{AlF}_3 \cdot 9\text{H}_2\text{O}$.

EXPERIMENTAL

Colorless $\text{AlF}_3 \cdot 9\text{H}_2\text{O}$ crystals were synthesized by the reaction of aluminum powder with a 15% aqueous solution of HF according to the procedure described earlier [3]. The chemical analysis, ^{19}F and ^{27}Al NMR spectroscopy (in solutions), DTA, and IR spectroscopy data have been reported elsewhere [2].

The X-ray diffraction data for $\text{AlF}_3 \cdot 9\text{H}_2\text{O}$ were collected on a Syntex $P2_1$ diffractometer (MoK_α radiation, graphite monochromator). The main crystallographic data and the results of the structure refinement are given in Table 1. Absorption was ignored. The structure was solved by combined direct methods and Fourier techniques using the SHELXS-97 [4] and SHELXL-97 [5] program packages. The positions of all the hydrogen atoms were established from difference Fourier syntheses. The structure was refined by the least-squares method in the anisotropic–isotropic approximation. The atomic coordinates and the thermal parameters are given in Table 2. In the model obtained, the aluminum atom is surrounded by six crystallographically equivalent ligands (the X position) at distances of 1.83 Å. However, according to the chemical analysis, the Al/F ratio in the compound under study is 1 : 3. The attempts to refine two partly occupied (by the F and O atoms) positions, artificially spaced by a distance of 0.2 Å (the minimum distance between these atoms being fixed as 0.15 Å), gave unsound thermal parameters for fluorine and oxygen atoms. The structure solution within the noncentrosymmetric space group with due regard for twinning did not lead to the separation of the X position

into the oxygen atom of the coordinated water molecule and the fluorine atom either. Analyzing the intermolecular contacts and the data on different refined arrangements of fluorine and oxygen atoms, we came to the conclusion that the X position is statistically occupied by the fluorine and oxygen atoms in a 1 : 1 ratio. The statistical distribution of fluoride ions and hydroxy ions in the coordination sphere of an aluminum atom is unreasonable from both chemical (the simultaneous presence of the hydroxy and oxonium ions in the structure) and crystallochemical standpoints (it is impossible to arrange all the hydrogen atoms so as to avoid

Table 1. Main crystallographic data and details of the X-ray diffraction experiment on $\text{AlF}_3 \cdot 9\text{H}_2\text{O}$

System	Rhombohedral
a , Å	6.9384(13)
α , deg	106.029(17)
Sp. gr.	$R\bar{3}$
V , Å ³	285.23(9)
Z	1
Temperature, K	255(3)
ρ , g/cm ³	1.433
μ , mm ⁻¹	0.241
Crystal dimensions, mm	0.4 × 0.4 × 0.3
θ_{max} , deg	37.6
Number of measured reflections	1131
Number of independent reflections	1013 [$R_{\text{int}} = 0.0389$]
Number of independent reflections with $I > 2(\sigma(I))$	376
Number of refined parameters	47
R , wR ($I > 2\sigma(I)$)	0.0322, 0.0623
R , wR (all reflections)	0.1377, 0.0679
Gof	1.025

Table 2. Atomic coordinates and thermal parameters of $\text{AlF}_3 \cdot 9\text{H}_2\text{O}$

Atom	<i>x</i>	<i>y</i>	<i>z</i>	$U_{\text{eq}}/U_{\text{iso}}, \text{\AA}^2$	Occupancy
Al(1)	0	0	0	0.0216(2)	
X	0.25668(13)	-0.01207(15)	0.14776(12)	0.0356(2)	
O(2)	0.66904(16)	0.27155(18)	0.31387(17)	0.0369(2)	
H(1)*	0.352(6)	0.060(6)	0.163(5)	0.046(10)	0.5
H(2)*	0.280(4)	-0.114(6)	0.192(4)	0.044(8)	0.5
H(3)*	0.771(5)	0.227(4)	0.273(4)	0.033(6)	0.5
H(4)*	0.676(4)	0.396(7)	0.306(3)	0.041(11)	0.62(6)
H(5)*	0.536(6)	0.182(4)	0.245(4)	0.040(7)	0.5
H(6)*	0.679(7)	0.279(8)	0.456(17)	0.09(2)	0.38(6)

$X = 0.5\text{F}(1) + 0.5\text{O}(1)$

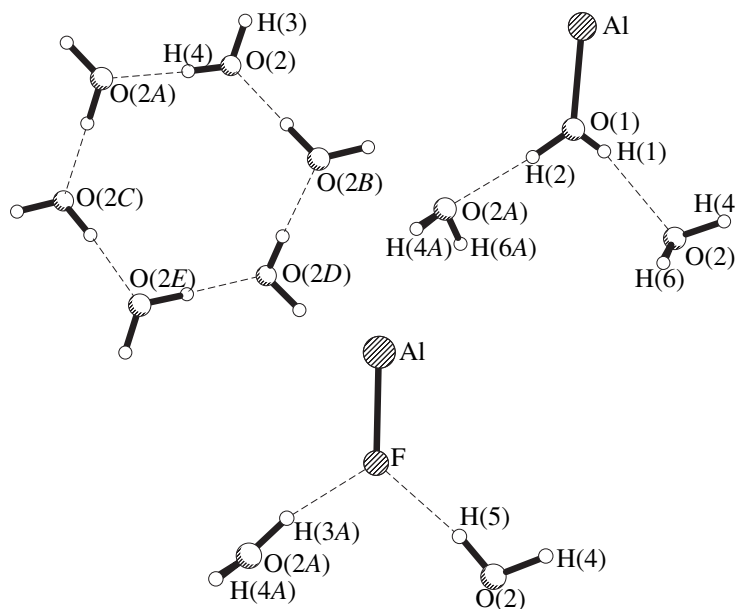
* Atoms were refined isotropically.

Table 3. Geometry of hydrogen bonds in the $\text{AlF}_3 \cdot 9\text{H}_2\text{O}$ structure

<i>D</i> -H... <i>A</i> bond	Distance, \AA			<i>DHA</i> angle, deg
	<i>D</i> -H	H... <i>A</i>	<i>D</i> ... <i>A</i>	
O(1)-H(1)...O(2)	0.67(4)	2.04(4)	2.6840(18)	159(3)
O(1)-H(2)...O(2) (<i>z</i> , <i>x</i> - 1, <i>y</i>)	0.88(4)	1.79(4)	2.6715(13)	177(3)
O(2)-H(3)...F(1) (<i>y</i> + 1, <i>z</i> , <i>x</i>)	0.93(4)	1.76(4)	2.6715(13)	167(2)
O(2)-H(4)...O(2) (- <i>y</i> + 1, - <i>z</i> + 1, - <i>x</i> + 1)	0.87(4)	1.89(4)	2.7547(13)	171(2)
O(2)-H(5)...F(1)	0.86(3)	1.83(3)	2.6840(18)	169(2)
O(2)-H(6)...O(2) (- <i>z</i> + 1, - <i>x</i> + 1, - <i>y</i> + 1)	0.95(10)	1.81(11)	2.7547(13)	171(5)

short H...H contacts). The geometric characteristics of the intermolecular F...O and O...O contacts indicate that the occupancies of the H(1)-H(3) and H(5) posi-

tions are equal to 0.5. The occupancies of the H(4) and H(6) positions were also refined (the sum of the occupancies equals unity).

**Fig. 1.** Scheme of hydrogen bonding in $\text{AlF}_3 \cdot 9\text{H}_2\text{O}$.

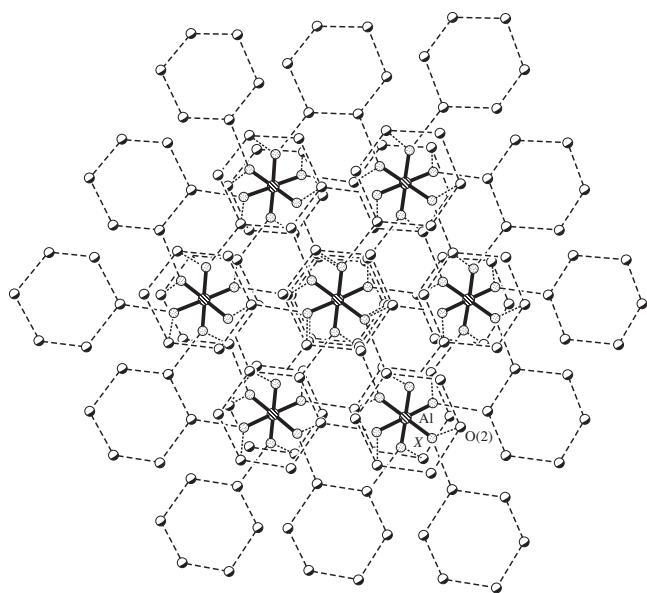


Fig. 2. $\text{AlF}_3 \cdot 9\text{H}_2\text{O}$ structure projected along the [111] direction.

RESULTS AND DISCUSSION

The $\text{AlF}_3 \cdot 9\text{H}_2\text{O}$ structure consists of $\text{AlF}_3(\text{H}_2\text{O})_3$ complexes and molecules of crystallization water. Since the aluminum atom occupies a particular point of the threefold inversion axis, its octahedral environment is close to ideal (the Al–X bond length is 1.8307(8) Å, and the X–Al–X angles are $6 \times 89.72(5)^\circ$, $6 \times 90.28(5)^\circ$, and $3 \times 180^\circ$). Almost the same bond length (1.826 Å) was found in $[\text{AlF}(\text{H}_2\text{O})_{0.5}\text{F}_{0.5}]_4(\text{H}_2\text{O})$ [6]. This Al–X bond length is closer to the typical Al–F bond length than to the Al–O(H₂O) bond length. In $[\text{AlF}_3(\text{H}_2\text{O})][\text{NH}_3\text{CH}_2\text{CH}_2\text{NH}_2\text{CH}_3]$ [1], these bond lengths are 1.79 and 2.01 Å, respectively.

All the positions of hydrogen atoms in the $\text{AlF}_3 \cdot 9\text{H}_2\text{O}$ structure were occupied only partly. In the case of the H(1) and H(2) atoms, this is associated with the fact that the mixed X position is only half-occupied by a water molecule. The H(3)–H(6) atoms are disordered in such a way that they form a tetrahedral environment around an oxygen atom (the HOH angles range within 99° – 114°). The disordered H(3) and H(5) positions also arise because of the mixed X position. This position (or, more precisely, the O(1) atom) plays the role of a donor in the O(1)···O(2) hydrogen bonds (Table 3) and an acceptor in the O(2)···F hydrogen bonds (Fig. 1). The H(4) and H(6) atoms are involved in the hydrogen bonds in the right and left forms of the $(\text{H}_2\text{O})_6$ hexamer, respectively. Due to the branched system of hydrogen

bonds, the complex molecules and the molecules of crystallization water are linked into a framework (Fig. 2). The $\text{AlF}_3 \cdot 9\text{H}_2\text{O}$ structure is responsible for the high solubility of the compound in water and polar organic solvents [2].

An analogous arrangement of the structural units was also observed in $\text{CrF}_3 \cdot 9\text{H}_2\text{O}$ (sp. gr. $R\bar{3}$, $a = 6.822$ Å, $\alpha = 105.17^\circ$) [7]. However, the $\text{CrF}_3 \cdot 9\text{H}_2\text{O}$ structure is composed of complex $[\text{Cr}(\text{H}_2\text{O})_6]^{3+}$ cations, fluoride anions, and molecules of crystallization water. The separation of the fluoride and oxygen positions in $\text{CrF}_3 \cdot 9\text{H}_2\text{O}$ lowers its symmetry. Unlike $\text{AlF}_3 \cdot 9\text{H}_2\text{O}$ containing six-membered $(\text{H}_2\text{O})_6$ rings, the $\text{CrF}_3 \cdot 9\text{H}_2\text{O}$ structure is characterized by the presence of $(\text{H}_2\text{O} \cdots \text{F})_3$ rings. In addition to $\text{CrF}_3 \cdot 9\text{H}_2\text{O}$, the analogous crystal structure was also observed for urotropine hexahydrate (sp. gr. $R\bar{3}m$, $a = 7.30$ Å, $\alpha = 105.4^\circ$) [8]. In the latter structure, a urotropine molecule occupies the position of $\text{AlF}_3(\text{H}_2\text{O})_3$, so that the general structural motif remains unchanged. Thus, despite different compositions and charges of the $\text{AlF}_3 \cdot 9\text{H}_2\text{O}$ molecular complex, the $\text{CrF}_3 \cdot 9\text{H}_2\text{O}$ ionic complex, and $(\text{CH}_2)_6\text{N}_4 \cdot 6\text{H}_2\text{O}$ organic hydrate, the crystal structures of these compounds are similar.

ACKNOWLEDGMENTS

This study was supported by the Russian Foundation for Basic Research, project no. 00-15-97432.

REFERENCES

1. S. P. Petrosyants, A. B. Ilyukhin, and Yu. A. Buslaev, *Zh. Neorg. Khim.* **37** (7), 1551 (1992).
2. S. P. Petrosyants, A. M. Shpirt, and Yu. A. Buslaev, *Zh. Neorg. Khim.* **46** (6), 983 (2001).
3. N. A. Matwiyoff and W. E. Wageman, *Inorg. Chem.* **9** (5), 1031 (1970).
4. G. M. Sheldrick, *SHELXS97: Program for the Solution of Crystal Structures* (Univ. of Göttingen, Göttingen, 1997).
5. G. M. Sheldrick, *SHELXL97: Program for the Refinement of Crystal Structures* (Univ. of Göttingen, Göttingen, 1997).
6. F. Olmi, C. Sabelli, and R. Trosti-Ferroni, *Eur. J. Mineral.* **5**, 1167 (1993).
7. M. Epple and W. Massa, *Z. Anorg. Allg. Chem.* **444** (7), 47 (1978).
8. T. C. W. Mak, *J. Chem. Phys.* **43**, 2799 (1965).

Translated by T. Safonova

STRUCTURES OF INORGANIC COMPOUNDS

Low-Temperature X-ray Studies of a $[(\text{CH}_3)_2\text{NH}_2]_2 \cdot \text{CuCl}_4$ Crystal

A. U. Sheleg*, E. M. Zub*, A. Ya. Yachkovskii*, and L. F. Kirpichnikova**

* Institute of Solid State and Semiconductor Physics, National Academy of Sciences,
ul. P. Brovki 17, Minsk, 220072 Belarus
e-mail: sheleg@ifftp.bas-net.by

** Shubnikov Institute of Crystallography, Russian Academy of Sciences,
Leninskiĭ pr. 59, Moscow, 117333 Russia
e-mail: luba@ns.crys.ras.ru

Received May 4, 2001

Abstract—The a , b , c lattice parameters of a $[(\text{CH}_3)_2\text{NH}_2]_2 \cdot \text{CuCl}_4$ crystal have been measured by the X-ray diffraction method within the temperature range of 100–300 K. The temperature dependences of thermal expansion coefficients $\alpha_a = f(T)$, $\alpha_b = f(T)$, and $\alpha_c = f(T)$ along the principal crystallographic axes and thermal expansion coefficient of the unit-cell volume $\alpha_V = f(T)$ are determined. It is found that all the three parameters, a , b , and c , vary with temperature in a complicated way and show jumplike anomalies in the $a = f(T)$, $b = f(T)$, and $c = f(T)$ curves at phase-transition temperatures $T_{c1} = 255$ K and $T_{c2} = 279$ K. An incommensurate phase with the modulation wave vector $\mathbf{q}_i = (1/2 + \delta)(\mathbf{a}^* + \mathbf{c}^*)$ is revealed in the temperature range 279–296 K. It is shown that the incommensurability parameter δ increases with an increase in temperature. © 2002 MAIK “Nauka/Interperiodica”.

INTRODUCTION

A crystal of composition $[(\text{CH}_3)_2\text{NH}_2]_2 \cdot \text{CuCl}_4$ (**I**) belongs to the crystal family described by the general formula A_2BX_4 and is also a representative of the group of crystals described by the general formula $[(\text{CH}_3)_2\text{NH}_2]_2 \cdot \text{MeCl}_4$ (Me = Cd, Co, Cu, Zn, etc.), whose properties have not yet been adequately studied. These crystals are of interest because they undergo a number of phase transitions depending on the temperature and the nature of metal ions. The parameters of these phase transitions are very sensitive to the degree of crystal perfection and to the type of crystal irradiation, e.g., with gamma quanta or electrons. It is well known that crystals **I** undergo two first-order phase transitions at the temperatures $T_{c1} = 253$ K and $T_{c2} = 279$ K and that between these temperatures they exhibit ferroelectric properties [1]. Studying birefringence, Vlokh *et al.* [2] revealed a second-order phase transition at $T_{c3} = 296$ K, most probably, with the formation of an incommensurate phase.

The existence of two first-order phase transitions and, possibly, of an incommensurate phase stimulated X-ray studies of these crystals with the aim of establishing the temperature variations in the unit-cell parameters, the thermal expansion coefficients, and satellite reflections indicative of the existence of a modulated structure.

EXPERIMENTAL

The unit-cell parameters of crystal **I** were determined on an Enraf-Nonius diffractometer (MoK $_{\alpha}$ radiation) at room temperature. X-ray patterns were processed with the use of the standard K4 program. It was found that, at room temperature, the crystal belongs to the orthorhombic system and has the unit-cell parameters $a = 9.9685 \pm 0.0005$ Å, $b = 11.3215 \pm 0.0005$ Å, and $c = 15.6460 \pm 0.0005$ Å. These parameters differ from the data obtained in [3], $a = 10.45$ Å, $b = 11.45$ Å, $c = 15.77$ Å.

The low temperature (100–300 K) X-ray diffraction studies were performed on a TUR M 62 diffractometer (CuK $_{\alpha}$ radiation). The specimens were {001}-, {010}-, and {101}-oriented single-crystal plates with dimensions $\sim 4 \times 4 \times 2$ mm. The temperature dependences of the unit-cell parameters were determined by measuring the Bragg angle 2θ of the (808), (010.0), and (008) reflections. The b - and c -parameters were measured on crystal plates whose surfaces were oriented parallel to the corresponding crystallographic planes with an accuracy of $\pm 4'–6'$. The a -parameter was determined from the temperature dependences of the interplanar spacing $d_{008} = f(T)$ and $d_{808} = f(T)$. The diffraction spectra were obtained by continuous $\theta–2\theta$ scanning while recording the intensity profiles of reflections. The 2θ angles were determined using the centers of gravity of the reflections. The specimen temperature was controlled by a special block based on a VRT-3 device. The temperature was measured by a copper–constantan

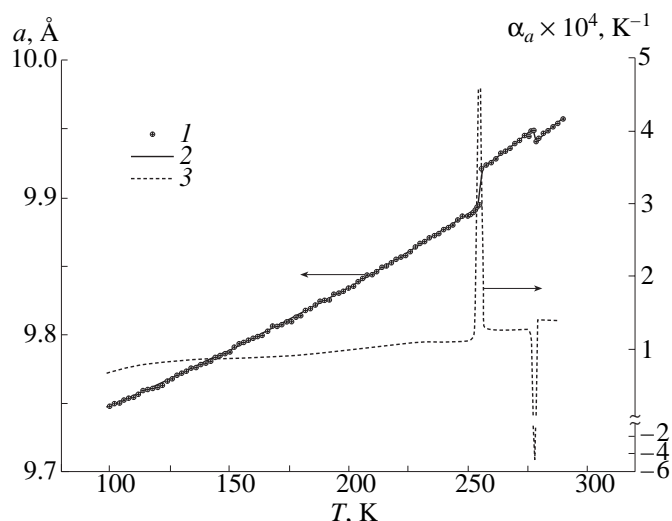


Fig. 1. Temperature dependence of the unit-cell parameter a : (1) experimental points, (2) approximated experimental data, and (3) temperature variation of the thermal expansion coefficient α_a .

thermocouple. Thus, the system allowed us to set the temperature and maintain it with an accuracy of ± 0.1 K in the whole temperature range studied (100–300 K). Prior to an X-ray experiment, each specimen was kept for 10–12 minutes at a given temperature. The diffraction angles were measured at a step of 1–2 K.

The experimentally obtained temperature dependences of the unit-cell parameters, $a = f(T)$, $b = f(T)$, $c = f(T)$, and unit-cell volume, $V = f(T)$, provided the determination of the corresponding thermal expansion coefficients $\alpha_a = f(T)$, $\alpha_b = f(T)$, $\alpha_c = f(T)$ along the principal crystallographic axes and of the unit-cell volume, $\alpha_V = f(T)$, in the temperature range 100–300 K. Each of these curves, $a = f(T)$, $b = f(T)$, $c = f(T)$, and $V = f(T)$, was approximated by three appropriate power polynomials of the type $L = A + \sum_i (-1)^i B_i T^i$ in three temperature ranges—100 K $- T_{c1}$, $T_{c1} - T_{c2}$, and $T_{c2} - 300$ K. The approximated temperature curves were divided into the segments of the length 0.7–1.5 K within which thermal expansion coefficients were calculated by the formula $\alpha_L = \frac{1}{L} \frac{\Delta L}{\Delta T}$, where L is the unit-cell parameter at the middle point of the given segment ΔT , T is the temperature, and ΔL is the change of the parameter L along this segment.

RESULTS

The temperature dependences of the unit-cell parameters, the unit-cell volume, and also the thermal expansion coefficients are shown in Figs. 1–4. The a -, b -, and c -parameters and the volume V increase with an increase in temperature up to the temperature of the phase transition, $T_{c1} = 255$ K. It should be noted that the

phase-transition temperature determined in our study ($T_{c1} = 255$) is higher by 2 K than that given in [1], which can be explained by the use of different specimens. The thermal expansion coefficients α_a , α_b , α_c , and α_V in this temperature range change insignificantly: α_a slightly increases with temperature, the curve $\alpha_b = f(T)$ goes through a small maximum in the vicinity of $T \approx 209$ K, and the curve $\alpha_c = f(T)$ shows two shallow minima at $T \approx 145$ and 238 K and a small maximum at $T \approx 196$ K. A more complicated behavior of the unit-cell parameters and thermal expansion coefficients along the crystallographic axes is observed at temperatures $T > T_{c1} = 255$ K. At the phase-transition temperature $T_{c1} = 255$ K, the a -parameter abruptly increases by 0.03 Å, then increases in the region of the ferroelectric phase, and then abruptly drops by 0.01 Å at the phase-transition temperature $T_{c2} = 279$ K. The a -parameter increases with a further increase in temperature. A sharp maximum at the phase-transition temperature $T_{c1} = 255$ K and a minimum at $T_{c2} = 279$ K are observed on the curve $\alpha_a = f(T)$ (Fig. 1). As is seen from Fig. 2, similar discontinuities were also observed for the b -parameter at the phase-transition temperatures $T_{c1} = 255$ K and $T_{c2} = 279$ K, but their magnitudes are more pronounced—0.02 Å in the upward and 0.055 Å in the downward directions. Within the existence range of the ferroelectric phase and also at $T > T_{c2}$, the b -parameter smoothly decreases. Like the $\alpha_b = f(T)$ curve, we observe a sharp positive peak at $T_{c1} = 255$ K on the $\alpha_a = f(T)$ curve and a negative peak at $T_{c2} = 279$ K, and a small minimum in the vicinity of ~ 271 K in the region of the ferroelectric phase.

The inset in Fig. 2 shows the variation in the parameter b in the vicinity of the phase transitions at T_{c1} and T_{c2} measured in the heating-cooling mode. It is seen that the b -parameter has a hysteresis close to both phase transitions— $\Delta T \approx 2$ K at T_{c1} and $\Delta T \approx 1$ K at T_{c2} . The existence of hysteresis confirms the assumption that the observed transformations are first-order phase transitions.

The temperature dependence of the parameter c in the range of phase transitions is a “mirror reflection” of the temperature dependence of the parameter b in the same temperature range: b increases whereas c decreases, and vice versa (Figs. 2, 3). With an increase in the temperature, c on the curve $c = f(T)$ dramatically decreases (by 0.02 Å) at the phase-transition temperature $T_{c1} = 255$ K. In the existence range of the ferroelectric phase c increases. Then, at $T_{c2} = 279$ K a jump in c by 0.04 Å occurs. At $T > T_{c2}$, the parameter c slightly increases up to 300 K. The thermal expansion coefficient α_c behaves in the same way: it has a sharp negative peak at $T_{c1} = 255$ K and a sharp positive peak at $T_{c2} = 279$ K. Such an “antiphase” temperature behavior of the b - and c -parameters explains the fact that the pronounced changes in the lattice parameters (to 0.055 Å)

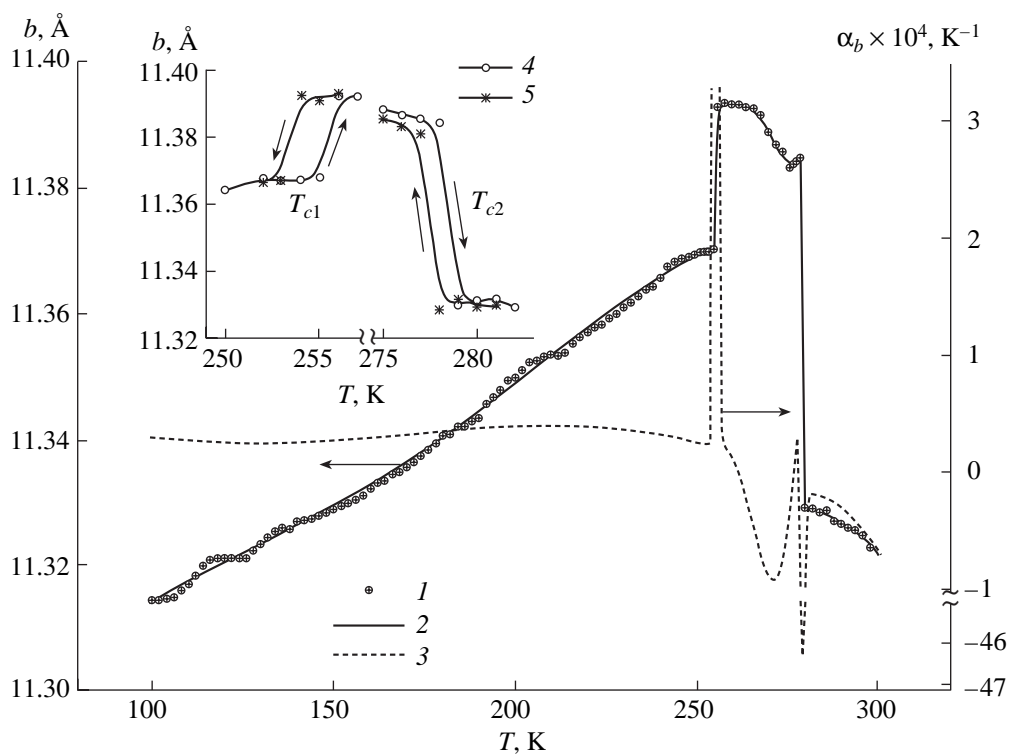


Fig. 2. Temperature dependence of the unit-cell parameter b : (1) experimental points, (2) approximated experimental data. (3) Temperature variation of the thermal expansion coefficient α_b . The inset shows the temperature hysteresis of the b -parameter at T_{c1} and T_{c2} : (4) heating, (5) cooling.

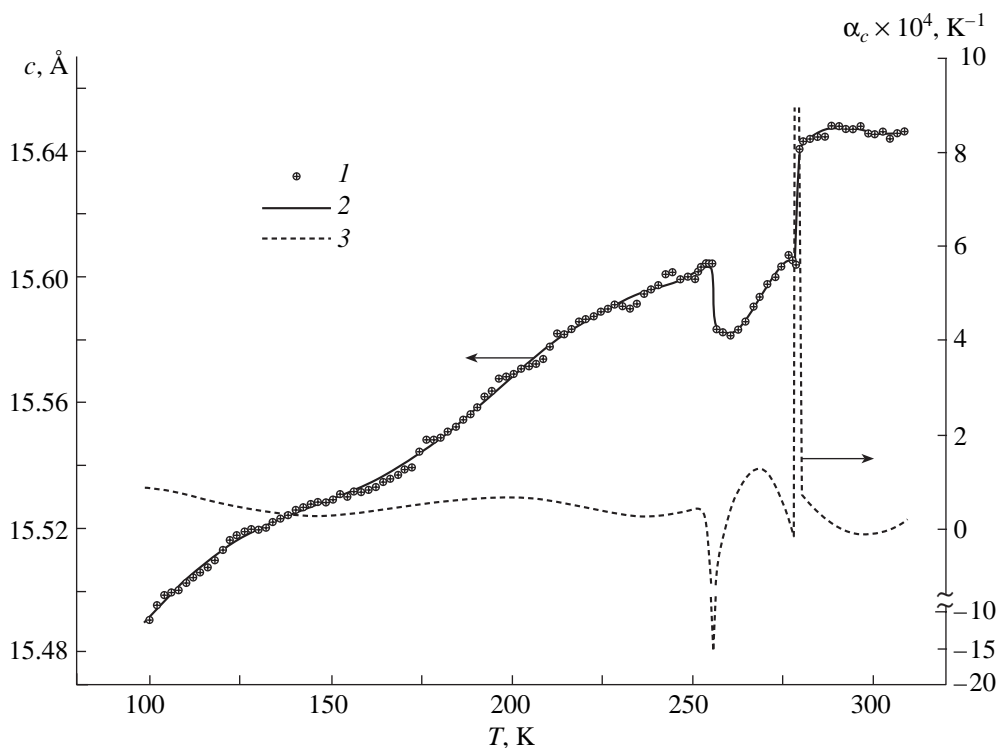


Fig. 3. Temperature dependence of the unit-cell parameter c : (1) experimental points, (2) approximated experimental data. (3) Temperature variation of the thermal expansion coefficient α_c .

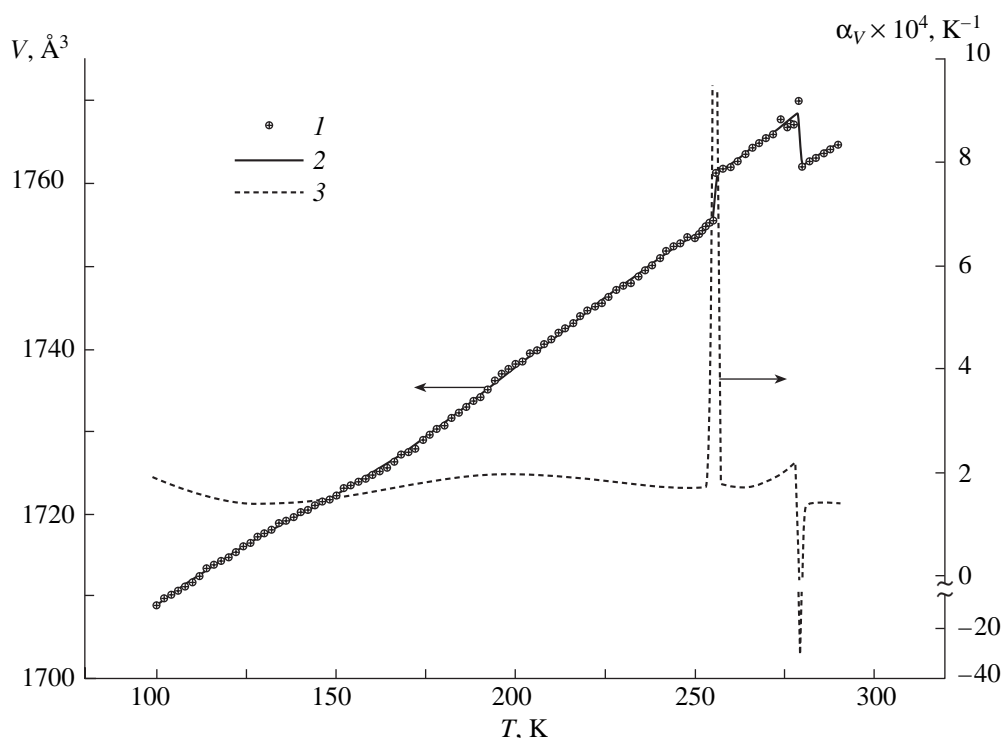


Fig. 4. Temperature dependence of the unit-cell volume V : (1) experimental points, (2) approximated experimental data, (3) temperature variation of the thermal expansion coefficient α_V .

in the range of phase transitions do not lead to crystal destruction. The changes in the unit-cell volume in the phase transitions are still comparatively weak (Fig. 4). As seen from Fig. 4, the thermal expansion coefficient only weakly depends on temperature in the whole temperature range studied except for the phase-transition temperatures T_{c1} and T_{c2} , where some anomalies are observed. However, the temperature dependence of α_V has a low minimum at $T \approx 136$ K and a weak maximum at $T \approx 200$ K.

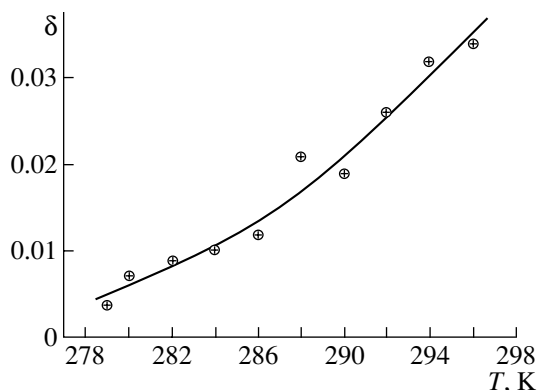


Fig. 5. Incommensurability parameter δ as a function of temperature.

The analysis of X-ray diffraction spectra obtained from the $(h0h)$ planes recorded at a step of 2 K in the temperature range 279–296 K revealed superstructural $(1/2 + \delta, 0, 1/2 + \delta)$ reflections, which allowed us to calculate the incommensurability parameter δ , whose temperature dependence is shown in Fig. 5. It is seen that δ increases with an increase in temperature. Thus, it has been shown that in the temperature range 279–296 K an incommensurate phase with the modulation wave vector $\mathbf{q}_i = (1/2 + \delta)(\mathbf{a}^* + \mathbf{c}^*)$ exists.

REFERENCES

1. Z. A. Bobrova, V. M. Varikash, A. I. Baranov, and L. A. Shuvalov, *Kristallografiya* **32** (1), 255 (1987) [*Sov. Phys. Crystallogr.* **32**, 148 (1987)].
2. O. G. Vlokh, V. B. Kapustyanyk, I. I. Polovinko, *et al.*, *Izv. Akad. Nauk SSSR, Ser. Fiz.* **54** (6), 1143 (1990).
3. A. Yu. Oleshchuk, P. A. Petrenko, Z. A. Bobrova, and T. N. Malinovskiĭ, in *Proceedings of the 4th All-Union School-Workshop "Ferroelastics"* (Dnepropetrovskii Univ., Dnepropetrovsk, 1988), p. 68.

Translated by A. Zaleskiĭ

Structures of Tetracyanoethylene and Its Tricyanovinyl Derivatives with Intramolecular Charge Transfer: A Review

L. A. Chetkina and V. K. Bel'skiĭ

Karpov Research Institute of Physical Chemistry, Russian State Scientific Center,
ul. Vorontsovo pole 10, Moscow, 103064 Russia

e-mail: belsky@cc.nifhi.ac.ru

Received September 26, 2000

Abstract—The results of X-ray structure investigations of crystalline compounds with a tricyanovinyl group (individual substances, molecular complexes, and ionic salts) and related compounds are generalized. The most interesting geometric and conformational characteristics of the molecules and ions are discussed. Consideration is given to the crystal chemical features of the compounds involved. The structural formulas of 73 compounds and the reliability factors (*R* factors) of crystal structure determination are given in the tables. © 2002 MAIK “Nauka/Interperiodica”.

CONTENTS

1. Introduction
 2. Molecular and Crystal Structures of Tetracyanoethylene from Diffraction Data
 3. Structural Features of Tricyanoethylenes and Related Compounds from X-ray Diffraction Data
 - 3.1. Tricyanovinyl Compounds
 - 3.2. Molecular Complexes and Ionic Salts of the Compounds with a Tricyanovinyl Group
 - 3.3. Organometallic Complexes and Ionic Salts with Tricyanoethenolate
 - 3.4. Tricyanopropenylidene Compounds
 - 3.5. Derivatives of Tricyanobutadienylidene and Its Homologs
 4. Conclusion
- References

1. INTRODUCTION

The design of new chemical compounds with important physicochemical properties necessitates the determination of their crystal and molecular structures with the aim of revealing a correlation between structure and properties.

The accumulation of experimental data at a very rapid pace has been in progress for the last few years due primarily to the advent of modern equipment and the development of applications software for diffraction methods. At present, research work that deals with the generalization of a large amount of structural data for different classes of compounds and, thus, provides a better insight into the structural regularities and structure–property relations have taken on special significance. In this respect, we continue a series of surveys concerned with specific classes of organic compounds

and their complexes that are of the greatest practical interest owing to their unique physicochemical properties. Among these compounds are polycyano-substituted substances. The organic compounds with a tricyanovinyl fragment also belong to this class of substances and will be considered in the present work.

It is known that the introduction of cyano groups into an acceptor molecule substantially enhances its electron-acceptor properties. Among the organic acceptors, the high electron affinity is observed for 7,7,8,8-tetracyanoquinodimethane ($E_a = 2.8$ eV) and tetracyanoethylene ($E_a = 2.75$ eV) [1, 2]. These acceptors have been used in the preparation of a great variety of charge-transfer complexes and radical ion salts with interesting electrical, magnetic, and other physicochemical properties. Structural data on the conducting molecular complexes and radical ion salts based on 7,7,8,8-tetracyanoquinodimethane were generalized earlier in the reviews [3, 4]. However, as far as we know, structural data for tetracyanoethylene derivatives have never been generalized. In the present work, we analyzed the results of investigations into the structure of tetracyanoethylene—the ancestor of a large class of organic and organometallic compounds (Section 2). These results were compared with the geometric parameters of the tetracyanoethylene monosubstituted derivatives discussed in Section 3.

Tricyanoethylenes and related compounds with a tricyanovinyl group also belong to strong organic acceptors. Their molecular complexes and ionic salts with organic and inorganic donors are well known by virtue of the unique combination of valuable properties, such as photoelectric sensitivity, nonlinearity of optical characteristics, etc. The derivatives of tetracyanoethylene in which one cyano group is replaced by an electron-donor fragment are typical donor–acceptor conju-

Table 1. Reliability factors (with the references) for two crystalline modifications of tetracyanoethylene

Cubic form, space group $Im\bar{3}$, $Z = 6$ ($2/m\ 2/m\ 2/m$)		Monoclinic form, space group $P2_1/n$, $Z = 2$ ($\bar{1}$)					
<i>R</i> factor	Reference	<i>R</i> factor	Reference	<i>R</i> factor	Reference	<i>R</i> factor	Reference
0.059	[28]	0.091	[31]	0.074** (5 K)	[34]	0.035	[30]
0.027*	[29]	0.091	[32]	0.100** (150 K)	[34]	0.034* (120 K)	[30]
0.034	[30]	0.035	[33]	0.085**	[34]	0.033*	[30]
0.024*	[30]	0.033*	[33]	0.037 (120 K)	[30]	0.030**	[35]

* Neutron single-crystal diffraction data.

** Neutron powder diffraction data.

gated systems with intramolecular charge transfer. The intramolecular charge transfer in these systems is revealed by an analysis of the electronic absorption spectra. The currently available spectral data on intramolecular-charge-transfer transitions that are treated as a special type of electronic transition are very scarce, especially compared to the results of extensive spectral investigations of charge-transfer complexes. In order to reveal the specific geometrical features associated with intramolecular charge transfer in the molecules involved and to compare these characteristics with the physicochemical properties, we considered the available data on organic compounds with a tricyanovinyl group whose crystal and molecular structures were determined earlier by X-ray diffraction analysis. For this purpose, we used the results of structural investigations [5–21], bibliographic information from the Cambridge Structural Database [22], and data taken from scientific journals and reference books published up to and including 1999.

2. MOLECULAR AND CRYSTAL STRUCTURES OF TETRACYANOETHYLENE FROM DIFFRACTION DATA

The synthesis of tetracyanoethylene $(CN)_2C=C(CN)_2$ [23] and analysis of numerous reactions of addition, substitution, and cyclization with its participation (see, for example, [23–27]) provided a way of preparing new dyes, strong acids, and new heterocyclic compounds. Tetracyanoethylene (also referred to as ethylenetetracarbonitrile) is the strongest π -acid and forms brightly colored molecular donor-acceptor complexes. Tetracyanoethylene crystallizes in two polymorphic modifications, namely, monoclinic and cubic modifications. The crystal and molecular structures of tetracyanoethylene were determined and subsequently refined using X-ray single-crystal diffraction, neutron single-crystal diffraction [28–33], and neutron powder diffraction [34, 35]. In the gas phase, tetracyanoethylene was characterized by electron diffraction analysis [36]. For two crystalline forms of tetracyanoethylene, the reliability factors (*R* factors) of the structure determination with the corresponding ref-

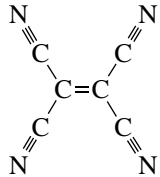
erences are presented in Table 1. The tetracyanoethylene molecules in the cubic modification (space group $Im\bar{3}$, $Z = 6$) has a high symmetry ($D_{2h}-mmm$), whereas the tetracyanoethylene molecules in the monoclinic modification (space group $P2_1/n$, $Z = 2$) retain only the center of symmetry. The geometric parameters of the tetracyanoethylene molecule in different phases are listed in Table 2.

It can be seen from Table 2 that, in both crystalline modifications, the bond lengths and angles of the tetracyanoethylene molecules are close to each other. In the cubic modification, the $C\equiv N$ bond is slightly longer and the $C-C-C$ bond angle is slightly smaller compared to those in the monoclinic modification. In the monoclinic crystals, the $C-C\equiv N$ cyano group has a more pronounced linear configuration. In the gas phase, the corresponding bonds in the tetracyanoethylene molecule are also close in length. As in unsubstituted ethylene, the $C=C$ bond length in crystalline tetracyanoethylene (the mean value is 1.346 Å), according to the X-ray diffraction data [28, 33], is somewhat shorter than that in gaseous tetracyanoethylene (1.357 Å). For ethylene, the $C=C$ bond lengths are equal to 1.313 [37] and 1.337 [38] Å, respectively. On the other hand, the bond lengths and angles obtained from the neutron diffraction data for tetracyanoethylene are close to those observed in the gas phase; however, all the bond lengths slightly exceed the standard value of the $C(sp^2) = C(sp^2)$ bond length (1.331 Å) [39]. The tetracyanoethylene molecule has a strictly planar configuration in the cubic modification and remains planar (to within 0.01 Å) in the monoclinic form.

Druck and Guth [33] performed the precision structural investigation of tetracyanoethylene in the monoclinic modification and revealed a certain statistical disorder in its structure: 3.8% of the tetracyanoethylene molecules in the X-ray diffraction experiment and 5.0% of the molecules in the neutron diffraction experiment were rotated by $\sim 90^\circ$ in the molecular plane with respect to the midpoint of the double $C=C$ bond.

Becker *et al.* [29] analyzed the X-ray diffraction and neutron diffraction data and obtained the difference ($X - N$) electron-density distribution for the cubic mod-

Table 2. Molecular geometry of tetracyanoethylene in different phases (bond lengths in Å and bond angles in degrees)

	Cubic crystals		Monoclinic crystals			Gas phase
	[28]	[29]*	[32]	[33]	[33]*	[36]
C=C	1.344(3)	1.355(2)	1.339(3)	1.348(2)	1.354(1)	1.357(10)
C–C	1.439(2)	1.431(1)	1.442(5)	1.438(2)	1.425(1)	1.435(10)
C≡N	1.153(2)	1.160(1)	1.135(6)	1.139(2)	1.146(1)	1.162(2)
C=C–C	122.2(1)	121.94(8)	121.0(4)	121.2(1)	121.07(7)	121.1
C–C–C	115.6(1)	116.11(8)	120.9(4)	121.0(1)	121.11(6)	
C–C≡N	178.2(1)	177.93(7)	118.1(3)	117.8(1)	117.82(6)	
			179.1(4)	179.3(8)	179.2(7)	
			179.4(4)	179.4(1.0)	179.0(5)	

* Neutron diffraction data.

ification of tetracyanoethylene. The electron densities determined for the C–C, C=C, and C≡N bonds are equal to 0.6, 0.4, and 0.9 e · Å⁻³, respectively. The height of the peak assigned to the lone electron pair of the nitrogen atom located on the extension of the C≡N bond is equal to 0.4 e · Å⁻³.

The recent investigation of monoclinic tetracyanoethylene was carried out by Chaplot *et al.* [35], who used neutron powder diffraction with a higher resolution than in their earlier work [34]. Analysis of the crystal structure of tetracyanoethylene in both phases and the molecular dynamics at different temperatures and pressures can give a deeper insight into the mechanisms of unusual reversible transitions from the cubic phase to the monoclinic phase in this compound (see [35] and references therein). The calculated charges at the atoms of the tetracyanoethylene molecule are given in [40].

3. STRUCTURAL FEATURES OF TRICYANOETHYLENES AND RELATED COMPOUNDS FROM X-RAY DIFFRACTION DATA

3.1. Tricyanovinyl Compounds

1,2,2-Tricyanovinyl compounds of the general formula (CN)₂C=C(CN)R, where R is the aromatic or heterocyclic electron-donor substituent, have been investigated by different physicochemical methods [23–27, 41–43]. The majority of tricyanovinyl derivatives are widely used as dyes and materials with nonlinear optical properties [44].

A specific feature of the tricyanovinyl compounds is that the electronic absorption spectra in the visible range contain an intense band associated with the

intramolecular charge transfer [41, 45, 46]. Some of these materials exhibit a substantial photoelectric sensitivity and can be used as photoconductors and efficient sensitizers in the manufacturing of electrophotographic polymer layers in electrophotography [47–49].

Table 3 presents tricyanovinyl compounds whose crystal and molecular structures are characterized by X-ray diffraction analysis. In this table, the column “R factor” includes the temperature of the measurements performed at low temperatures. For tricyanovinylbenzene (compound **1**), our earlier attempts (Povet’eva, Chetkina, and Il’ina, 1981) to determine the structure only on the basis of the experimental data collected at room temperature have failed because of the strong structural disorder. Recently, Bock *et al.* [50] managed to solve the structure of this compound (by using low-temperature experimental data) and the structure of disubstituted benzene—1,4-bis(tricyanovinyl)benzene (compound **2**). Even at 150 K, structure **1** is disordered; more precisely, the molecule is disordered over two positions with an occupancy of 0.5. The molecule has a nearly planar configuration: the tricyanovinyl group deviates from the ring plane by 6° at one position and by 11° at the other position. In centrosymmetric molecule **2**, the tricyanovinyl groups are oppositely rotated with respect to the benzene plane through an angle of 48°. Bock *et al.* [50] analyzed the data available in the Cambridge Structural Database and proved that this angle is maximum for tetracyanoethylenes. In the related centrosymmetric molecule of 1,4-bis(dicyanovinyl)benzene, the rotation angle is equal to 14° [57].

Tricyanovinylarylamines (compounds **3–7**) belong to compounds with a pronounced intramolecular charge transfer. Tricyanovinylarylamines are brightly

colored crystalline materials with a metallic luster. According to [41], the tricyanovinylarylamine molecules possess a large dipole moment. These properties stem from the fact that the tricyanovinylarylamine molecules contain both the strong electron-acceptor tricyanovinyl group and electron-donor amino groups interacting through the π -conjugated system. It is also known that tricyanovinylarylamines exhibit photoelectric sensitivity and, hence, can be used as sensitizers of electrophotographic layers [47, 49].

Poly(tricyanovinylamides) were prepared by the reaction of tetracyanoethylene with polyamides. The structure of poly(tricyanovinylamides) was determined using the specially synthesized model compounds, including compounds **4** and **5** (Table 3). The UV spectra of the tricyanovinyl polymers and their model compounds show an intense broad absorption band attributed to the intramolecular-charge-transfer transition. A number of tricyanovinyl polymers are characterized by a considerable photoelectric sensitivity and have found use as materials for high-strength polymer films [58].

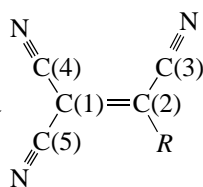
The photoelectric properties of tricyanovinylarylamines (compounds **3–5**) are reported in [5]. The temperature dependence of the photoconductivity for tricyanovinylarylamine single crystals is analyzed in [49]. Investigation into the crystal structure of tricyanovinylarylamines is of particular interest for understanding the generation and motion of charge carriers in these and other compounds with intramolecular charge transfer.

In crystals of *p*-tricyanovinyl-*N,N*-dimethylaniline (compound **3**), the molecular conformation is nearly planar: the dimethylamino and tricyanovinyl groups are rotated with respect to the phenylene ring through angles of 7° and 2° , respectively. The planar molecular geometry, the shortening of the bond between the Me_2N group and the phenylene ring to the sesquibond (1.36 Å), and the quinoid-like structure of the ring suggests a strong conjugation in the molecule and a considerable shift in the electron density from the donor dimethylamino group to the acceptor tricyanovinyl group. This assumption is also confirmed by the UV spectroscopic data [58] and an unusually large dipole moment ($\sim 10 D$) [41, 44]. Analysis of the bond lengths in molecule **3** allows us to assume that the intramolecular charge transfer occurs in the ground state of the molecule with the charge $+\delta$ at the N amine atom and the charge $-\delta$ at the C(1) atom of the tricyanovinyl group. In the crystal, the molecules form stacks with an alternation of the acceptor and donor moieties of the neighboring molecules. This packing of molecules in the crystal and relatively short intermolecular distances (the shortest distances C...C and C...N are equal to 3.48 and 3.27 Å, respectively), most likely, enhance a substantial photoelectric sensitivity caused by the charge transfer between the molecules upon photoexcitation [5]. Moreover, compound **3** possesses a high molecular second-order nonlinear optical susceptibility and can

be used in the production of materials for nonlinear optics [44].

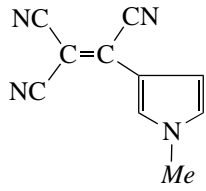
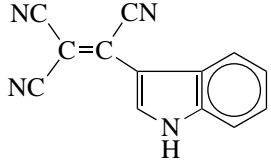
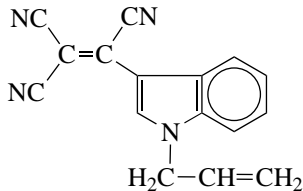
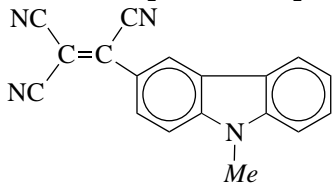
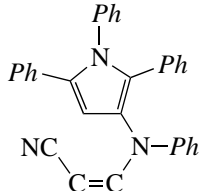
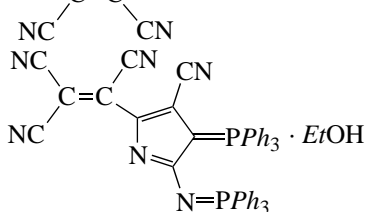
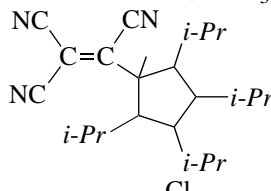
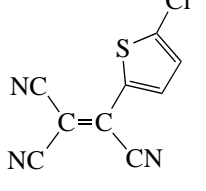
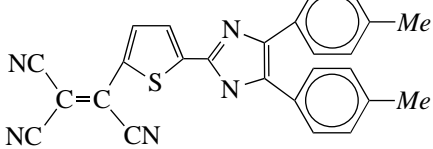
Analysis of the spectral characteristics of *p*-tricyanovinyldiphenylamine (compound **4**) revealed that an appreciable charge transfer occurs even in the ground state [58]. In the crystal, molecule **4** consists of three planar fragments rotated with respect to each other: the dihedral angle formed by the rings is equal to 39° and the dihedral angle between the phenylene ring and the tricyanovinyl group is 18° . Steric hindrances bring about a considerable increase in the bond angles CNC (127°) and CCN (123° and 127°). The amine nitrogen atom lies in the planes of the adjacent rings. The molecular layers with the shortest contacts between the N atoms of the nitrile groups can be conventionally separated in the crystal. A partial overlapping of the donor and acceptor moieties of the neighboring molecules leads to a decrease in the C...C distances to 3.40 Å due to the π - π interaction. This is accompanied by the formation of the NH...N intermolecular hydrogen bond (3.04 Å) between the amino group and the N atom of the cyano group (the mean-statistic length of this bond is 2.98 Å [59]). Single crystals **4** are characterized by a considerable photoelectric sensitivity in the visible spectral range [5].

Single crystals of *p*-tricyanovinyltriphenylamine (compound **5**) in two modifications were prepared from solutions in different solvents. The *p*-tricyanovinyltriphenylamine molecule has a nonplanar configuration in both modifications, namely, the monoclinic (**5a**) and orthorhombic (**5b**) modifications. The molecular configuration is determined by steric factors and the conjugation of the donor triphenylamine and acceptor tricyanovinyl moieties of the molecule. The amine nitrogen atom is characterized by a strictly planar configuration of the C–N bonds in **5a** and a nearly planar configuration in **5b**. The deviation from the plane of three C atoms bonded to the N atom is equal to 0.056 Å. The phenyl rings are rotated with respect to this plane through angles of 52° and 54° in **5a** and through angles of 50° and 55° in **5b**. The rotation angle for the phenylene ring is equal to only 24° in **5a** and 20° in **5b**. The molecular configurations in the monoclinic and orthorhombic modifications considerably differ in the angle of rotation of the planar tricyanovinyl group with respect to the plane of the phenylene ring (20° in **5a** and 3° in **5b**). The rotation of the tricyanovinyl group about the C(2)–R bond is governed by both the molecular packing in the crystal and the conjugation with the amine fragment of the molecule. According to [5], the monoclinic and orthorhombic crystals exhibit different photoelectric sensitivities. It should be noted that, in this case, the photocurrent multiplication upon illumination of the orthorhombic crystals is several orders of magnitude larger than that of the monoclinic crystals. This difference can be associated with a more flattened molecular fragment consisting of the tricyanovinyl group and the phenylene ring.

Table 3. Tricyanovinyl compounds of the general formula

Compound no.	Formula	<i>R</i> factor	References
1		0.062 (150 K)	[50]
2		0.032	[50]
3		0.079	[7]
4		0.096	[8]
5		5a 0.056 5b 0.051	[5] [6]
6		0.048	[51]
7		0.052	[11]
8		0.041	[10]

Table 3. (Contd.)

Compound no.	Formula	<i>R</i> factor	References
9		0.037	[13]
10		0.034	[12]
11		0.055	[15]
12		0.054	[9]
13		0.078 (-150°C)	[52]
14		0.079	[53]
15		0.044	[54]
16		0.051	[55]
17		0.066	[56]

Note: Hereafter, the structural numbering of atoms differs from the chemical numbering.

When synthesizing the tricyanovinyl derivatives of substituted phenylhydrazones, Tosi *et al.* [51] prepared compound **6**. For this compound, the spectroscopic properties were analyzed and the structure was determined by X-ray diffraction [51]. The dihedral angle between the tricyanovinyl group and the phenylene ring is equal to only 1.1° . This angle is minimum among those observed in tricyanovinylarylamines. The non-hydrogen atoms in the molecule are located in virtually the same plane (the maximum deviation is 0.07 \AA). In molecule **6**, the bond lengths are close to those observed in the other tricyanovinylarylamines. Crystals **6** are electric insulators [51].

p-Tricyanovinyl-*N*-ethyl-*N*-(β -cyanoethyl)aniline (compound **7**) was synthesized according to the standard procedure used for the tricyanovinylation of anilines [24]. In molecule **7**, the geometry of the main fragment composed of the phenylene ring and the tricyanovinyl group is similar to that observed in compound **3**. In the tricyanovinyl group, the C(1)=C(2) double bond (1.369 \AA) is longer than and the C–C bridging bond with the phenylene ring (1.428 \AA) shorter than both the normal bond [39] and those observed in the tetracyanoethylene molecule [28, 33]. These changes in the bond lengths in the tricyanovinyl group, a pronounced quinoid-like structure of the phenylene ring, and the shortening of the C(*sp*²)–N bond in the amine group to the sesquibond (1.356 \AA) can be caused by the intramolecular charge transfer. The main fragment of the molecule is virtually planar (the dihedral angle is equal to only 3.3°). This implies that single crystals of compound **7** should possess a considerable photoelectric sensitivity [11], as is the case with the other tricyanovinylarylamines (compounds **3**, **4**, **5a**, **5b**) studied in our earlier works. The planes of the ethyl and cyanoethyl groups are almost perpendicular to the plane of the main fragment of the molecule (the dihedral angles with the ring plane are equal to 85.5° and 82.9° , respectively). The bonds at the amine nitrogen atom have a planar configuration. As in the other tricyanovinylarylamines crystals, the shortest intermolecular contacts are formed by the nitrogen atoms of the nitrile groups. In the aforementioned structures of tricyanovinylarylamines compounds, the geometric parameters of the tricyanovinyl group are close to those determined for the cubic [28, 29] and monoclinic [31, 32] modifications of tetracyanoethylene with due regard for an asymmetric substitution for one of the nitrile groups. In the tricyanovinyl fragment, the C(2)–C(3) bond of the cyano group in the 1 position is longer than the two other (approximately equal) bonds C–C(N) in the 2,2 position.

There is a certain correlation between the photoelectric properties and the crystal structures of compounds **3**, **4**, **5a**, **5b**, and **7**. A comparison of the molecular geometry with the photoelectric sensitivity of the single crystals [5, 11] and the activation energy for photoconduction [49] shows that the photocurrent multiplication factor *k* depends on the degree of planarity of the

molecular fragment involving the phenylene ring and the tricyanovinyl group. In compounds **4** and **5a** with a small value of *k* (~ 2 – 5), the dihedral angles ω between the phenylene ring and the tricyanovinyl group are equal to 18° and 20° , respectively. A high photoelectric sensitivity ($k \sim 10^3$) and a low activation energy of photocurrent are observed in compounds **3**, **5b**, and **7** ($\omega = 2^\circ$, 3° , and 3.3° , respectively). Therefore, the higher degree of molecular planarity, which corresponds to a more pronounced conjugation, facilitates the intramolecular charge transfer from the donor to the acceptor group in tricyanovinylarylamines and provides the geometric prerequisites favorable to the photoelectric effect. Certainly, this analysis should take into account the molecular packing in crystals and the mutual arrangement of the donor and acceptor fragments in the neighboring molecules. The stacking packing of molecules **3** with alternation of the donor and acceptor fragments of the neighboring molecules encourages the intermolecular charge transfer and increases the photo-sensitivity. Crystal structures **5a** and **5b** have almost the same molecular packing: no short contacts between the donor and acceptor fragments of the neighboring molecules are observed, most likely, due to the screening of the amine nitrogen atom by the strongly rotated phenyl rings. The higher photosensitivity of the orthorhombic modification can be associated primarily with the planarity of the main fragment of the molecule ($\omega = 3^\circ$). It can be assumed that the molecular conformation is responsible for the initial stage of photoconduction, i.e., for the transition of the molecule to the excited state, and that the further process is governed by the molecular packing in the crystal in the presence of the intermolecular and intramolecular charge transfers. According to Vozzhennikov *et al.* [49], the photoconduction kinetics is controlled by the conformation of molecules and their packing in the crystal. A correlation between the photoelectric properties and the molecular planarity was also assumed earlier for acceptor compounds—dicyanomethylene derivatives of fluorene (see [6] and references therein).

In compound **8** (1-tricyanovinylazulene), azulene—a nonbenzenoid aromatic compound whose electron-donor ability is characterized by an ionization potential of 7.41 eV —serves as an electron-donor substituent [60]. The main procedures of synthesizing azulene hydrocarbons, their chemical properties, and practical applications (such as drugs, dyes, optical sensitizers, and photoconductors) were described in [42, 61, 62]. Structural studies of these compounds were carried out by Kaftory *et al.* [63] and Nather *et al.* [64]. Investigations into the photoelectric properties of 1-tricyanovinylazulene demonstrated that single crystals of this compound possess photoelectric sensitivity [10]. Molecule **8** has a nonplanar configuration: the tricyanovinyl group is rotated with respect to the azulene moiety through an angle of 26.3° . In this molecule, the azulene fragment is slightly distorted at the expense of bending the seven-membered ring and adopts the con-

formation of a strongly flattened boat. The changes observed in the geometric parameters of the tricyanovinyl group (an increase in the C=C double bond length to 1.378 Å and others) are likely caused by the intramolecular charge transfer. An interesting packing of molecules in the crystal consists of well-defined molecular stacks. Inside each stack, virtually parallel planar donor and acceptor fragments of the neighboring molecules overlap with each other, which can encourage the intermolecular charge transfer.

Now, we consider the tricyanovinyl derivatives of nitrogen-containing heterocyclic compounds that belong to a large family of conjugated dyes with intramolecular charge transfer. A structure analysis of 3-tricyanovinyl-*N*-methylpyrrole (compound **9**) revealed that the tricyanovinyl group is in the 3 position of the *N*-methylpyrrole fragment and not in the 2 position, as was predicted earlier in [25, 42, 45]. This molecule is planar (to within 0.05 Å): the dihedral angle between the pyrrole and tricyanovinyl fragments is equal to only 0.7°. Substantial changes in the bond lengths in the acceptor tricyanovinyl group and the donor pyrrole ring suggest an intensive intramolecular charge transfer. In the crystal, the molecules form layers with an interlayer spacing of 3.28 Å, thus inducing an intermolecular charge transfer.

Molecules of 3-tricyanovinylindole (compound **10**) exhibit a nearly planar configuration. The dihedral angle between the indole and tricyanovinyl fragments is equal to 3.5°. As in structure **9**, changes in the bond lengths indicate an intensive intramolecular charge transfer. The crystal has a layered chain structure. The molecules are linked together into chains through the NH...N hydrogen bonds with a length of 2.953 Å, which is close to the mean-statistic value (2.98 Å) [59]. 3-Tricyanovinylindole was synthesized according to the procedure described in [25, 65]. This compound possesses photosensitivity and can be used as a photoconductor and an efficient sensitizer in the production of electrophotographic polymer films [47, 66].

Similar properties are revealed in 1-allyl-3-tricyanovinylindole (compound **11**) [47, 66, 67]. In molecule **11**, the -CH₂-CH=CH₂ allyl group is disordered over two positions with an occupancy of 0.5 for two terminal carbon atoms. The geometric parameters of molecules **10** and **11** are close to each other. This indicates that the attachment of the allyl group affects the molecular geometry only slightly. The dihedral angle between the planar tricyanovinyl group and the indole fragment (planar to within 0.013 Å) is equal to 5.6°. The disordered allyl group is considerably rotated (through 72.4° and 68.8°) with respect to the indole fragment. The intramolecular charge transfer in this molecule is confirmed by spectral data.

Tricyanovinyl derivatives of *N*-alkylcarbazole [68], for example, 3-tricyanovinyl-*N*-methylcarbazole (compound **12**), appeared to be highly efficient sensitizers of polymer photoconductors widely used in electropho-

tography. The attachment of the acceptor tricyanovinyl group breaks the symmetry of the donor fragment of this molecule, unlike two independent *N*-methylcarbazole molecules [17]. The carbazole moiety of molecule **12** is slightly distorted: the angles between the planes of the five-membered and six-membered rings are equal to 0.6° and 0.9°, respectively (for *N*-methylcarbazole, the folding angles are equal to 1.4° and 1.7° for molecule *A* and 1.2° and 1.3° for molecule *B* [17]). Molecule **12** as a whole is nearly planar: a small angle (3°) of rotation of the tricyanovinyl fragment with respect to the carbazole moiety does not disturb the conjugation between the donor and acceptor molecular fragments, which likely favors the intramolecular charge transfer. Molecules of compound **12** in the crystal are packed in stacks. Along any stack, the carbazole moiety of one molecule faces the tricyanovinyl group of the neighboring molecule.

Compounds **16** and **17** belong to tricyanovinylthiophene derivatives. A number of new tricyanovinylthiophenes have been synthesized in recent years. These compounds have attracted considerable interest because they can be used both as acceptors in donor-acceptor π -conjugated systems with nonlinear optical properties [44, 55, 56] and as electron acceptors for organic metals [55]. Molecule **16** has a nonplanar configuration: the angle between the thiophene ring and the tricyanovinyl fragment is equal to 9°. A series of nonlinear optical chromophores was prepared by a new technique (tricyanovinylation of imidazolethiophenes) [56]. Among these compounds, compound **17** was characterized structurally. In the sterically strained molecule **17**, the *Ph* rings are rotated through different angles (59.3° and 12.4°) with respect to the imidazole ring [56].

3.2. Molecular Complexes and Ionic Salts of the Compounds with a Tricyanovinyl Group

Compounds with a tricyanovinyl group form molecular complexes and a large number of ionic salts with organic molecules, metal atoms, and organometallic compounds. The compounds whose structure is determined by X-ray diffraction analysis are presented in Table 4.

Crystals of 3-(tricyanovinyl)phenoxazine were grown from a solution in dimethyl sulfoxide with the formation of the 1 : 1 molecular complex with dimethyl sulfoxide (compound **18**) [14]. The phenoxazine fragment adopts a butterfly conformation. The dihedral angle between the tricyanovinyl group with a nearly planar (to within 0.087 Å) configuration and the plane of the nearest carbon ring of phenoxazine is equal to 16.5°. In the crystal, molecules of the complex are linked by the strong intermolecular hydrogen bonds NH...O, in which the N...O (2.76 Å) contact is shorter than the mean-statistic length (2.89 Å) [59].

Table 4. Molecular complexes and ionic salts of the compounds containing the tricyanovinyl group

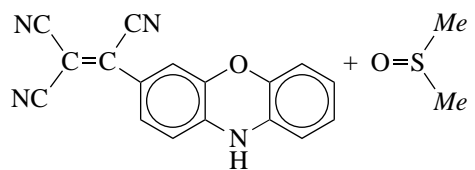
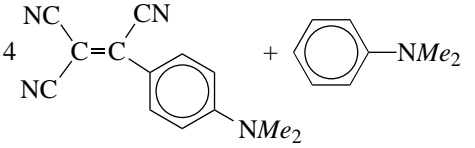
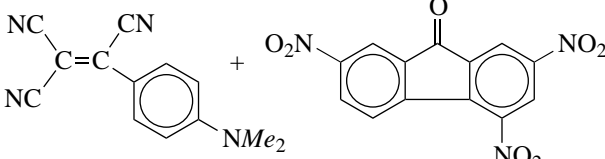
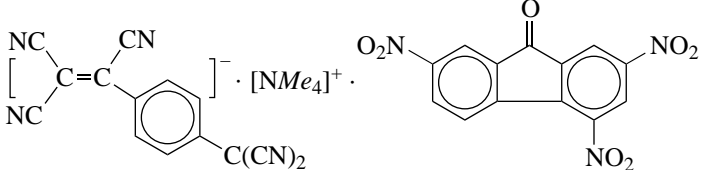
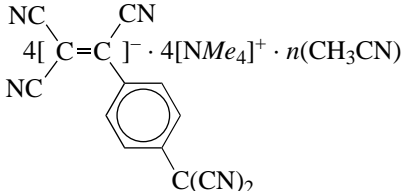
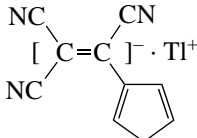
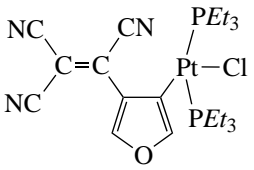
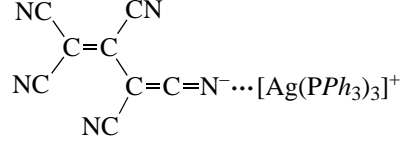
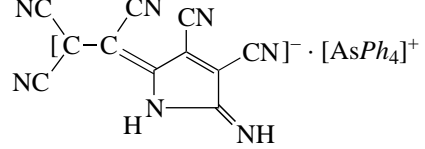
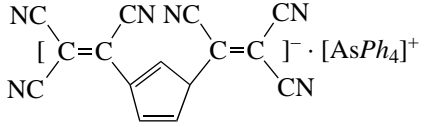
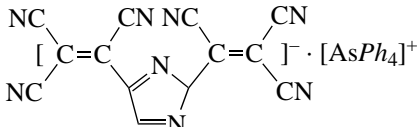
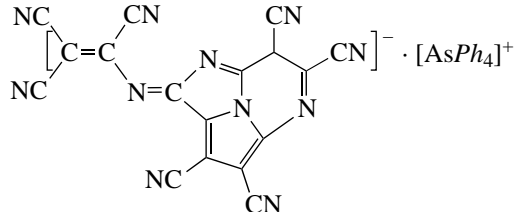
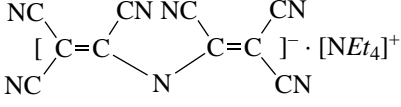
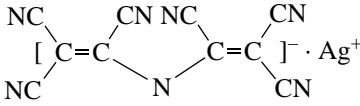
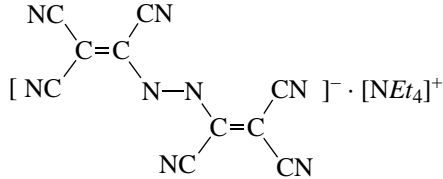
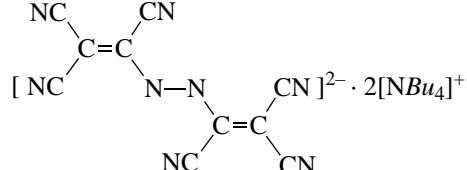
Compound no.	Composition of the complex (salt)	R factor*	References
18		0.062	[14]
19			[69, 70]
20			[69–71]
21		0.157	[71]
22			[71]
23		0.060 (–160°C)	[72]
24		0.048	[73]
25		0.072	[74]
26		0.066	[75]
27		0.0623	[76]

Table 4. (Contd.)

Compound no.	Composition of the complex (salt)	R factor*	References
28		0.0561	[76]
29		0.069	[77, 78]
30		0.044	[79]
31		0.049 (120 K)	[79]
32		0.075	[80]
33		0.051	[80]

* For compounds **19**, **20**, and **22**, only the unit cell parameters and the space group are determined by X-ray powder diffraction.

Upon the complex formation, the same molecule can play the role of a donor and an acceptor. Sandman *et al.* [69–71] were the first to reveal that *p*-tricyanovinyl-*N,N*-dimethylaniline (compound **3**) has an intermolecular π -amphoteric nature. For example, this molecule serves as an acceptor in complex **19** and as a donor in complex **20**. The *p*-tricyanovinylphenyldicyanome-thide monoanion manifests the donor properties in ternary complexes **21** and **22**. Salt **21** is the first structurally characterized π -complex of the donor monoanion with the neutral acceptor [71].

In organometallic salt **23**, the thallium atoms are sandwiched between the cyclopentadienyl rings. The anion is almost planar: the cyclopentadienyl ring (in which the bonds are not delocalized) is rotated with respect to the tricyanovinyl group through an angle of 8°. Freeman *et al.* [72] proposed to use compound **23** in the synthesis of tricyanovinyl-substituted metallocenes. In the structure of the [cyano(tricyanovinyl)ketimino-*N*]-tris(triphenylphosphine)silver salt (compound **25**),

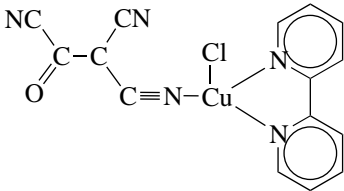
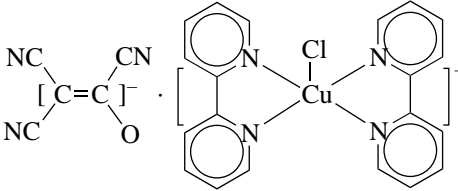
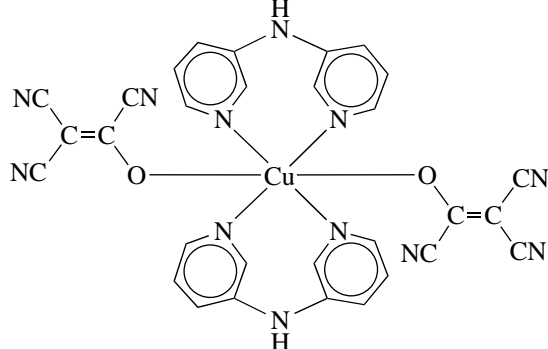
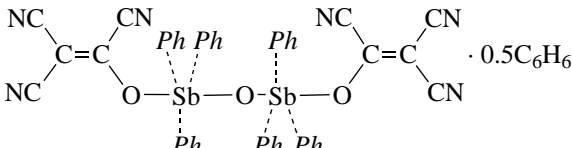
the ketimine group of the anion interacts with the silver cation [74].

New carbocyanine dyes—four organometallic salts (compounds **26–29**) with the tetraphenylarsonium cation and new heterocyclic polycyanocarbanions with one (compounds **26**, **29**) and two (compounds **27**, **28**) tricyanovinyl groups—were synthesized by the condensation reactions [75–78], which are very unusual in the chemistry of tetracyanoethylenes. The structures of these compounds were characterized by X-ray diffraction analysis, and the structure of the carbanions was confirmed by spectral data. Since these carbanions contain a large number of cyano groups, they can be strong electron acceptors and, hence, can be used in the synthesis of new organic metals. According to Bonamico *et al.* [76], the crystals of 1,3-bis(tricyanovinyl) derivatives of the cyclopentadienyl (salt **27**) and imidazolyl (salt **28**) anions are isomorphous and consist of isolated cations and anions packed in stacks. In structure **28**, one of the tricyanovinyl groups is disordered over two posi-

Table 5. Ionic salts and organometallic complexes with tricyanoethenolate

Compound no.	Composition of the complex (salt)	<i>R</i> factor	References
34		0.049	[81]
35		0.069	[82]
36		0.036	[83]
37		0.043	[84]
38		0.051	[84]
39		0.065 (-40°C)	[85]

Table 5. (Contd.)

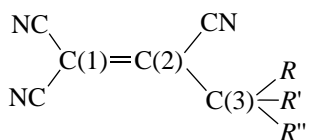
Compound no.	Composition of the complex (salt)	R factor	References
40		0.046	[86]
41		0.046	[85]
42		0.072	[87]
43		0.105	[88]

tions with occupancies of 0.56 and 0.44. In tetraphenylarsonium salt **29**, the heterocyclic fragment of the anion consists of three fused rings, namely, the pyrimidine, imidazole, and pyrrole rings [78]. It seems likely that, in their earlier work [77], Bonamico and coworkers mistakenly assigned the sorts of nitrogen and carbon atoms in the N=C bond linking the tricyanovinyl group and the heterocycle. The anion has a planar structure to within 0.02 Å (without regard for the CN groups). The motif of the crystal packing is similar to that revealed in ionic salts **27** and **28**. In each stack, the interplanar distance between the anions is alternately equal to 3.30 and 3.33 Å, which suggests a high degree of the π - π interaction [78].

The considerable interest expressed by researchers in polycyanocarbanions is motivated by their practical use both as materials with important electrical and magnetic properties and as dyes. Four ionic salts were investigated by X-ray diffraction. Two tricyanovinyl groups in the anion are linked by the aza bridge in compounds **30** and **31** [79] and by the diaza bridge in compounds **32** and **33** [80]. The structure of tetraethylam-

monium salt **30** is built up of the $[C_{10}N_7]^-$ anions and $[NEt_4]^+$ cations. In crystals **31**, the silver cations occupy two crystallographically nonequivalent special positions on the twofold axis and at the center of symmetry. In this structure, the anions play the role of bridging ligands: each anion is firmly bonded to four different Ag cations through the N atoms of the four outer cyano groups. In both structures, five atoms of the central bridge lie in the same plane (to within 0.04 Å) and six cyano groups deviate insignificantly from this plane. It is worth noting that the C-C(N) bond lengths in the outer cyano groups (1.419–1.425 Å in compound **30**) are considerably shorter than those in the inner cyano groups (1.459 and 1.460 Å in compound **30**); however, the C≡N bond lengths differ only slightly, and the C=C bond lengths in the tricyanovinyl groups are equal to 1.361 and 1.382 Å in compound **30** [79]. Close values of the bond lengths, but with a lower accuracy, were obtained for the anion in salt **31**.

Decoster *et al.* [80] determined the structural characteristics of tetraalkylammonium salts **32** and **33**. In

Table 6. Tricyanopropenylidene compounds of the general formula  and their salts

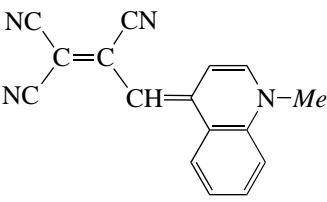
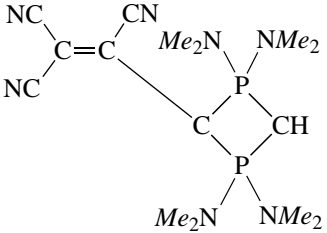
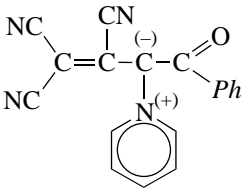
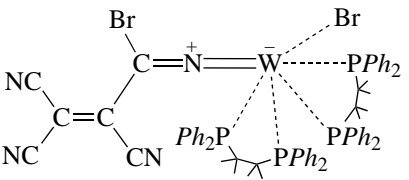
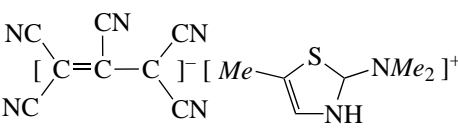
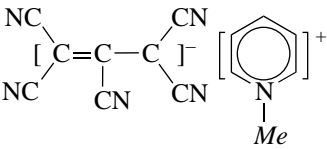
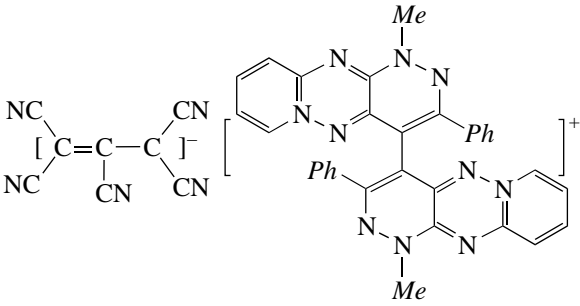
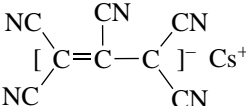
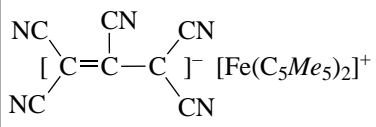
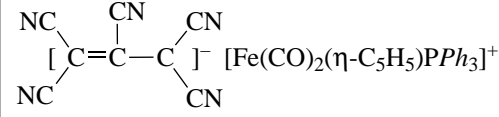
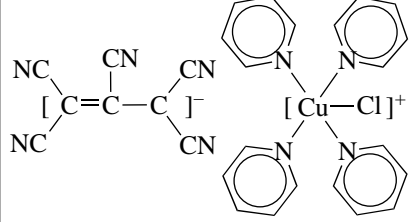
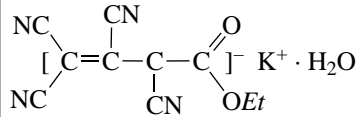
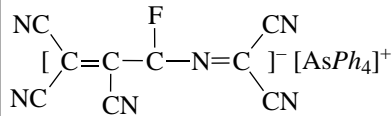
Compound no.	Formula	R factor	References
44		0.039	[89]
45		0.047	[90]
46		0.041	[91]
47		0.043	[92]
48		0.045	[93]
49		0.052 (153 K)	[94]
50		0.076	[95]
51		0.047	[96]

Table 6. (Contd.)

Compound no.	Formula	R factor	References
52	 $[\text{C}(\text{CN})_2=\text{C}(\text{CN})]^- [\text{Fe}(\text{C}_5\text{Me}_5)_2]^+$	0.036 (-100°C)	[97]
53	 $[\text{C}(\text{CN})_2=\text{C}(\text{CN})]^- [\text{Fe}(\text{CO})_2(\eta\text{-C}_5\text{H}_5)\text{PPh}_3]^+$	0.055	[98]
54	 $[\text{C}(\text{CN})_2=\text{C}(\text{CN})]^- [\text{Cu}-\text{Cl}]^+$	0.090	[99]
55	 $[\text{C}(\text{CN})_2=\text{C}(\text{CN})\text{C}(=\text{O})\text{OEt}]^- \text{K}^+ \cdot \text{H}_2\text{O}$	0.045	[94]
56	 $[\text{C}(\text{CN})_2=\text{C}(\text{CN})\text{N}=\text{C}]^- [\text{AsPh}_4]^+$	0.057	[100]

both structures, two tricyanovinyl groups are in the *trans* position with respect to the N–N bond. In crystals **32**, the asymmetric part of the unit cell involves two cations and two anions. In this case, two crystallographically independent anions form a dimer in which the nearly parallel midplanes of the anions are characterized by a shortened interplanar distance (on average, 3.0 Å). In ionic salt **33**, the dianion has a centrosymmetric structure and two cations are related by the inversion center. The dianion with the approximate symmetry C_{2h} is planar to within 0.03 Å. Judging from the bond lengths (C=C, 1.416 Å and C–C(N), 1.464 Å in the inner cyano group and C=C, 1.421 Å and C–C(N), 1.411 Å in the outer cyano groups), the delocalization should occur in each $\text{NC}(\text{CN})\text{C}(\text{CN})_2$ fragment of the dianion [80].

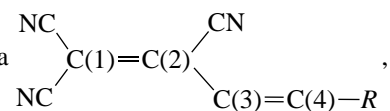
3.3. Organometallic Complexes and Ionic Salts with Tricyanoethenolate

The structurally characterized compounds with the $[(\text{CN})_2\text{C}=\text{C}(\text{CN})\text{O}]^-$ tricyanoethenolate fragment, which serves as an anion or a ligand in the organometallic complexes, are presented in Table 5. The geometric parameters of ionic salt **34** were determined by Neseterov [81]. A nearly planar anion of tricyanoethenolate has a conjugated structure with delocalized bonds: the C–O distance (1.234 Å) is longer than the standard

length of the $\text{C}(sp^2)=\text{O}$ nonconjugated bond (1.199 Å) [39] and the bond length (1.218 Å) found in the cation of compound **34**; moreover, the length of the central C=C bond (1.399 Å) substantially exceeds the standard length of the $\text{C}(sp^2)=\text{C}(sp^2)$ bond (1.331 Å) [39]. The conjugation occurs with the participation of two cyano groups in the 1,1 position. In these groups, the C–C(N) bonds (1.417 and 1.414 Å) are appreciably shorter than the C–C(N) bond (1.487 Å) in the third cyano group. In the crystal, the cations are joined into the centrosymmetric dimers by the $\text{NH}\cdots\text{O}$ intermolecular hydrogen bonds (2.958 Å) (the mean-statistic length of these hydrogen bonds is 2.89 Å [59]). In turn, the dimers and two anions form tetramers through the weak $\text{NH}\cdots\text{N}(\equiv\text{C})$ hydrogen bonds.

In principle, Dahl [82] solved the structure of salt **35**, which crystallizes with the dioxane molecule. Unfortunately, both ions and the solvent molecule appeared to be disordered over positions: the occupancies are equal to 0.58 and 0.42 for the tricyanoethenolate anion, 0.70 and 0.30 for the cation, and 0.50 and 0.50 for the dioxane molecule. The crystal packing is determined primarily by a large number of hydrogen bonds [82].

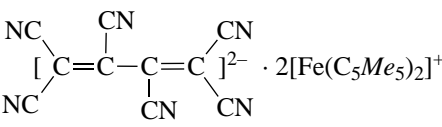
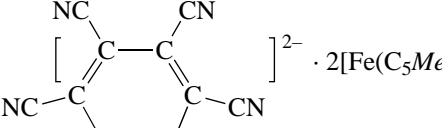
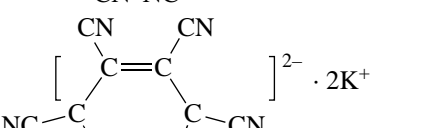
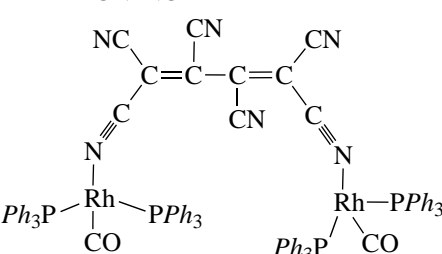
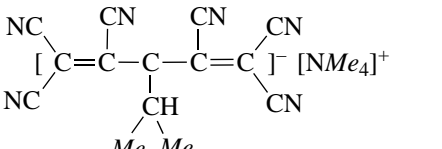
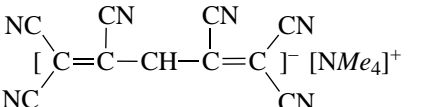
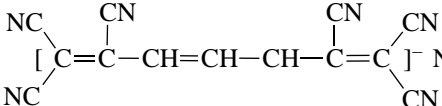
The reaction of ferrocene with tetracyanoethylene produced the previously unknown product (compound **36**) with an unusual stoichiometry. According to X-ray structure analysis, the crystal contains both ferrocene

Table 7. Derivatives of tricyanobutadienyldiene and its homologs of the general formula

their complexes, and salts

Compound no.	Formula	R factor	References
57		0.030	[16]
58		0.031 (178 K)	[101]
59		0.086 (-100°C)	[102]
60		0.042	[103]
61		0.032	[104, 105]
62		0.041	[106, 107]
63		0.042	[108]
64		0.049	[108]
65		0.051	[108]
66		0.062 (-106°C)	[109]

Table 7. (Contd.)

Compound no.	Formula	R factor	References
67	 $[\text{C}(\text{CN})_2=\text{C}(\text{CN})]^{2-} \cdot 2[\text{Fe}(\text{C}_5\text{Me}_5)_2]^+$	0.072 (-100°C)	[102]
68	 $[\text{C}(\text{CN})_2=\text{C}(\text{CN})]^{2-} \cdot 2[\text{Fe}(\text{C}_5\text{Me}_5)_2]^+$	0.045	[102]
69	 $[\text{C}(\text{CN})_2=\text{C}(\text{CN})]^{2-} \cdot 2\text{K}^+$	0.072	[110]
70		0.058	[111]
71	 $[\text{C}(\text{CN})_2=\text{C}(\text{CN})]^- [\text{NMe}_4]^+$	0.112	[112]
72	 $[\text{C}(\text{CN})_2=\text{C}(\text{CN})]^- [\text{NMe}_4]^+$	0.069	[113]
73	 $[\text{C}(\text{CN})_2=\text{C}(\text{CN})]^- \text{NH}_4^+$	0.069	[114]

and ferrocenium ions. In the crystal structure, ferrocene and the tricyanoethenolate anion form donor-acceptor (1 : 2) stacks and cations form virtually linear separate stacks. The tricyanoethenolate anions in the structure are disordered with respect to the *m* plane and occupy two positions with an occupancy of 0.5. In the anion, the bond lengths (C=C, 1.387 Å and C-O, 1.246 Å) [83] are close to those determined in [81].

In three manganese compounds, the tricyanoethenolate fragment plays the role of either a ligand in organometallic complexes **37** and **38** or an anion in salt **39**. Sato *et al.* [84] determined the crystal structures of the tricyanoethenolate adducts of the manganese complexes with the tetradentate Schiff base (compounds **37** and **38**). Tricyanoethenolate interacts with manganese either through the O atom in compound **37** or through

the N atom of the cyano group in compound **38**. The water molecule found in crystal **38** participates in the formation of the hydrogen bond with the N atom of the adjacent fragment of tricyanoethenolate, thus forming a chain structure. In salt **39**, the ions are located at the centers of symmetry and the tricyanoethenolate anion is disordered over two equiprobable positions. Structure **39** consists of centrosymmetric sixfold-coordinated manganese cationic complexes linked together by a chain of tricyanoethenolate anions. The bridge between the pairs of Mn atoms is alternately formed by an N or O atom due to the anion disordering [85].

In compounds **40**, **41**, and **42**, tricyanoethenolate enters into the composition of the copper complexes. In compound **40**, the Cu atom is coordinated by the ethenolate anion through the N atom of the cyano group

in the same manner as in structure **38** of the manganese complex. In compound **41**, the ethenolate anion is not involved in the coordination sphere of the Cu atom. Complex **42** has the center of symmetry; hence, this compound represents the *trans* complex. The Cu atom is sixfold-coordinated, and the ethenolate ligands at two axial positions are bonded to the Cu atom through the O atom. The tricyanoethenolate anion has a planar structure with a maximum atomic deviation of 0.028 Å [87].

In crystal solvate **43**, the antimony complex occupies the general position and the solvate molecule of benzene is located at the inversion center. In this structure, the ethenolate ligands are also bonded through the O atom but to different Sb atoms linked by the oxygen bridge. Thus, as was noted by Brandon *et al.* [85], tricyanoethenolate is coordinationally flexible and either can be bonded to the metal atom through the O atom (compounds **37**, **42**, and **43**), the N atom (compounds **38** and **40**), and the O and N atoms (compound **39**) or can serve as a noncoordinated anion (structures **34–36** and **41**). The data obtained in [82, 83, 85–88] on the chemically equivalent bond lengths and bond angles in the $[\text{C}_2(\text{CN})_3\text{O}]^-$ ion are summarized in [85].

3.4. Tricyanopropenylidene Compounds

Similar to the tricyanovinyl compounds, tricyanopropenylidene compounds of the general formula $(\text{CH})_2\text{C}=\text{C}(\text{CN})-\text{C}-\text{R}$ are the tetracyanoethylene derivatives. Table 6 presents the tricyanopropenylidene compounds and the ionic salts whose crystals are characterized by X-ray diffraction analysis. Since molecule **44** contains the strong electron-acceptor tricyanopropenylidene group and the electron-donor dihydroquinoline moiety interacting through the π -conjugated system, this compound can be assigned to conjugated systems with intramolecular charge transfer. The crystal is built up of two symmetrically independent molecules (**I** and **II**) with a similar geometry. The tricyanopropenylidene fragments are nearly planar and form dihedral angles of 8.6° (molecule **I**) and 10.8° (molecule **II**) with the planar dihydroquinoline moieties. This indicates that the molecules are slightly twisted around the $\text{CH}=\text{C}$ bond. The bond lengths are considerably redistributed in the conjugated chain between the donor and acceptor fragments of the molecule due to a substantial intramolecular charge transfer. In the tricyanopropenylidene group, the formally double bonds $\text{CH}=\text{C}$ (1.416 Å in **I** and 1.420 Å in **II**) and $\text{C}=\text{C}$ (1.411 Å in **I** and 1.401 Å in **II**) are appreciably longer than the normal bond (1.331 Å [39]) and the $\text{C}=\text{C}$ bond in the tricyanovinyl group of the tricyanovinyl compounds. In the crystal, molecules **I** and **II** form stacks with short interplanar distances (3.341, 3.449, and 3.347 Å), which can encourage the intermolecular charge transfer [89].

In betaine structure **46**, the molecule involves a nearly planar fragment composed of the C(3), C(2), and

C(1) atoms and the two outer nitrile groups. The bond lengths [$\text{C}(1)-\text{C}(2)$, 1.408 Å; $\text{C}(2)-\text{C}(3)$, 1.384 Å; and $\text{C}(1)-\text{C}(\text{N})$, 1.411 and 1.413 Å] indicate that the delocalization of the negative charge occurs in the planar conjugated ilide fragment $\text{C}(3)=\text{C}(2)-\text{C}(1)(\text{CN})_2$. The coordination plane of the C atom in the carbonyl group is rotated with respect to the ilide fragment through an angle of 142.5°. Large rotation angles are observed for the *Py*⁺ (107.5°) and *Ph* (60.9°) substituents. In the tungsten complex (compound **47**), the tricyanopropenylidene group serves as a ligand. In the structure, one of the outer cyano groups is disordered over positions with occupancies of 0.65 and 0.35. The interaction with the W atom occurs through the N bridge.

In recent years, increased interest has been expressed by researchers in the structural characteristics of pericyanocarbanions, including pentacyanopropenides. These ions form stable salts and metal complexes. The organic (compounds **48–50**) and organometallic (compounds **51–54**) salts with 1,1,2,3,3-pentacyanopropenide were characterized structurally. The geometry of the 1,1,2,3,3-pentacyanopropenide anion $[(\text{CN})_2\text{C}(1)=\text{C}(2)(\text{CN})-\text{C}(3)(\text{CN})_2]^-$ (structure **48**) was determined for the first time by Bertolasi and Gilli [93]. The $\text{C}(2)-\text{C}(3)$ bond lengths (1.370 Å) and, especially, the $\text{C}(1)=\text{C}(2)$ bond lengths (1.405 Å) are closer to the sesquibond length. The pentacyanopropenide ion has an almost planar, slightly asymmetric structure. For the major part, the asymmetry resides in the large difference between the C–C bond lengths in the central carbon chain. The ion pair is linked by the $\text{NH}\cdots\text{N}$ hydrogen bond (2.869 Å) (the mean-statistic length of this bond is 2.98 Å [59]). The cation and the anion lie in the same plane: the angle between the cation and the anion is equal to only 1.1°. The crystal structure consists of infinite columns in which the anion is sandwiched between the cations. This arrangement of ions suggests that the $\pi-\pi$ interaction occurs with intermolecular charge transfer [93].

Hipps *et al.* [96] determined the crystal structure and measured the spectral characteristics of cesium salt **51**. Moreover, these authors performed quantum-chemical calculations of the geometric parameters of the pentacyanopropenide anion for comparison with the bond lengths found experimentally. This anion is almost planar: the maximum deviation of the N atom of the outer cyano group is equal to 0.20 Å. The C–C bond lengths in the carbon chain are 1.395 and 1.398 Å. The symmetry of the pentacyanopropenide anion is similar to the C_{2v} symmetry. The crystal structure consists of layers. In each layer, the anion is surrounded by the four nearest-neighbor Cs atoms. The coordination sphere of the anion also involves two Cs atoms of the adjacent layers. The mean interlayer distance is equal to 3.19 Å [96].

In crystals of ionic salt **52** with interesting magnetic properties, the cation is located at the center of symmetry and the planar pentacyanopropenide anion with the

C_{2v} pseudosymmetry lies on the axis 2 passing through the central CCN group. The bond lengths in the anion (C–C, 1.396 Å; C–CN, 1.423 Å for the outer groups and 1.451 Å for the central nitrile group; C≡N, 1.142–1.155 Å) are in agreement with those obtained in [93, 96]. The structure consists of alternating cations and anions arranged in such a way that the planes of the pentacyanopropenide anions and five-membered rings are aligned parallel to each other with an interplanar distance of 3.44 Å [97]. In iron salt **53**, whose structure is characterized by X-ray diffraction analysis, the pentacyanopropenide anion is disordered over two orientations with an occupancy of 0.5 for all the atoms. Consequently, the geometric parameters of the pentacyanopropenide anion cannot be determined with sufficient accuracy. The geometric parameters of the pentacyanopropenide anion were also determined with a low accuracy for the structure of copper salt **54**, in which the planar pentacyanopropenide anion is not involved in the coordination of the metal atom [99].

The crystal structures of the potassium hydrate salt **55** and tetraphenylarsonium salt **56** were also determined by X-ray diffraction. In crystal **55**, the ethyl group is disordered over two positions with occupancies of 0.7 and 0.3. The carbanion in salt **56** is nonplanar, most likely, due to internal steric effects. The atomic deviations from the midplane of the anion fall in the range from 0.103 to –0.095 Å. The C–C bond lengths (1.393 and 1.391 Å) in the carbon chain correspond to the sesquibond. The averaged bond lengths in five cyano groups (C–CN, 1.435 Å; C≡N, 1.146 Å) agree with those observed in the other cyano compounds.

3.5. Derivatives of Tricyanobutadienyldiene and Its Homologs

Tricyanobutadienyldiene derivatives of aromatic heterocyclic compounds belong to the class of conjugated dyes with intramolecular charge transfer and can be used as efficient photosensitizers. Table 7 presents the structurally characterized compounds and their complexes and salts.

Molecule **57** consists of the electron-donor acridone and electron-acceptor tricyanobutadiene fragments. The acridone fragment adopts a butterfly conformation: the dihedral angle between the outer rings is equal to 159.2° and the folding angles of the outer rings, the carbonyl group, and the CNC plane from the plane of four carbon atoms of the central heterocycle are equal to 8.9° and 12.1°, 8.7°, and 20.4°, respectively. In the structures of *N*-methylacridone [18], *N*-ethylacridone [19], and *N*-phenylacridone [20], the outer rings of the acridone moiety in the molecule are coplanar and the central heterocycle has the conformation of a flattened boat. Therefore, the attachment of the tricyanobutadiene group leads to a considerable distortion of the acridone moiety in molecule **57**. The planar butadiene fragment is rotated with respect to the donor molecular

fragment through an angle of 37.0°. As in the structures of the other tricyanovinyl compounds [12, 14], the tricyanovinyl fragment is almost planar. In the molecule, the tricyanobutadiene moiety, as a whole, is nonplanar; however, the bond lengths [C(1)=C(2), 1.371 Å; C(2)–C(3), 1.419 Å; and C(3)=C(4), 1.349 Å] in the butadiene chain indicate that the conjugation of the bonds is retained in the chain. It should be noted that, in the unsubstituted butadiene molecule, the C–C bond length is equal to 1.465 (1.467) Å and the C=C bond length is 1.345 (1.349) Å [38, 115]. In crystal **57**, the molecules are joined through the van der Waals contacts and the intermolecular hydrogen bonds between the CH groups of the six-membered rings and the nitrile N atoms. The H...N distances (2.38 and 2.60 Å) and the CHN angles (151° and 143°) are in agreement with those reported by Taylor and Kennard [116].

Hopf *et al.* [101] performed the reaction of cyano(phenylethynyl)ethylene (a potential acceptor for charge-transfer complexes) with tetrathiafulvalene and, instead of the expected charge-transfer complex, obtained an unusual compound (**58**), whose structure was determined by X-ray diffraction analysis. Crystal structure **58** is characterized by the mutually perpendicular arrangement of two nearly planar halves of the molecule: the dihedral angle about the central C(3)–C(*Ph*) bond is equal to 96.79°.

Among the six well-known polycyano acceptors, the hexacyanobutadiene $C_4(CN)_6$ (compound **59**), which was synthesized in 1964 (see the reference in [106]) possesses the strongest electron affinity (3.3 eV) [1, 2]. In the crystal, the hexacyanobutadiene molecule consisting of two tricyanoethylene fragments occupies the general position and has a nonplanar structure with a torsion angle of 140.1° at the central C(2)–C(3) bond; i.e., it deviates from the *trans* conformation by 40°. In the hexacyanobutadiene molecule, the length of the central C(2)–C(3) bond is equal to 1.487 Å and the averaged lengths of the C=C, C–CN, and C≡N bonds are 1.307, 1.459, and 1.124 Å, respectively. The lengths of the C–CN bonds depend on their location in the molecule [102].

The polycyano-substituted derivatives of butadiene form organometallic complexes (compounds **60** and **61**). In structure **60**, the N atom of the cyano(tricyanovinyl)keteniminato ligand is involved in the coordination of the ruthenium atom. A comparison with the geometry of the related molecules demonstrated that the charge is predominantly delocalized in the dicyanomethylene molecular fragment and in the carbon chain [103]. It was shown that the tricyanobutadienyldiene ligand is a very good π -acceptor. In the structure of complex **61**, the terminal C atom of the butadiene chain is bonded to two Fe atoms. The bridging ligand has a planar structure and exhibits a strong electron delocalization: the single C–CH bond (1.406 Å) is shortened, whereas the CH=C bonds (1.358 Å) and, especially, the C=C bonds (1.382 Å) are longer than

those observed in hexacyanobutadiene [102] and tetracyanoethylene [28, 33].

Hexacyanobutadiene and aromatic compounds form charge-transfer complexes **62**–**65**. Hexacyanobutadiene can be treated as a chemical extended analogue of tetracyanoethylene. However, the number of known charge-transfer complexes with hexacyanobutadiene is considerably smaller than that with tetracyanoethylene. In the crystal structure of the 1 : 1 complex of hexacyanobutadiene with perylene (compound **62**), the acceptor and donor molecules are located at the centers of symmetry and alternate with each other in columns; i.e., they form a mixed-type packing. Moreover, the hexacyanobutadiene and perylene molecules form alternating single-component layers with an interplanar distance of 3.2 Å and a dihedral angle of 2.88°. In this complex, the hexacyanobutadiene molecule is ordered. Single crystal **62** is an insulator with a neutral ground state [106, 107].

The crystal structures of the 1 : 2 (compound **63**) and 1 : 1 (compounds **64** and **65**) molecular complexes of hexacyanobutadiene with tetrathiafulvalene derivatives have been determined. In all three complexes, the hexacyanobutadiene molecule is orientationally disordered. In the structures of complexes **64** and **65**, unlike the structure of complex **62**, the donor and hexacyanobutadiene molecules are packed in separate stacks. The disordered hexacyanobutadiene molecule has the *m* symmetry in structures **63** and **64** and is centrosymmetric in complex **65**. Analysis of the electrical properties of these compounds [117, 118] demonstrated that complex **63** is a semiconductor, whereas complexes **64** and **65** are insulators.

Hexacyanobutadiene can be easily transformed into the radical ion and then into the dianion. The ionic salts of hexacyanobutadiene with decamethylferrocenium (compounds **66**–**68**) are characterized structurally. In the charge-transfer complex with the monoanion (compound **66**), both components are centrosymmetric. In the crystal, the planar anions are disordered over two equivalent *trans* orientations and sandwiched between parallel *C_p* rings of two neighboring cations. In this case, the dihedral angle between the anion and the ring planes is equal to 26.4°. The complex in the ground state is a ferromagnet. According to the magnetic susceptibility and Mössbauer data, the ordering temperature of the crystal structure is equal to 7.5 ± 0.5 K [109].

The geometry of the ordered planar dianion, which is located at the center of symmetry in the crystal and has the *trans* configuration with the approximate symmetry *C_{2h}*, is determined in the 1 : 2 ionic salt with the dianion (compound **67**). The distribution of bond lengths in the carbon chain of the dianion differs substantially from that observed in the neutral hexacyanobutadiene molecule [102]: the central bond C(2)–C(3) (1.342 Å) is appreciably shorter than the terminal formally double bonds C(1)=C(2) (1.401 Å). The mean lengths of the C–CN and C≡N bonds are equal to 1.459

and 1.128 Å, respectively. In the structure of salt **68**, the cation and the planar dianion with the *cis* configuration lie on the axis 3 and are disordered.

The structure of potassium salt **69** was solved, and the geometric parameters of the hexacyanobutadiene dianion in the *cis* conformation were determined [110]. As in the *trans* form, the central C(2)–C(3) bond (1.399 Å) in the *cis* dianion is shorter than the terminal bonds [C(1)=C(2), 1.442 Å and C(3)=C(4), 1.434 Å]. The dianion geometry suggests a high degree of charge delocalization. In this structure, unlike the structures considered above [102], the dianion is nonplanar: the C(1)C(2)C(3)C(4) torsion angle is equal to 12° and the terminal cyano groups are rotated about the C(1)–C(2) and C(3)–C(4) bonds. A considerable deviation from planarity and a certain distortion of the bond angles (an increase to 127.6°) result in a decrease in the dianion strain. The deviation from the *C₂* symmetry can be associated with a particular crystal packing [110].

Schlotter and Ibers [111] determined the structure of compound **70** and showed that the hexacyanobutadiene dianion is bound to the Rh atoms through the Rh–N bonds with the formation of the binuclear complex. The bridging ligand has a *trans* structure. The central carbon chain is nonplanar; the torsion angles about the bonds C(1)–C(2) (1.455 Å), C(2)–C(3) (1.359 Å), and C(3)–C(4) (1.444 Å) are equal to 38°, 8.5°, and 25°, respectively. It was demonstrated that the transition metals change the electronic nature of the dianion [111].

Ionic salts **71** and **72** with the pentadienide bridge and six cyano groups in the anion can be classified as compounds related to tricyanobutadienyldiene derivatives.

In ionic salts **71**–**73**, the monoanion contains two terminal tricyanoethylene fragments that are linked by the carbon bridge and form the five-membered central carbon chain in compounds **71** and **72** and the seven-membered chain in compound **73**. In structure **71**, the anion occupies the general position and is partly disordered. The anion adopts a helical configuration due to large steric strains that are predominantly induced by the isopropyl group at the central C atom. Three almost planar fragments can be distinguished in the molecule: the tricyanoethylene groups are rotated with respect to the plane of four central C atoms [C–C(CH)–C] through 19.4° and 40.7° [112].

A comparison of the anion structures is of particular interest in the study of crystals **72** and **73** [113]. In crystal **72**, the anion lies in the *m* plane and has a symmetry similar to the *C_{2v}* symmetry. In the carbon chain, the C–C bond lengths fall in the range 1.388–1.404 Å and the bond angles increase to 130° for CC(H)C and 123° and 125° for CCC(H). In structure **73**, the anion with the seven-membered polyene chain slightly deviates from a planar configuration: the root-mean-square deviation from the plane passing through all the atoms of the carbanion is equal to 0.079 Å. The anion, as a whole, consists of two planar halves with the approximate symme-

try $C_s (m)$. The outer cyano groups are slightly rotated toward the anion plane. The bond lengths in the heptatriene chain fall in the range 1.378–1.397 Å. As in the other polycyanocarbanions, the bond lengths in the outer and inner cyano groups differ from each other: the mean lengths of the C–C(N) and C≡N bonds are equal to 1.430 and 1.139 Å for the outer cyano groups and 1.468 and 1.121 Å for the inner cyano groups, respectively.

4. CONCLUSION

Thus, we generalized the available data (obtained by different diffraction methods) on the molecular structure of the cubic and monoclinic crystals of tetracyanoethylene—the ancestor of a large class of charge-transfer complexes and radical ion salts.

The structures of 17 individual tricyanoethylene derivatives, which have the general formula $(CN)_2C=C(CN)R$ (R is the aromatic or heterocyclic electron-donor substituent) and are typical conjugated systems with pronounced intramolecular charge transfer, have been analyzed using X-ray diffraction data. It is found that, owing to the steric interactions and intramolecular charge transfer, the geometric parameters of the tricyanovinyl fragment in the molecular structure of the tricyanoethylene derivatives differ from those of the unsubstituted tetracyanoethylene. A more flattened molecular structure favors the intramolecular charge transfer. The features observed in the molecular structure of tricyanovinylarylamine (the lengthening of the C=C double bond in the tricyanovinyl fragment, the shortening of the C–C bond with the phenylene ring, a well-pronounced quinoid character of the bonds involved in the phenylene ring, and the shortening of the C(sp^2)–N bond in the amine group to the sesquibond) can be associated with the intramolecular charge transfer. Similar changes in the geometric parameters are also observed in the tricyanovinyl derivatives of the nitrogen-containing heterocyclic compounds, which also belong to the class of conjugated compounds with intramolecular charge transfer.

The molecular conformation of the tricyanovinyl compounds is characterized by the rotation of the tricyanovinyl group with respect to the planar donor fragment. The dihedral angle in monosubstituted tricyanoethylenes does not exceed 26°.

For a series of tricyanovinyl derivatives, the structure of molecules and their packing in the crystal are compared with the photoelectric properties of the single crystals. The specific features in the crystal and molecular structures confirm the previously revealed dependence of the photocurrent multiplication on the geometric parameters of the molecules.

The structural features of 16 molecular complexes and ionic salts with the tricyanovinyl group are examined. Of particular interest are the poorly investigated

complexes and salts in which the tricyanovinyl compounds exhibit an amphoteric nature.

In the structures of ten compounds in which the tricyanoethenolate fragment can serve as an anion of the salt or as a ligand of the organometallic complex, the tricyanoethenolate anions are disordered in a number of cases. In the organometallic compounds, the tricyanoethenolate fragment interacts with the metal atoms either through the O atom of the carbonyl group or through the N atom of the cyano group.

Among the representatives of the related class of tricyanopropenylidene derivatives, four individual compounds and seven ionic salts are characterized structurally. It is established that the seven compounds involve the pentacyanopropenide anion.

The structural features of the tricyanobutadiene derivatives, their complexes, and salts are analyzed using 17 structures as examples. Hexacyanobutadiene is one of the strongest acceptors and can form either charge-transfer complexes with aromatic compounds (four structures) or ionic salts (five structures) in which it can be in the form of a monoanion or a dianion.

ACKNOWLEDGMENTS

We acknowledge the support of the Russian Foundation for Basic Research (project no. 99-07-90133) in the payment of the license to use the Cambridge Structural Database.

This work was supported in part by the Russian Foundation for Basic Research, project no. 00-03-32578.

REFERENCES

1. V. É. Kamar and O. Ya. Neĭland, *Usp. Khim.* **46**, 945 (1977).
2. E. C. Chen and W. E. Wentworth, *J. Chem. Phys.* **63**, 3183 (1975).
3. R. P. Shibaeva and L. O. Atovmyan, *Zh. Strukt. Khim.* **13**, 546 (1972).
4. B. P. Bespalov and V. V. Titov, *Usp. Khim.* **44**, 2249 (1975).
5. L. A. Chetkina, E. G. Popova, V. M. Vozzhennikov, and B. V. Kotov, *Zh. Strukt. Khim.* **17**, 114 (1976).
6. E. G. Popova, L. A. Chetkina, and B. V. Kotov, *Zh. Strukt. Khim.* **17**, 510 (1976).
7. L. A. Chetkina, E. G. Popova, B. V. Kotov, *et al.*, *Zh. Strukt. Khim.* **17**, 1060 (1976).
8. E. G. Popova, L. A. Chetkina, and B. V. Kotov, *Zh. Strukt. Khim.* **19**, 1071 (1978).
9. E. G. Popova, L. A. Chetkina, and B. V. Kotov, *Zh. Strukt. Khim.* **22** (2), 116 (1981).
10. L. A. Chetkina, V. E. Zavodnik, and B. P. Bespalov, *Kristallografiya* **26**, 729 (1981) [*Sov. Phys. Crystallogr.* **26**, 415 (1981)].
11. Z. P. Povet'eva, L. A. Chetkina, and B. P. Bespalov, *Zh. Strukt. Khim.* **23** (2), 168 (1982).

12. L. A. Chetkina, I. M. Gel'fand, S. L. Ginzburg, *et al.*, *Kristallografiya* **28**, 470 (1983) [*Sov. Phys. Crystallogr.* **28**, 277 (1983)].
13. L. A. Chetkina, V. E. Zavodnik, and I. G. Il'ina, *Kristallografiya* **28**, 699 (1983) [*Sov. Phys. Crystallogr.* **28**, 413 (1983)].
14. L. A. Chetkina, V. E. Zavodnik, E. G. Popova, and B. P. Bespalov, *Kristallografiya* **34**, 1022 (1989) [*Sov. Phys. Crystallogr.* **34**, 619 (1989)].
15. L. A. Chetkina, G. N. Kurov, L. L. Dmitrieva, and A. N. Sobolev, *Kristallografiya* **36**, 499 (1991) [*Sov. Phys. Crystallogr.* **36**, 274 (1991)].
16. L. A. Chetkina, G. N. Kurov, and L. L. Dmitrieva, *Kristallografiya* **40**, 669 (1995) [*Crystallogr. Rep.* **40**, 617 (1995)].
17. E. G. Popova and L. A. Chetkina, *Zh. Strukt. Khim.* **20**, 665 (1979).
18. A. V. Dzyabchenko, V. E. Zavodnik, and V. K. Bel'skii, *Kristallografiya* **25**, 72 (1980) [*Sov. Phys. Crystallogr.* **25**, 38 (1980)].
19. V. E. Zavodnik, L. A. Chetkina, and G. A. Val'kova, *Kristallografiya* **24**, 592 (1979) [*Sov. Phys. Crystallogr.* **24**, 339 (1979)].
20. V. E. Zavodnik, L. A. Chetkina, and G. A. Val'kova, *Kristallografiya* **26**, 392 (1981) [*Sov. Phys. Crystallogr.* **26**, 223 (1981)].
21. V. E. Zavodnik and L. A. Chetkina, *Kristallografiya* **33**, 374 (1988) [*Sov. Phys. Crystallogr.* **33**, 220 (1988)].
22. *Cambridge Structural Database: Release 1999*.
23. T. L. Cairns, R. A. Carboni, D. D. Coffman, *et al.*, *J. Am. Chem. Soc.* **80**, 2775 (1958).
24. B. C. McKusick, R. E. Heckert, T. L. Cairns, *et al.*, *J. Am. Chem. Soc.* **80**, 2806 (1958).
25. G. N. Sausen, V. A. Engelhardt, and W. J. Middleton, *J. Am. Chem. Soc.* **80**, 2815 (1958).
26. Z. Rappoport, *J. Chem. Soc.*, 4498 (1963).
27. W. A. Sheppard and R. M. Henderson, *J. Am. Chem. Soc.* **89**, 4446 (1967).
28. R. G. Little, D. Pautler, and P. Coppens, *Acta Crystallogr., Sect. B: Struct. Crystallogr. Cryst. Chem.* **27**, 1493 (1971).
29. P. Becker, P. Coppens, and F. K. Ross, *J. Am. Chem. Soc.* **95**, 7604 (1973).
30. U. Druck, H. Guth, E. Hellner, *et al.*, *Acta Crystallogr., Sect. A: Found. Crystallogr.* **40**, C164 (1984).
31. D. A. Bekoe and K. N. Trueblood, *Z. Kristallogr.* **113**, 1 (1960).
32. D. A. Bekoe and K. N. Trueblood, in *Abstracts of the American Crystallographic Association Meeting, 1964*, p. 87.
33. U. Druck and H. Guth, *Z. Kristallogr.* **161**, 103 (1982).
34. S. L. Chaplot, A. Mierzejewski, and G. S. Pawley, *Acta Crystallogr., Sect. C: Cryst. Struct. Commun.* **40**, 663 (1984).
35. S. L. Chaplot, R. Chakravarthy, W. I. F. David, and J. Tomkinson, *J. Phys.: Condens. Matter* **3**, 9271 (1991).
36. H. Hope, *Acta Chem. Scand.* **22**, 1057 (1968).
37. G. J. H. van Nes and A. Vos, *Acta Crystallogr., Sect. B: Struct. Crystallogr. Cryst. Chem.* **35**, 2593 (1979).
38. L. V. Vilkov, V. S. Mastryukov, and N. I. Sadova, *Determination of Geometric Structures of Free Molecules* (Khimiya, Moscow, 1978), p. 74.
39. F. H. Allen, O. Kennard, D. G. Watson, *et al.*, *J. Chem. Soc., Perkin Trans. 2*, No. 12, S1 (1987).
40. D. E. Williams and S. R. Cox, *Acta Crystallogr., Sect. B: Struct. Sci.* **40**, 404 (1984).
41. I. Agranat, Z. Rappoport, and H. Weiler-Feilchenfeld, *Trans. Faraday Soc.* **66**, 769 (1970).
42. K. Nowak and H. Poradowska, *Wiad. Chem.* **41**, 21 (1987).
43. B. P. Bespalov, E. V. Getmanova, and A. G. Abolin, *Zh. Org. Khim.* **16**, 1896 (1980).
44. H. E. Katz, K. D. Singer, J. E. Sohn, *et al.*, *J. Am. Chem. Soc.* **109**, 6561 (1987).
45. A. Sasaki, J. Aihara, and Y. Matsunaga, *Bull. Chem. Soc. Jpn.* **47**, 2926 (1974).
46. J. Aihara, K. Araya, and Y. Matsunaga, *Bull. Chem. Soc. Jpn.* **54**, 615 (1981).
47. B. V. Kotov, G. I. Rybalko, I. G. Il'ina, *et al.*, in *Proceedings of the III All-Union Conference "Nonsilverhalide and Unusual Photoprocesses: Electrophotography," Vilnius, 1980*, p. 103.
48. N. A. Vasilenko, G. I. Rybalko, B. V. Kotov, *et al.*, in *Proceedings of the All-Union Conference "Nonsilverhalide and Unusual Photoprocesses," Suzdal, 1984*, Vol. 1, p. 109.
49. V. M. Vozzhennikov, V. L. Materikin, and B. V. Kotov, *Zh. Fiz. Khim.* **53**, 1580 (1979).
50. H. Bock, W. Seitz, N. Nagl, *et al.*, *Z. Naturforsch. B* **52**, 1125 (1997).
51. G. Tosi, P. Bruni, L. Cardellini, and G. Bocelli, *Gazz. Chim. Ital.* **114**, 111 (1984).
52. J. J. Stezowski, *Acta Crystallogr., Sect. B: Struct. Crystallogr. Cryst. Chem.* **33**, 2472 (1977).
53. P. A. Koutentis, C. W. Rees, A. J. P. White, and D. J. Williams, *J. Chem. Soc., Perkin Trans. 1*, 2765 (1998).
54. M. L. Hays, D. J. Burkey, J. S. Overby, *et al.*, *Organometallics* **17**, 5521 (1998).
55. A. I. de Lucas, N. Martin, P. de Miguel, *et al.*, *J. Mater. Chem.* **5**, 1141 (1995).
56. X. R. Bu, H. Li, D. van Derveer, and E. A. Mintz, *Tetrahedron Lett.* **37**, 7331 (1996).
57. A. P. Krukoni, J. Silverman, and N. F. Yannoni, *Cryst. Struct. Commun.* **3**, 233 (1974).
58. V. I. Berendyaev, N. N. Voznesenskaya, B. V. Kotov, *et al.*, *Vysokomol. Soedin., Ser. B* **18**, 585 (1976).
59. L. N. Kuleshova and P. M. Zorkii, *Acta Crystallogr., Sect. B: Struct. Crystallogr. Cryst. Chem.* **37**, 1363 (1981).
60. V. K. Potapov, *Usp. Khim.* **39**, 2078 (1970).
61. K. Hafner and K. L. Moritz, *Angew. Chem.* **72**, 918 (1960).
62. V. B. Mochalin and Yu. N. Porshnev, *Usp. Khim.* **46**, 1002 (1977).
63. M. Kaftory, M. Botoshansky, J. Daub, and A. Mirlach, *Acta Crystallogr., Sect. C: Cryst. Struct. Commun.* **53**, 1907 (1997).

64. C. Nather, C. Arad, and H. Bock, *Acta Crystallogr., Sect. C: Cryst. Struct. Commun.* **53**, 76 (1997).
65. R. Foster and P. Hanson, *Tetrahedron* **21**, 255 (1965).
66. Fr. Patent No. 1 560 973 (1969); FRG Patent No. 1 772 283 (1968).
67. G. N. Kurov, V. I. Smirnov, N. A. Shipitsyna, *et al.*, USSR Inventor's Certificate No. 1 083 153, *Byull. Izobret.*, No. 12, 152 (1984).
68. US Patent No. 4006017 (1977); FRG Patent No. 2 513 150 (1975).
69. D. J. Sandman and A. F. Richter, *J. Am. Chem. Soc.* **101**, 7079 (1979).
70. D. J. Sandman, A. F. Richter, D. E. Warner, and G. T. Fekete, *Mol. Cryst. Liq. Cryst.* **60**, 21 (1980).
71. D. J. Sandman, S. J. Grammatica, T. J. Holmes, and A. F. Richter, *Mol. Cryst. Liq. Cryst.* **59**, 241 (1980).
72. M. B. Freeman, L. G. Sneddon, and J. C. Huffman, *J. Am. Chem. Soc.* **99**, 5194 (1977).
73. K. Onitsuka, H. Urayama, K. Sonogashira, and F. Ozawa, *Chem. Lett.*, 1019 (1995).
74. L. Jager, C. Tretner, K. Sunkel, and J. Kozisek, *Z. Anorg. Allg. Chem.* **624**, 1381 (1998).
75. G. Dessy, V. Fares, A. Flamini, and A. M. Giuliani, *Angew. Chem., Int. Ed. Engl.* **24**, 426 (1985).
76. M. Bonamico, V. Fares, A. Flamini, *et al.*, *J. Chem. Soc., Perkin Trans. 2*, 1447 (1988).
77. M. Bonamico, V. Fares, A. Flamini, and P. Imperatori, *Z. Kristallogr.* **185**, 208 (1988).
78. M. Bonamico, V. Fares, A. Flamini, and P. Imperatori, *J. Chem. Soc., Perkin Trans. 2*, 121 (1990).
79. M. Decoster, J. E. Guerchais, Y. Le Mest, *et al.*, *Polyhedron* **15**, 195 (1996).
80. M. Decoster, F. Conan, M. Kubicki, *et al.*, *J. Chem. Soc., Perkin Trans. 2*, 265 (1997).
81. V. N. Nesterov, *Kristallografiya* **44**, 471 (1999) [*Crystallogr. Rep.* **44**, 431 (1999)].
82. T. Dahl, *Acta Chem. Scand. A* **37**, 353 (1983).
83. B. W. Sullivan and B. M. Foxman, *Organometallics* **2**, 187 (1983).
84. Y. Sato, H. Miyasaka, N. Matsumoto, and H. Okawa, *Inorg. Chim. Acta* **247**, 57 (1996).
85. E. J. Brandon, G. P. A. Yap, A. L. Rheingold, *et al.*, *Inorg. Chim. Acta* **240**, 515 (1995).
86. R. A. Jacobson and W. P. Jensen, *Inorg. Chim. Acta* **52**, 219 (1981).
87. C. C. Fuller and R. A. Jacobson, *Inorg. Chim. Acta* **48**, 191 (1981).
88. G. L. Breneman, *Acta Crystallogr., Sect. B: Struct. Crystallogr. Cryst. Chem.* **35**, 731 (1979).
89. V. N. Nesterov, A. M. Shestopalov, V. E. Shklover, *et al.*, *Izv. Akad. Nauk SSSR, Ser. Khim.*, 690 (1991).
90. K. Peters, E.-M. Peters, and K. Lange, *Z. Kristallogr.* **202**, 314 (1992).
91. V. N. Nesterov, V. E. Shklover, Yu. T. Struchkov, *et al.*, *Acta Crystallogr., Sect. C: Cryst. Struct. Commun.* **47**, 109 (1991).
92. H. M. Colquhoun, A. E. Crease, S. A. Taylor, and D. J. Williams, *J. Chem. Soc., Dalton Trans.*, 2781 (1988).
93. V. Bertolasi and G. Gilli, *Acta Crystallogr., Sect. C: Cryst. Struct. Commun.* **39**, 1242 (1983).
94. S. Siaka, P. M. Lukin, O. E. Nasakin, *et al.*, *Zh. Org. Khim.* **33**, 905 (1997).
95. Z. Riedl, G. Hajos, A. Messmer, *et al.*, *J. Chem. Soc., Chem. Commun.*, 757 (1997).
96. K. W. Hipps, U. Geiser, U. Mazur, and R. D. Willett, *J. Phys. Chem.* **88**, 2498 (1984).
97. J. S. Miller, J. C. Calabrese, H. Rommelmann, *et al.*, *J. Am. Chem. Soc.* **109**, 769 (1987).
98. G. A. Sim, D. I. Woodhouse, and G. R. Knox, *J. Chem. Soc., Dalton Trans.*, 629 (1979).
99. W. P. Jensen and R. A. Jacobson, *Inorg. Chim. Acta* **50**, 189 (1981).
100. G. J. Palenik, *Acta Crystallogr.* **20**, 471 (1966).
101. H. Hopf, M. Kreutzer, and P. G. Jones, *Angew. Chem., Int. Ed. Engl.* **30**, 1127 (1991).
102. J. S. Miller, J. C. Calabrese, and D. A. Dixon, *J. Phys. Chem.* **95**, 3139 (1991).
103. M. I. Bruce, R. C. Wallis, B. W. Skelton, and A. H. White, *J. Chem. Soc., Dalton Trans.*, 2205 (1981).
104. M. Etienne and L. Toupet, *J. Organomet. Chem.* **344**, C19 (1988).
105. M. Etienne, J. Talarmin, and L. Toupet, *Organometallics* **11**, 2058 (1992).
106. H. Yamochi, G. Saito, T. Sugano, *et al.*, *Chem. Lett.*, 1303 (1986).
107. H. Yamochi, G. Saito, T. Sugano, *et al.*, *Synth. Met.* **19**, 533 (1987).
108. C. Katayama, M. Honda, H. Kumagai, *et al.*, *Bull. Chem. Soc. Jpn.* **58**, 2272 (1985).
109. J. S. Miller, J. H. Zhang, and W. M. Reiff, *J. Am. Chem. Soc.* **109**, 4584 (1987).
110. E. Maverick, E. Goldish, J. Bernstein, *et al.*, *J. Am. Chem. Soc.* **94**, 3364 (1972).
111. R. Schlodder and J. A. Ibers, *Inorg. Chem.* **13**, 2870 (1974).
112. J. C. Huffman, *Cryst. Struct. Commun.* **5**, 187 (1976).
113. R. L. Sass and T. D. Nichols, *Z. Kristallogr.* **140**, 1 (1974).
114. J. Edmonds, J. K. Herdklotz, and R. L. Sass, *Acta Crystallogr., Sect. B: Struct. Crystallogr. Cryst. Chem.* **26**, 1355 (1970).
115. K. Kveseth, R. Saip, and D. A. Kohl, *Acta Chem. Scand. A* **34**, 31 (1980).
116. R. Taylor and O. Kennard, *J. Am. Chem. Soc.* **104**, 5063 (1982).
117. G. Saito, T. Enoki, H. Inokuchi, *et al.*, *Mol. Cryst. Liq. Cryst.* **120**, 345 (1985).
118. J. Tanaka, C. Katayama, H. Kumagai, *et al.*, *Mol. Cryst. Liq. Cryst.* **125**, 223 (1985).

Translated by O. Borovik-Romanova

STRUCTURES OF ORGANIC COMPOUNDS

Interaction of Cystamine with Palladium(II) Monoethanolamine Complex: Crystal Structure of $[\text{Pd}(\text{NH}_2\text{CH}_2\text{CH}_2\text{OH})_4][\text{Pd}_6(\text{NH}_2\text{CH}_2\text{CH}_2\text{S})_8]\text{Cl}_6 \cdot 5\text{H}_2\text{O}$

Kh. I. Gasanov, A. S. Antsyshkina, G. G. Sadikov, N. A. Ivanova,
D. I. Mirzai, I. A. Efimenko, and V. S. Sergienko

Kurnakov Institute of General and Inorganic Chemistry, Russian Academy of Sciences,
Leninskiĭ pr. 31, Moscow, 119991 Russia

e-mail: antas@igic.ras.ru

Received January 14, 2002

Abstract—The new compound $[\text{Pd}(\text{NH}_2\text{CH}_2\text{CH}_2\text{OH})_4][\text{Pd}_6(\text{NH}_2\text{CH}_2\text{CH}_2\text{S})_8]\text{Cl}_6 \cdot 5\text{H}_2\text{O}$ (**I**) is synthesized and its crystal structure is determined. The crystals are monoclinic, $a = 25.625(6)$ Å, $b = 9.633(5)$ Å, $c = 24.847(7)$ Å, $\beta = 91.47(2)^\circ$, $Z = 4$, and space group $C2/c$. The structural units of crystals **I** are the centrosymmetric hexanuclear $[\text{Pd}_6(\text{NH}_2\text{CH}_2\text{CH}_2\text{S})_8]^{4+}$ cations, the mononuclear $[\text{Pd}(\text{NH}_2\text{CH}_2\text{CH}_2\text{OH})_4]^{2+}$ cations with C_2 symmetry, the Cl^- anions, and crystallization water molecules. In the hexanuclear cation, the interaction between the Pd atoms occurs through the S atoms of the mercaptoethylamine ligands. The Pd(2) and Pd(3) atoms and the ligands form two metalochelate fragments in which the N and S atoms are located in *cis* positions. The average lengths of the Pd–S and Pd–N bonds are equal to 2.274(1) and 2.074(6) Å, respectively. The metalochelate fragments are joined to each other and to their centrosymmetric analogues through the Pd(1) atom, which coordinates four S atoms [the average Pd–S_{av} bond length is 2.332(1) Å]. In the mononuclear cation, the Pd(4) atom coordinates four N atoms of the monoethylamine ligands [the Pd–N bond lengths are 2.045(6) and 2.056(6) Å]. The shortest Pd···Pd distance is equal to 3.207(1) Å. The bonding in the structure is provided by numerous hydrogen bonds with the participation of all the H₂O molecules, NH₂ groups, and Cl[−] anions. © 2002 MAIK “Nauka/Interperiodica”.

INTRODUCTION

The interaction of acido palladium complexes with cystamine $\text{H}_2\text{NCH}_2\text{CH}_2\text{—S—S—CH}_2\text{CH}_2\text{NH}_2$ ($L\text{H}_2$) leads to the formation of compounds with different compositions and structures, depending on the pH of the medium. For example, in aqueous media at pH 1–7, the disulfide bond in cystamine is broken with the formation of the mercamine $\text{NH}_2\text{CH}_2\text{CH}_2\text{SH}$ ($L\text{H}$) and its coordination to palladium. This results in the formation of the complexes of compositions PdL'_2 [1], $\text{Pd}_2(L\text{H})_2\text{Cl}_4$ with Cl or S bridging atoms (depending on the reaction temperature), and $\text{Pd}_2L'_2\text{Cl}_2$ with Cl bridging atoms and a bidentate ligand coordination [2]. In nonaqueous media, the cationic–anionic complex of composition $[\text{LH}_4][\text{PdCl}_4]$ can be formed without breaking the S–S bond in cystamine and coordination of this ligand to palladium [3].

The complex involving the noncluster hexanuclear cation $[\text{Pd}_6L'_8]\text{Cl}_4$ (**II**) is formed at pH ~ 10 [4, 5].

In the present work, we investigated the interaction of the palladium ethanolamine complex $\text{PdCl}_2(\text{NH}_2\text{CH}_2\text{CH}_2\text{OH})_2$ with cystamine dihydrochloride $\text{NH}_2\text{CH}_2\text{CH}_2\text{—S—S—CH}_2\text{CH}_2\text{NH}_2 \cdot 2\text{HCl}$ and performed X-ray structure analysis of

the final reaction product—the compound $[\text{Pd}(\text{NH}_2\text{CH}_2\text{CH}_2\text{OH})_4][\text{Pd}_6(\text{NH}_2\text{CH}_2\text{CH}_2\text{S})_8]\text{Cl}_6 \cdot 5\text{H}_2\text{O}$ (**I**).

EXPERIMENTAL

Synthesis. The complex *trans*- $\text{PdCl}_2(\text{NH}_2\text{CH}_2\text{CH}_2\text{OH})_2$ was synthesized according to the procedure described in [6]. Cystamine dihydrochloride (Fluka) was used without additional purification.

Compound **I** was synthesized by two methods.

Method 1. A solution of cystamine dihydrochloride (0.3345 g, 0.1485 mmol) in water (7 ml) was added to a filtered solution of $\text{PdCl}_2(\text{NH}_2\text{CH}_2\text{CH}_2\text{OH})_2$ (0.3541 g, 0.1485 mmol) in water (10 ml) with stirring. An orange precipitate formed, which dissolved upon heating to 50°C, and the solution turned light yellow. The solution was evaporated at 70°C to a volume of 5 ml and left to crystallize at room temperature. Yellow crystals precipitated were filtered off and dried in air.

For $\text{Pd}_7\text{N}_{12}\text{C}_{24}\text{H}_{86}\text{O}_9\text{S}_8\text{Cl}_6$ anal. calcd. (%): Pd, 39.18; Cl, 11.19; N, 8.84.

Found (%): Pd, 40.02; Cl, 10.95; N, 9.20.

Method 2. A solution of ethanol (0.5057 g, 8.3169 mmol) in water (10 ml) was added, with stir-

ring, to a filtered solution prepared at 50°C from palladium chloride (0.2650 g, 1.4937 mmol) and a mixture of water (20 ml) with concentrated hydrochloric acid (5 ml). A 0.5 M aqueous solution of cystamine dihydrochloride (3 ml) was added to the prepared solution to the formation of an orange solution, to which a 25% ammonia solution was added dropwise to pH 7. The reaction mixture was evaporated at 50°C in a water bath to a volume of 10 ml and left to crystallize at room temperature. Within four days, yellow crystals precipitated. The crystals were filtered off, washed with water, and dried at room temperature to a constant weight.

For $\text{Pd}_7\text{N}_{12}\text{C}_{24}\text{H}_{86}\text{O}_9\text{S}_8\text{Cl}_6$ anal. calcd. (%): Pd, 39.18; Cl, 11.19; N, 8.84.

Found (%): Pd, 38.64; Cl, 10.80; N, 7.80.

The Pd content in compound **I** was determined after calcination at 850°C according to the procedure described in [7, 8]. The Cl content was evaluated using the Schönheerr method, and the N content was determined by the Dumas method [9].

X-ray diffraction analysis. Crystals **I** are monoclinic, $a = 25.625(6)$ Å, $b = 9.633(5)$ Å, $c = 24.847(7)$ Å, $\beta = 91.47(2)^\circ$, $V = 6131(3)$ Å³, $M = 1901$, $F(000) = 3752$, $\rho_{\text{calcd}} = 2.059$ g/cm³, μ_{Mo} = 2.59 mm⁻¹, $Z = 4$, and space group $C2/c$.

The experimental data were collected on an Enraf-Nonius CAD4 diffractometer ($\lambda\text{MoK}\alpha$, graphite monochromator, $\theta/2\theta$ scan mode, $2\theta_{\text{max}} = 56^\circ$).

Structure **I** was solved by the direct method with the use of 3973 reflections. The hydrogen atoms were located from the difference Fourier syntheses. The structure was refined by the least-squares procedure using 3952 reflection with $F_o \geq 4\sigma(F_o)$. The non-hydrogen atoms were refined in the anisotropic approximation, and the hydrogen atoms were refined in the isotro-

pic approximation. The final R values were as follows: $R_1 = 0.0287$, $wR_2 = 0.0721$, and $Goof = 1.060$ for 3952 reflections; $\Delta\rho_{\text{max}} = 0.92$ e/Å³; and $\Delta\rho_{\text{min}} = -0.78$ e/Å³.

The calculations were performed according to the SHELXS86 [10] and SHELXL93 [11] software packages.

The atomic coordinates and thermal parameters for structure **I** are listed in Table 1. The bond lengths and angles are presented in Table 2.

RESULTS AND DISCUSSION

The structural units of crystals **I** are the centrosymmetric hexanuclear cationic complexes $[\text{Pd}_6(\text{NH}_2\text{CH}_2\text{CH}_2\text{S})_8]^{4+}$ (Fig. 1a), the mononuclear cationic complexes $[\text{Pd}(\text{NH}_2\text{CH}_2\text{CH}_2\text{OH})_4]^{2+}$ with C_2 symmetry (Fig. 1b), the anions Cl^- , and the crystallization water molecules in general positions.

The structure of the hexapalladium cation in compound **I** is virtually identical to that of the corresponding cation in the compound $[\text{Pd}_6(\text{NH}_2\text{CH}_2\text{CH}_2\text{S})_8]\text{Cl}_4$ (**II**) [4]. The cation structure is formed by three pairs of Pd atoms, which do not interact directly. The coordination polyhedra of the Pd(1), Pd(2), and Pd(3) atoms have the shape of nearly planar squares. The Pd(2) and Pd(3) atoms each coordinate two N atoms and two S atoms of two deprotonated β -mercaptoethylamine ligands, thus closing the five-membered chelate metallo-cycles with the N and S atoms in the *cis* positions. The average lengths of the Pd–N and Pd–S bonds are equal to 2.074(6) and 2.274(1) Å, respectively. Similar bonds in structure **II** are somewhat lengthened [2.091(6) and 2.280(1) Å]. In structure **I**, a small tetrahedral distortion of the coordination core PdN_2S_2 is observed in both metallo-cycles. The deviation of the N and S atoms from

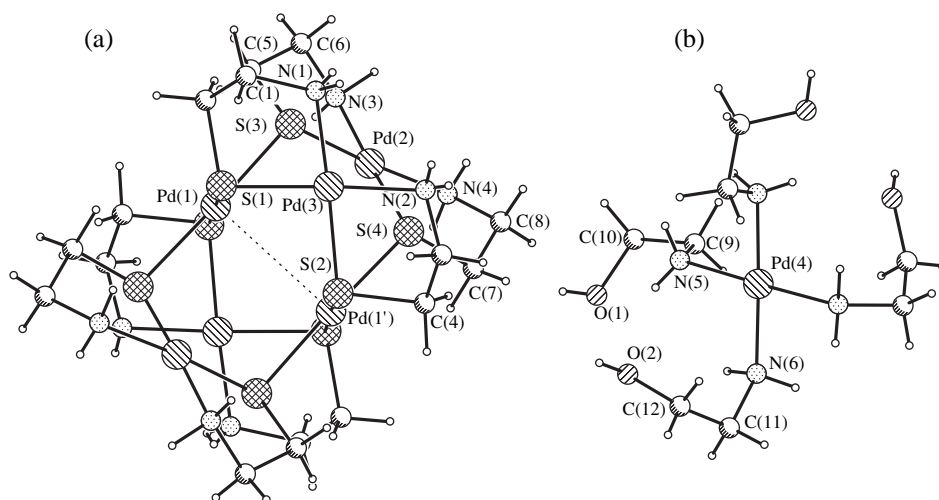


Fig. 1. Cationic complexes in structure **I**: (a) hexanuclear $[\text{Pd}_6(\text{NH}_2\text{CH}_2\text{CH}_2\text{S})_8]^{4+}$ and (b) mononuclear $[\text{Pd}(\text{NH}_2\text{CH}_2\text{CH}_2\text{OH})_4]^{2+}$ complexes.

Table 1. Atomic coordinates and thermal parameters (U_{eq}/U_{iso}) for compound **I**

Atom	x	y	z	$U_{eq}/U_{iso}, \text{\AA}^2$
Pd(1)	0.25782(2)	0.08767(4)	0.51205(2)	0.0224(1)
Pd(2)	0.21318(2)	0.17429(4)	0.37278(2)	0.0251(1)
Pd(3)	0.12494(2)	0.22164(4)	0.53581(2)	0.0263(1)
Pd(4)	0.0	0.94546(7)	0.25	0.0324(2)
S(1)	0.18903(5)	0.0856(2)	0.57199(6)	0.0278(3)
S(2)	0.17352(5)	0.4172(2)	0.54759(6)	0.0289(3)
S(3)	0.19981(6)	0.0263(2)	0.44245(6)	0.0282(3)
S(4)	0.18244(5)	0.3504(1)	0.41835(6)	0.0274(3)
Cl(1)	0.1823(1)	-0.0478(2)	0.7138(1)	0.0469(4)
Cl(2)	0.0375(1)	-0.1932(2)	0.4442(1)	0.0598(5)
Cl(3)	-0.0433(1)	0.3465(2)	0.3396(1)	0.0617(5)
O(w1)	0.1640(3)	-0.3605(7)	0.6692(4)	0.088(3)
O(w2)	0.0552(3)	0.4921(9)	0.3976(3)	0.104(3)
O(w3)	0.0000(0)	0.536(1)	0.2500(0)	0.092(4)
O(1)	0.1646(2)	0.7316(6)	0.2343(3)	0.074(2)
O(2)	0.0895(2)	0.9524(6)	0.3479(2)	0.059(1)
N(1)	0.0788(3)	0.0447(7)	0.5341(4)	0.041(2)
N(2)	0.0661(2)	0.3515(6)	0.5076(3)	0.043(1)
N(3)	0.2376(3)	0.0011(6)	0.3309(2)	0.037(1)
N(4)	0.2190(3)	0.3086(6)	0.3075(2)	0.039(1)
N(5)	0.0563(2)	0.7951(6)	0.2486(3)	0.039(1)
N(6)	0.0580(2)	1.0928(6)	0.2499(2)	0.039(1)
C(1)	0.0982(3)	-0.0629(7)	0.5723(3)	0.041(2)
C(2)	0.1558(3)	-0.0813(7)	0.5645(3)	0.034(1)
C(3)	0.0721(3)	0.4907(8)	0.5313(3)	0.045(2)
C(4)	0.1258(3)	0.5436(7)	0.5212(3)	0.038(2)
C(5)	0.2264(3)	-0.1316(6)	0.4124(3)	0.036(1)
C(6)	0.2157(3)	-0.1283(7)	0.3528(3)	0.037(1)
C(7)	0.1918(3)	0.4940(7)	0.3669(3)	0.037(2)
C(8)	0.1843(3)	0.4325(7)	0.3126(3)	0.041(2)
C(9)	0.0776(3)	0.7677(8)	0.1957(3)	0.044(2)
C(10)	0.1251(4)	0.676(1)	0.1994(5)	0.061(3)
C(11)	0.0717(4)	1.1643(9)	0.3015(4)	0.056(2)
C(12)	0.0622(4)	1.079(1)	0.3489(4)	0.059(2)
H(11)	0.083(3)	-0.156(8)	0.569(3)	0.06(2)
H(12)	0.097(3)	-0.021(9)	0.600(3)	0.06(3)
H(21)	0.171(2)	-0.145(7)	0.594(3)	0.04(2)
H(22)	0.160(2)	-0.113(6)	0.537(2)	0.01(2)
H(31)	0.068(2)	0.466(7)	0.570(3)	0.04(2)
H(32)	0.050(3)	0.557(7)	0.519(3)	0.05(2)
H(41)	0.136(2)	0.637(6)	0.541(2)	0.03(2)
H(42)	0.128(2)	0.551(6)	0.488(2)	0.02(2)
H(51)	0.264(3)	-0.139(6)	0.415(2)	0.04(2)
H(52)	0.205(3)	-0.196(8)	0.432(3)	0.06(2)
H(61)	0.232(2)	-0.206(6)	0.337(2)	0.02(2)
H(62)	0.180(2)	-0.127(6)	0.346(2)	0.03(2)

Table 1. (Contd.)

Atom	<i>x</i>	<i>y</i>	<i>z</i>	$U_{eq}/U_{iso}, \text{\AA}^2$
H(71)	0.168(2)	0.560(6)	0.371(2)	0.03(2)
H(72)	0.230(2)	0.530(6)	0.375(2)	0.03(2)
H(81)	0.151(2)	0.405(6)	0.304(2)	0.03(2)
H(82)	0.192(2)	0.500(8)	0.286(3)	0.05(2)
H(91)	0.085(3)	0.844(7)	0.178(3)	0.04(2)
H(92)	0.050(3)	0.723(7)	0.172(3)	0.05(2)
H(101)	0.138(3)	0.654(9)	0.178(3)	0.05(3)
H(102)	0.119(3)	0.581(8)	0.212(3)	0.05(2)
H(111)	0.055(4)	1.241(9)	0.298(4)	0.09(3)
H(112)	0.106(3)	1.185(7)	0.299(3)	0.04(2)
H(121)	0.027(3)	1.065(6)	0.352(2)	0.03(2)
H(122)	0.064(3)	1.120(9)	0.380(4)	0.07(3)
H(1N1)	0.047(3)	0.070(9)	0.541(3)	0.07(3)
H(2N1)	0.072(3)	0.029(9)	0.511(3)	0.06(3)
H(1N2)	0.070(2)	0.364(7)	0.475(3)	0.03(2)
H(2N2)	0.040(3)	0.321(8)	0.514(3)	0.05(2)
H(1N3)	0.221(3)	-0.004(9)	0.292(3)	0.09(3)
H(2N3)	0.267(3)	0.005(9)	0.332(3)	0.06(3)
H(1N4)	0.250(3)	0.345(8)	0.310(3)	0.06(2)
H(2N4)	0.205(4)	0.273(9)	0.281(4)	0.09(3)
H(1N5)	0.075(3)	0.816(7)	0.272(3)	0.04(2)
H(2N5)	0.036(3)	0.722(8)	0.263(3)	0.07(3)
H(1N6)	0.049(2)	1.161(7)	0.230(3)	0.04(2)
H(2N6)	0.092(4)	1.041(9)	0.238(3)	0.10(3)
H(1w1)	0.170(3)	-0.285(7)	0.681(3)	0.03(2)
H(2w1)	0.125(3)	-0.355(8)	0.665(3)	0.07(3)
H(1w2)	0.057(2)	0.568(7)	0.351(3)	0.03(2)
H(2w2)	0.026(4)	0.44(1)	0.371(4)	0.08(4)
H(1w3)	0.002(5)	0.47(1)	0.277(4)	0.16(5)
H(1)	0.167(6)	0.82(1)	0.230(6)	0.16(5)
H(2)	0.082(5)	0.93(1)	0.366(5)	0.13(5)

the mean plane passing through these atoms is equal to $\pm 0.018 \text{ \AA}$ for Pd(2)N₂S₂ and $\pm 0.025 \text{ \AA}$ for Pd(3)N₂S₂.

The chelate fragments containing the Pd(2) and Pd(3) atoms are joined to each other and to their centrosymmetric analogues Pd(2)' and Pd(3)' through the Pd(1) and Pd(1)' atoms. These atoms each coordinate four bridging S atoms. The average Pd–S bond lengths in structures **I** and **II** are equal to 2.332(1) and 2.336(1) \AA , respectively.

In compound **I**, the shortest distance Pd(1)···Pd(1)' is equal to 3.207(1) \AA and the other distances Pd···Pd are 3.712(1) and 3.703(1) \AA . The corresponding distances in compound **II** are equal to 3.202(1), 3.722(1), and 3.689(1) \AA .

The hexanuclear complex involves the two mutually perpendicular eight-membered rings Pd₄S₄ composed of the alternating Pd and S atoms. Both rings adopt a chair-type conformation: the Pd(2) and Pd(2)' atoms deviate from the central planar fragment Pd(1)S(3)S(4)Pd(1)'S(3)'S(4)' in opposite directions by 1.38 \AA , and the deviations of the Pd(3) and Pd(3)' atoms from the plane Pd(1)S(1)S(2)Pd(1)'S(1)'S(2)' are equal to $\pm 1.40 \text{ \AA}$.

The nonplanar conformation of the eight-membered metalocycles possibly results from an additional (secondary) interaction of the Pd(2) and Pd(3) atoms with the S atoms of the adjacent perpendicularly oriented cycle: the Pd(2) atom deviates from the plane of the coordination square N(3)N(4)S(3)S(4) by 0.067 \AA

Table 2. Bond lengths and angles in compound I

Bond	<i>d</i> , Å	Bond	<i>d</i> , Å
Pd(1)···Pd(1)'	3.207(1)		
Pd(1)–S(1)	2.337(1)	Pd(1)–S(2)	2.330(1)
Pd(1)–S(3)	2.328(2)	Pd(1)–S(4)	2.334(1)
Pd(2)–S(3)	2.275(2)	Pd(2)–S(4)	2.272(2)
Pd(2)–N(3)	2.071(6)	Pd(2)–N(4)	2.084(6)
Pd(3)–S(1)	2.269(1)	Pd(3)–S(2)	2.272(1)
Pd(3)–N(1)	2.075(6)	Pd(3)–N(2)	2.067(6)
Pd(4)–N(5)	2.045(6)	Pd(4)–N(6)	2.056(6)
S(1)–C(2)	1.826(7)	S(2)–C(4)	1.836(7)
S(3)–C(5)	1.833(6)	S(4)–C(7)	1.834(7)
O(1)–C(10)	1.42(1)	O(2)–C(12)	1.41(1)
N(1)–C(1)	1.48(1)	N(2)–C(3)	1.47(1)
N(3)–C(6)	1.477(9)	N(4)–C(8)	1.494(9)
N(5)–C(9)	1.46(1)	N(6)–C(11)	1.49(1)
C(1)–C(2)	1.50(1)	C(3)–C(4)	1.49(1)
C(5)–C(6)	1.50(1)	C(7)–C(8)	1.48(1)
C(9)–C(10)	1.50(1)	C(11)–C(12)	1.46(1)
Bond angle	ω , deg	Bond angle	ω , deg
S(1)Pd(1)S(2)	178.36(5)	S(1)Pd(1)S(3)	89.62(5)
S(1)Pd(1)S(4)	91.19(5)	S(2)Pd(1)S(3)	90.04(5)
S(2)Pd(1)S(4)	89.07(5)	S(3)Pd(1)S(4)	177.53(6)
S(3)Pd(2)S(4)	93.10(5)	S(3)Pd(2)N(3)	86.0(2)
S(3)Pd(2)N(4)	175.4(2)	S(4)Pd(2)N(3)	177.3(2)
S(4)Pd(2)N(4)	86.0(2)	N(3)Pd(2)N(4)	94.6(2)
S(1)Pd(3)S(2)	92.24(5)	S(1)Pd(3)N(1)	86.6(2)
S(1)Pd(3)N(2)	176.4(2)	S(2)Pd(3)N(1)	173.6(2)
S(2)Pd(3)N(2)	86.2(2)	N(1)Pd(3)N(2)	94.6(3)
N(5)Pd(4)N(6)	88.7(2)	Pd(1)S(1)Pd(3)	107.02(6)
Pd(1)S(1)C(2)	107.4(2)	Pd(3)S(1)C(2)	97.9(2)
Pd(1)S(2)Pd(3)	108.77(6)	Pd(1)S(2)C(4)	107.0(2)
Pd(3)S(2)C(4)	98.4(2)	Pd(1)S(3)Pd(2)	107.48(6)
Pd(1)S(3)C(5)	106.0(2)	Pd(2)S(3)C(5)	98.4(2)
Pd(1)S(4)Pd(2)	108.01(6)	Pd(1)S(4)C(7)	105.8(2)
Pd(2)S(4)C(7)	98.8(2)	Pd(3)N(1)C(1)	112.2(5)
Pd(3)N(2)C(3)	110.3(5)	Pd(2)N(3)C(6)	111.9(4)
Pd(2)N(4)C(8)	112.1(4)	Pd(4)N(5)C(9)	115.1(5)
Pd(4)N(6)C(11)	118.1(5)	N(1)C(1)C(2)	108.4(6)
S(1)C(2)C(1)	109.8(5)	N(2)C(3)C(4)	109.3(6)
S(2)C(4)C(3)	108.7(5)	S(3)C(5)C(6)	108.9(5)
N(3)C(6)C(5)	108.7(6)	S(4)C(7)C(8)	109.8(5)
N(4)C(8)C(7)	109.4(6)	N(5)C(9)C(10)	111.7(7)
O(1)C(10)C(9)	112.5(8)	N(6)C(11)C(12)	113.2(7)
O(2)C(12)C(11)	112.3(8)		

Table 3. Parameters of hydrogen bonds in structure **I**

Bond no.	Bond	Distance, Å			Angle, deg
		A...B	A-H	H...B	
1	O(w1)-H...Cl(1)	3.150(7)	0.73(7)	2.42(7)	175(7)
2	O(w1)-H...Cl(3)	3.099(8)	1.00(9)	2.15(9)	174(7)
3	O(w2)-H...Cl(2)	3.271(9)	0.83(9)	2.44(8)	178(9)
4	O(w2)-H...Cl(3)	3.209(9)	0.89(9)	2.31(9)	178(9)
5	O(w3)-H...Cl(3)	3.103(7)	0.92(7)	2.31(8)	148(7)
6	O(1)-H...Cl(1)	3.142(7)	0.85(6)	2.29(8)	173(7)
7	O(2)-H...Cl(2)	3.114(8)	0.74(7)	2.47(7)	144(6)
8	N(1)-H...Cl(2)	3.359(8)	0.88(8)	2.49(8)	169(6)
9	N(1)-H...Cl(1)	3.348(7)	0.66(8)	2.77(2)	148(6)
10	N(2)-H...O(w2)	3.085(9)	0.78(8)	2.39(9)	150(7)
11	N(2)-H...Cl(2)	3.311(7)	0.78(7)	2.55(7)	165(4)
12	N(3)-H...Cl(1)	3.237(7)	0.98(7)	2.27(8)	172(9)
13	N(3)-H...O(w1)	2.907(7)	0.74(7)	2.35(8)	134(8)
14	N(4)-H...Cl(1)	3.468(8)	0.90(8)	2.68(7)	148(7)
15	N(4)-H...O(1)	3.277(7)	0.90(7)	2.69(8)	124(6)
16	N(4)-H...Cl(1)	3.541(8)	0.72(7)	2.86(8)	158(8)
17	N(5)-H...O(2)	3.001(7)	0.75(8)	2.36(7)	145(7)
18	N(5)-H...O(w3)	2.887(7)	0.99(8)	2.01(7)	146(7)
19	N(6)-H...Cl(3)	3.317(7)	0.91(9)	2.43(8)	167(6)
20	N(6)-H...Cl(1)	3.360(8)	1.05(9)	2.37(8)	157(7)

toward the S(1)' and S(2)' atoms, and the Pd(3) atom is displaced from the N(1)N(2)S(1)S(2) plane by 0.091 Å toward the S(3)' and S(4)' atoms.

In the mononuclear cation $[\text{Pd}(\text{NH}_2\text{CH}_2\text{CH}_2\text{OH})_4]^{2+}$ of compound **I**, the Pd atom coordinates four N atoms of four monodentate hydroxyethylamine ligands [the Pd(4)-N bond lengths are equal to 2.045(6) and 2.056(6) Å]. The central fragment Pd(4)N₄ is planar to within ± 0.007 Å.

The structural units in crystal **I** are linked together by numerous hydrogen bonds, which involve all the Cl anions, water molecules, and O atoms of the hydroxy groups (Table 3). In all the hydrogen bonds, the amino groups serve as proton donors. In crystal **I**, as in crystal **II**, the Cl ions participate as proton acceptors in the hydrogen bonds with the N atoms of the amino groups and the O atoms of water molecules.

The similarity of the hexanuclear cationic complexes in compounds **I** and **II** leads to a certain structural similarity of their crystals as a whole. For example, in both compounds, the principal axes of the local symmetry C_{4h} pass through the Pd(1) and Pd(1)' atoms and are almost parallel to the crystallographic axes with the minimum unit cell parameter: $b = 9.63$ Å in compound **I** and $a = 9.67$ Å in compound **II**. The misorientation angles between the axes in the complexes and the above

crystallographic axes are also virtually identical and are equal to 12.8° and 11.9°, respectively. The cationic complexes are aligned along these crystallographic axes and form columns surrounded by Cl anions attached by hydrogen bonds. Owing to the congruence of complexes **I** and **II**, the hydrogen bond directions (governed by the orientation of the NH₂ groups) appear to be the same (Fig. 2). The participation of structural units (Cl and H₂O) in the formation of the hydrogen bonds also turns out to be similar in many respects. The difference actually resides in the fact that one amino group in structure **II** does not participate in hydrogen bonds, whereas the amino group in structure **I** forms the bifurcated hydrogen bond (Table 3, bonds nos. 14, 15) with the Cl(1) atom and the hydroxyl O atom of the monoethanolamine ligand in the mononuclear cationic complex. Moreover, in structure **I**, the arrangement of the Cl(1) and Cl(2) atoms, together with the corresponding hydrogen bonds (nos. 12, 14, 16 and 8, 9, 11), is quite adequate for the local symmetry of the complex. As a result, in structure **I**, the hexanuclear cation in which all the H atoms of the amino groups are involved in the hydrogen bonds appears to be in a more isotropic force field and has a more pronounced local symmetry C_{4h} . In particular, the folding angles made by the planes of the Pd(2) and Pd(3) coordination squares with the central planes of the eight-membered rings are virtually equal to each other (62.3° and 62.7°). At the same time, the asymmetry of intermolecular contacts with neighbors in the cations of structure **II** results in a noticeable deviation from an "ideal" symmetry: the aforementioned angles (51.5° and 69.4°) differ considerably. A certain redistribution of bond lengths and bond angles is also likely caused by external actions.

Despite certain differences in specific features of the interaction, the columns in structures **I** and **II** form layers with a very similar structure. These layered fragments contain the hexanuclear complexes related only by the inversion centers and the associated Cl atoms. The columns are directly linked by double hydrogen bridges through the Cl(2) atoms (hydrogen bonds nos. 8, 9, 11). The layers are parallel to the coordinate plane (001) in structure **I** and to the diagonal plane (011) in structure **II**. The distances between columns in the layers are equal to 12.80 Å in compound **I** and 12.90 Å in compound **II**.

It is evident that the structures under consideration are characterized by different packings of layers. In structure **I**, since the local symmetry C_{4h} occurs outside the complex, it is possible to distinguish layered fragments extending in the perpendicular direction. In this case, the screw axis 2₁ is the controlling symmetry element and the layers are directly joined by a number of hydrogen bonds with the participation of the bridging Cl(1) atom (hydrogen bonds nos. 12, 14, 16). In combination, both systems of layers form a framework consisting of columns with channels of a square cross sec-

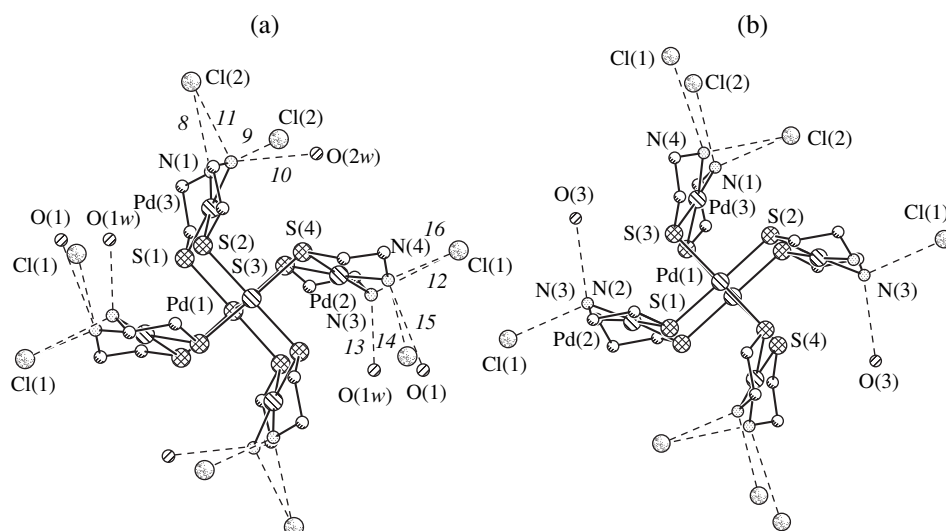


Fig. 2. A system of hydrogen bonds in the hexapalladium complexes. Projections along the lattice axes nearest to the principal axes of the C_{4h} local symmetry: (a) the b -axis in structure **I** and (b) the a -axis in structure **II**.

tion. In structure **II**, the cross section of channels is triangular in shape.

Undeniably, the main reason for the difference between structures **I** and **II** lies in the different compositions of the compounds and, primarily, in the presence of the second cationic complex with its different nature in compound **I**. In crystals **II**, no hydrogen bonds, in principle, can occur between similar cationic complexes. A quite different situation is observed in the case of compound **I** involving the second cation $[\text{Pd}(\text{NH}_2\text{CH}_2\text{CH}_2\text{OH})_4]^{2+}$ with four hydroxyl groups. In compound **I**, the hydrogen bonds are formed both between the different-type cationic complexes (hydrogen bond no. 15) and between the cations $[\text{Pd}(\text{NH}_2\text{CH}_2\text{CH}_2\text{OH})_4]^{2+}$ (hydrogen bond no. 17). The mononuclear cations joined through their subsystem of hydrogen bonds, the Cl(3) atoms, and the crystallization water molecules occupy channels formed between the layers of hexanuclear cationic complexes.

REFERENCES

1. D. C. Jicha and D. H. Bush, *Inorg. Chim. Acta* **1** (4), 177 (1962).
2. I. A. Efimenko, Kh. I. Gasanov, N. A. Ivanova, *et al.*, *Koord. Khim.* **26** (2), 117 (2000).
3. I. A. Zakharova, in *Research in Inorganic Chemistry and Chemical Technology* (Nauka, Moscow, 1982), p. 171.
4. Yu. E. Gorbunova, Yu. N. Mikhaïlov, A. P. Kurbakova, and I. A. Efimenko, *Koord. Khim.* **19** (4), 322 (1993).
5. I. A. Efimenko, Kh. I. Gasanov, Yu. E. Gorbunova, *et al.*, *Dokl. Akad. Nauk* **326** (4), 654 (1992).
6. Kh. I. Gasanov, S. S. Fatullaeva, D. I. Mirzai, and I. A. Efimenko, in *Proceedings of the XVI Mendeleev Congress on General and Applied Chemistry, Moscow, 1998*, p. 67.
7. S. Livingstone, *Rhenium, Rhodium, Palladium, Osmium, Iridium, and Platinum* (Pergamon, Oxford, 1975; Mir, Moscow, 1978).
8. S. I. Ginzburg, K. A. Gladyshevskaya, N. A. Ezerskaya, *et al.*, *Guide on Chemical Analysis of Platinum Metals and Gold* (Nauka, Moscow, 1965).
9. V. A. Klimov, *Basic Micromethods of Analyzing Organic Compounds* (Khimiya, Moscow, 1967).
10. G. M. Sheldrick, *SHELXS86: Program for the Solution of Crystal Structures* (Univ. of Göttingen, Göttingen, 1986).
11. G. M. Sheldrick, *SHELXL93: Program for the Refinement of Crystal Structures* (Univ. of Göttingen, Göttingen, 1993).

Translated by O. Borovik-Romanova

STRUCTURES OF ORGANIC COMPOUNDS

X-ray Structure Investigation of Two Polymorphic Modifications of 1-Acetyl-3-(4-Nitrophenyl)-5-(2'-Furyl)pyrazoline

K. Yu. Suponitskiĭ, D. V. Gusev, L. N. Kuleshova, and M. Yu. Antipin

Nesmeyanov Institute of Organoelement Compounds, Russian Academy of Sciences,

ul. Vavilova 28, Moscow, 119991 Russia

e-mail: lukul@xrlab.ineos.ac.ru

Received July 5, 2001

Abstract—Two polymorphic modifications of 1-acetyl-3-(4-nitrophenyl)-5-(2'-furyl)pyrazoline (**I**) are investigated by X-ray diffraction with the purpose of analyzing the factors responsible for the formation of crystal structures of the optical nonlinear organic compounds. Both modifications crystallize simultaneously upon slow evaporation of a solution of compound **I** in an isopropanol–acetonitrile (3 : 1) mixture. It is found that the molecular geometry of the polymorphic modifications is characterized by the rotation of the furan substituent with respect to the plane of the pyrazoline ring. The molecular hyperpolarizabilities (β) of both conformers are calculated. © 2002 MAIK “Nauka/Interperiodica”.

INTRODUCTION

The ability of organic compounds to form crystal packings (polymorphic modifications) differing in structure and symmetry provides a means of synthesizing new optical nonlinear crystalline materials. In this respect, considerable recent attention has been concentrated on the search for new polymorphic modifications of organic compounds with high molecular hyperpolarizability (β) [1–4]. Among these compounds are different molecular conjugated systems with donor–acceptor substituents. However, the nonlinear optical effect can manifest itself only in crystals with a noncentrosymmetric space group. In particular, Hall *et al.* [1] described the polymorphism of 1-(4-methoxyphenyl)-3-(4-nitrophenyl)pyrazoline with high molecular hyperpolarizability. For this compound, four polymorphic modifications (two of which belong to the noncentrosymmetric space group $P2_1$) were prepared through crystallization from different solvents. For the purpose of analyzing the possible polymorphism of other derivatives of this series, we prepared polymorphic modifications of 1-acetyl-3-(4-nitrophenyl)-5-(2'-furyl)pyrazoline (**I**) and performed an X-ray structure investigation of these compounds.

EXPERIMENTAL

Synthesis and crystallization. 3-(4-Nitrophenyl)-5-(2'-furyl)pyrazoline¹ was synthesized by the condensation of 2-furaldehyde-(4-nitroacetophenone) in an alcohol solution with hydrazine hydrate. Unfortunately, many attempts to prepare high-quality single crystals

were unsuccessful because the compound synthesized was unstable in the majority of the solvents used in our experiments. With the aim of increasing the stability of the product, we synthesized its acyl derivative, namely, 1-acetyl-3-(4-nitrophenyl)-5-(2'-furyl)pyrazoline (**I**). Upon slow evaporation of a solution of **I** in an isopropanol–acetonitrile (3 : 1) mixture, thin light yellow needle-shaped crystals (modification *A*) precipitated simultaneously with light yellow prismatic crystals (modification *B*).

X-ray diffraction analysis. Crystals of modification *A* ($C_{15}H_{13}N_3O_4$) are triclinic; at 110 K, the unit cell parameters are as follows: $a = 6.709(2)$ Å, $b = 8.276(3)$ Å, $c = 13.782(6)$ Å, $\alpha = 72.726(8)^\circ$, $\beta = 89.023(9)^\circ$, $\gamma = 68.799(11)^\circ$, $V = 677.8(4)$ Å³, $d_{\text{calcd}} = 1.466$ g cm⁻³, $Z = 2$, and space group $P\bar{1}$. A set of experimental reflections was collected on a SMART 1000 CCD automated diffractometer (λ MoK α ; graphite monochromator; ω step-scan mode; step width, 0.3° in ω ; scan time, 25 s; $2\theta < 60^\circ$). An analysis of the reciprocal lattice revealed twinned crystals. The contributions of both components were taken into account in the processing of the experimental set of intensities according to the GEMINI program [5]. The structure was solved by the direct method and refined using the full-matrix least-squares procedure in the anisotropic approximation for F_{hkl}^2 . The hydrogen atoms were located from the electron-density difference synthesis and refined in the isotropic approximation. The final discrepancy factors are as follows: $R_1 = 0.1186$, $wR_2 = 0.2800$ for all 5895 unique reflections, and $GOF = 0.814$. The high R factors can be explained by the poor quality of the twinned crystal. The atomic coordinates and isotropic equivalent (iso-

¹The atomic numbering used in this work differs from that accepted in the system of notations recommended by the International Union of Pure and Applied Chemistry (IUPAC).

Table 1. Atomic coordinates ($\text{\AA} \times 10^4$; for H atoms, $\times 10^3$) and isotropic equivalent (isotropic for H atoms) thermal parameters U ($\text{\AA}^2, \times 10^3$) for modification A

Atom	<i>x</i>	<i>y</i>	<i>z</i>	<i>U</i>	Atom	<i>x</i>	<i>y</i>	<i>z</i>	<i>U</i>
N(1)	1643(6)	1781(5)	2627(3)	21(1)	C(12)	-4644(8)	7514(8)	3008(4)	26(1)
N(2)	362(6)	2070(5)	3391(3)	19(1)	C(13)	-4550(8)	6811(8)	4037(4)	27(1)
N(3)	8800(6)	2489(6)	-462(3)	24(1)	C(14)	-945(6)	1111(6)	3743(4)	19(1)
O(1)	-2677(5)	5341(5)	4413(3)	29(1)	C(15)	-778(8)	-406(7)	3330(4)	22(1)
O(2)	-2156(5)	1495(5)	4387(3)	29(1)	H(1)	318(7)	104(6)	100(4)	7(10)
O(3)	8800(6)	1626(6)	-1045(3)	37(1)	H(2)	575(9)	93(8)	-17(5)	29(14)
O(4)	10011(6)	3331(6)	-495(3)	34(1)	H(4)	823(7)	417(6)	95(4)	8(11)
C(1)	4322(7)	1817(7)	1026(4)	21(1)	H(5)	574(8)	430(8)	223(4)	25(15)
C(2)	5837(8)	1701(7)	322(4)	25(1)	H(8A)	169(7)	515(6)	284(3)	0(10)
C(3)	7238(7)	2600(7)	303(3)	20(1)	H(8B)	358(7)	354(7)	370(4)	10(11)
C(4)	7225(7)	3560(7)	962(4)	21(1)	H(9)	109(9)	281(9)	456(5)	36(16)
C(5)	5711(7)	3671(7)	1679(4)	21(1)	H(11)	-258(12)	674(11)	204(6)	60(20)
C(6)	4293(6)	2752(6)	1728(3)	17(1)	H(12)	-553(7)	846(6)	257(4)	0(10)
C(7)	2747(6)	2818(6)	2503(3)	19(1)	H(13)	-545(11)	698(9)	464(5)	46(18)
C(8)	2356(8)	3932(8)	3227(4)	23(1)	H(15A)	-40(12)	-28(11)	277(7)	60(20)
C(9)	525(7)	3511(7)	3799(4)	19(1)	H(15B)	-189(9)	-104(8)	356(5)	33(15)
C(10)	-1555(7)	5141(6)	3577(4)	21(1)	H(15C)	30(11)	-122(9)	382(5)	45(19)
C(11)	-2658(7)	6413(7)	2728(4)	24(1)					

Table 2. Atomic coordinates ($\text{\AA} \times 10^4$) and isotropic equivalent (isotropic for H atoms) thermal parameters U ($\text{\AA}^2, \times 10^3$) for modification B

Atom	<i>x</i>	<i>y</i>	<i>z</i>	<i>U</i>	Atom	<i>x</i>	<i>y</i>	<i>z</i>	<i>U</i>
O(1)	4106(1)	764(1)	7205(1)	36(1)	C(12)	2189(2)	449(1)	5921(2)	42(1)
O(2)	4073(1)	-2114(1)	7737(1)	39(1)	C(13)	2779(2)	1071(1)	6697(2)	40(1)
O(3)	11508(1)	2013(1)	12724(1)	44(1)	C(14)	4747(2)	-1745(1)	8597(1)	31(1)
O(4)	11990(1)	2825(1)	11113(1)	40(1)	C(15)	4749(2)	-2095(1)	9903(1)	36(1)
N(1)	6412(1)	-550(1)	9295(1)	28(1)	H(1)	7694(18)	112(11)	11186(14)	31(4)
N(2)	5562(1)	-981(1)	8383(1)	30(1)	H(2)	9346(19)	1023(12)	12401(16)	42(5)
N(3)	11294(1)	2214(1)	11630(1)	33(1)	H(4)	10767(18)	2237(11)	9243(15)	35(4)
C(1)	8323(2)	540(1)	10805(1)	30(1)	H(5)	9075(18)	1352(11)	8045(15)	34(4)
C(2)	9299(2)	1069(1)	11505(1)	32(1)	H(8A)	7951(18)	-160(11)	7020(14)	31(4)
C(3)	10199(2)	1687(1)	10901(1)	29(1)	H(8B)	6888(18)	665(12)	7081(15)	36(4)
C(4)	10122(2)	1811(1)	9633(1)	31(1)	H(9)	5971(17)	-1036(11)	6554(14)	31(4)
C(5)	9133(2)	1280(1)	8941(1)	31(1)	H(11)	3110(20)	-851(14)	5482(18)	56(6)
C(6)	8240(2)	633(1)	9513(1)	27(1)	H(12)	1260(20)	502(13)	5458(18)	52(5)
C(7)	7227(2)	56(1)	8774(1)	28(1)	H(13)	2480(20)	1664(13)	6978(16)	48(5)
C(8)	7062(2)	76(1)	7383(1)	31(1)	H(15A)	3850(20)	-2422(13)	10028(17)	47(5)
C(9)	5727(2)	-564(1)	7138(1)	29(1)	H(15B)	4810(20)	-1624(15)	10522(19)	59(6)
C(10)	4336(2)	-87(1)	6713(1)	30(1)	H(15C)	5600(30)	-2467(16)	10040(20)	70(7)
C(11)	3199(2)	-306(1)	5927(1)	37(1)					

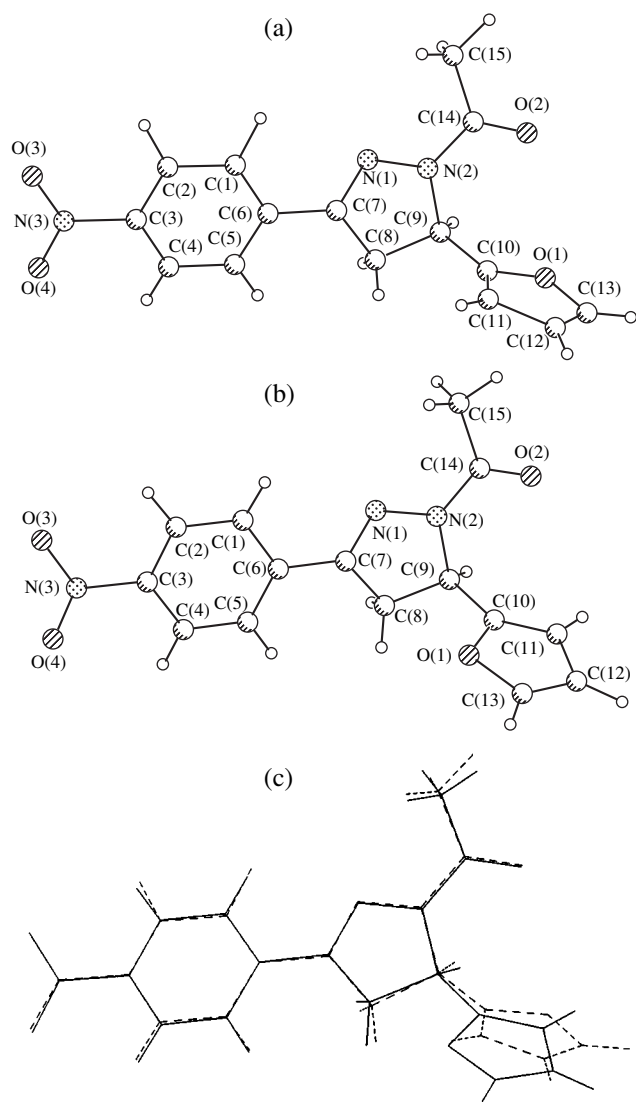


Fig. 1. A general view of molecule **I**: (a) modification *A*, (b) modification *B*, and (c) comparison of the molecular structures in modifications *A* and *B*.

tropic for H atoms) thermal parameters for modification *A* are presented in Table 1.

Crystals of modification *B* ($C_{15}H_{13}N_3O_4$) are monoclinic; at 110 K, the unit cell parameters are as follows: $a = 8.9521(13)$ Å, $b = 14.679(2)$ Å, $c = 10.8300(15)$ Å, $\beta = 91.620(3)^\circ$, $V = 1422.6(3)$ Å³, $d_{\text{calcd}} = 1.397$ g cm⁻³, $Z = 4$, and space group $P2_1/n$. The intensities of 9432 reflections were measured on the same diffractometer (ω step-scan mode; step width, 0.3° in ω ; scan time, 10 s; $2\theta < 60^\circ$). The structure was solved by the direct method and refined using the full-matrix least-squares procedure in the anisotropic approximation for F_{hkl}^2 . The hydrogen atoms were located from the electron-density difference synthesis and refined in the isotropic approx-

imation. The refinement was carried out using 4128 unique reflections ($R_{\text{int}} = 0.0192$). The final discrepancy factors are as follows: $R_1 = 0.0467$ for 3114 reflections with $I > 2\sigma(I)$, $wR_2 = 0.1044$ for all the unique reflections, and $GOF = 0.927$. The atomic coordinates and isotropic equivalent (isotropic for H atoms) thermal parameters for modification *B* are listed in Table 2. All the calculations were performed on an IBM PC AT with the SHELXTL97 software package [6].

Calculation of hyperpolarizability. The molecular hyperpolarizability β was calculated by the finite-field method [7] (included in the MOPAC program package [8]) in the framework of the AM1 parametrization [9]. The data derived from the MOPAC program were processed according to the HYPER program [10] in order to calculate the components of the β tensor. Then, the vector part of the hyperpolarizability was estimated from the β tensor components.

RESULTS AND DISCUSSION

The molecular structures of compound **I** in polymorphic modifications *A* and *B* are displayed in Figs. 1a and 1b, respectively. All the bond lengths and bond angles in molecule **I** correspond to the mean-statistic values [11, 12]. For different polymorphic modifications of compound **I**, the root-mean-square deviations of the relevant geometric parameters of the molecule are within the limits of experimental error. A comparison of the molecular structures of **I** in modifications *A* and *B* is shown in Fig. 1c. For the benefit of clarity, we brought the centers of gravity of molecules *A* and *B* into coincidence according to the OFIT procedure included in the XP software package. As is clearly seen from Fig. 1c, the molecular conformations of both modifications are characterized by a rotation of the furan ring with respect to the plane of the pyrazoline moiety of the molecule. The basic parameters characterizing the structure of molecule **I** are given in Table 3. In both modifications, molecule **I** contains three planar rings. The angles between the planes of the benzene and pyrazoline rings in modifications *A* and *B* are equal to 8.8° and 2.3° , respectively. This suggests that the benzene and pyrazoline rings can be conjugated along the C(6)–C(7)–N(1)–N(2) bonds. This assumption is also confirmed by the following bond lengths: C(7)–N(1), 1.297(6) Å in modification *A* and 1.290(2) Å in modification *B* (for pyrazole, the mean value is 1.329 Å); and N(1)–N(2), 1.369(5) Å in modification *A* and 1.383(2) Å in modification *B* (for pyrazole, the mean value is 1.366 Å). The furan ring is rotated with respect to the planar (conjugated) moiety of the molecule either through 91.7° in modification *A* or through 80.4° in modification *B*.

The differences in the conformations of molecules *A* and *B* bring about the formation of different crystal packings. In modification *A*, the stacks of molecules with a parallel orientation are aligned along the shortest

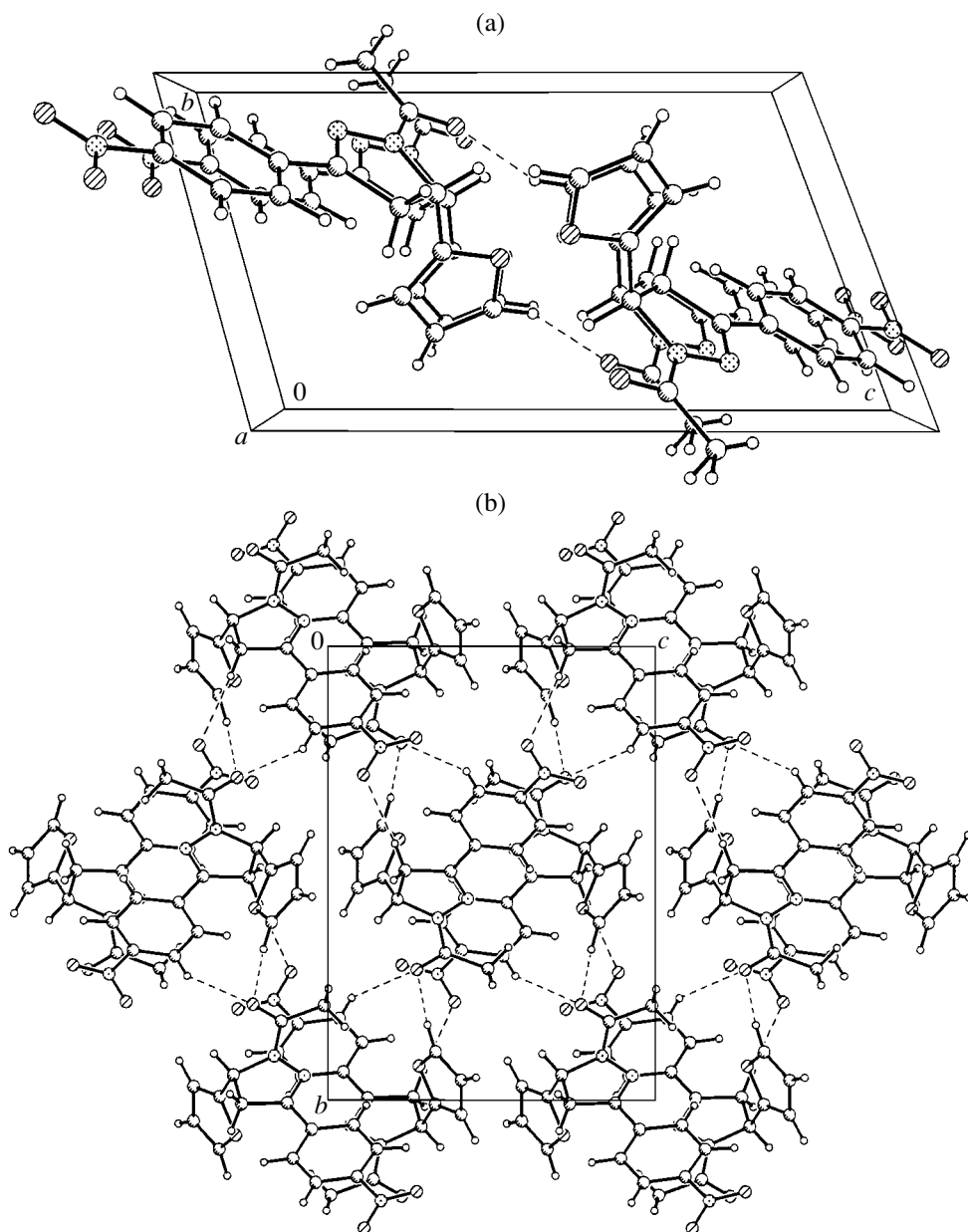


Fig. 2. Molecular packings in crystal I: (a) modification A and (b) modification B.

unit-cell dimension (a). In each stack, the distance between the molecular planes is equal to 2.87 \AA .² The molecules of the adjacent stacks are joined into dimers through the short contacts $C(13)\text{--}H(13)\cdots O(2)$ ($-1-x, 1-y, 1-z$) [$C\cdots O$, $3.313(6) \text{ \AA}$; $H\cdots O$, 2.29 \AA ; and the angle at the H atom is 158°]³ about the centers of symmetry (Fig. 2a). In modification B, the stacks of mole-

cules with an antiparallel orientation are aligned along the crystallographic direction a (Fig. 2b). In each stack, the interplanar distances between the neighboring molecules are different and equal to 3.04 \AA ($1-x, -y, 2-z$) and 3.38 \AA ($2-x, -y, 2-z$). The molecular stacks are linked by the short contacts $C(4)\text{--}H(4)\cdots O(2)$ ($1.5-x, 0.5+y, 1.5-z$) [$C\cdots O$, $3.114(2) \text{ \AA}$; $H\cdots O$, $2.27(2) \text{ \AA}$; and the angle at the H atom is $134(1)^\circ$].

² The root-mean-square plane of the molecule passes through the C(1), C(2), C(3), C(4), C(5), C(6), C(7), C(8), C(9), N(1), N(2), N(3), O(3), and O(4) atoms.

³ The bond lengths and angles for the C–H \cdots O contacts are calculated under the assumption that the C–H distance is equal to 1.08 \AA .

Since the density of crystals A ($d_{\text{calcd}} = 1.466 \text{ g cm}^{-3}$) is considerably higher than the density of crystals B ($d_{\text{calcd}} = 1.397 \text{ g cm}^{-3}$), it is assumed that the former crystals are more thermodynamically stable [13]. However, the calculation of the intermolecular interaction

Table 3. Basic parameters characterizing the molecular structure of **I**

Torsion angle, deg	Modification A	Modification B
N(2)–C(9)–C(10)–C(11)	67.0	–100.7
N(2)–C(9)–C(10)–O(1)	–108.3	78.9
N(1)–N(2)–C(9)–C(10)	–114.7	–110.3
C(14)–N(2)–C(9)–C(10)	65.4	74.0
C(1)–C(6)–C(7)–N(1)	–10.2	–0.9
C(5)–C(6)–C(7)–C(8)	–5.8	–1.5
Root-mean-square plane of the molecule	δ , Å	
C(1), C(2), C(3), C(4), C(5), C(6)	0.009	0.008
N(1), N(2), C(7), C(8), C(9)	0.027	0.009
C(10), C(11), C(12), C(13), O(1)	0.004	0.001

energies in the polymorphic modifications⁴ has demonstrated that the crystal packing of modification A is only slightly more energetically favorable ($E_A = -27.9$ kcal mol⁻¹ and $E_B = -26.7$ kcal mol⁻¹). Moreover, the detailed analysis of the energies of the pair intermolecular contacts has revealed that, despite the shorter interplanar distances between the neighboring molecules in stacks of modification A, the interaction energy inside the molecular stack of this modification (-7.4 kcal mol⁻¹) is higher than those of modification B [-13.1 kcal mol⁻¹ ($1-x, -y, 2-z$) and -11.8 kcal mol⁻¹ ($2-x, -y, 2-z$)]. This difference can be explained by the fact that the skew conformation of the molecules inside the stacks of modification A is more pronounced: the angles between the molecular plane and the *a*-axis in modifications A and B are equal to 28.6° and 47.2°, respectively. However, modification A is characterized by the stronger interaction between the molecular stacks [-8.8 kcal mol⁻¹ ($1-x, 1-y, -z$)]. As a consequence, the gain in the total energy for modification A is approximately equal to 1 kcal mol⁻¹.

In both modifications, the energies of the packings are found to be close to each other. In this respect, it is of interest to compare the intramolecular interaction energies of these conformers. For this purpose, we performed molecular dynamics calculations of the intramolecular energies of both conformers in the framework of the MM3 method [16–18]. We calculated the energies of individual molecules whose geometry corresponded to the geometry of the conformers

⁴ The calculation of the intermolecular interaction energies was performed by the atom–atom potential method using the parametrization proposed by Mirsky [14], which was included in the NONVPOT software package [15].

revealed by X-ray diffraction analysis. The difference in the calculated energies of conformers A and B is found to be small (2 kcal mol⁻¹). It is worth noting that, in modification A, the structure of an individual molecule is less energetically favorable and the molecular packing is more energetically favorable (by 1.2 kcal mol⁻¹) as compared to those in modification B. For these conformations, the barrier to rotation of the furan ring with respect to the C(9)–C(10) bond is equal to 4.0 kcal mol⁻¹. It may be assumed that the molecular structures of modifications A and B are already different in their solutions. In our opinion, it is this circumstance that can lead to the formation of different crystal packings.

CONCLUSIONS

The molecular hyperpolarizabilities (β) have been evaluated using the experimentally established geometries of conformers A and B. The calculated hyperpolarizabilities of these conformers are very close in magnitude: $\beta_A = 34.1 \pm 0.1$ ($\times 10^{-51}$ cm³ B⁻²) and $\beta_B = 33.3 \pm 0.1$ ($\times 10^{-51}$ cm³ B⁻²). This result is not surprising because the difference in the structures of the conjugated moieties is insignificant. Judging from the molecular hyperpolarizabilities obtained in the present work, organic compounds of this class are very promising for the creation of new optical nonlinear materials.

ACKNOWLEDGMENTS

This work was supported by the Russian Foundation for Basic Research, project nos. 00-03-32840a, 00-15-97359, and 01-03-06143.

REFERENCES

1. S. R. Hall, P. V. Kolinsky, R. Jones, *et al.*, *J. Cryst. Growth* **79**, 745 (1986).
2. K. Nakatsu, N. Yoshie, H. Yoshioka, *et al.*, *Mol. Cryst. Liq. Cryst. Sci. Technol., Sect. A* **182**, 59 (1990).
3. F. Pan, C. Bossard, M. S. Wong, *et al.*, *Chem. Mater.* **9**, 1328 (1997).
4. A. Gleixner, J. Hiller, T. Debaerdemaeker, *et al.*, *Z. Kristallogr.* **213**, 411 (1998).
5. *GEMINI: Autoindexing Program for Twinned Crystals. Version 1.0, Release 10/1999, Copyright* (Bruker AXT, Madison, 1999).
6. G. M. Sheldrick, *SHELXTL97, Version 5.10: An Integrated System for Solving, Refining and Displaying Crystal Structures from Diffraction Data* (Bruker AXS, Madison, 1997).
7. H. A. Kurtz, J. J. P. Stewart, and K. M. Dieter, *J. Comput. Chem.* **11**, 82 (1990).
8. *QCPE MOPAC: Quantum Chemistry Program Exchange. Version 6* (1990).
9. M. J. S. Dewar, E. G. Zoebish, E. F. Healy, and J. J. P. Stewart, *J. Am. Chem. Soc.* **107**, 3902 (1985).

10. B. H. Cardelino, C. E. Moore, and R. E. Stickel, *J. Phys. Chem.* **95**, 8645 (1991).
11. F. H. Allen, O. Kennard, D. G. Watson, *et al.*, *J. Chem. Soc., Perkin Trans. 2*, No. 12, S1 (1987).
12. A. G. Orpen, L. Brammer, F. H. Allen, *et al.*, *J. Chem. Soc., Dalton Trans.* 1, S1 (1989).
13. A. I. Kitaigorodsky, *Molecular Crystals* (Nauka, Moscow, 1971).
14. K. Mirsky, in *Computing in Crystallography: Proceedings of the International Summer School in Crystallographic Computing* (Delft Univ. Press, Twente, 1978), p. 169.
15. V. I. Shil'nikov, *Kristallografiya* **39**, 647 (1994) [*Crystallogr. Rep.* **39**, 581 (1994)].
16. N. L. Allinger, Y. H. Yuh, and J.-H. Lii, *J. Am. Chem. Soc.* **111**, 8551 (1989).
17. J.-H. Lii and N. L. Allinger, *J. Am. Chem. Soc.* **111**, 8566 (1989).
18. J.-H. Lii and N. L. Allinger, *J. Am. Chem. Soc.* **111**, 8576 (1989).

Translated by O. Borovik-Romanova

STRUCTURES
OF ORGANIC COMPOUNDS

**X-ray Diffraction Study of the First Monomeric Dioxygermylene
Ge(OCH₂CH₂NMe₂)₂ Stabilized by Two Ge ← N Intramolecular
Coordination Bonds: The Influence of Ge ← N Intramolecular
Coordination Bonds on the Structure
and Packing of Molecules in Crystals**

V. N. Khrustalev*, I. V. Borisova**, N. N. Zemlyansky**,
Yu. A. Ustynyuk***, and M. Yu. Antipin*

* Nesmeyanov Institute of Organoelement Compounds, Russian Academy of Sciences,
ul. Vavilova 28, Moscow, GSP-1, 119991 Russia
e-mail: vkh@xrlab.ineos.ac.ru

** State Research Center of Russian Federation "State Research Institute of Chemistry and Technology
of Organoelement Compounds," sh. Ėntuziastov 38, Moscow, 111123 Russia
e-mail: zemlyan@mail.cnt.ru

*** Moscow State University, Vorob'evy gory, Moscow, 119899 Russia
e-mail: yust@nmr.chem.msu.su

Received October 29, 2001

Abstract—The molecular and crystal structures of the first monomeric dioxygermylene Ge(OCH₂CH₂NMe₂)₂ (**I**) stabilized by two Ge ← N intramolecular coordination bonds are determined by X-ray diffraction analysis. The Ge ← N bond lengths in two independent molecules are equal to 2.329(2), 2.337(2) and 2.324(2), 2.346(2) Å, respectively. The central germanium atom plays the role of a spiro atom between two five-membered heterocycles in the envelope conformation and adopts a trigonal-bipyramidal configuration with a lone electron pair in the equatorial position. Compound **I** has two planar-chiral isomers which crystallize jointly. Molecules in the crystal have a layered packing (molecular layers are perpendicular to the [001] direction) composed of four translationally independent equivalent layers. These layers are spaced at 1/4*c* intervals and displaced with respect to each other by approximately +0.35*a*, −1/4*b*, −0.35*a*, and +1/4*b*, respectively. The characteristic displacement of the layers and their proper symmetry (*pb*2) that differs from the symmetry of the crystal (space group *P*₂₁₂₁) determine a large variety of pseudosymmetry operations. © 2002 MAIK "Nauka/Interperiodica".

INTRODUCTION

In recent years, considerable interest has been expressed by researchers in compounds of Group IVA bivalent elements, which possess unique chemical properties but are unstable under normal conditions. This interest is associated with the successful development of techniques for stabilizing these compounds through steric and electronic mechanisms. The steric stabilization consists in screening *M*(II) atoms by bulky substituents. In the case of electronic stabilization, the *M*(II) atoms are involved in a system of conjugated bonds or different coordination interactions. More than 100 monomeric compounds of bivalent germanium, tin, and lead have been known to date [1], the majority of which have been synthesized over the last five years. Among them, 20 compounds belong to oxygen-containing compounds [2–17]. However, monomeric oxygen-containing compounds of bivalent germanium, tin, and lead, as a rule, can be obtained only

using a combined approach to their stabilization. Note that, in this case, the steric stabilization plays a decisive role. In the present work, we undertook an X-ray structure investigation of the first monomeric dioxygermylene Ge(OCH₂CH₂NMe₂)₂ (**I**) stabilized by two Ge ← N intramolecular coordination bonds. The specific feature of dioxygermylene **I** is the absence of steric stabilization.

EXPERIMENTAL

Crystals **I** (C₈H₂₀GeN₂O₂, *M* = 248.85) are orthorhombic, space group *P*₂₁₂₁; at 110 K: *a* = 10.1606(12) Å, *b* = 11.2693(14) Å, *c* = 20.387(2) Å, *V* = 2334.3(5) Å³, *Z* = 8, *d*_{calcd} = 1.416 g cm^{−3}, *F*(000) = 1040, and *μ* = 2.601 mm^{−1}.

The unit cell parameters and intensities of 27 535 reflections were measured on a Bruker SMART CCD 1000 automated diffractometer (*T* = 110 K,

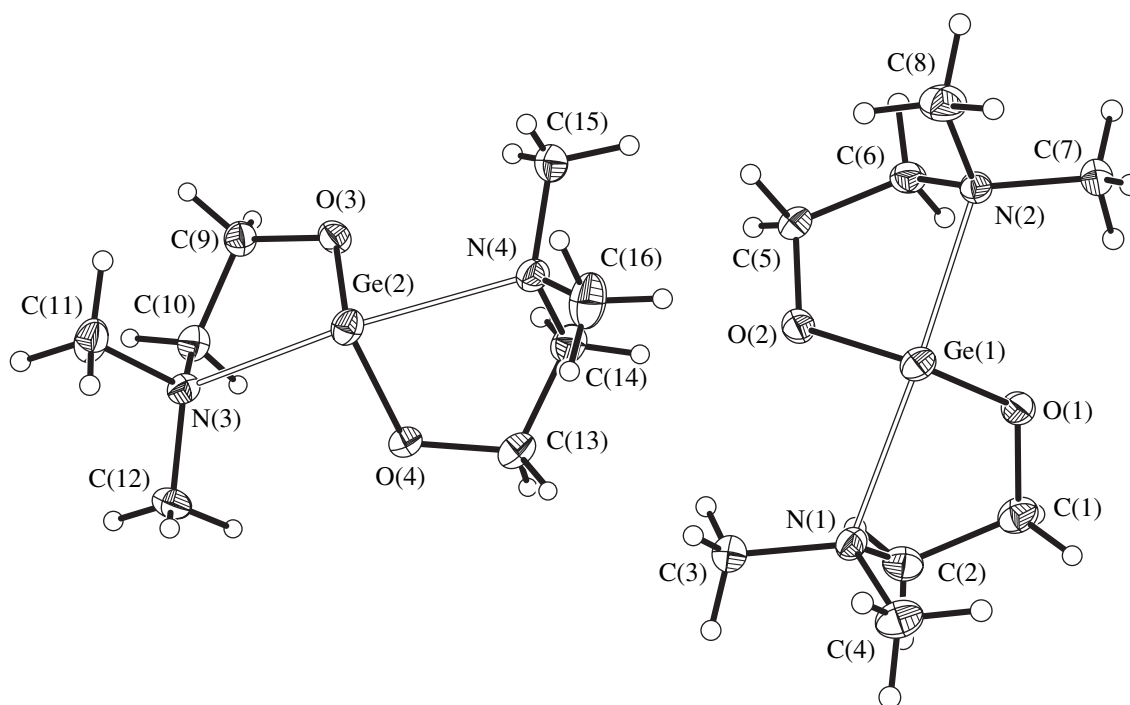


Fig. 1. Molecular structure of compound **I**. Two independent molecules with anisotropic displacement ellipsoids at the 50% probability level are shown.

$\lambda\text{MoK}\alpha$, ω scan mode with a step of 0.3° and an exposure time of 10 s per frame, $\theta_{\text{max}} = 30^\circ$). Absorption correction was semiempirically included in calculations with the SADABS program [18]. The structure was solved by the direct method and refined by the full-matrix least-squares procedure in the anisotropic approximation for the non-hydrogen atoms. The hydrogen atoms were located in the difference Fourier map and refined in the isotropic approximation. The absolute structure was determined by refining the Flack parameter, which was equal to 0.003(7). The final discrepancy factors were as follows: $R_1 = 0.0230$ for 5412 unique reflections with $I > 2\sigma(I)$ and $wR_2 = 0.0449$ for all 6786 independent reflections. All the calculations were performed with the SHELXTL PLUS (Version 5.10) software package [19]. Tables of atomic coordinates, bond

lengths, bond and torsion angles, and anisotropic thermal parameters have been deposited in the Cambridge Structural Database.

RESULTS AND DISCUSSION

The X-ray diffraction investigation has revealed that the dioxygermylene $\text{Ge}(\text{OCH}_2\text{CH}_2\text{NMe}_2)_2$ has a monomeric structure and is stabilized by two $\text{Ge}(\text{II}) \leftarrow \text{N}$ intramolecular coordination bonds. The lengths of these bonds [for two independent molecules, 2.329(2), 2.337(2) and 2.324(2), 2.346(2) Å, respectively] considerably exceed the lengths of all the known $\text{Ge}(\text{II}) \leftarrow \text{N}$ coordination bonds (Table 1) [1]. Analysis of the data available in the Cambridge Structural Database for germylenes, stannylenes, and plumbylenes stabilized by $M(\text{II}) \leftarrow \text{N}$ coordination bonds demonstrates that the

Table 1. Mean lengths* (Å) of the $M(\text{II}) \leftarrow \text{N}$ intramolecular coordination bonds in $\text{Ge}(\text{II})$, $\text{Sn}(\text{II})$, and $\text{Pb}(\text{II})$ monomeric compounds

$M(\text{II}) \leftarrow \text{N}$	N_{ar} (one bond)	N_{ar} (two bonds)	N_{sp^3} (one bond)	N_{sp^3} (two bonds)
$\text{Ge}(\text{II})$	2.082 [20]	2.280 [21, 22]	2.116 [23–25]**	2.334 [this work]
$\text{Sn}(\text{II})$	2.300 [20, 27, 28]	2.441 [16, 17, 21, 27]	2.370 [29–33]	2.538 [10, 34–37]
$\text{Pb}(\text{II})$		2.601 [21, 38, 39]***		2.695 [41]

* In all experiments, the error in measurements of the $M(\text{II}) \leftarrow \text{N}$ bond lengths does not exceed 0.008 Å.

** Data for the $(\text{NMe}_2\text{CH}_2\text{CH}_2)\text{Me}_4\text{CpGeCl}$ [26] compound [26] with the $\text{Cp}-\text{Ge}(\text{II})$ π bond are not included. In this compound, the $\text{Ge}(\text{II}) \leftarrow \text{N}$ distance is equal to 2.286(3) Å.

*** Data for lead 8-mercaptoquinolinolate [40] are not included because of the very low accuracy of the experiment ($R = 0.131$).

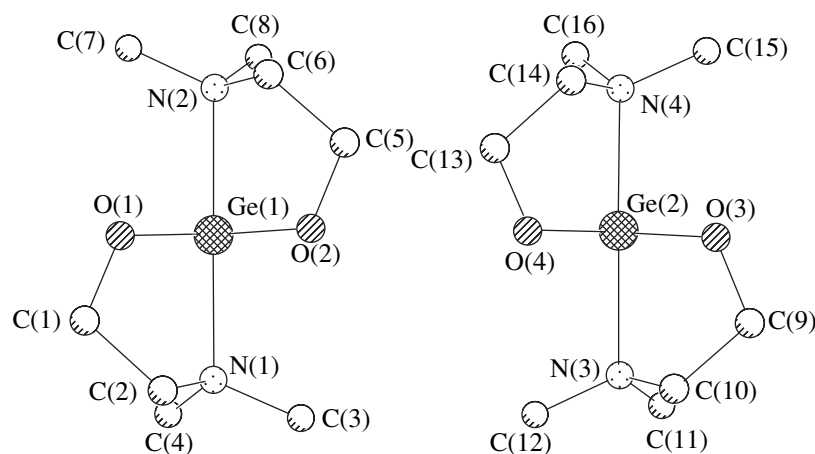


Fig. 2. Planar-chiral isomers of compound **I**.

lengthening of the $M(\text{II}) \leftarrow N_{sp^3}$ coordination bonds as compared to the $M(\text{II}) \leftarrow N_{ar}$ bonds and the lengthening of the $M(\text{II}) \leftarrow N$ coordination bonds for the fourfold-coordinated $M(\text{II})$ atom as compared to the $M(\text{II}) \leftarrow N$ bonds for the threefold-coordinated $M(\text{II})$ atom are common structural features of these compounds (Table 1). It should be noted that, although the range of $M(\text{II}) \leftarrow N$ intermolecular coordination bond lengths is wider than that of $M(\text{II}) \leftarrow N$ intramolecular coordination bond lengths, the mean lengths of coordination bonds of both types are very close to each other [1]. It is of interest that $\text{Sn}(\text{II})$ and $\text{Pb}(\text{II})$ compounds stabilized by two $M(\text{II}) \leftarrow N_{sp^3}$ coordination bonds have a common structural feature: in all these compounds, the lengths of the formally equivalent $M(\text{II}) \leftarrow N_{sp^3}$ bonds in identical axial positions are not equal; on the contrary, they differ significantly from each other. However, these bond lengths level off when the lone electron pair of the $M(\text{II})$ atom is bound by different acceptors, such as BH_3 [25] or transition metals [34, 36, 42, 43].

The $\text{Ge}(\text{II})\text{--O}$ bond lengths [1.864(1), 1.868(1) and 1.861(1), 1.870(1) Å in two independent molecules] in compound **I** virtually coincide with the corresponding bond lengths in the dioxygermylenes studied earlier in [4, 12, 14].

Table 2. Coordinates of one of the Ge atoms in four translationally independent layers

Atom	<i>x</i>	<i>y</i>	<i>z</i>
Ge(1) (first layer)	0.0748(1)	0.6385(1)	0.1540(1)
Ge(2) (second layer)	0.4205(1)	0.6257(1)	0.3473(1)
Ge(1) (third layer)	0.4252(1)	0.3615(1)	0.6540(1)
Ge(2) (fourth layer)	0.0795(1)	0.3743(1)	0.8473(1)

The central germanium atom plays the role of a spiro atom between two five-membered heterocycles in the envelope conformation and has a trigonal-bipyramidal configuration with a lone electron pair in the equatorial position. The bond angles in molecule **A** are as follows: $\text{O}(1)\text{--Ge}(1)\text{--O}(2) = 98.79(6)^\circ$, $\text{O}(1)\text{--Ge}(1)\text{--N}(1) = 80.78(6)^\circ$, $\text{O}(1)\text{--Ge}(1)\text{--N}(2) = 83.89(6)^\circ$, $\text{O}(2)\text{--Ge}(1)\text{--N}(1) = 84.21(6)^\circ$, $\text{O}(2)\text{--Ge}(1)\text{--N}(2) = 80.48(6)^\circ$, and $\text{N}(1)\text{--Ge}(1)\text{--N}(2) = 156.38(6)^\circ$. The bond angles in molecule **B** are as follows: $\text{O}(3)\text{--Ge}(2)\text{--O}(4) = 98.91(7)^\circ$, $\text{O}(3)\text{--Ge}(2)\text{--N}(3) = 81.00(6)^\circ$, $\text{O}(3)\text{--Ge}(2)\text{--N}(4) = 83.85(6)^\circ$, $\text{O}(4)\text{--Ge}(2)\text{--N}(3) = 84.00(6)^\circ$, $\text{O}(4)\text{--Ge}(2)\text{--N}(4) = 80.22(6)^\circ$, and $\text{N}(3)\text{--Ge}(2)\text{--N}(4) = 156.11(6)^\circ$. Owing to the formation of the $\text{Ge}(\text{II}) \leftarrow N$ intramolecular coordination bonds, compound **I** has two planar-chiral isomers which crystallize jointly (Fig. 2). It is worth noting that each isomer can have three conformers, namely, two *cis* and one *trans* conformers with respect to the deviations of the C(2) and C(6) atoms in molecule **A** and the C(10) and C(14) atoms in molecule **B** from the planes of the corresponding heterocycles. However, only one *cis* conformer can exist in the crystal [the deviations of the C(2), C(6), C(10), and C(14) atoms from the planes of the corresponding heterocycles are equal to -0.546 , -0.565 , -0.555 , and -0.555 Å, respectively]. Apparently, this stems from the fact that the free lone electron pair of the Ge atom tends to occupy the maximum volume in the space, thus giving rise to steric interactions responsible for the conformation observed in molecules of compound **I**.

Most likely, it is this structure of molecules **I** that determines their layered packing in the crystal (the layers are perpendicular to the [001] direction). This packing involves four translationally independent equivalent layers, which are spaced at $1/4c$ intervals and displaced with respect to each other by approximately $+0.35a$, $-1/4b$, $-0.35a$, and $+1/4b$, respectively (Fig. 3, Table 2). The layers are arranged in pairs in such a manner that the lone electron pairs of the germanium atoms

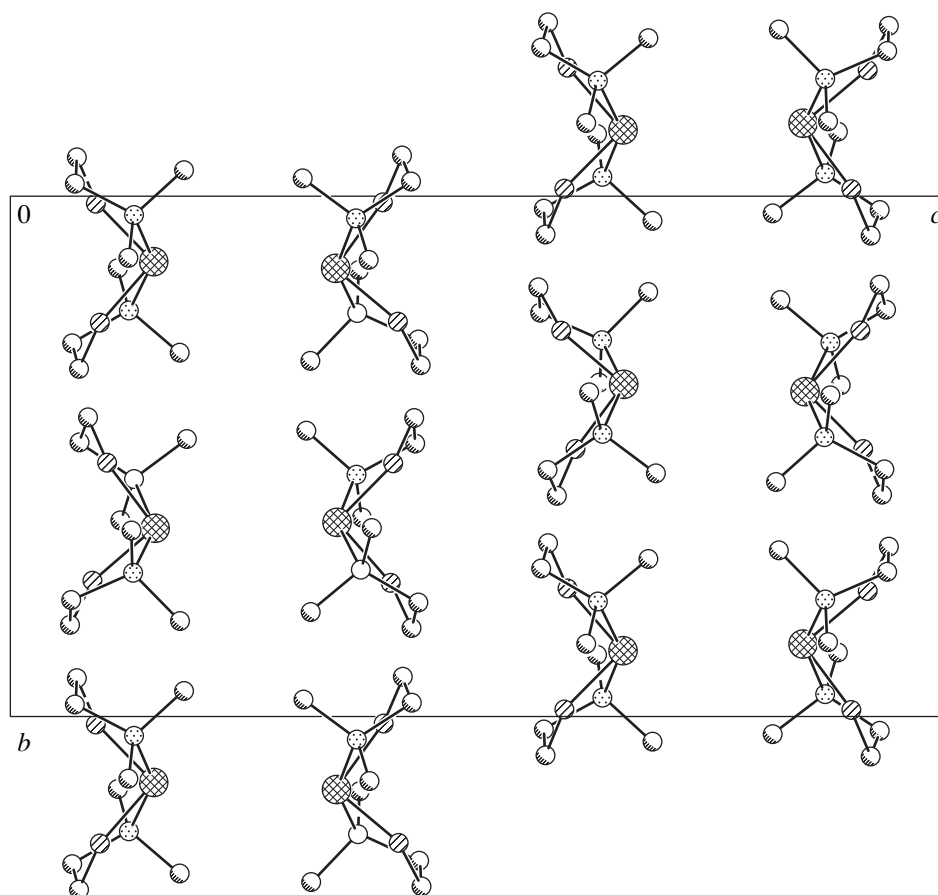


Fig. 3. Layered packing of molecules I in the crystal.

are directed toward each other. With due regard for the characteristic displacement of the layers, this picture resembles an engagement of gears (in which lone electron pairs of the germanium atoms in molecules of each

layer serve as teeth). In pairs of the layers thus arranged, the direction of tooth engagement alternately changes to mutually perpendicular. This gives four translationally independent layers. As a result, the

Table 3. Determination of the space group of symmetry of crystal I

Reflections	<i>P</i>	<i>A</i>	<i>B</i>	<i>C</i>	<i>I</i>	<i>F</i>
<i>N</i> (total)	0	13880	13875	13853	13873	20804
<i>N</i> (<i>I</i> > 3σ)	0	8902	8866	5956	8837	11862
$\langle I \rangle$	0.0	12.2	12.2	2.8	12.1	9.0
$\langle I/\sigma \rangle$	0.0	12.3	12.2	5.1	12.2	9.9

$|E^2 - 1| = 0.972$ (for centrosymmetric and noncentrosymmetric structures, the expected values are equal to 0.968 and 0.736, respectively)

Reflections	b--	c--	n--	2₁--	-c-	-a-	-n-	-2₁-	--a	--b	--n	--2₁
<i>N</i> (total)	791	784	789	18	717	714	715	20	398	402	400	36
<i>N</i> (<i>I</i> > 3σ)	358	453	451	2	301	79	304	0	250	247	165	1
$\langle I \rangle$	1.9	20.6	20.5	0.1	15.0	0.4	15.1	0.1	20.0	20.2	2.9	0.2
$\langle I/\sigma \rangle$	4.4	13.8	13.7	0.8	12.2	1.2	12.3	0.5	16.5	17.1	6.0	1.0

Note: *N* is the number of reflections violating the given element of symmetry, and *I* is the intensity of reflections. Elements of pseudosymmetry are marked in bold type.

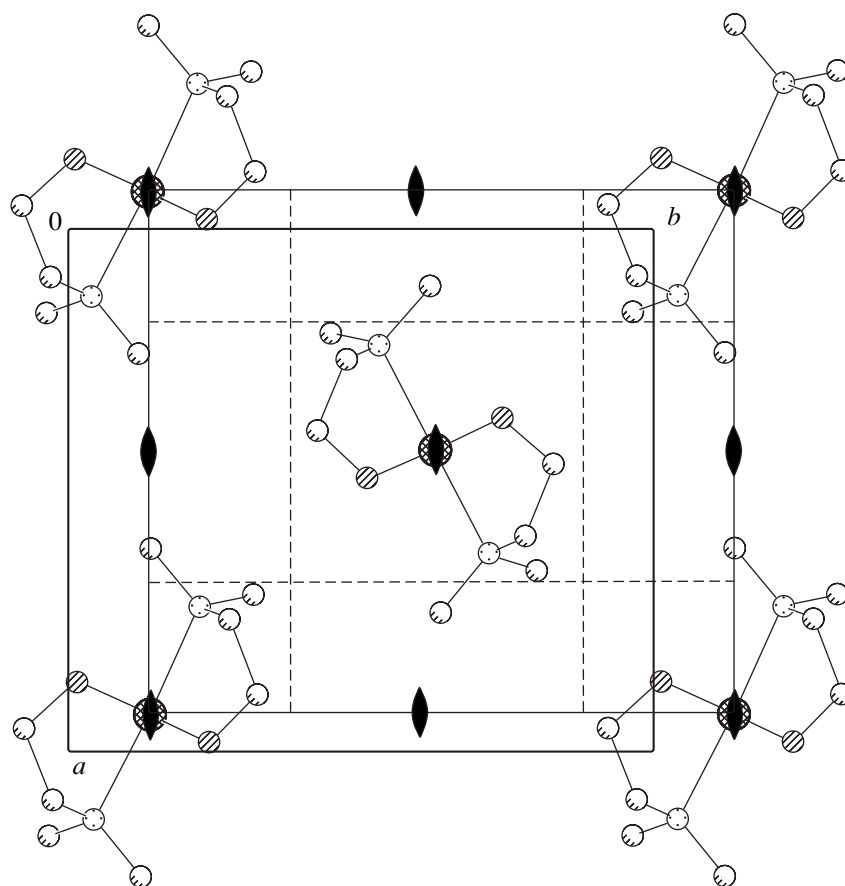


Fig. 4. Structure and symmetry of layers in crystal I. The heavy line indicates the true unit cell.

methylene fragments of molecules in one pair of layers are brought into the free space (cavities) of molecules in another pair, which provides a closer packing (Fig. 3).

It should be noted that the molecules have the proper symmetry 2, whereas the layers formed by the molecules are characterized by $pba2$ symmetry (Fig. 4), which differs from the symmetry of the crystal due to the displacement of the layers with respect to each other. As a consequence, there exist a large number of pseudosymmetry operations, which, in particular, manifest themselves in pseudoabsences of the corresponding reflections (Table 3). The decrease observed in the intensities of the reflections that correspond to the Bravais body-centered C cell and the n glide reflection plane is determined by the position of the heavy germanium atom. The decrease in the intensities of the reflections attributed to the Bravais face-centered F cell and the possible occurrence of the inversion center is governed by the mutual arrangement of the layers. The decrease in the intensities of the reflections assigned to the a and b glide reflection planes is associated with the proper symmetry of the layers. The absence of the reflections corresponding to the 2_1 screw axes is caused by the proper symmetry of the crystal lattice. In the case

of the layers arranged precisely above each other without displacement, the crystal lattice should possess $Pbam$ symmetry. However, the steric interactions in this situation should lead to an increase in the interlayer spacing, which would result in a looser packing.

Crystal structure I is one more prominent example of a layered three-dimensional molecular packing described by Britton [44]. This packing is responsible for different pseudosymmetry operations in crystals of chemical compounds which, as a rule, possess proper symmetry elements.

ACKNOWLEDGMENTS

This work was supported by the Russian Foundation for Basic Research, project nos. 00-03-32807a, 00-15-97359, and 01-03-06143.

REFERENCES

1. F. H. Allen and O. Kennard, *Chem. Design Autom. News* **8** (1), 31 (1993); *Cambridge Crystallographic Database: Release 2001* (Cambridge, 2001).
2. M. B. Cingi, A. G. Manfredotti, C. Guastini, and A. Musatti, *Gazz. Chim. Ital.* **105**, 117 (1975).

3. P. F. R. Ewings, P. G. Harrison, and A. Mangia, *J. Organomet. Chem.* **114**, 35 (1976).
4. T. Fjeldberg, P. B. Hitchcock, M. F. Lappert, *et al.*, *Chem. Commun.*, 939 (1985).
5. G. Bettermann and A. J. Arduengo, *J. Am. Chem. Soc.* **110**, 877 (1988).
6. A. M. van den Bergen, J. D. Cashion, G. D. Fallon, and B. O. West, *Aust. J. Chem.* **43**, 1559 (1990).
7. H. Braunschweig, R. W. Chorley, P. B. Hitchcock, and M. F. Lappert, *Chem. Commun.*, 1311 (1992).
8. D. M. Barnhart, D. L. Clark, and J. G. Watkin, *Acta Crystallogr., Sect. C: Cryst. Struct. Commun.* **50**, 702 (1994).
9. P. C. Christidis, I. A. Tossidis, and C. A. Hondroudis, *Z. Kristallogr.* **209**, 975 (1994).
10. D. A. Atwood, J. A. Jegier, K. J. Martin, and D. Rutherford, *J. Organomet. Chem.* **503**, C4 (1995).
11. J. Parr, A. T. Ross, and A. M. Z. Slawin, *J. Chem. Soc., Dalton Trans.*, 1509 (1996).
12. Suh Seigi and D. M. Hoffman, *Inorg. Chem.* **35**, 6164 (1996).
13. A. Castineiras, R. Domínguez, L. Bresolin, *et al.*, *Z. Naturforsch. B* **53**, 81 (1998).
14. T. Hascall, A. L. Rheingold, I. Guzei, and G. Parkin, *Chem. Commun.*, 101 (1998).
15. M. C. Kuchta, J. M. Hahn, and G. Parkin, *J. Chem. Soc., Dalton Trans.*, 3559 (1999).
16. C. Kitamura, A. Yoneda, K.-I. Sugiura, and Y. Sakata, *Acta Crystallogr., Sect. C: Cryst. Struct. Commun.* **55**, 876 (1999).
17. C. Kitamura, N. Maeda, N. Kamada, *et al.*, *J. Chem. Soc., Perkin Trans. 1*, 781 (2000).
18. G. M. Sheldrick, *SADABS, Version 2.01: Bruker / Siemens Area Detector Absorption Correction Program* (Bruker AXS, Madison, 1998).
19. G. M. Sheldrick, *SHELXL97, Version 5.10: An Integrated System for Solving, Refining, and Displaying Crystal Structures from Diffraction Data* (Bruker AXS, Madison, 1997).
20. S. Benet, C. J. Cardin, D. J. Cardin, *et al.*, *Organometallics* **18**, 389 (1999).
21. Leung Wing-Por, Kwok Wai-Him, Weng Lin-Hong, *et al.*, *J. Chem. Soc., Dalton Trans.*, 4301 (1997).
22. G. Ossig, A. Meller, C. Bronneke, *et al.*, *Organometallics* **16**, 2116 (1997).
23. M. Veith, P. Hobein, and R. Rosler, *Z. Naturforsch. B* **44**, 1067 (1989).
24. H. Schmidt, S. Keitemeyer, B. Neumann, *et al.*, *Organometallics* **17**, 2149 (1998).
25. C. Drost, P. B. Hitchcock, and M. F. Lappert, *Organometallics* **17**, 3838 (1998).
26. P. Jutzi, H. Schmidt, B. Neumann, and H.-G. Stammer, *J. Organomet. Chem.* **499**, 7 (1995).
27. B. S. Jolly, M. F. Lappert, L. M. Engelhardt, *et al.*, *J. Chem. Soc., Dalton Trans.*, 2653 (1993).
28. C. J. Cardin, D. J. Cardin, S. P. Constantine, *et al.*, *J. Chem. Soc., Dalton Trans.*, 2749 (1998).
29. A. Tzschach, K. Jurkschat, M. Scheer, *et al.*, *J. Organomet. Chem.* **259**, 165 (1983).
30. M. Veith, M. Jarczyk, and V. Huch, *Chem. Ber.* **121**, 347 (1988).
31. M. Veith, M. Olbrich, W. Shihua, and V. Huch, *J. Chem. Soc., Dalton Trans.*, 161 (1996).
32. M. Veith, B. Schillo, and V. Huch, *Angew. Chem., Int. Ed. Engl.* **38**, 182 (1999).
33. J.-L. Faure, H. Gornitzka, R. Reau, *et al.*, *Eur. J. Inorg. Chem.*, 2295 (1999).
34. K. Angermund, K. Jonas, C. Kruger, *et al.*, *J. Organomet. Chem.* **353**, 17 (1988).
35. J. T. B. H. Jastrzebski, P. A. van der Schaaf, J. Boersma, *et al.*, *Organometallics* **8**, 1373 (1989).
36. J. T. B. H. Jastrzebski, P. A. van der Schaaf, J. Boersma, *et al.*, *J. Organomet. Chem.* **367**, 55 (1989).
37. J. E. Anderson, S. M. Sawtelle, J. S. Thompson, *et al.*, *Inorg. Chem.* **31**, 2778 (1992).
38. L. Ya. Pech, V. S. Fundamentskii, Ya. K. Ozols, *et al.*, *Latv. PSR Zinat. Akad. Vestis, Khim. Ser.*, 394 (1985).
39. L. Pech, Yu. Bankovskii, V. Fundamentskii, *et al.*, *Latv. Khim. Zh.*, 488 (1992).
40. V. M. Agre and E. A. Shugam, *Zh. Strukt. Khim.* **12**, 102 (1971).
41. N. Seidel, K. Jacob, A. A. H. van der Zeijden, *et al.*, *Organometallics* **19**, 1438 (2000).
42. H.-P. Abicht, K. Jurkschat, A. Tzschach, *et al.*, *J. Organomet. Chem.* **326**, 357 (1987).
43. J. T. B. H. Jastrzebski, H. A. Sypkens, F. J. A. des Tombe, *et al.*, *J. Organomet. Chem.* **396**, 25 (1990).
44. D. Britton, *Acta Crystallogr., Sect. B: Struct. Sci.* **56**, 828 (2000).

Translated by O. Borovik-Romanova

STRUCTURES OF ORGANIC COMPOUNDS

X-ray Mapping in Heterocyclic Design: VIII. Synthesis and X-ray Diffraction Study of Dimethyl 3-(*p*-Chlorobenzoyl)-5-Chloroindolizine-1,2-Dicarboxylate and the Product of Its Cyclization 1,2-Bis(carbomethoxy)-6-Chloro-3*H*-Isoquinolino[1,2,3-*d,c*]indolizine-3-one

V. B. Rybakov, E. V. Babaev, and K. Yu. Pasichnichenko

Faculty of Chemistry, Moscow State University, Vorob'evy gory, Moscow, 119899 Russia

e-mail: rybakov@biocryst.phys.msu.su

Received December 19, 2001

Abstract—Dimethyl 3-(*p*-chlorobenzoyl)-5-chloroindolizine-1,2-dicarboxylate, $C_{19}H_{13}Cl_2NO_5$, (**2**) and the product of its cyclization 1,2-bis(carbomethoxy)-6-chloro-3*H*-isoquinolino[1,2,3-*d,c*]indolizine-3-one, $C_{19}H_{12}ClNO_5$, (**3**) are synthesized, and their molecular and crystal structures are determined by the single-crystal X-ray diffraction technique. Crystals **2** are monoclinic, $a = 9.627(3)$ Å, $b = 6.646(2)$ Å, $c = 28.500(9)$ Å, $\beta = 98.72(2)^\circ$, $Z = 4$, and space group $P2_1/c$. Crystals **3** are monoclinic, $a = 7.048(4)$ Å, $b = 10.582(4)$ Å, $c = 21.760(7)$ Å, $\beta = 97.23(4)^\circ$, $Z = 4$, and space group $P2_1/c$. The structures are solved by the direct method and refined in the anisotropic approximation by the full-matrix least-squares procedure to $R = 0.0504$ and 0.0510 for **2** and **3**, respectively. In both structures, the intramolecular and intermolecular contacts involving the C, H, and O atoms are observed. © 2002 MAIK "Nauka/Interperiodica".

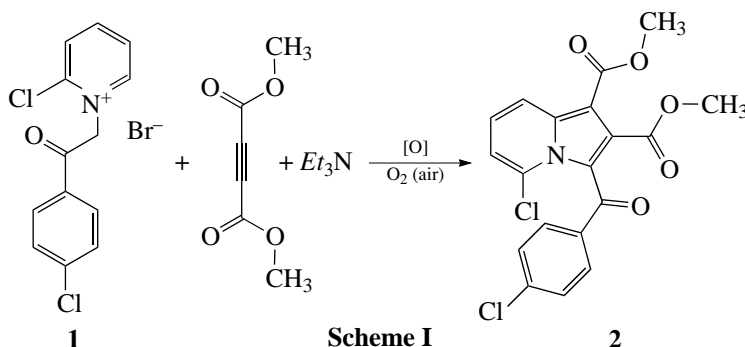
INTRODUCTION

This paper continues our structural investigations of heterocyclic compounds that are able to enter readily into various rearrangements and reactions of ring transformations [1–14]. As in the previous studies, we have performed the step-by-step structure determination of all the intermediates and the final products of the multistage cyclization and recyclization reactions. Note that data on the molecular structures discussed in this

paper are not available in the Cambridge Structural Database [15].

EXPERIMENTAL

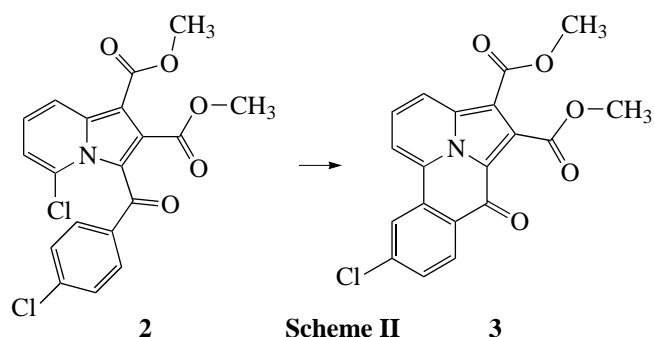
Synthesis. Indolizine **2** was synthesized by the reaction between the pyridinium salt **1** and dimethyl acetylenedicarboxylate according to the following scheme:



Salt **1** (1.5 g, 4.32 mmol) and dimethyl acetylenedicarboxylate (0.642 g, 4.52 mmol) were dissolved in dry dimethylformamide (*DMF*) (17 ml) on heating to 40°C . After the solution was cooled to room temperature, absolute Et_3N (0.496 g, 4.91 mmol) was added to it.

The resultant reddish brown solution was allowed to stand for a day at room temperature and was then poured into water (400 ml) on stirring. The precipitate was filtered off, washed with water (5×30 ml), and dried. The resultant greenish amorphous powder was

dissolved in a minimum amount of *MeOH*, the solution was passed through a column filled with SiO_2 (Silpearl, $l_{\text{col}} = 5$ cm, $d_{\text{col}} = 2$ cm, *MeOH* as an eluent) in order to remove impurities of resins and *DMF*, the eluate was evaporated to dryness, and the residue (1.70 g, 96.8%) was purified by column chromatography on SiO_2 (Silpearl, $l_{\text{col}} = 8$ cm, $d_{\text{col}} = 1.5$ cm, benzene : acetone = 10 : 1 as an eluent). The yellow substance obtained was indolizine **2**, $T_{\text{mp}} = 175\text{--}177^\circ\text{C}$ (*MeOH*). The yield was 0.71 g (40%). The ^1H NMR spectrum agrees with the formula assigned to this substance. Indolizine **2** is unstable: on long standing or under the effect of aluminum oxide, this compound undergoes an intramolecular cyclization. We found that the product of this cyclization has a tetracyclic structure of **3**:



A weighed portion of **2** (20 mg) was dissolved in CHCl_3 (20 ml), Al_2O_3 [0.5 g; for chromatography, activity grade III (Brockman)] was added to the solution, and the solvent was evaporated to dryness. Aluminum oxide with the substance absorbed was allowed to stand at room temperature for two days and was then treated twice with CHCl_3 (20 ml). The extract was

evaporated. The yield of **3** was 15 mg (83%); $T_{\text{mp}} = 193\text{--}194^\circ\text{C}$.

X-ray diffraction analysis. The data sets for X-ray analysis were collected at room temperature on an Enraf–Nonius CAD4 four-circle automated diffractometer (MoK_α radiation, graphite monochromator, ω -2 θ scan mode) [16]. The unit cell parameters were determined and refined using 25 reflections in the θ range $14^\circ\text{--}16^\circ$. The crystal data for compounds **2** and **3** are summarized in Table 1. The crystals of the compounds studied are small in size and are characterized by small linear absorption coefficients; therefore, the empirical absorption correction was not applied.

The primary processing of the sets of diffraction data was performed with the WinGX98 program [17]. The structures were solved by the direct method. The coordinates and thermal parameters for all the non-hydrogen atoms were refined in the anisotropic approximation. All the calculations on the solution and refinement of the crystal structures were performed with the SHELX97 program package [18]. All the hydrogen atoms in both structures were located from the difference Fourier syntheses and refined in the isotropic approximation of thermal parameters. The atomic coordinates and equivalent thermal parameters for compounds **2** and **3** are listed in Tables 2 and 3, respectively. The spatial arrangement of atoms in molecules **2** and **3** and the atomic numbering, which were obtained with the PLUTON96 program [19], are shown in Figs. 1 and 2, respectively. For convenient comparison of the geometric parameters in the two molecules, we used a unified atomic numbering. The interatomic distances in structures **2** and **3** were calculated with the PARST95 program [20]. They are listed in Tables 4–6.

Table 1. Crystal data and details of the X-ray diffraction experiment and refinement for structures **2** and **3**

Compound	$\text{C}_{19}\text{H}_{13}\text{Cl}_2\text{NO}_5$ (2)	$\text{C}_{19}\text{H}_{12}\text{ClNO}_5$ (3)
Crystal system	Monoclinic	Monoclinic
Space group	$P2_1/c$	$P2_1/c$
a , Å	9.627(3)	7.048(4)
b , Å	6.646(2)	10.582(4)
c , Å	28.500(9)	21.760(7)
β , deg	98.72(2)	97.23(4)
V , Å ³	1802.4(9)	1610(1)
Z	4	4
ρ_{calcd} , g/cm ³	1.497	1.525
$\mu(\text{Mo}, K_\alpha)$, cm ⁻¹	3.92	2.70
Crystal size, mm	$0.24 \times 0.12 \times 0.06$	$0.50 \times 0.20 \times 0.10$
θ_{max} , deg	25	26
Number of reflections with $I \geq 2\sigma(I)$ /Number of parameters	1679/297	2538/284
R_1/wR_2	0.0504/0.0575	0.0510/0.0426
$\Delta\rho_{\text{max}}/\Delta\rho_{\text{min}}$, e/Å ³	0.173/−0.196	0.159/−0.166

Table 2. Atomic coordinates ($\times 10^4$) and isotropic thermal parameters U_{eq} ($\text{\AA}^2 \times 10^3$) for molecule **2**

Atom	<i>x</i>	<i>y</i>	<i>z</i>	$U_{\text{eq}}/U_{\text{iso}}$	Atom	<i>x</i>	<i>y</i>	<i>z</i>	$U_{\text{eq}}/U_{\text{iso}}$
Cl(1)	2392(1)	1572(2)	1586(1)	51(1)	C(14)	-2082(3)	4406(6)	-18(1)	61(2)
Cl(2)	-2706(1)	6002(2)	-483(1)	125(1)	C(15)	-1769(4)	2404(6)	-103(1)	59(2)
N(1)	133(2)	1089(4)	2015(1)	22(1)	C(16)	-1273(3)	1200(7)	261(1)	58(1)
O(1)	-4394(2)	1008(4)	2310(1)	61(1)	C(17)	-3213(3)	1239(6)	2494(1)	35(1)
O(2)	-2823(2)	1475(4)	2960(1)	45(1)	C(18)	-3903(3)	1447(6)	3252(1)	59(1)
O(3)	-4238(2)	2646(4)	1320(1)	61(1)	C(19)	-3452(3)	1222(7)	1384(1)	50(1)
O(4)	-3624(2)	-507(4)	1143(1)	58(1)	C(20)	-4803(4)	-559(7)	775(1)	91(2)
C(2)	-842(3)	1044(5)	1596(1)	35(1)	H(6)	-250(20)	1260(50)	3138(8)	56(9)
C(3)	-2147(3)	1194(5)	1736(1)	27(1)	H(7)	2200(20)	1300(40)	3237(7)	55(9)
C(4)	-1988(3)	1273(5)	2234(1)	24(1)	H(8)	3380(20)	1270(50)	2556(8)	49(9)
C(5)	-574(3)	1252(5)	2407(1)	26(1)	H(12)	-1170(20)	4480(40)	1115(9)	67(10)
C(6)	239(3)	1250(5)	2864(1)	30(1)	H(13)	-2090(20)	6600(40)	492(8)	62(10)
C(7)	1644(3)	1267(6)	2918(1)	39(1)	H(15)	-1920(20)	1840(40)	-431(8)	64(10)
C(8)	2358(3)	1258(5)	2519(1)	35(1)	H(16)	-1020(20)	-230(40)	202(9)	68(10)
C(9)	1585(3)	1246(5)	2073(1)	35(1)	H(18A)	-3460(20)	1650(40)	3612(8)	59(10)
C(10)	-523(3)	564(5)	1115(1)	48(1)	H(18B)	-4410(30)	70(50)	3218(9)	83(12)
O(10)	94(2)	-1033(4)	1057(1)	63(1)	H(18C)	-4620(20)	2620(40)	3150(7)	36(9)
C(11)	-1099(3)	1927(6)	731(1)	42(1)	H(20A)	-4860(20)	-1960(40)	609(8)	60(10)
C(12)	-1355(3)	3934(5)	800(1)	45(1)	H(20B)	-4700(20)	570(40)	533(8)	59(10)
C(13)	-1876(4)	5207(6)	433(1)	67(2)	H(20C)	-5720(20)	-300(50)	917(8)	69(11)

Table 3. Atomic coordinates ($\times 10^4$) and isotropic thermal parameters U_{eq} ($\text{\AA}^2 \times 10^3$) for molecule **3**

Atom	<i>x</i>	<i>y</i>	<i>z</i>	$U_{\text{eq}}/U_{\text{iso}}$	Atom	<i>x</i>	<i>y</i>	<i>z</i>	$U_{\text{eq}}/U_{\text{iso}}$
Cl(2)	8183(1)	7124(1)	2456(1)	71(1)	C(19)	7616(5)	1835(3)	-851(1)	45(1)
N(1)	7310(3)	5100(2)	-316(1)	33(1)	C(20)	9794(6)	143(3)	-930(2)	78(1)
C(2)	7676(4)	3821(2)	-208(1)	35(1)	O(1)	6997(3)	2793(2)	-2105(1)	71(1)
C(3)	7495(4)	3233(2)	-776(1)	35(1)	O(2)	6423(3)	4857(2)	-2251(1)	58(1)
C(4)	7071(4)	4123(3)	-1240(1)	36(1)	O(3)	6278(3)	1119(2)	-874(1)	59(1)
C(5)	6936(4)	5315(3)	-952(1)	36(1)	O(4)	9431(3)	1482(2)	-876(1)	53(1)
C(6)	6504(4)	6541(3)	-1150(1)	43(1)	O(10)	8355(3)	2242(2)	524(1)	56(1)
C(7)	6432(4)	7477(3)	-716(1)	44(1)	H(6)	6180(30)	6660(20)	-1640(9)	46(8)
C(8)	6822(4)	7211(3)	-87(1)	44(1)	H(7)	6030(40)	8350(20)	-887(11)	68(10)
C(9)	7261(4)	6015(3)	128(1)	34(1)	H(8)	6680(30)	7740(20)	187(9)	27(8)
C(10)	8063(4)	3369(3)	416(1)	40(1)	H(13)	7460(30)	7400(20)	1150(9)	41(8)
C(11)	8064(4)	4332(3)	905(1)	37(1)	H(15)	8870(30)	4560(20)	2426(8)	32(7)
C(12)	7691(4)	5598(3)	767(1)	33(1)	H(16)	8810(30)	2960(20)	1579(9)	32(7)
C(13)	7717(4)	6461(3)	1256(1)	40(1)	H(18A)	5660(40)	5490(30)	-3072(13)	116(14)
C(14)	8107(4)	6042(3)	1854(1)	44(1)	H(18B)	4990(40)	3920(30)	-3024(13)	102(12)
C(15)	8473(4)	4778(3)	1995(1)	50(1)	H(18C)	7460(40)	4280(30)	-3004(12)	83(12)
C(16)	8453(4)	3918(3)	1515(1)	47(1)	H(20A)	10940(50)	70(40)	-859(17)	190(20)
C(17)	6844(4)	3835(3)	-1899(1)	46(1)	H(20B)	9350(40)	-330(20)	-1336(11)	70(10)
C(18)	6145(6)	4660(4)	-2921(1)	78(1)	H(20C)	9200(40)	-400(30)	-606(12)	95(12)

Table 4. Interatomic distances d (Å) in structures **2** and **3**

Bond	d (2)	d (3)	Bond	d (2)	d (3)
Cl(1)–C(9)	1.706(3)		C(10)–O(10)	1.239(4)	1.229(3)
Cl(2)–C(14)	1.732(4)	1.736(3)	C(10)–C(11)	1.464(4)	1.473(4)
N(1)–C(9)	1.386(3)	1.370(3)	C(11)–C(16)	1.412(4)	1.392(4)
N(1)–C(2)	1.402(3)	1.392(3)	C(11)–C(12)	1.376(5)	1.391(4)
N(1)–C(5)	1.399(3)	1.396(3)	C(12)–C(13)	1.380(5)	1.401(4)
C(2)–C(3)	1.378(4)	1.376(3)	C(13)–C(14)	1.378(5)	1.368(3)
C(2)–C(10)	1.484(4)	1.432(3)	C(14)–C(15)	1.393(5)	1.389(4)
C(3)–C(4)	1.406(4)	1.385(3)	C(15)–C(16)	1.339(5)	1.385(4)
C(3)–C(19)	1.484(4)	1.492(4)	C(17)–O(1)	1.187(3)	1.200(3)
C(4)–C(5)	1.376(3)	1.416(4)	C(17)–O(2)	1.336(3)	1.337(3)
C(4)–C(17)	1.483(4)	1.456(3)	O(2)–C(18)	1.425(4)	1.460(3)
C(5)–C(6)	1.413(3)	1.389(4)	C(19)–O(3)	1.208(5)	1.206(3)
C(6)–C(7)	1.339(4)	1.374(4)	C(19)–O(4)	1.336(5)	1.341(3)
C(7)–C(8)	1.416(4)	1.392(4)	O(4)–C(20)	1.425(4)	1.447(4)
C(8)–C(9)	1.370(4)	1.370(4)	C(9)–C(12)		1.456(3)

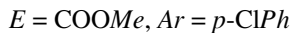
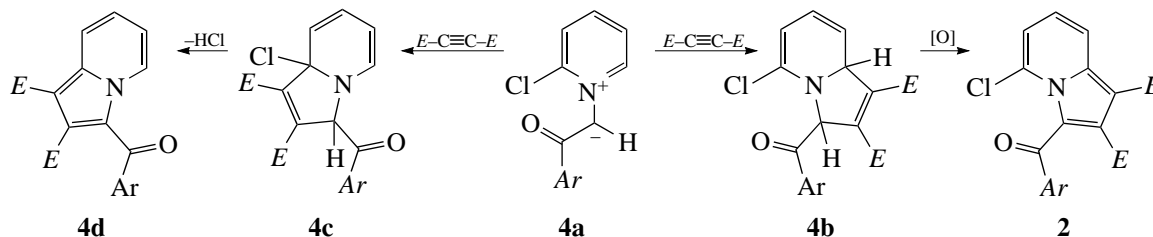
Table 5. Parameters of intramolecular and intermolecular contacts in structure **2**

D–H	$d(D-H)$, Å	$d(D\cdots A)$, Å	$d(H\cdots A)$, Å	$\omega(D-H\cdots A)$, deg	A	Symmetry operation
C(6)–H(6)	0.97(3)	3.005(4)	2.45(2)	116(2)	O(2)	[x ; y ; z]
C(16)–H(16)	1.00(3)	2.860(4)	2.57(3)	97(2)	O(10)	[x ; y ; z]
C(7)–H(7)	0.98(2)	3.721(4)	2.96(3)	135(2)	O(4)	[$-x$; $y + 1/2$; $1/2 - z$]
C(6)–H(6)	0.97(3)	3.622(4)	2.90(3)	132(2)	O(10)	[$-x$; $y + 1/2$; $1/2 - z$]
C(8)–H(8)	0.98(2)	3.285(4)	2.36(2)	156(2)	O(1)	[$x + 1$; y ; z]
C(13)–H(13)	0.97(3)	3.461(4)	2.91(2)	117(2)	O(10)	[x ; $y + 1$; z]
C(15)–H(15)	1.00(2)	3.486(5)	2.74(3)	132(2)	O(10)	[$-x$; $-y$; $-z$]
C(18)–H(18B)	1.04(3)	3.426(4)	2.56(3)	141(2)	O(3)	[$-x - 1$; $y - 1/2$; $1/2 - z$]
C(18)–H(18C)	1.05(2)	3.694(4)	2.71(2)	157(2)	O(1)	[$-x - 1$; $y + 1/2$; $1/2 - z$]

RESULTS AND DISCUSSION

The transformation of pyridinium salt **1** into indolizine **2** provides an example of 1,3-dipolar cycloaddition, which is characteristic of *N*-phenacylpyridinium ylides

of the **4a** type. The specific feature of the reaction described is the regioselective cycloaddition of acetylene dienophile through the formation of adduct **4b** (followed by oxidation to indolizine **2**):

**Scheme III**

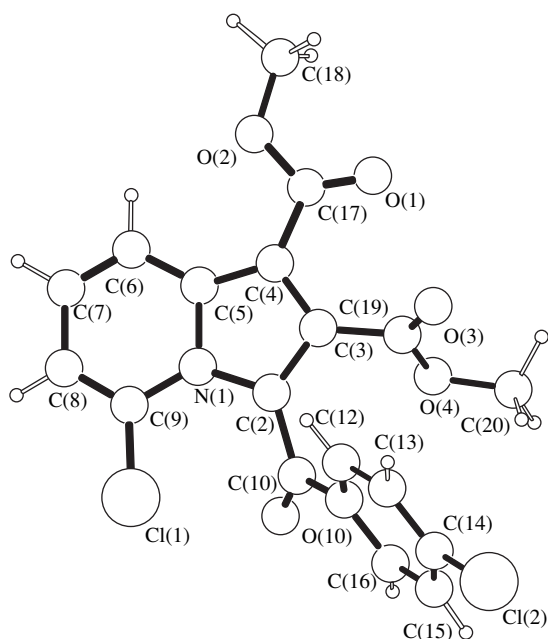


Fig. 1. Structure of molecule **2** and the atomic numbering.

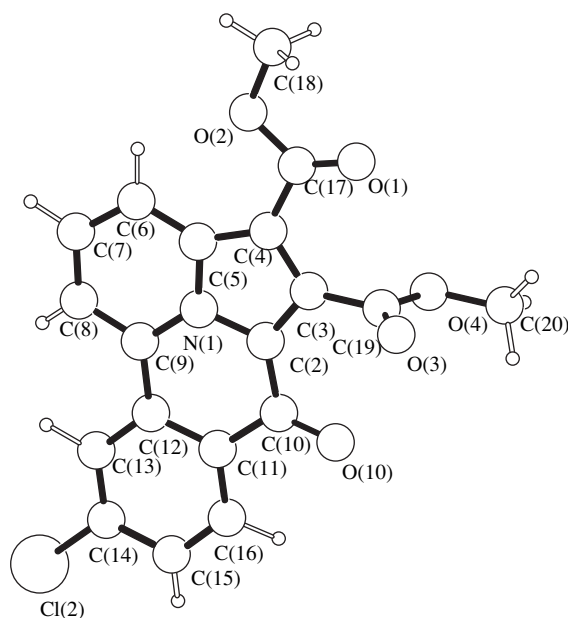


Fig. 2. Structure of molecule **3** and the atomic numbering.

An alternative cycloaddition resulting in the formation of cycloadduct **4c** would necessarily be followed by the aromatization of this structure to indolizine **4d**. Our special experiments (independent synthesis of indolizine **4d** and comparison of its chromatographic behavior with that of trace contaminants that are formed in the reaction mixture) revealed that indolizine **4d** is not formed even in trace amounts.

In the structure of heterocycle **2**, the indolizine bicyclic is planar (the atomic deviations from the rms plane are within 0.06 Å). The dihedral angle between the planes of the indolizine nucleus of the molecule and the phenyl ring of the benzoyl group is 75.1(1)°. The O(10) atom deviates from the plane of the phenyl ring and the plane of the indolizine bicyclic by 0.366(6) and 1.372(5) Å, respectively. The dihedral angles formed by the planar C(17)O(1)O(2)C(18) and C(19)O(3)O(4)C(20) ester radicals (the atomic deviations from each of the rms planes are within 0.1 Å) with

the nine-membered bicyclic are equal to 7.0(1)° and 66.8(1)°, respectively. Earlier [21], we studied the crystal structure of dimethyl 3-(*p*-nitrobenzoyl)-5-chloroindolizine-1,2-dicarboxylate, C₁₉H₁₃ClN₂O₇. The similarity of the structural fragments of these two compounds allows us to compare their geometric parameters. In these molecules, the O(1)C(17)C(4)C(3) torsion angles of the C(17)O(1)O(2)C(18) ester groups are +5.3(6)° (**2**) and -176.2(2)° [21] and the O(3)C(19)C(3)C(4) torsion angles of the C(19)O(3)O(4)C(20) ester groups are +66.0(6)° (**2**) and -98.3(3)° (*p*-nitro derivative [21]). This reorientation of the ester fragments is not accompanied by changes in their geometric characteristics; that is, their bond lengths and angles are equal within standard deviations. The same tendency is observed in the molecule as a whole.

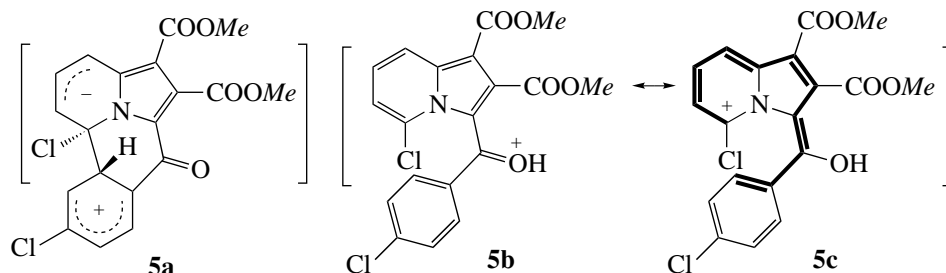
The tetracyclic product **3** is formed from indolizine **2** through the formation of the C–C bond between the

Table 6. Parameters of intramolecular and intermolecular contacts in structure **3**

D–H	$d(D-H)$, Å	$d(D\cdots A)$, Å	$d(H\cdots A)$, Å	$\omega(D-H\cdots A)$, deg	A	Symmetry operation
C(6)–H(6)	1.07(2)	2.981(3)	2.35(2)	116(1)	O(2)	[<i>x</i> ; <i>y</i> ; <i>z</i>]
C(16)–H(16)	1.05(2)	2.786(3)	2.40(2)	100(1)	O(10)	[<i>x</i> ; <i>y</i> ; <i>z</i>]
C(7)–H(7)	1.02(2)	3.870(4)	2.94(2)	152(2)	O(3)	[<i>x</i> ; <i>y</i> + 1; <i>z</i>]
C(8)–H(8)	0.83(2)	3.663(4)	2.97(2)	142(2)	O(3)	[1 – <i>x</i> ; 1 – <i>y</i> ; – <i>z</i>]
C(13)–H(13)	1.03(2)	3.143(4)	2.62(2)	111(1)	O(4)	[2 – <i>x</i> ; 1 – <i>y</i> ; – <i>z</i>]
C(18)–H(18A)	0.99(3)	3.324(4)	2.60(3)	130(2)	O(3)	[1 – <i>x</i> ; 1/2 + <i>y</i> ; – <i>z</i> – 1/2]
C(20)–H(20C)	1.04(3)	2.927(4)	2.59(3)	98(2)	O(10)	[2 – <i>x</i> ; – <i>y</i> ; – <i>z</i>]

benzoyl group and the pyridine fragment of indolizine followed by dehydrohalogenation. The mechanism of this transformation is somewhat unusual. Although the chlorine atom in the α position with respect to the nitrogen atom of the pyridine fragment is probably rather mobile, it is difficult to assume that the chlorine atom is

replaced by the benzoyl fragment according to the mechanism of aromatic nucleophilic substitution (it is apparent that the benzoyl group in the *ortho* position is not nucleophilic). Therefore, it is highly improbable that the reaction mechanism includes the formation of intermediate **5a**:



Scheme IV

The only reasonable explanation for the mechanism of the cyclization observed is provided by the following hypothesis. Indolizine **2** undergoes cyclization under the effect of either Al_2O_3 or acids (as was observed in our special experiments). Acids (as well as the acid OH groups, which are always present in aluminum oxide) protonate the benzoyl group of indolizine **2** to form cation **5b** (scheme IV). This direction of protonation of 3-acylindolizines is well known [22]. In this case, the indolizine skeleton and the adjacent benzoyl fragment form a common system (shown by heavy lines in intermediate **5c**) that consists of eleven atoms and contains a total of ten π electrons. Evidently, the ten-electron system can undergo a pericyclic cyclization reaction, which is allowed by the Woodward–Hoffmann rules. This unusual 1,11-cyclization would result (upon the detachment of HCl) in the formation of tetracycle **3**.

The tetracyclic system **3** is planar and consists of 19 atoms, including C(17) and C(19) (Fig. 2). The rms atomic deviations from this plane are within 0.036(3) Å. The ester radicals are also planar (the rms atomic deviations are within 0.003 Å in each of them), and their arrangement is quite different from that in **2**: the C(17)O(1)O(2)C(18) group is almost coplanar with the heterocyclic system [the dihedral angle is 0.68(7)°], whereas the C(19)O(3)O(4)C(20) group is situated almost perpendicularly to the latter system [the dihedral angle is 88.13(9)°]. This position of the ester groups with respect to the heterocyclic nucleus of the molecule is due to the minimum repulsion of the O(10) and O(1) atoms from the O(3) and O(4) atoms, respectively.

In molecules **2** and **3**, the intramolecular C(6)–H(6)···O(2) and C(16)–H(16)···O(10) hydrogen bonds have almost identical geometric parameters (Tables 5, 6). The parameters of the intermolecular contacts involving the C, H, and O atoms are also included in these tables.

ACKNOWLEDGMENTS

The synthetic part of this work was supported by the Russian Foundation for Basic Research, project no. 99-03-33076. We also acknowledge the support of the Russian Foundation for Basic Research in the payment of the license for using the Cambridge Structural Database, project no. 99-07-90133.

REFERENCES

1. E. V. Babaev, A. V. Efimov, S. G. Zhukov, and V. B. Rybakov, *Khim. Geterotsikl. Soedin.*, No. 7, 983 (1998).
2. E. V. Babaev, S. V. Bozhenko, D. A. Maiboroda, *et al.*, *Bull. Soc. Chim. Belg.* **106** (11), 631 (1997).
3. S. G. Zhukov, V. B. Rybakov, E. V. Babaev, *et al.*, *Acta Crystallogr., Sect. C: Cryst. Struct. Commun.* **53**, 1909 (1997).
4. E. V. Babaev, S. V. Bozhenko, S. G. Zhukov, and V. B. Rybakov, *Khim. Geterotsikl. Soedin.*, No. 8, 1105 (1997).
5. V. B. Rybakov, S. G. Zhukov, E. V. Babaev, *et al.*, *Kristallografiya* **44** (6), 1067 (1999) [*Crystallogr. Rep.* **44**, 997 (1999)].
6. V. B. Rybakov, S. G. Zhukov, E. V. Babaev, *et al.*, *Kristallografiya* **45** (1), 108 (2000) [*Crystallogr. Rep.* **45**, 103 (2000)].
7. V. B. Rybakov, S. G. Zhukov, E. V. Babaev, *et al.*, *Kristallografiya* **45** (2), 292 (2000) [*Crystallogr. Rep.* **45**, 261 (2000)].
8. V. B. Rybakov, S. G. Zhukov, E. V. Babaev, and E. J. Sonneveld, *Kristallografiya* **46** (3), 435 (2001) [*Crystallogr. Rep.* **46**, 385 (2001)].
9. E. V. Babaev, V. B. Rybakov, S. G. Zhukov, and I. A. Orlova, *Khim. Geterotsikl. Soedin.*, No. 4, 542 (1999).
10. S. G. Zhukov, E. V. Babaev, V. V. Chernyshev, *et al.*, *Z. Kristallogr.* **215**, 306 (2000).
11. V. B. Rybakov, S. G. Zhukov, K. Yu. Pasichnichenko, and E. V. Babaev, *Koord. Khim.* **26** (9), 714 (2000).

12. V. B. Rybakov, S. I. Troyanov, E. V. Babaev, *et al.*, *Kristallografiya* **46** (6), 1069 (2001) [*Crystallogr. Rep.* **46**, 986 (2001)].
13. V. B. Rybakov, E. V. Babaev, K. Yu. Pasichnichenko, and E. J. Sonneveld, *Kristallografiya* **47** (1), 76 (2002) [*Crystallogr. Rep.* **47**, 69 (2002)].
14. V. B. Rybakov, E. V. Babaev, and V. V. Chernyshev, *Kristallografiya* **47** (3), 473 (2002) [*Crystallogr. Rep.* **47**, 428 (2002)].
15. F. H. Allen and O. Kennard, *Chem. Design Automat. News* **8** (1), 31 (1993).
16. *Enraf–Nonius CAD4 Software: Version 5.0* (Enraf–Nonius, Delft, The Netherlands, 1989).
17. L. J. Farrugia, *WinGX98: X-ray Crystallographic Programs for Windows* (Univ. of Glasgow, Glasgow, 1998).
18. G. M. Sheldrick, *SHELX97: Program for the Solution and Refinement of Crystal Structures* (Univ. of Göttingen, Göttingen, 1997).
19. A. L. Spek, *PLUTON96: Molecular Graphics Program* (University of Utrecht, Utrecht, 1996).
20. M. Nardelli, *J. Appl. Crystallogr.* **28**, 659 (1995).
21. E. V. Babaev, K. Yu. Pasichnichenko, V. B. Rybakov, and S. G. Zhukov, *Khim. Geterotsikl. Soedin.*, No. 10, 1378 (2000).
22. E. V. Babaev, V. N. Torocheshnikov, and S. I. Bobrovskii, *Khim. Geterotsikl. Soedin.*, No. 9, 1235 (1995).

Translated by I. Polyakova

STRUCTURES OF MACROMOLECULAR COMPOUNDS

Three-Dimensional Structure of the Arg32His Mutant of the Human Tumor Necrosis Factor Determined at 2.5 Å Resolution from X-ray Data for a Twin Crystal

P. V. Afonin*, A. V. Fokin*, L. N. Shingarova*, V. G. Korobko*, I. N. Tsygannik*, I. V. Artem'ev*,
S. V. Pletnev**, W. Pangborn***, W. L. Duax***, and V. Z. Pletnev*

* Shemyakin Institute of Bioorganic Chemistry, Russian Academy of Sciences,
ul. Miklukho-Maklaya 16/10, Moscow, 117997 Russia
e-mail: pletnev@tek.siobc.ras.ru

** Shubnikov Institute of Crystallography, Russian Academy of Sciences,
Leninskiĭ pr. 59, Moscow, 117333 Russia

*** Hauptman–Woodward Medical Research Institute,
73 High Street, Buffalo, New York, 14203-1196 USA

Received December 12, 2001

Abstract—The three-dimensional structure of the Arg32His mutant of the human tumor necrosis factor (TNF- α) was established at 2.5 Å resolution by the molecular replacement method. The crystals of the mutant belong to sp. gr. R3. The specimen has a hemihedral twinning fraction of approximately one half with the twin law corresponding to an additional twofold axis along the *a*- or *b*-axis of the crystal lattice. The model analysis of interactions between functionally important loop 29–36 of the mutant and the receptors *p55* and *p75* was performed. © 2002 MAIK “Nauka/Interperiodica”.

INTRODUCTION

The tumor necrosis factor (TNF- α), one of the most important immune mediators and an antiinflammatory cytokine, is produced mainly by activated macrophages [1]. The protein TNF- α was first discovered as a factor released into blood upon bacterial infections [2] and was initially characterized as a protein inducing the necrosis of tumor tissues of mice [3]. The protein TNF- α is characterized by the selective *in vitro* cytotoxic activity with respect to a large number of tumor and transformed cell lines [3–5]. Similar cytotoxic action [6] is also characteristic of another protein, lymphotoxin (TNF- β), produced primarily by T lymphocytes. Both cytokines are closely related immune-system factors against bacterial infections, which act as mediators of inflammatory and immune reactions and compete for binding with the same cell receptors [1, 7, 8]. The typical biological effects of TNF- α and TNF- β are manifested via interactions with two types of receptors, which are called *p55* and *p75* in accordance with their molecular weights [9–11]. The amino-acid sequences of the extracellular portions of both receptors are essentially homologous, and these domains are characterized by a fourfold repetition of the structure motif containing six cysteine residues. In contrast, the intracellular domains of both receptors show no significant sequence homology, which is indicative of different signal-transduction pathways. It was found that the receptors impart different biological functions of TNF- α and

TNF- β . For example, the interaction of TNF- α with the *p55* receptor induces cytotoxic activity [12–14], the expression of adhesion molecules of epithelial cells and keratinocytes [15–17], the activation of the NF- κ B transcription factor [15, 18], and the induction of the transcription of mRNA which codes Mn superoxide dismutase [13, 19].

The three-dimensional structures of native TNF- α and a number of its derivatives with site mutations in the regions that are of functional importance for interactions with receptors have been established by methods of protein crystallography [20–25]. The structure of the TNF- β in the complex with the *p55* receptor was also determined [26]. Having ~32% homology between the amino-acid sequences of TNF- α and TNF- β , these proteins are structurally similar (the rms deviation of the superimposed C $^{\alpha}$ atoms is ~0.87 Å). The interactions of TNF- α and TNF- β with the receptors begin with the formation of the cytokine molecule trimers both in solution [27, 28] and in the crystalline state as is exemplified by the crystal structure of the TNF- β -*p55* complex [26, 29].

The regions of the TNF- α and TNF- β molecules essential for binding with the receptors and responsible for their biological activity were identified by the mutation analysis [30–34]. These regions reside in the lower part of the bell-shaped trimer and consist mainly of three triads of surface loop regions located at the interfaces between each pair of the adjacent subunits. In par-

Table 1. Crystallographic and X-ray diffraction data for H32-TNF- α

Parameters		
Conditions of crystallization	Solution (1 μ l): 0.02 M Tris-HCl, pH 8.0, 0.15 M NaCl, protein (50 mg/ml) Reservoir solution (1 μ l): 0.2 M MES, pH 6.4, 2.0 M MgSO ₄	
Molecular weight, Da	~16280	
Sp. gr.	R3	
Unit-cell parameters	<i>a</i> , Å	66.235
	<i>b</i> , Å	66.235
	<i>c</i> , Å	85.186
	γ , deg	120.0
Hexagonal setting	<i>Z</i>	9
	<i>V</i> _{cell} , Å ³	323 649
Resolution, Å	2.5	
Matthews coefficient, Å ³ /Da	2.21	
Number of reflections with ($F \geq 0$)	3789	
Number of reflections with ($F \geq 2\sigma_F$)	3651	
Data completeness, %	78.6	
<i>R</i> _{merge}	0.103	

ticular, it was confirmed that one of the loop regions, 29–36, is involved in binding with the receptor.

In this study, we established the three-dimensional structure of the Arg32His mutant of human tumor necrosis factor (H32-TNF- α) by X-ray diffraction analysis and examined the structure–function relationships.

EXPERIMENTAL

The crystals of the H32-TNF- α mutant were grown by the vapor-diffusion hanging-drop techniques under conditions that were slightly different from those used for the growth of the native protein [35] (Table 1).

The X-ray diffraction patterns indicated sp. gr. R32. However, as evidenced by the calculated Matthews coefficient [36], the asymmetric part of the unit cell in this case must contain a molecule with a molecular weight half as large as that of the monomer of the H32-TNF- α mutant. Hence, it was concluded that the crystals in fact belong to sp. gr. R3, whereas the observed higher symmetry of the X-ray diffraction pattern was attributed to twinning.

The X-ray data were collected on an automated R-Axis II diffractometer (Rigaku, Japan) equipped with an Image Plate detector at 18°C. The statistical analysis of the X-ray data with the use of the CNS program package (version 1.0) [37] confirmed crystal twinning with the characteristic parameters $\langle |I_o|^2 \rangle / \langle |I_o| \rangle^2 = 1.65$

Table 2. Statistics of the crystallographic refinement of the H32-TNF- α structure

Parameters		
Number of amino-acid residues		148
Number of non-hydrogen atoms of the protein		1158
Number of water molecules		26
<i>R</i> _{twin} ($F \geq 0$)		0.106
<i>R</i> _{twin(free)} (using 10% of X-ray data, $F \geq 0$)		0.237
<i>R</i> _{twin} ($F \geq 2\sigma_F$)		0.100
<i>R</i> _{twin(free)} (using 10% of X-ray data, $F \geq 2\sigma_F$)		0.230
Average <i>B</i> factor (over structure), Å ²		43.8
<i>rmsd</i>	Backbone	2.74
	Side chains	3.40
<i>rmsd</i> of <i>B</i> factors, * Å ²	Bond lengths, Å	0.006
	Bond angles, deg	1.208
<i>rmsd</i> of parameters from the ideal values	Torsion angles, deg	25.826
	Planarity, deg	0.867
The Ramachandran plot statistics of the ϕ and ψ angles for amino-acid residues (Gly and Pro are ignored) over the regions of the Ramachandran plot, %	Favoured regions	71.4
	Additional allowed regions	25.4
Angles ω , deg	Generously allowed regions	3.2
	Disallowed regions	0.0
Positional error, Å	Average	179.9
	Standard deviation	0.9
Standard deviation of the chiral angles $\xi(C_\alpha-N-C-C_\beta)$, deg	According to Luzzati [41]	0.19
		0.9

Note: The relative rms deviations of the *B* factors for pairs of covalently bonded atoms are given.

and $\langle |F_o|^2 \rangle / \langle |F_o| \rangle^2 = 0.86$. In the absence of twinning, these parameters are equal to 2.0 and 0.785, respectively [38], whereas for a specimen with 50% hemihedral twinning fraction they are equal to 1.5 and 0.865, respectively [38]. The twinning fraction (about 50%) is related to the basic crystal domain by a twofold axis parallel to the *a*- or *b*-axis of the unit cell.

The H32-TNF- α structure was solved by the molecular replacement method without regard for twinning with the aid of the X-PLOR program package (version 3.1) [39] and with the use of 3651 structure factors, $F \geq 2\sigma_F$, in the resolution shell between 10 and 3 Å. The structure of one of the TNF- α mutants (PDB code 4TSV) determined at 1.8 Å resolution [23] was used as the starting model. The subsequent refinement of the structure was carried out in several steps using the CNS

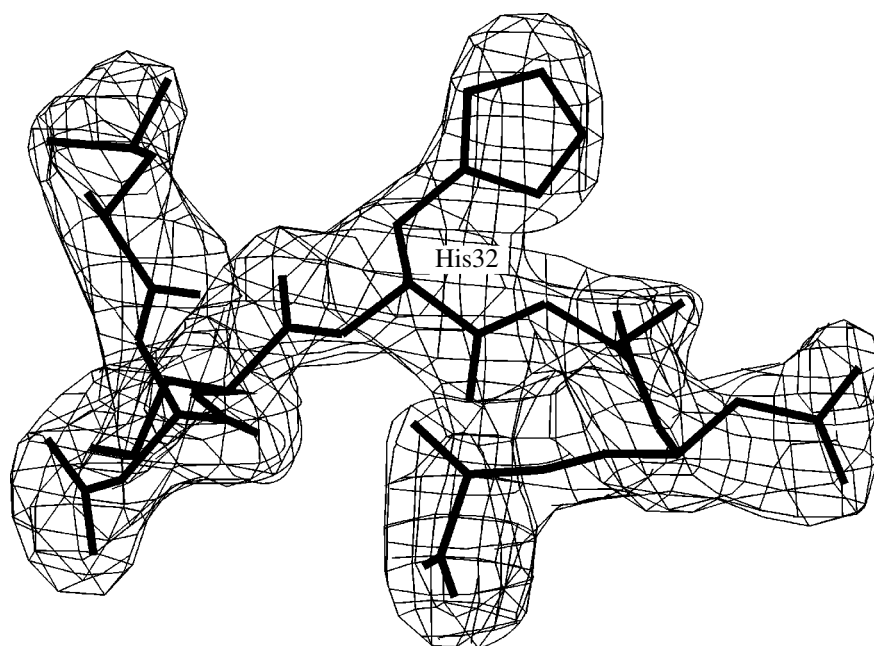


Fig. 1. Fragment of the functionally important region of TNF- α with the mutated His32 residue in to the electron density (the level $\rho \geq 1\sigma_\rho$).

program package. Calculations by the slow-cooling procedure were alternated with the manual correction of the molecular geometry on an OCTANE graphics station (Silicon Graphics) using the CHAIN program [40].

In the CNS program [37], the X-ray term of the minimized functional with allowance for the contribution of the twinning fraction is represented by the function

$$E_{xref} = \Sigma\{|F_o(hkl)| - k[(1 - \theta)|F_c(hkl)|^2 + \theta|F_c(h'k'l')|^2]^{1/2}\}^2 \quad [37],$$

where k is the scale factor, θ is the relative content of the twinning fraction (0.50), and the relation between the hkl and $h'k'l'$ reflections is determined by the twinning type (in our case, $h' = h, k' = -h - k, l' = -l$). Following the common practice for crystals with the θ parameter close to 50% [38], the intensities of the corresponding pairs of twin-related reflections were averaged. In all stages of the refinement, the calculated structure factors F_c were corrected for the contribution from the bulk solvent. The electron-density maps were calculated using not the structure factors $|F_o(hkl)|$ but the values calculated from the X-ray diffraction data with the coordinates of the model structure

$$F_{detwin} = \{0.5[|F_o(hkl)|^2 + k'(|F_c(hkl)|^2 - |F_c(h'k'l')|^2)]\}^{1/2} \quad [37].$$

The crystallographic R factor,

$$R_{twin} = \Sigma\{|F_o(hkl)| - k[(1 - \theta)|F_c(hkl)|^2 + \theta|F_c(h'k'l')|^2]^{1/2}\} / \Sigma|F_o(hkl)| \quad [37],$$

characterizing the validity of the refined H32-TNF- α structure was $\sim 10.0\%$ (the corresponding statistical data are given in Table 2). The final electron-density



Fig. 2. Topology of the spatial arrangement of the trimer of the Arg32His mutant of TNF- α . The individual monomers are differently shaded; the strands of the β -structure are indicated by arrows.

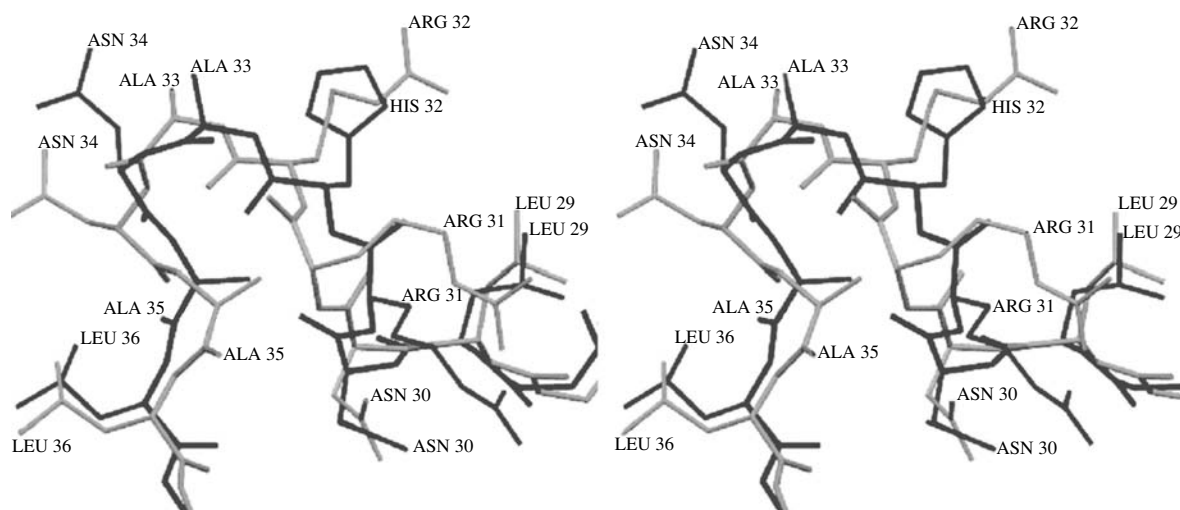


Fig. 3. Stereoview of the loops 29–36 of the superimposed molecules of H32-TNF- α (black) and native TNF- α (grey).

map calculated by the $(2F_{\text{detwin}} - F_c)$ coefficients is of high quality and, on the whole, is adequate to the amino-acid sequence of the protein (Fig. 1). The crystal structure has 26 ordered water molecules located in the first and second shells on the surface of the TNF- α

molecule and characterized by electron-density maxima higher than 1.0σ , temperature factors B lower than 70 \AA^2 , and lengths of hydrogen bonds to the nearest atoms of the protein molecule ranging from 2.5 to 3.5 \AA .

Table 3. Conformational parameters (φ and ψ) and rms deviations (RMSD) of the superimposed C^α atoms of loop regions 29–26 in the TNF- α and TNF- β structures

		TNF- α					TNF- β	
		native	mutant forms				complex with the <i>p55</i> receptor	
amino-acid residues	torsion angles, deg	[20]	<i>R32H</i> , this study	<i>R31D</i> [24]	<i>A84V</i> [25]	<i>L29S</i> <i>S52I</i> <i>Y56F</i> [23]	[26]	amino-acid residues
<i>Leu29</i>	φ	-158.9	-119.7	-152.5	-121.3	-147.5	-143.7	<i>Arg46</i>
	ψ	149.9	154.0	146.5	148.0	141.4	159.6	
<i>Asn30</i>	φ	-127.5	-122.7	-114.7	-102.4	-104.5	-129.4	<i>Ala47</i>
	ψ	-133.9	-35.4	28.4	-155.2	4.8	17.5	
<i>Arg31</i>	φ	60.0	-70.9	-130.1	40.3	-89.5	-102.1	<i>Asn48</i>
	ψ	-33.1	67.1	-2.2	29.9	66.2	10.7	
<i>Arg32</i>	φ	-65.0	-155.7	-120.2	-106.1	-151.1	-142.0	<i>Thr49</i>
	ψ	-163.7	146.1	170.1	-177.2	148.9	162.9	
<i>Ala33</i>	φ	-39.3	-56.0	49.0	-30.7	-71.1	53.8	<i>Asp50</i>
	ψ	-68.0	150.4	-136.4	-31.7	154.5	-138.8	
<i>Asn34</i>	φ	-130.9	54.5	-109.9	-159.9	67.2	-96.9	<i>Arg51</i>
	ψ	67.9	26.0	41.3	40.5	21.4	19.8	
<i>Ala35</i>	φ	-116.2	-113.5	-61.8	-73.9	-125.1	-76.0	<i>Ala52</i>
	ψ	78.6	126.6	74.5	116.8	155.7	155.8	
<i>Leu36</i>	φ	-83.6	-98.2	-61.2	-105.8	-137.4	-171.9	<i>Phe53</i>
	ψ	140.7	163.0	159.5	121.5	150.3	165.7	
RMSD, \AA		0.75	0.0	0.87	0.91	0.44	0.65	

Table 4. Stabilizing interactions of the equivalent functional loops 29–36 of TNF- β , TNF- α , and H32-TNF- α with the *p55* receptor

TNF- β - <i>p55</i> [26]			TNF- α and H32-TNF- α - <i>p55</i> (model)		
type of interaction	TNF- β	<i>p55</i>	type of interaction	TNF- α and H32-TNF- α	<i>p55</i>
<i>H</i> bond, potential salt bridge	Arg46 (N ⁿ)	Ser72 (O ^y) Glu56 (O ^e)		Leu29	
Potential <i>H</i> bond	Asn48 (N ^{δ2})	Glu56 (O ^e)	Salt bridge	Arg31 (N ⁿ)	Glu56 (O ^e)
Potential <i>H</i> bond	Thr49 (O ^y H)	Cys70 (O)	<i>H</i> bond	Arg32 (N ⁿ)/His32 (N ^{e2})	Ser72 (O ^y H)
<i>H</i> bond	Asp50 (O ^{δ})	Ser72 (O ^y H)	Hydrophobic	Ala33 (C ^B)	Leu71 (C ^{δ2})

RESULTS AND DISCUSSION

As was expected, the H32-TNF- α molecules form trimers (Fig. 2). On the whole, this spatial organization is virtually identical to the structure of native TNF- α [20] and is similar to the TNF- β structure in the complex with the *p55* receptor [26] (the rms deviations (RMSD) of the superimposed C $^{\alpha}$ atoms of the individual monomers are equal to ~ 0.9 Å). For each monomer, the chain-folding topology can be described as an elongated sandwich consisting of two twisted antiparallel β -sheets. In the structure under consideration, the replacement of Arg32 by His residue occurs in the loop region 29–36 located between two β strands *a* and *a'* (Fig. 3). This region is of functional importance for interactions with receptors [20]. The least-squares superposition of the H32-TNF- α structure to the known structures of native TNF- α , its mutant forms [20, 23–25], and the TNF- β -*p55* complex [26] are indicative of a certain conformational and positional lability of the loop 29–36. This lability is characterized by the RMSD values for the C $^{\alpha}$ atoms ranging from 0.44 to 0.91 Å (Table 3).

Analysis of the models built from the TNF- β -*p55* complex by replacing the TNF- β molecule by the molecules of native TNF- α and the H32-TNF- α mutant demonstrated that the pattern of the interactions between loop 29–36 of TNF- α and receptor *p55* is somewhat different from that observed for equivalent loop 46–53 in the TNF- β -*p55* complex. However, in both cases, the numbers of stabilizing interactions remain at the same level (Table 4). In principle, the replacement of Arg32 by His residue has no substantial effect on the general character of interactions in this local region. Nevertheless, the selective evaluation of the Coulomb energy of interactions between these residues and the receptor indicates that the recognition of arginine is favored over that of histidine. These results confirmed the experimental evidence that the H32-TNF- α mutant has a rather satisfactory ability to bind the *p55* receptor, although one would expect a slight decrease in the selectivity of its binding in comparison with native TNF- α . The latter conclusion is indirectly confirmed by a noticeable decrease in the cytotoxic activity of this mutant form [1].

The rather high homology between the amino-acid sequences ($\sim 30\%$) of the extracellular domains (residues 1–153) of the *p55* and *p75* receptors presupposes a similar backbone folding [42]. The model analysis showed that the regions of the receptors interacting with the residue in position 32 of TNF- α are absolutely identical (the Glu56, Cys70, Leu71, Ser72, and Cys73 residues), which, by analogy with the *p55* receptor, indicates that the character of the binding of native TNF- α with the *p75* receptor is similar to that of the mutant.

ACKNOWLEDGMENTS

This study was supported by the Russian Foundation for Basic Research, project no. 01-04-48174.

REFERENCES

1. L. N. Shingarova, L. N. Sagaridak, R. L. Turetskaya, *et al.*, *Bioorg. Khim.* **22**, 243 (1996).
2. W. B. Coley, *Am. J. Med. Sci.* **105**, 487 (1893).
3. L. J. Old, *Science* **230**, 630 (1985).
4. E. A. Carswell, L. J. Old, R. L. Kassel, *et al.*, *Proc. Natl. Acad. Sci. USA* **72**, 3366 (1975).
5. B. Beutler, D. Greenwald, J. D. Hulmes, *et al.*, *Nature* **316**, 552 (1985).
6. G. E. Nedwin, S. L. Naylor, A. Y. Sakaguchi, *et al.*, *Nucleic Acids Res.* **13**, 6361 (1985).
7. N. L. Paul and N. H. Ruddle, *Annu. Rev. Immunol.* **6**, 407 (1988).
8. B. Beutler, *Tumor Necrosis Factors: The Molecules and Their Emerging Role in Medicine* (Raven Press, New York, 1992).
9. H. Loetscher, Y.-C. E. Pan, H. W. Lahm, *et al.*, *Cell* **61**, 351 (1990).
10. T. J. Shall, M. Lewis, K. J. Koller, *et al.*, *Cell* **61**, 361 (1990).
11. C. A. Smith, T. Davis, D. Anderson, *et al.*, *Science* **248**, 1019 (1990).
12. C. Brakebusch, Y. Nophar, O. Kemper, *et al.*, *EMBO J.* **11**, 943 (1990).
13. L. A. Tartaglia, R. F. Weber, I. S. Figari, *et al.*, *Proc. Natl. Acad. Sci. USA* **88**, 9292 (1991).
14. L. A. Tartaglia and D. V. Goeddel, *J. Biol. Chem.* **267**, 4304 (1992).

15. F. Mackay, H. Loetscher, G. Gehr, *et al.*, *J. Exp. Med.* **177**, 1277 (1992).
16. K. M. Thorp, C. Southern, I. N. Bird, and N. Matthews, *Cytokine* **4**, 313 (1992).
17. U. Trefzer, M. Brockhaus, H. Loetscher, *et al.*, *J. Invest. Dermatol.* **97**, 911 (1992).
18. S. Schutze, K. Potthof, T. Machleidt, *et al.*, *Cell* **71**, 765 (1992).
19. C. H. W. Wong, J. H. Elwell, L. W. Oberley, and D. V. Goeddel, *Cell* **58**, 923 (1989).
20. M. J. Eck and S. R. Sprang, *J. Biol. Chem.* **264**, 17 595 (1989).
21. M. J. Eck, M. Ultsch, E. Rinderknecht, *et al.*, *J. Biol. Chem.* **267**, 2119 (1992).
22. E. Y. Jones, D. I. Stuart, and N. P. C. Walker, *Nature* **338**, 225 (1989).
23. S. S. Cha, J. S. Kim, H. S. Cho, *et al.*, *J. Biol. Chem.* **273** (4), 2153 (1998).
24. C. Reed, Z. Q. Fu, J. Wu, *et al.*, *Protein Eng.* **10**, 1101 (1997).
25. F. C. Bernstein, T. F. Koetzle, G. J. Williams, *et al.*, *J. Mol. Biol.* **112**, 535 (1977).
26. D. W. Banner, A. D'Arcy, W. Janes, *et al.*, *Cell* **73**, 431 (1993).
27. D. Pennica, W. J. Kohr, B. M. Fendly, *et al.*, *Biochemistry* **31**, 1134 (1992).
28. H. Loetscher, R. Gentz, M. Zulauf, *et al.*, *J. Biol. Chem.* **269**, 18 324 (1994).
29. A. D'Arcy, D. W. Banner, W. Janes, *et al.*, *J. Mol. Biol.* **229**, 555 (1993).
30. M. R. Shalaby, A. Sundan, H. Laetscher, *et al.*, *J. Exp. Med.* **172**, 1517 (1990).
31. R. Kircheis, J. Milleck, V. G. Korobko, *et al.*, *Immunology* **76**, 433 (1992).
32. C. R. Goh, C. S. Loh, and A. G. Porter, *Protein Eng.* **4**, 385 (1991).
33. X. Van Ostade, J. Tavernier, T. Prange, and W. Fiers, *EMBO J.* **10**, 827 (1991).
34. H. Loetscher, D. Stueber, D. Banner, *et al.*, *J. Biol. Chem.* **268**, 26 350 (1993).
35. M. J. Eck, B. Beutler, G. Kuo, *et al.*, *J. Biol. Chem.* **263**, 12 816 (1988).
36. B. W. Matthews, *J. Mol. Biol.* **33**, 491 (1968).
37. A. T. Brunger, P. D. Adams, G. M. Clore, *et al.*, *Acta Crystallogr., Sect. D: Biol. Crystallogr.* **54**, 905 (1998).
38. T. O. Yeates, *Methods Enzymol.* **276**, 344 (1997).
39. A. T. Brunger, *X-PLOR (Version 3.1/3.851) Manual* (Yale University, New Haven, 1992).
40. T. A. Jones, *J. Appl. Crystallogr.* **11**, 268 (1978).
41. P. V. Luzzati, *Acta Crystallogr.* **5**, 802 (1952).
42. Z.-Q. Fu, R. W. Harrison, C. Reed, *et al.*, *Protein Eng.* **8**, 1233 (1995).

Translated by T. Safonova

REAL CRYSTAL
STRUCTURE

Study of Characteristics of Plastic Deformation in Amorphous Fe–Cr–Mo–V–B–Si Alloy by the Method of Local Deformation

M. N. Vereshchagin*, V. G. Shepelevich**, O. M. Ostrikov*, and S. N. Tsybrankova*

* State Technological University, Gomel, Belarus

** Belarussian State University, Minsk, Belarus

Received October 5, 2001

Abstract—Characteristics of plastic deformation in the amorphous Fe–Cr–Mo–V–B–Si alloy have been studied by the method of local deformation. It is established that plastic deformation in the rapidly quenched iron-based alloy proceeds by two channels. The model for interpreting the energy aspects of plastic deformation in amorphous materials is suggested. © 2002 MAIK “Nauka/Interperiodica”.

INTRODUCTION

The well-known methods of extension and contraction are often inapplicable to the studies of plastic deformation in amorphous ribbons prepared by rapid quenching because of the high brittleness and small thicknesses of these ribbons. Therefore, the development of a convenient precision method for studying pronounced plastic deformation in amorphous alloys is an important problem. Another interesting problem is the detailed study of the characteristics of plastic deformation in the amorphous alloy in the Fe–Cr–Mo–V–B–Si system, because the nature of defects formed during the deformation of amorphous materials is still not quite clear.

EXPERIMENTAL

The starting material for preparing an amorphous metal ribbon in the process of rapid quenching of the melt was the alloy in the Fe–Cr–Mo–V–B–Si system. Vacuum melting of the charge and its subsequent rapid quenching allowed us to obtain 15-mm-wide amorphous ribbons. Alloy was melted in a crucible in the form of a quartz tube with a 0.25- to 0.30-mm-long slot under excessive argon pressure (0.2–0.5 MPa). The melt temperature was recorded by a Krok-2 pyrometer with an accuracy of $\pm 2^\circ\text{C}$. The angular velocity of the copper disk-crystallizer of radius 0.35 m ranged from 50 to 60 rps and was recorded by a PDF-1 angle-data transmitter in the control system with an electric drive of a type SEU-7885. The ribbon thickness varied from 30 to 80 μm . The rate of ribbon cooling was $8 \times 10^5 \text{ }^\circ\text{C/s}^{-1}$.

The X-ray diffraction analysis was performed on a DRON-3 diffractometer (monochromatic CuK_α radiation) at the following parameters: voltage 30 kV, current 20 mA, counter rate 2 deg/min. The standard was

the initial alloy of the above composition annealed at 850°C .

The structure was studied in an optical Neophot-21 microscope and a CamScan-4 scanning electron microscope.

The characteristics of plastic deformation in the Fe–Cr–Mo–V–B–Si alloy were studied by the method of local deformation of the surface, which reduced to deformation of an amorphous material by the Vickers pyramid of a PMT-3 device [1–3]. Using a CamScan-4 microscope, we obtained the micrographs of typical plastic-deformation patterns in an amorphous alloy; then the geometric parameters of plastic deformation were measured.

EXPERIMENTAL RESULTS AND THEIR DISCUSSION

X-ray diffraction studies showed that the Fe–Cr–Mo–V–B–Si alloy is amorphous under X-ray radiation, which is seen from the absence of the diffraction peaks at angles $2\theta > 45^\circ$.

The typical deformation patterns around the depression produced by the Vickers pyramid on the surface of the amorphous Fe–Cr–Mo–V–B–Si alloy under an applied load of up to 1 N are shown in Fig. 1. One can see the system of scalelike shears around the indentation.

With an increase in the load applied to the indenter, a new type of defect is formed (Fig. 2)—the rays propagating from the depression made by the indenter, which, in fact, are the bands of shear of one part of the material with respect to another.

The quantitative and geometrical characteristics of these signs of plastic deformation in the amorphous Fe–Cr–Mo–V–B–Si alloy are shown in Figs. 3–5. It is seen from Fig. 3 that the number of scale pileups formed due

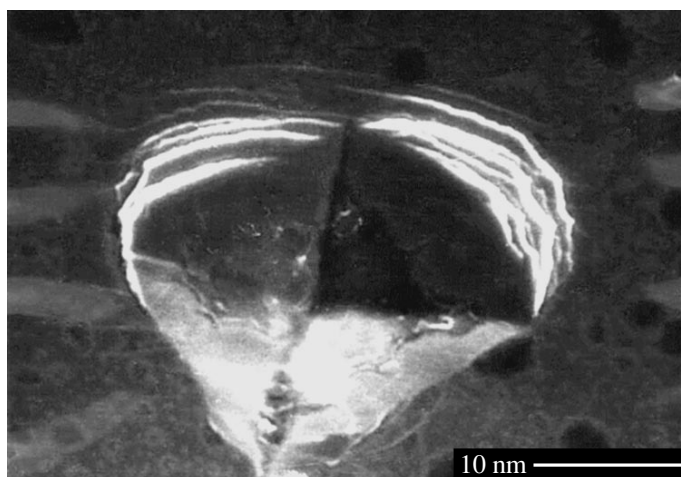


Fig. 1. Scale pileups around the indenter depression.

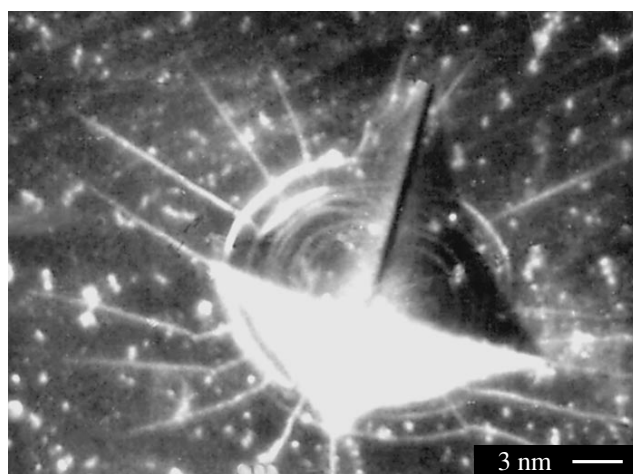


Fig. 2. Shear bands. The micrograph was obtained in a CamScan-34 scanning electron microscope.

to shear N_{sp} per one indentation first increases with an increase in the load applied to the indenter (up to 1 N) and then decreases; in other words, the function $N_{sp} = f(P)$ has an extremum, which is often evidence of the

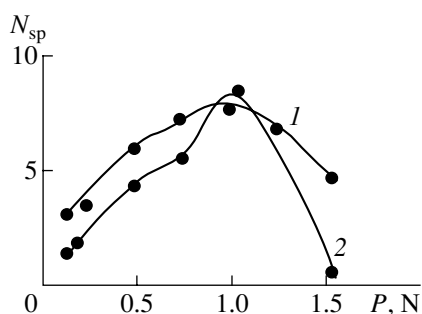


Fig. 3. The average number N_{sp} of scale pileups as a function of load P applied to the indenter. (1) The ribbon side which in the process of its preparation was in contact with air, (2) the ribbon side which in the process of its preparation was in contact with the copper disk-crystallizer.

occurrence of two or several competing processes such that different processes dominate at different stages of deformation [4]. In our case, the formation of scale pileups (Fig. 1) compete with the formation of shear bands (Fig. 2) under loads exceeding 1 N (Figs. 4 and 5).

The appearance of a new channel of plastic deformation results in the redistribution of the deformation energy between the scale pileups and shear bands. As a result, less energy is consumed for the formation of defects shown in Fig. 1, and, thus, the number of these defects decreases.

The formation of defects shown in Fig. 2 under pronounced loads seems to be associated with the higher critical stresses of their formation in comparison with the critical stresses necessary for the formation of scale pileups.

As is seen from Figs. 4 and 5, the dependences of the average number of shear bands, N_{sb} , on the load applied to the indenter and the average length of the glide trace,

L_{sb} , on the load applied to the indenter are similar. Prior to the application of a 1-N-load to the indenter, the number of shear bands and their lengths are equal to zero; then, these parameters continue increasing linearly.

It should be indicated that the experimental dependences $N_{sp} = f(P)$, $N_{sb} = f(P)$, and $L_{sb} = f(P)$ are different for the two sides of the ribbon. The number of scale pileups around the indenter offset formed on the ribbon side which was in contact with air in the process of its preparation is considerably larger than on the other side of the ribbon. On the contrary, the number of shear bands due to deformation was larger if the indenter was applied to the side of the ribbon that, in the process of its preparation, was in contact with the copper disk-crystallizer. Moreover, on this side of the ribbon, shear bands started forming under lower load values (of the order of 0.75 N). The increment in the number and the length of shear bands is also larger on the ribbon side which was in contact with the disk-crystallizer during the ribbon preparation.

Now, consider the mechanisms of the formation of defects shown in Figs. 1, 2. It is well known that, during shear in single-crystal materials, the atoms in the shear plane occupy the sites of the neighboring atoms but the material preserves its structure and the shear plane has only a small number of defects [5]. The situation is quite different if the shear takes place in an amorphous material. Generally speaking, in this case, atoms cannot occupy the sites of the neighboring atoms. This results in local changes in their density in the shear plane. As was shown in [6], this creates favorable conditions for the formation of micropores in the shear plane (Fig. 6). Along with micropores, there are also the regions of cohesion of the amorphous-material parts lying on different sides of the shear plane (Fig. 6). Obviously, the cohesion-force value in these regions shown in Fig. 6 is much lower than the cohesion-force value in the defect-free region of the amorphous material, because the area of the cohesion region in the shear plane is finite and rather small. As a result, at considerable deformation stresses when the shear plane emerges at the surface, this cohesion practically cannot be detected, because the external stresses are so high that it is almost impossible to prevent a further shear, which results in the separation of weakly bound cohesion regions and the opening of a crack propagating along the shear plane [6].

Thus, the formation of shear bands proceeds in four stages: (1) the appearance of local plastic flow and the activation of the sources of the formation of shear bands; (2) nucleation and development of shear bands with the formation of micropores and regions where parts of the material located on different sides of the shear are bound by cohesion forces; (3) the emergence of the shear bands to the surface; and (4) the fracture of the cohesion regions with a further increase in external stresses.

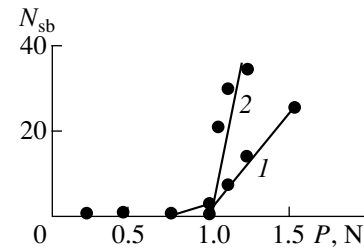


Fig. 4. The average number N_{sb} of shear bands as a function of load P applied to the indenter. (1) The ribbon side that was in contact with air, (2) the ribbon side that was in contact with the copper disk-crystallizer.

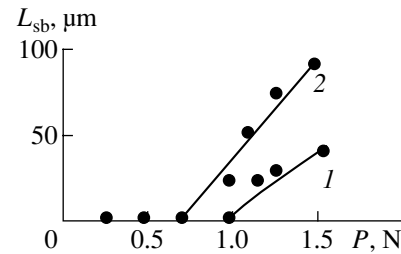


Fig. 5. The average length of glide traces L_{sb} as a function of load P applied to the indenter. (1) The ribbon side that was in contact with air, (2) the ribbon side that was in contact with the copper disk-crystallizer.

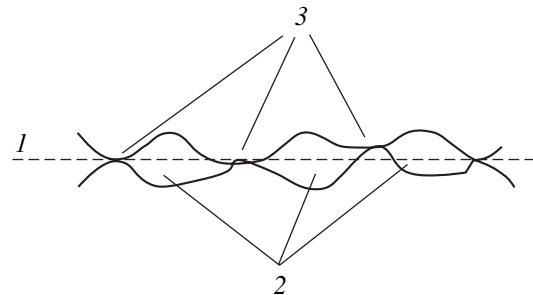


Fig. 6. Schematic representation of the shear-band in an amorphous material. (1) Trace of the shear plane, (2) pores, (3) the sites of cohesion of the parts of an amorphous material located on different sides of the shear plane.

In turn, the last stage can proceed in several steps. At the first step, the primary shear takes place, as a result of which the pores and cohesion regions are formed. If the shear band does not emerge to the surface as in the case of the local deformation observed in our case, the cohesion regions can increase because of diffusion and pronounced material compression in the shear plane. If the shear band emerges to the surface, these forces are somewhat less pronounced because of the absence of the compressive-stress localization at the top of the shear band.

Slight material deformation after the emergence of the shear band to the surface at the second step results in the formation of shear bands in the cohesion regions

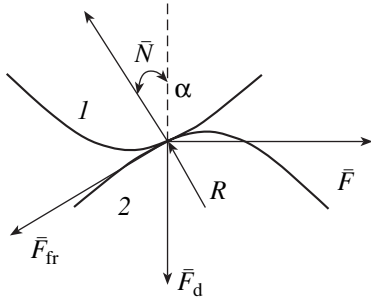


Fig. 7. Schematic illustrating the calculation of the energy of formation of shear bands and scale pileups.

of the primary band. At this step, new cohesion regions can form, especially under high compressive stresses. Under quasi-static loading, the shear bands in the cohesion regions can repeatedly form until the formation of a crack and its opening. The development of the crack is more probable in the presence of pores and misfit stresses formed because the displaced atoms in amorphous materials cannot occupy the sites of the neighboring atoms as in single crystals.

At high deformation stresses, crack formation can also happen at the first step of the fourth stage of formation of the shear-band. At extremely high stresses, cracks can also be nucleated at the third and fourth stages.

It should be indicated that the formation of scale pileups is similar to the formation of shear bands with the only difference that, according to [7], in the approximation of the quasi-static loading and an ideal elastic-plastic medium, scale pileups can be formed under conditions of hydrostatic compression of the material fulfilled in the vicinity of the indenter. The emergence of the scales to the surface occurs along the glide lines [7] that describe the stressed state in the vicinity of the indenter, which suggests that this process is more energetically favorable at the initial stage of deformation than the formation of shear bands in the form of rays propagating from the indenter.

Now, consider the energy aspect of the defect formation during deformation. In our case, the general energy balance can be written as

$$W_d = W_{sb} + W_{sp} + W_{oth}, \quad (1)$$

where W_d is the deformation energy, W_{sb} is the energy of formation of shear bands, W_{sp} is the energy of formation of scale pileups, and W_{oth} is the energy losses for the formation of other channels of plastic deformation not considered in this study.

According to [7], in the approximation of quasi-static loading and an ideally plastic medium, the material in the vicinity of the indenter during deformation is under

conditions of hydrostatic compression. Therefore, the deformation energy is determined by the relationship

$$W_d = \frac{1}{2E} \left(\frac{P}{S} \right)^2 V, \quad (2)$$

where E is the Young's modulus, P is the load applied to the indenter, S is the area of the depression projection onto the plane normal to the direction of loading, and V is the volume of the deformed material. In our case,

$$S = \frac{d^2}{2}, \quad V = \frac{d^3}{42}, \quad (3)$$

where d is the length of the diagonal of the depression produced by the indenter on the surface of the amorphous material, which is related to the depth of the indenter penetration into the material h , as $d = 7h$.

In order to determine W_{sb} and W_{sp} , consider Fig. 7. Elements 1 and 2 in Fig. 7 are the contacting parts of the shear band (Fig. 6) located on the different sides of this band. In the first approximation, during the formation of a pore under the action of an external force F , element 1 covers a distance equal to a quarter-circumference of the radius equal to the curvature radius R of element 2. The internal-friction force F_{fr}^* does the work

$$A_{fr} = \frac{\pi}{2} F_{fr} R. \quad (4)$$

The potential energy E_1 of the lift of element 1 on top of element 2 is determined by the force of pressure of element 1 onto element 2, F_d^* . Then, under the approximation that element 2 in the section normal to the shear plane has the shape of half-circumference of radius R , we can write

$$E_1 = F_d R. \quad (5)$$

Taking into account that $F_{fr} = \mu N$ and $F_d = N \cos \alpha$ (where α is the angle formed by the directions of the action of the force F_d^* and the response to this action N^* (Fig. 7) and μ is the friction coefficient for elements 1 and 2), we obtain from Eq. (5)

$$dE_1 = -\frac{\sin \alpha}{\mu} F_{fr} R d\alpha. \quad (6)$$

Performing the integration in Eq. (6) with respect to α within the limits from $\frac{\pi}{2}$ to zero, we arrive at

$$E_1 = \frac{1}{\mu} F_{fr} R. \quad (7)$$

Summing up Eqs. (4) and (7), we obtain the energy of formation of the i th relative displacement of two elements located on different sides of the shear plane as

$$(W_{sb})_i = \left(\frac{\pi}{2} + \frac{1}{\mu} \right) F_{fr} R. \quad (8)$$

Now, assume that all the elements of type 2 (Fig. 7) that form the shear plane have approximately the same dimension R as the element considered above. We also assume that, during formation of a shear band, the unit displacement by distance R takes place. Then, Eq. (8) for the energy of the unit shear takes the form

$$(W_{\text{sb}})_1 = n \left(\frac{\pi}{2} + \frac{1}{\mu} \right) F_{\text{fr}} R, \quad (9)$$

where n is the number of elements of type 2 in a single shear band.

Multiplying Eq. (9) by the number of shear bands formed in the vicinity of the indenter N , and assuming that all these bands are of the same length, we obtain

$$W_{\text{sb}} = nN \left(\frac{\pi}{2} + \frac{1}{\mu} \right) F_{\text{fr}} R. \quad (10)$$

In the above equation, $N = N_{\text{sb}}$ (Fig. 4). Taking into account that, according to the above model, $L_{\text{sb}} = 2nR$, we can pass in Eq. (10) to the quantities that can be determined experimentally:

$$W_{\text{sb}} = \frac{1}{2} \left(\frac{\pi}{2} + \frac{1}{\mu} \right) L_{\text{sb}} N_{\text{sb}} F_{\text{fr}}. \quad (11)$$

Assuming that the mechanism of formation of scale pileups is similar to that of the formation of shear bands and using Eq. (11) for W_{sp} , we can write

$$W_{\text{sp}} = \frac{1}{2} \left(\frac{\pi}{2} + \frac{1}{\mu} \right) L_{\text{sp}} N_{\text{sp}} F_{\text{fr}}. \quad (12)$$

Now, substituting Eqs. (2), (10), and (11) into Eqs. (1), we obtain

$$\frac{1}{E} \left(\frac{2P}{d^2} \right)^2 \frac{d^3}{42} \quad (13)$$

$$= \left(\frac{\pi}{2} + \frac{1}{\mu} \right) F_{\text{fr}} (L_{\text{sb}} N_{\text{sb}} + L_{\text{sp}} N_{\text{sp}}) + W_{\text{oth}},$$

whence it follows that

$$F_{\text{fr}} = \xi / (L_{\text{sb}} N_{\text{sb}} + L_{\text{sp}} N_{\text{sp}}), \quad (14)$$

$$\text{where } \xi = \left(\frac{1}{E} \left(\frac{2P}{d^2} \right)^2 \frac{d^3}{42} - W_{\text{oth}} \right) / \left(\frac{\pi}{2} + \frac{1}{\mu} \right).$$

In the above equation, we managed to determine the quantities L_{sb} , N_{sb} , and N_{sp} experimentally (Figs. 3–5). The quantity L_{sb} can also be determined experimentally from the following expression:

$$L_{\text{sp}} \approx \frac{\pi}{4} d, \quad (15)$$

where it is assumed that the length of the scale pileup is equal to a quarter-circumference of the diameter close to d .

Taking into account that in [8]

$$P = \frac{Hd^2}{49k}, \quad (16)$$

where H is microhardness, k is the geometrical parameter (equal to $k = 0.03797$ for a Vickers pyramid), the quantity ξ can be conveniently written in the form $\xi =$

$$\left(\frac{1}{42E} \left(\frac{2H}{49k} \right)^2 \left(\frac{49kP}{H} \right)^{\frac{3}{2}} - W_{\text{oth}} \right) / \left(\frac{\pi}{2} + \frac{1}{\mu} \right),$$

and expression (15) can be written as $L_{\text{sp}} \approx \frac{7\pi}{4} \sqrt{\frac{kP}{H}}$. The character of the dependences of L_{sb} , N_{sb} , and N_{sp} on P can be chosen based on the experimental curves shown in Figs. 3–5. In our case, we have

$$N_{\text{sb}} = P(b_1 - a_1 P), \quad (17)$$

$$N_{\text{sb}} = 0, \quad \text{for } P < 100 \text{ g}, \quad (18)$$

$$N_{\text{sb}} = a_2 P - b_2, \quad \text{for } P > 1 \text{ N},$$

$$L_{\text{sb}} = 0, \quad \text{for } P < 100 \text{ g}, \quad (19)$$

$$\text{and } L_{\text{sb}} = a_3 P - b_3, \quad \text{for } P > 1 \text{ N},$$

where a_1 , a_2 , a_3 and b_1 , b_2 , b_3 are the empirical coefficients determined from Figs. 3–5.

Substituting Eqs. (15) and (17)–(19) into Eq. (14), we obtain that at $P < 1 \text{ N}$

$$F_{\text{fr}} = \frac{\alpha P \sqrt{P} - W_{\text{oth}}}{\beta \gamma P \sqrt{P} (b_1 - a_1 P)}; \quad (20)$$

and at $P > 1 \text{ N}$

$$F_{\text{fr}} = \frac{\alpha P \sqrt{P} - W_{\text{oth}}}{\beta (\gamma P \sqrt{P} (b_1 - a_1 P) + (a_2 P - b_2)(a_3 P - b_3))}. \quad (21)$$

In Eqs. (20) and (21), $\alpha = \frac{1}{42E} \left(\frac{2H}{49k} \right)^2 \left(\frac{49k}{H} \right)^{\frac{3}{2}}$ and

$$\beta = \frac{\pi}{2} + \frac{1}{\mu}, \quad \gamma = \frac{7\pi}{4} \sqrt{\frac{k}{H}}.$$

Taking into account that $E \approx 1.7 \times 10^{11} \text{ N/m}^2$, $H \approx 15.0 \text{ GPa}$, and $\mu \approx 0.1$, we obtain the following values of the above parameters: $\alpha \approx 0.3 \text{ N}^{-\frac{1}{2}} \text{ m}$, $\beta \approx 11.6$, $\gamma \approx 9.4 \times 10^{-6} \text{ N}^{-\frac{1}{2}} \text{ m}$. Taking into account these values and assuming that $b_1 = 2a_1 = 2$, $a_2 = b_2 = 1$, and $a_3 = b_3 = 10^{-4} \text{ m}$ at $P = 1 \text{ N}$, we can construct the theoretical curves $|F_{\text{fr}}^*| = f(P)$ (where $F_{\text{fr}}^* = \beta F_{\text{fr}}$). In the absence of shear bands, these curves at $W_{\text{oth}} = 0, 1, \text{ and } 5 \text{ J}$ are shown in Fig. 8. It is seen that at the initial stage the friction force (proportional to the

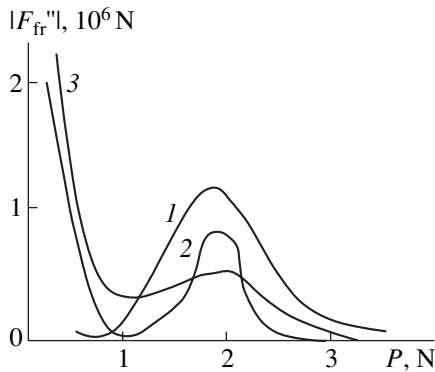


Fig. 8. Dependences $|F_{fr}^*| = f(P)$ at different values of W_{oth} : (1) 0, (2) 1, and (3) 5 J.

compression force of the material parts on both sides of the shear plane) has rather high values. Then, with an increase in the load up to the value providing the formation of shear bands, the friction force falls to zero and, thus, activates the channels of plastic deformation. A further increase in the load promotes an increase in $|F_{fr}^*|$ and reduces the probability of formation of new scale pileups.

The curve $|F_{fr}^*| = f(P)$ in the case of formation of shear bands has a similar shape to that of the curve in Fig. 8 (in this case, the maximum observed at a load of 2 N is higher by an order of magnitude than that observed in the formation only of scale pileups). Therefore, upon the application of a 1-N load to the indenter, the formation of new scale pileups becomes less probable. Experimentally, this can be seen from the residual deformation pattern, where the shear bands and scale pileups are indented by the indenter, as is shown in Fig. 2.

CONCLUSION

Thus, applying the method of local deformation to studying plastic deformation in the amorphous Fe–Cr–Mo–V–B–Si alloy, we established that deformation proceeds along two channels—the formation of shear bands and the formation of scale pileups. We also established the stages of inclusion of these channels into the process of plastic deformation: first, scale pileups are formed and only then, shear bands. It is shown theoretically that the activation of plastic deformation by the formation of shear bands takes place only within a certain range of loads applied to the indenter (about 1 N).

REFERENCES

1. O. M. Ostrikov, *Zh. Tekh. Fiz.* 70 (12), 39 (2000) [*Tech. Phys.* **45**, 1549 (2000)].
2. O. M. Ostrikov, *Fiz. Met. Metalloved.* **90** (1), 91 (2000).
3. O. M. Ostrikov, *Fiz. Met. Metalloved.* **89** (5), 106 (2000).
4. V. S. Savenko and O. M. Ostrikov, *Izv. Akad. Nauk Belarusi, Ser. Fiz.-Mat. Nauk*, No. 2, 96 (1998).
5. J. P. Hirth and J. Lothe, *Theory of Dislocations* (McGraw-Hill, New York, 1967; Atomizdat, Moscow, 1972).
6. A. M. Glezer and B. V. Molotilov, *Structure and Mechanical Properties of Amorphous Alloys* (Metallurgiya, Moscow, 1992).
7. K. Johnson, *Contact Mechanics* (Cambridge Univ. Press, Cambridge, 1987; Mir, Moscow, 1989).
8. A. M. Korsunsky, M. R. McGurk, S. J. Bull, and T. F. Page, *Surf. Coat. Technol.* **99**, 171 (1998).

Translated by L. Man

REAL CRYSTAL
STRUCTURE

Serrated Plastic Deformation in LiF Single Crystals at High Temperatures

N. P. Skvortsova

Shubnikov Institute of Crystallography, Russian Academy of Sciences,
Leninskii pr. 59, Moscow, 117333 Russia

e-mail: skvor@ns.crys.ras.ru

Received October 16, 2001

Abstract—The serrated plastic flow in LiF single crystals has been studied in the mode of active deformation at high temperatures ($T = 573$ – 1093 K). The parameters of the jumps in the deforming stresses (normalized amplitude and relaxation time of stress oscillations) were determined at the stage of strain softening under conditions of uniaxial compression and tension. It was shown that the jump parameters are essentially dependent on the type of the stressed state and the deformation temperature. The activation energy of serrated deformation in shear bands was established to be close to the migration energy for cation vacancies. © 2002 MAIK “Nauka/Interperiodica”.

INTRODUCTION

During the last two decades, the high-temperature localization of plastic strains has widely attracted the attention of researchers. This phenomenon can be described as the stain-induced stratification of crystals at temperatures exceeding $0.5T_m$ and the formation of highly strained domains (localized shear bands, LSBs) with shear strains of the order of $\sim 10^3$ – $10^4\%$ within the practically unstrained matrix [1–7]. These crystallographic shear strains arise in crystals with various types of crystal lattice [6, 8] and are associated with the formation of a specific fine-grain dislocation structure [9, 10] in the zones of intense plastic flow of the material. It was found [11, 12] that the formation of LSBs occurs at the stage of steady-state flow in the absence of hardening (stage III of hardening) and stems from the local loss of plastic stability and the drastic decrease in material resistance. Earlier, the correlation between the oscillations in deforming stresses on the deformation curves and the number of LSBs was established [13]. The systematic detailed study of the relations between plastic instability, the fluctuations of deforming stresses, and the rate of shear deformation is very important for understanding the physical mechanisms underlying the formation of localized shear bands. In the present paper, we analyze statistically the quasi-periodic oscillations in the deforming stresses on the diagrams of the uniaxial compression and tension of LiF single crystals deformed under high-deformations and temperatures ($T = 573$ – 1093 K or $(0.5$ – $0.96)T_m$).

EXPERIMENTAL TECHNIQUE

We studied LiF single crystals (0.002 wt % Mg) grown from melt, annealed for 60 h in air at 973 K, and

then slowly cooled. Samples cleaved along the cleavage planes in the shape of $\sim 4 \times 4 \times 20$ -mm³ rectangular bars were used in tensile tests; $\sim 5 \times 5 \times 10$ -mm³ samples were used in compression tests. The samples for tensile tests were fixed in the clamps by an adhesive mixture of liquid glass and kaolin [14], which provided a firm contact at all temperatures. The high-temperature tensile tests were performed in a special furnace with a heater made of electrical steel which was placed into the back-spacing with ruby cross-heads. This reduced the chemical interaction between samples and the material of cross-heads and reduced heat losses at the end faces at high temperatures. The temperature gradient in the 90-mm-long working zone of the furnace did not exceed $\pm 2\%$. All the experiments were performed under atmospheric pressure in air. The samples were deformed along the [001] direction at a constant clamp speed of about 0.83×10^{-6} m/s in the temperature range $T = (0.5$ – $0.96)T_m$ up to large strains using the Ingstrom testing machine. The testing machine rigidity was about 720 kg. wt./mm. The load was measured with an accuracy of ± 5 g. wt. The parameters of the serrated deformation were determined at the stage of strain softening at deformation $\varepsilon \cong 15\%$ from the deformation curves (Fig. 1). The depth of large stress jumps, $\Delta\sigma_{\text{ext}}$, was normalized to the value of the maximum deforming stress, σ_u , for each stress oscillation. The times of the stress oscillations, Δt , were determined as the time intervals between pronounced stress jumps correlating with nucleation and the evolution of shear strains in LSBs. The accuracy of the measurements of amplitudes and relaxation times of oscillations in deforming stresses was about 10%.

The statistical distributions of the amplitudes and the relaxation periods of stress oscillations corresponding to the plastic flow in LSBs were analyzed within the

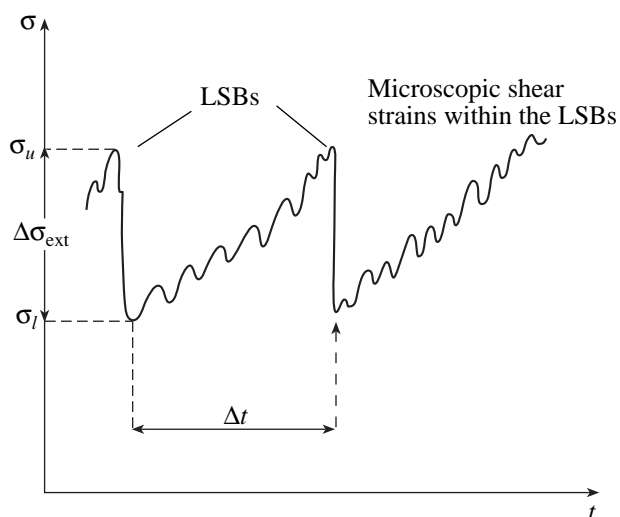


Fig. 1. Schematic illustrating oscillations in deforming stresses corresponding to LSBs and microscopic shear strains within LSBs. The parameters characterizing serrated deformation are indicated; σ_u and σ_l are the maximum and minimum stresses, respectively, $\Delta\sigma_{\text{ext}}$ is the amplitude of stress jump.

temperature range 573–1093 K. We also calculated the distributions of the deformation parameters for microscopic shear strains in LSBs within the temperature range 973–1093 K. The total volumes of the statistical sample n for each investigated parameter of serrated deformation in different temperature ranges are indicated in the table. The structure of the deformed samples was studied by the methods of selective chemical etching, and optical and interferometric microscopy.

The LSBs were identified using the glide steps at the side faces of the sample under oblique illumination in a Neophot microscope.

EXPERIMENTAL RESULTS AND DISCUSSION

Under conditions of high-temperature deformation, the compression and tension diagrams exhibit oscillations in the deforming stress with different amplitudes, which indicates the pronounced nonuniformity of the plastic flow. Typical examples of stress oscillations on the compression diagram of a LiF single crystal at strain rate $\dot{\epsilon}_a = 0.92 \times 10^{-4} \text{ s}^{-1}$ and $T = 1043 \text{ K}$ are shown in Fig. 2. The yield drop is followed by the range of serrated flow almost without any hardening, which extended up to the strain value $\epsilon \cong 25\%$. Quasi-periodic oscillations in deforming stresses with relatively large jump parameters ($\Delta\sigma/\sigma$ and Δt) correspond to the well-developed LSBs (Figs. 1, 2a). The instabilities in the microscopic flow in LSBs are also reflected in the deformation curves as oscillations with very low values of the jump parameters corresponding to microscopic shear strains within the LSBs. Comparing the data obtained on different samples, we established that the characteristics of the periodic stress jumps on deformation curves are independent of the strain magnitude. In the range of large strains ($\epsilon > 25\%$), the identification of LSBs is rather difficult, since the stress oscillations are irregular, which can be explained by the possible destruction of the material in the zones of its intense plastic flow (Fig. 2b).

The parameters of serrated deformation are strongly dependent on the stressed state and the temperature

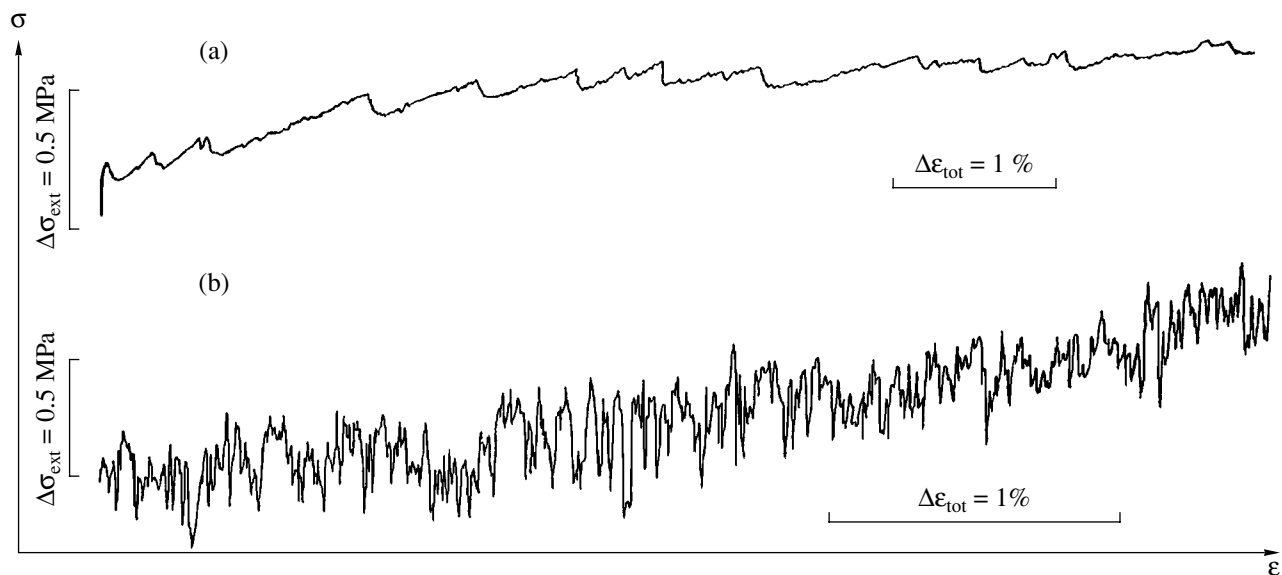


Fig. 2. Deformation curves corresponding to the compression of a LiF crystal at $T = 1043 \text{ K}$, $\dot{\epsilon}_a = 0.92 \times 10^{-4} \text{ s}^{-1}$, and at the total average strain (a) $\epsilon \cong 7\%$ and (b) $\epsilon \geq 25\%$; $\Delta\epsilon_{\text{tot}}$ is the total strain.

maintained in the course of the experiment. The examples of statistical distributions of amplitudes and relaxation times of stress oscillations corresponding to the localized plastic flow in LSBs under uniaxial compression and tension are shown in Fig. 3. It is clearly seen that these distributions are asymmetric (elongated toward the oscillations with relatively high values of the jump parameters). The asymmetry becomes more pronounced at higher deformation temperatures. The mean relative amplitudes $\langle \Delta\sigma/\sigma \rangle$ of the stress jumps corresponding to the local shear strains in LSBs (vertical lines in Figs. 3a and 3b) are about 3 and 6% for compression and tension, respectively, at $T = 0.85T_m$. The maximum oscillation amplitude increases from ~ 12 to $\sim 20\%$ in the transition from compression to tension. Also, the amplitude of stress oscillations corresponding to LSBs is about an order of magnitude higher than that of stress oscillations corresponding to microscopic shear strains in LSBs (Fig. 2a). Under the given experimental conditions, the mean relaxation times $\langle \Delta t \rangle$ are equal to about 87 and 190 s, respectively. We observed an approximate triple increase in the maximum relaxation time (from ~ 270 to 840 s) with the change in the experimental conditions (Figs. 3c, 3d).

The temperature dependences of $\langle \Delta\sigma/\sigma \rangle$ and $\langle \Delta t \rangle$ obtained by processing the data of the deformation curves for LiF crystals are shown in the Arrhenius coordinates in Fig. 4. In the temperature range under study, the amplitude of stress jumps dependent on the rates of formation and annihilation of dislocations exponentially increased with the temperature in both compression and tension experiments (Fig. 4a). An increase in the jump amplitudes was accompanied by an increase in $\langle \Delta t \rangle$ values (from several seconds in the temperature range $(0.5-0.7)T_m$ up to hundreds of seconds at $T > 0.7T_m$). Within a rather good approximation, the experimental data obtained can be described by the following equations:

$$\langle \Delta\sigma/\sigma \rangle = (\Delta\sigma/\sigma)_0 \exp(-U/kT), \quad (1)$$

$$\langle \Delta t \rangle = (\Delta t)_0 \exp(-U/kT), \quad (2)$$

where k is the Boltzmann constant, $(\Delta\sigma/\sigma)_0 \cong 40.5$ and $(\Delta t)_0 \cong 1.63 \times 10^5$ s are the constants characterizing the given material, and U is the activation energy corresponding to serrated deformation in LSBs. The activation energy determined from the slope of the dependences of $\ln\langle \Delta\sigma/\sigma \rangle$ and $\ln\langle \Delta t \rangle$ on $1/T$ is equal to about 0.6 eV (Figs. 4a, 4b). The parameters characterizing serrated high-temperature deformation correlate well with the discrete changes in the deformation relief and the dislocation-related microstructure in LSBs of the deformed samples. According to the experimental data on the evolution of the localized shear bands [13, 15], the rise L of the shear steps in the screw components of the LSBs ranged from about 4 to about 140 μm at temperatures $T = 673-1043$ K. The plots $\ln L$ versus $1/T$ showed that the experimental points fit a straight line

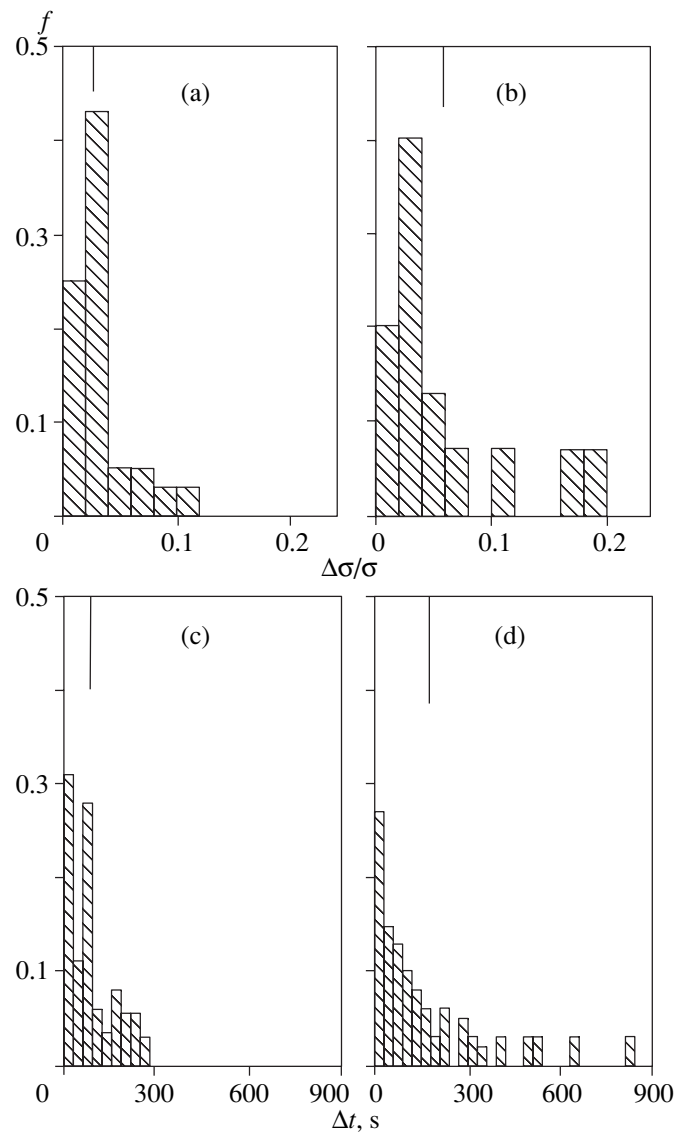


Fig. 3. Statistical distributions of oscillations in deforming stresses (corresponding to LSBs) over (a, b) the normalized amplitude and (c, d) period of stress oscillations under conditions of (a, c) uniaxial compression and (b, d) tension of the crystals at $T = 973$ K ($0.85T_m$) and $\epsilon = 15\%$ (for each distribution, vertical lines indicate the mean parameter values characterizing serrated deformation).

with the slope corresponding to activation energy U of the formation of the local shear strains in LSBs, $U = 0.57$ eV [15]. This confirms the correctness of the activation-energy value determined above and approximately agrees with the migration energy of cation vacancies in LiF (0.65 eV [16]).

Earlier experimental data on the parameters characterizing the activation of the high-temperature localization demonstrated that the rate of formation of local shear strains is controlled by the processes of dislocation climb and annihilation dependent on vacancy diffusion [15, 17]. As in [18], we first performed the quantitative analysis of serrated high-temperature deformation in LiF single crystals in the temperature range 573–

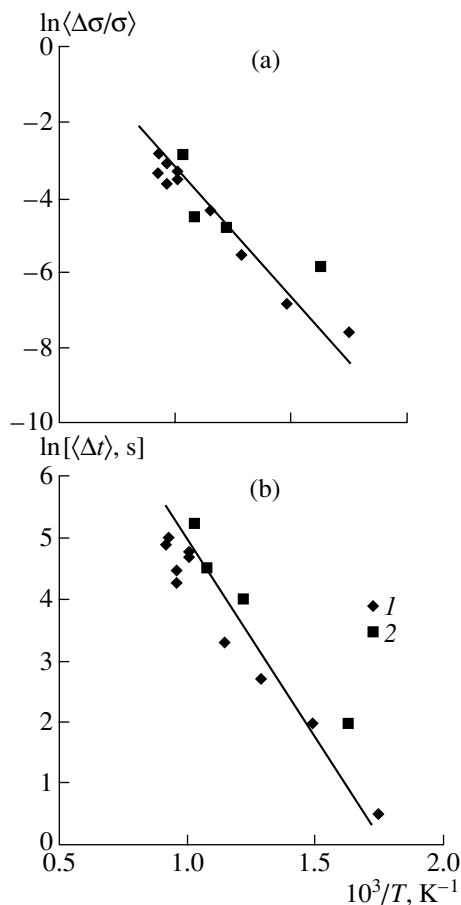


Fig. 4. Temperature dependence of (a) average values of normalized amplitudes and (b) period of stress oscillations in deforming stresses at the stage of steady-state flow in LSBs during (1) compression and (2) tension.

1093 K. It is shown that the parameters characterizing the stress jumps (amplitude, period of the stress oscillations) depend on the type of the stressed state and drastically increase in the transition from compression to tension. We also demonstrated the exponential form of the temperature dependences of the parameters characterizing the fluctuations in deforming stresses. The activation energies of serrated deformation and formation of a deformation relief (shear steps in LSBs) turn out to be close. This allows one to consider the approach to the study of LSBs suggested in the present paper as an *in situ* study of the high-temperature localization of plastic deformation.

Total volume of statistical sample, n , used in determination of the parameters characterizing serrated deformation of LiF crystals

Temperature of measurements (K)	T/T_m	Number of deformed samples	Number of measurements n
573–673	0.50–0.59	3	600
773–923	0.68–0.81	4	400
973–1093	0.85–0.96	7	250

Some results of this study were reported at the VI Interstate Seminar on the Structural Foundations of Material Modification by the Methods of Nontraditional Technologies (June 12–15, 2001, Obninsk, Russia) [18].

ACKNOWLEDGMENTS

The author is grateful to Prof. V.R. Regel and to Prof. V.I. Alshits for their interest in her study and fruitful discussion of the results.

REFERENCES

- G. V. Berezhkova, N. P. Skvortsova, V. R. Regel', and P. P. Perstnev, *Fiz. Tverd. Tela (Leningrad)* **26** (4), 1074 (1984) [*Sov. Phys. Solid State* **26**, 654 (1984)].
- G. V. Berezhkova, *Kristallografiya* **42** (2), 368 (1997) [*Crystallogr. Rep.* **42**, 327 (1997)].
- B. I. Smirnov, R. S. Chudnova, and V. V. Shpeĭzman, in *Proceedings of the 3rd All-Union Seminar "Structure of Dislocations and Mechanical Properties of Metals and Alloys"* (Inst. Fiziki Metallov Ural'skogo Nauchnogo Tsentra Akad. Nauk SSSR, Sverdlovsk, 1984), p. 39.
- B. I. Smirnov, R. S. Chudnova, and V. V. Shpeĭzman, *Fiz. Tverd. Tela (St. Petersburg)* **34** (6), 1759 (1992) [*Sov. Phys. Solid State* **34**, 936 (1992)].
- R. O. Kaibyshev and O. C. Sitdikov, in *Proceedings of the First International Conference on Recrystallization and Grain Growth*, Ed. by G. Gottstein and D. A. Molodov (Springer-Verlag, Berlin, 2001), p. 955.
- V. V. Demchenko and A. A. Urusovskaya, *Cryst. Res. Technol.* **28** (3), 415 (1993).
- V. N. Starenchenko, Yu. A. Abzaev, and N. A. Koneva, *Fiz. Met. Metalloved.* **64** (6), 1178 (1987).
- B. I. Smirnov, *Mater. Sci. Eng. A* **233**, 56 (1997).
- G. V. Berezhkova and N. P. Skvortsova, *Kristallografiya* **39** (3), 567 (1994) [*Crystallogr. Rep.* **39**, 507 (1994)].
- N. P. Skvortsova, *Materialovedenie*, No. 4, 10 (1999).
- N. P. Skvortsova and G. V. Berezhkova, *Cryst. Res. Technol.* **21** (7), 939 (1986).
- G. V. Berezhkova and N. P. Skvortsova, *Fiz. Tverd. Tela (Leningrad)* **33** (2), 400 (1991) [*Sov. Phys. Solid State* **33**, 230 (1991)].
- G. V. Berezhkova and N. P. Skvortsova, *Latv. J. Phys. Techn. Sci.*, No. 4, 34 (1991).
- B. I. Smirnov, R. S. Chudnova, and V. V. Shpeĭzman, *Fiz. Tverd. Tela (Leningrad)* **23** (10), 2964 (1981) [*Sov. Phys. Solid State* **23**, 1729 (1981)].
- N. P. Skvortsova, *Cryst. Res. Technol.* **31** (3), 373 (1996).
- P. Suptitz and J. Teltow, *Phys. Status Solidi* **23**, 9 (1967).
- N. P. Skvortsova, *Fiz. Tverd. Tela (St. Petersburg)* **37** (11), 3347 (1995) [*Phys. Solid State* **37**, 1839 (1995)].
- N. P. Skvortsova, in *Proceedings of the VI Interstate Seminar on Structural Foundations of Material Modification by the Methods of Nontraditional Technologies*, Obninsk, 2001, p. 154.

Translated by K. Kugel

PHYSICAL PROPERTIES
OF CRYSTALS

Modern Application Packages for Rigorous Solution of Problems of Light Propagation in Anisotropic Layered Media. I. General Solution of Boundary Problems in Crystal Optics

A. F. Konstantinova*, K. K. Konstantinov**, B. V. Nabatov*,
and E. A. Evdishchenko*

* Shubnikov Institute of Crystallography, Russian Academy of Sciences,
Leninskiĭ pr. 59, Moscow, 117333 Russia
e-mail: afkonst@ns.crys.ras.ru

** Institute of Mechanical Engineering, Russian Academy of Sciences,
Malyĭ Khariton'evskii per. 4, Moscow, 101830 Russia

Received February 21, 2002

Abstract—A new approach to the solution of the boundary problems of light propagation in optically active anisotropic absorbing media has been suggested. Unlike a number of already existing approaches, the new approach is based on the use of a computer mathematical system—the integrated application package Mathematica-4.1 and the method suggested by Berreman. It is shown that the special functions integrated into the package allow one to calculate the characteristics of the reflected and transmitted light for an arbitrary class of crystals and construct their dependences on various optical parameters. The examples of the application of the package Mathematica-4.1 for solving various problems of crystal optics are considered. © 2002 MAIK “Nauka/Interperiodica”.

INTRODUCTION

The solution of the boundary problems of light propagation through crystalline plates and layered media with due regard for its multiple reflection is considered in a large number of works. In optically active media, these problems become rather complicated, and the corresponding calculations and the analytical expressions are rather cumbersome. These problems are solved by different methods. Thus, F.I. Fedorov suggested the covariant method, which provided a rather compact solution of this complex problem [1]. His method allowed one to solve many boundary problems in crystal optics [2–6]. Nevertheless, in complicated cases, one has to use computers.

D. Berreman [7] suggested the method of 4×4 matrices for studying the reflection and transmission of polarized light incident onto planar layered anisotropic media at a certain angle. The method is considered in detail elsewhere [8]. Since the development of this method, numerous practical problems of ellipsometry of layered isotropic media and optics of liquid crystals have been solved by the method. The programs for this method are written in several languages (C, C++, FORTRAN, Visual Basic, etc.), so each program is written in a different way and is therefore not accessible to all users. However, the Berreman method did not find extensive application for solving various problems of crystal optics, so that it is possible to state that it is hardly used in practice. Possibly, this is partly associ-

ated with the fact that most of the problems of crystal optics have already been solved, and, in many practically important instances, very convenient analytical expressions have already been derived.

At present, any problem of light propagation in plates and layered systems with an arbitrary set of optical properties, including anisotropy, absorption, and optical activity, can be solved by the Berreman method with the aid of the system of computer mathematics—the application package Mathematica-4.1 or any other similar software package. In this case, there is no need to write complex programs. Below, we discuss this method in application to the boundary problems of crystal optics.

Despite the fact that the Berreman method has already been stated in detail elsewhere [7, 8], we consider in brief the necessary data from these works to show what new possibilities are provided by this method for solving the boundary problems of crystal optics and what advantages for their solution are provided by the application of the Mathematica-4.1 package.

THE BERREMAN METHOD

First, formulate the problem to be solved. Let a plane monochromatic wave with the wavelength λ be incident from isotropic medium I with the refractive index n_i onto a plane-parallel plate of thickness d cut out from an anisotropic optically active (gyrotropic) absorbing crystal at an angle ϕ_i (Fig. 1). Upon the wave refraction by medium II, two waves propagate from the

upper face of the plate toward its lower face and two waves propagate in the backward direction from the upper and lower faces and undergo numerous reflection. The light exits to medium III at an angle ϕ_t with the refractive index n_t .

The transition matrix for the system of the principal axes of the tensors which describe the properties of the anisotropic medium to the Cartesian coordinate system xyz can be written with the aid of the Eulerian angles φ , θ , and ψ as

$$\begin{pmatrix} \cos \varphi \cos \psi - \cos \theta \sin \varphi \sin \psi & \cos \psi \sin \varphi + \cos \theta \cos \varphi \sin \psi & \sin \theta \sin \psi \\ -\cos \theta \cos \psi \sin \varphi - \cos \varphi \sin \psi & \cos \theta \cos \varphi \cos \psi - \sin \varphi \sin \psi & \cos \psi \sin \theta \\ \sin \theta \sin \varphi & -\cos \varphi \sin \theta & \cos \theta \end{pmatrix}. \quad (1)$$

In the Mathematica-4.1 package, the Eulerian angles determine three successive rotations: through angle φ around the z -axis, angle θ around the x -axis, and angle ψ around the z -axis.

The Maxwell equations for the fields in a medium can be written in the Cartesian coordinate system as a single matrix equation. In its abridged form it can be written as

$$\mathbf{O}\mathbf{G} = (1/c)\partial\mathbf{C}/\partial t, \quad (2)$$

where \mathbf{O} is the block matrix operator

$$\mathbf{O} = \begin{pmatrix} 0 & \text{rot} \\ -\text{rot} & 0 \end{pmatrix}, \quad (3)$$

where \mathbf{O} is the zeroth 3×3 matrix, \mathbf{G} and \mathbf{C} are the generalized vector-columns and $\mathbf{G} = [E_x, E_y, E_z, H_x, H_y, H_z]$, $\mathbf{C} = [D_x, D_y, D_z, B_x, B_y, B_z]$,

$$\mathbf{G} = \begin{bmatrix} \mathbf{E} \\ \mathbf{H} \end{bmatrix}, \quad \mathbf{C} = \begin{bmatrix} \mathbf{D} \\ \mathbf{B} \end{bmatrix}. \quad (4)$$

Here, \mathbf{E} and \mathbf{H} are the intensity vectors of the electric and magnetic fields, \mathbf{D} and \mathbf{B} are the vectors of the elec-

tric and magnetic induction. The relationships between the induction and the field are set by the constitutive equations, and for introduced \mathbf{G} and \mathbf{C} , can be written as

$$\mathbf{C} = \mathbf{M}\mathbf{G}, \quad (5)$$

where the block matrix \mathbf{M} is called the optical matrix and, in the general form, is written as

$$\mathbf{M} = \begin{pmatrix} \varepsilon & \rho \\ -\rho' & \mu \end{pmatrix}. \quad (6)$$

Here, ε and μ are the tensors of dielectric permittivity and magnetic susceptibility and ρ and ρ' are the tensors which describe the optical activity of crystals. The form of blocks of the matrix \mathbf{M} depends on the constitutive equations, which, in the general case, have the form

$$\mathbf{D} = \varepsilon\mathbf{E} + \rho\mathbf{H}, \quad \mathbf{B} = \mu\mathbf{H} + \rho'\mathbf{E}. \quad (7)$$

If \mathbf{G} is written as $\mathbf{G} = \exp(-i\omega t)\mathbf{\Gamma}$, where $\mathbf{\Gamma}$ depends only on the spatial coordinates, then Eqs. (2) and (4) yield

$$\mathbf{O}\mathbf{\Gamma} = (-i\omega/c)\mathbf{M}\mathbf{\Gamma}. \quad (8)$$

Equality (8) is, in fact, the abridged matrix form of the system of six first-order differential equations.

It was shown in [7, 8] that for homogeneous plane waves, $\partial/\partial x = i\xi$ and $\partial/\partial y = 0$, where $\xi = n_i \sin \phi_i$. Then the rotor operator is simplified to the form

$$\text{curl} = \begin{bmatrix} 0 & -\partial/\partial z & 0 \\ \partial/\partial z & 0 & -i\xi \\ 0 & i\xi & 0 \end{bmatrix}. \quad (9)$$

In this case, system of equations (8) includes two homogeneous linear algebraic and four differential equations. Solving the algebraic equations with respect to the field components E_z and H_z and substituting the expressions thus obtained into the differential equations, we arrive at the system of four homogeneous linear differential equations of the first order with respect to the unknown field components $E_x, E_y, H_x,$ and H_y ,

$$\frac{\partial}{\partial z}\boldsymbol{\psi} = i\omega\mathbf{\Delta}\boldsymbol{\psi}, \quad (10)$$

where $\boldsymbol{\psi} = [E_x, H_y, E_y, -H_x]$ is the generalized vector-column of the field and $\mathbf{\Delta}$ is the differential 4×4 prop-

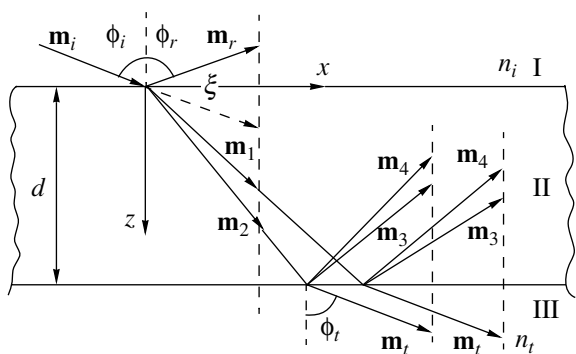


Fig. 1. Reflection and transmission of a plane wave with due regard for multiple reflection at the oblique incidence of light onto the system: (I) isotropic ambient medium, (II) anisotropic plate; (III) isotropic substrate. The y -axis is normal to the drawing plane; $\mathbf{m}_i = n_i \mathbf{n}_i$ are the refraction vectors of the incident (i) and reflected (r) waves, the waves refracted in the forward (1, 2) and backward (3, 4) directions, and the transmitted (t) waves, where n_j are the corresponding refractive indices and \mathbf{n}_j are the corresponding wave normals.

agation matrix for the given medium. Obviously, the elements of the matrix $\mathbf{\Delta}$ are the functions of the elements of the optical 6×6 -matrix \mathbf{M} and the direction of the wave normal of the incident wave, i.e., $\Delta = f(\epsilon, \mu, \rho, \rho', \varphi, \theta, \psi, \phi_i, n_i)$. Equation (10) is the wave equation of the generalized field vector $\boldsymbol{\psi}$.

In [7, 8], it was suggested that Eq. (10) be integrated by dividing the anisotropic medium of thickness d into layers of small thicknesses so that within each such layer the elements of the matrix $\mathbf{\Delta}$ are independent of z . As a result, for a layer of thickness h , the solution has the form

$$\boldsymbol{\psi}(z + h) = \exp(i\omega h \mathbf{\Delta}) \boldsymbol{\psi}(z) = \mathbf{L}(h) \boldsymbol{\psi}(z). \quad (11)$$

The matrix $\mathbf{L}(h) = \exp(i\omega h \mathbf{\Delta})$, which describes the transformation of the field of a light wave during its propagation through a plate, is called the layer matrix. The further solution of the problem reduces to the determination of the layer matrix $\mathbf{L}(h)$. It was suggested [7, 8] that the function $\mathbf{L}(h)$ be expanded into a series in powers of $\mathbf{\Delta}$. Obviously, this expansion is only approximate. In [9], the layer matrix $\mathbf{L}(h)$ is determined with the use of the similarity transformation. With this aim, one has to determine numerically the eigenvalues and eigenvectors of the matrix $\mathbf{\Delta}$ for each layer. These quantities characterize the plane waves propagating in the layer upon the incidence onto it of a wave with the given wave-normal vector. It is also suggested that the orthogonality relationships be used to determine the analytical form of the similarity transformation. This method is rather cumbersome and requires considerable computational resources. The rigorous expression of the layer matrix $\mathbf{L}(h)$ is calculated with the invocation of the Sylvester theorem [10]. Once the layer matrix is determined, one can pass to the direct solution of the boundary problem of light propagation in a layered system.

SOLUTION OF BOUNDARY PROBLEMS IN CRYSTAL OPTICS

Now, we shall show how to solve the boundary problems of the light propagation in a crystalline plate by the Berreman method with the use of application package Mathematica-4.1. It should be noted that, within the framework of the application package Mathematica-4.1, the problem can be solved by two different ways. The first one reduces to the transformation of the symbols at each stage of the procedure and results in the derivation of the corresponding analytical expressions. The second way, more often used in programming reduces, first, to the determination of the variables necessary for the solution, which are defined as the functions of the initial parameters, and only then various computations, including algebraic ones, are performed. In fact, this is the main advantage of the application package Mathematica-4.1 over traditional programming languages. The built-in logic of the algebraic

and symbol transformations of the package allows one to set the functions of both the numerical and algebraic parameters. The computation algorithm provides a "hybrid" of symbolic and numerical programming. It should also be emphasized that some package functions used in our computations are available only in version 4.1; in other words, the method suggested here cannot be completely realized within the old package versions 2.0 and 3.

The concrete form of the constitutive equations is very important in the application of the Berreman method. General constitutive equation (7) are used in the rigorous theory of optically active crystals [11] as

$$\mathbf{D} = \epsilon \mathbf{E} + i \alpha \mathbf{H}, \quad \mathbf{B} = \mu \mathbf{H} - i \tilde{\alpha} \mathbf{E}, \quad (12)$$

i.e., $\rho = i\alpha$ and $\rho' = -i\tilde{\alpha}$, where the tilde indicates the transposition.

The constitutive equations used in different theories of optical activity will be compared in our following publications.

The physical meaning of α is a pseudotensor, but it is referred to differently. Often, it is referred to as the gyration tensor with the omission of the prefix *pseudo* [11–14], sometimes it is called the tensor of optical rotation [7, 8, 10] (despite the fact that this tensor defines the optical rotation only in isotropic compounds and anisotropic crystals, where the light propagates along the optic axis). We stick to the terminology most widespread in crystal optics and hereafter refer to α as the gyration tensor.

It should also be indicated that, in the presence of absorption, all the tensors in the constitutive equations become complex. All the tensors for uni- and biaxial orthorhombic crystals have the same systems of the principal axes, irrespective of the presence and absence of absorption if the tensor α has no nondiagonal elements. The situation becomes much more complicated if the tensors have no such systems. This can happen in monoclinic and triclinic crystals. Therefore, the latter crystals should be studied separately.

Now, we pass to the direct description of the ways of solving the formulated problem. First, the form of all the tensors, ϵ , μ , and α , should be set in the principal coordinate system defined by the triad of the Eulerian angles φ , θ , and ψ ($\varphi = 0$, $\theta = 0$, and $\psi = 0$). Thanks to the interface used in the Mathematica-4.1 system and the convenient representation of the input data, all the tensors can be set in a very clear symbolic and numerical form and can readily be modified. Thus, the block optical matrix \mathbf{M} is readily determined. The built-in function sets the rotation matrix for the transition from the principal coordinate system of the tensor to a new coordinate system chosen in the formulation of the concrete problem. Then, the form of each tensor is determined in the new coordinate system, and the matrix \mathbf{M} is constructed.

The stage of the solution following the determination of all the tensors ϵ , μ , and α is the determination of the matrix Δ . In all the studies known to us, the matrices Δ are determined with the use of the relationships indicated in [7, 8]. The corresponding procedure is rather complicated and cumbersome. The possibilities provided by Mathematica-4.1 allow one to avoid writing all the elements of the matrix Δ . The form of the matrix Δ depends on the form of the constitutive equations. It should also be noted that the matrix Δ is of interest by itself, and the consideration of its form and properties for crystals from different symmetry classes is a subject of special consideration.

Using Mathematica-4.1, one can readily obtain the expression for the layer matrix $\mathbf{L}(h)$ with the aid of the built-in function called the "matrix exponent":

$$\mathbf{L}(h) = \text{MatrixExp}(i2\pi h\Delta/\lambda). \quad (13)$$

As was indicated in [7, 8], the matrix $\mathbf{L}(h)$ relates the fields at the entrance and exit surfaces of the plate (for each layer, $h = d$):

$$\boldsymbol{\psi}_t(d) = \mathbf{L}(d)(\boldsymbol{\psi}_i(0) + \boldsymbol{\psi}_r(0)), \quad (14)$$

where the subscripts i , r , and t indicate the incident, reflected, and transmitted waves, respectively, whereas, similar to [7, 8], the generalized fields are written as

$$\boldsymbol{\psi}_i = \begin{bmatrix} E_{ip} \cos \phi_i \\ n_i E_{ip} \\ E_{is} \\ n_i E_{is} \cos \phi_i \end{bmatrix}, \quad \boldsymbol{\psi}_r = \begin{bmatrix} -E_{rp} \cos \phi_r \\ n_i E_{rp} \\ E_{rs} \\ -n_i E_{rs} \cos \phi_r \end{bmatrix}, \quad (15)$$

$$\boldsymbol{\psi}_t = \begin{bmatrix} E_{tp} \cos \phi_t \\ n_t E_{tp} \\ E_{ts} \\ n_t E_{ts} \cos \phi_t \end{bmatrix},$$

where E_{ip} and E_{is} are the known components of the electric field of the incident wave of any polarization (linear, circular, or elliptic) and E_{rp} , E_{rs} , E_{tp} , and E_{ts} are the components of the electric fields of the reflected and transmitted waves. Here, the subscript p indicates the wave polarization parallel to the incidence plane (the p -polarization) and the subscript s indicates the polarization normal to this plane (the s -polarization).

Thus, for a linearly polarized incident wave with the azimuth β_p , the components E_{ip} and E_{is} are

$$E_{ip} = \cos \beta_p, \quad E_{is} = \sin \beta_p, \quad (16)$$

where $\beta_p = 0^\circ$ corresponds to the p -polarization of the incident light and $\beta_p = 90^\circ$, to the s -polarization. For the circularly polarized light we have

$$E_{ip} = \mp i\sqrt{2}/2, \quad E_{is} = \sqrt{2}/2, \quad (17)$$

where the upper sign corresponds to the right-hand circular polarization.

When writing Eq. (15), we took into account that, in the optically isotropic and nonmagnetic ambient media, the components of the magnetic field are proportional to the corresponding orthogonal components of the electric field with the proportionality coefficient being equal to the refractive index of the medium.

Writing the generalized vectors of the fields of the incident, reflected, and transmitted waves $\boldsymbol{\psi}_j$ ($j = i, r, t$) as is suggested in [7, 8], we can solve the system of linear algebraic equations (14) with respect to the unknown components of the fields of the reflected and transmitted waves. To solve the boundary problem, we introduce a new generalized field vector \mathbf{Q} which includes the components of the electric fields of the transmitted and reflected waves,

$$\mathbf{Q} = [E_{tp}, E_{ts}, E_{rp}, E_{rs}] \quad (18)$$

and related to the generalized vectors of the fields of the transmitted $\boldsymbol{\psi}_t$ and reflected $\boldsymbol{\psi}_r$ waves by the relationships

$$\boldsymbol{\psi}_t = T_m \mathbf{Q}, \quad \boldsymbol{\psi}_r = R_m \mathbf{Q}, \quad (19)$$

where

$$T_m = \begin{pmatrix} \cos \phi_t & 0 & 0 & 0 \\ n_t & 0 & 0 & 0 \\ 0 & 1 & 0 & 0 \\ 0 & n_t \cos \phi_t & 0 & 0 \end{pmatrix},$$

$$R_m = \begin{pmatrix} 0 & 0 & -\cos \phi_i & 0 \\ 0 & 0 & n_i & 0 \\ 0 & 0 & 0 & 1 \\ 0 & 0 & 0 & -n_i \cos \phi_i \end{pmatrix}.$$

Then Eq. (14) can be rewritten as

$$T_m \mathbf{Q} = \mathbf{L} \boldsymbol{\psi}_i + \mathbf{L} R_m \mathbf{Q}, \quad (20)$$

whence the vector introduced earlier is determined as

$$\mathbf{Q} = (T_m - \mathbf{L} R_m)^{-1} \mathbf{L} \boldsymbol{\psi}_i. \quad (21)$$

Calculating the vector \mathbf{Q} , we can determine the components of the fields of the reflected and transmitted waves. Knowing these components, we can write the reflection and transmission matrices for the plate in the form [8]

$$\mathbf{E}_r = \begin{bmatrix} E_{rp} \\ E_{rs} \end{bmatrix} = \mathbf{R} \mathbf{E}_i = \begin{pmatrix} r_{pp} & r_{ps} \\ r_{sp} & r_{ss} \end{pmatrix} \begin{bmatrix} E_{ip} \\ E_{is} \end{bmatrix}, \quad (22)$$

$$\mathbf{E}_t = \begin{bmatrix} E_{tp} \\ E_{ts} \end{bmatrix} = \mathbf{T} \mathbf{E}_i = \begin{pmatrix} t_{pp} & t_{ps} \\ t_{sp} & t_{ss} \end{pmatrix} \begin{bmatrix} E_{ip} \\ E_{is} \end{bmatrix}.$$

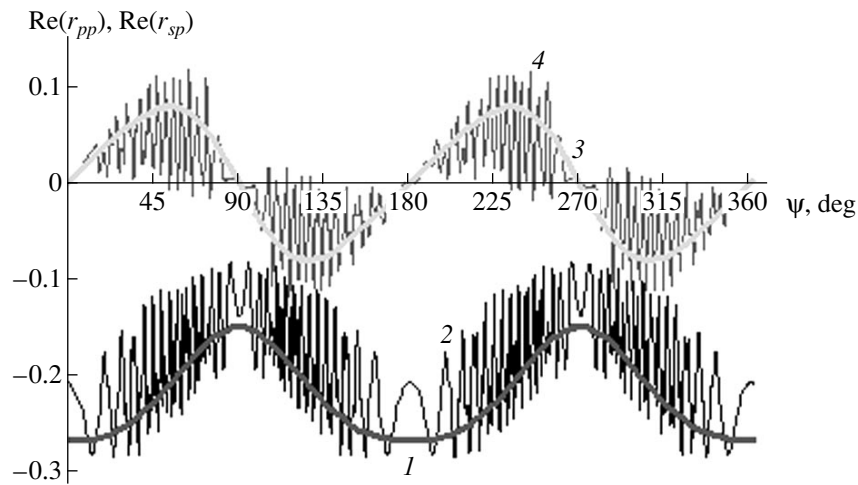


Fig. 2. Real parts of the reflection coefficients $\text{Re}(r_{pp})$ and $\text{Re}(r_{sp})$ as functions of the azimuthal rotation angle ψ at two plate thicknesses: (1) $\text{Re}r_{pp}$, $d = 0.2$, (2) $\text{Re}r_{pp}$, $d = 100$, (3) $\text{Re}r_{sp}$, $d = 0.2$, (4) $\text{Re}r_{sp}$, $d = 100 \mu\text{m}$; $n_1 = 1.344$, $n_2 = 1.411$, and $n_3 = 1.651$ (the refractive indices are equal to those of sodium nitrite NaNO_2); $n_t = 1.6$, $\theta = 90^\circ$, and $\phi_i = 70^\circ$.

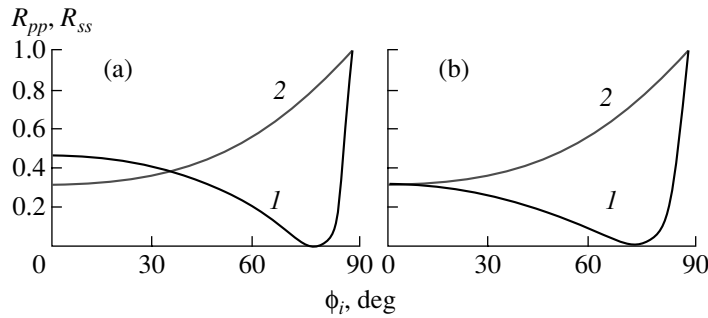


Fig. 3. Reflectivity R_{ij} as a function of the angle of light incidence ϕ_i for an absorbing $2\text{-}\mu\text{m}$ -thick plate (1) R_{pp} , the p -polarized incident light; (2) R_{ss} , the s -polarized incident light. (a) Biaxial crystal: $n_1 = 5.12 + i0.635$, $n_2 = 4.37 + i0.817$, $n_3 = 3.41 + i0.723$ (the refractive indices are equal to those of antimony glance, class 222), $\theta = 90^\circ$, $\psi = 0^\circ$; (b) isotropic crystal: $n_1 = n_2 = n_3 = 3.41 + i0.723$.

The matrices \mathbf{R} and \mathbf{T} are the complex amplitude reflection and transmission matrices, respectively. Once the reflection and transmission coefficients are determined, one can calculate the reflectivity and transmissivity as

$$R_{ij} = (\text{Re}r_{ij})^2 + (\text{Im}r_{ij})^2, \quad (23)$$

$$T_{ij} = (\text{Re}t_{ij})^2 + (\text{Im}t_{ij})^2, \text{ where } ij = p, s,$$

and also the reflectance and transmittance (the amplitude of the incident wave is assumed to be unity) as

$$R = |E_{rp}|^2 + |E_{rs}|^2, \quad (24)$$

$$T = (|E_{tp}|^2 + |E_{ts}|^2)n_t \cos \phi_t / n_i \cos \phi_i.$$

One should pay attention to the factor $(n_t \cos \phi_t / n_i \cos \phi_i)$ in Eqs. (24). If the refractive indices of the ambient media are equal, $n_t = n_i$, this factor is unity and, thus, is omitted in the formulas. If $n_t \neq n_i$, the law of energy conservation $R + T = 1$ [15] is fulfilled

only if this factor is also taken into account, which can be considered as a certain criterion of the correctness of the computations.

The components of the reflection and transmission matrices (22) thus determined allow one to calculate the characteristics of the polarizations of the reflected and transmitted waves, i.e., the azimuths $\chi_{r,t}$ and the ellipticities $k_{r,t} = \tan \gamma_{r,t}$ written in the form

$$\begin{aligned} \tan 2\chi_{r,t} &= 2 \text{Re}(E_{rs,ts}/E_{rp,tp}) / (1 - |E_{rs,ts}/E_{rp,tp}|^2), \\ \sin 2\gamma_{r,t} &= 2 \text{Im}(E_{rs,ts}/E_{rp,tp}) / (1 + |E_{rs,ts}/E_{rp,tp}|^2). \end{aligned} \quad (25)$$

In crystal optics, one often has to study the variation in the intensity of the light transmitted in the direction normal to the plate located between arbitrarily oriented polarizer (β_p) and analyzer (β_A). In this case, the light intensity can be written in different ways, in particular,

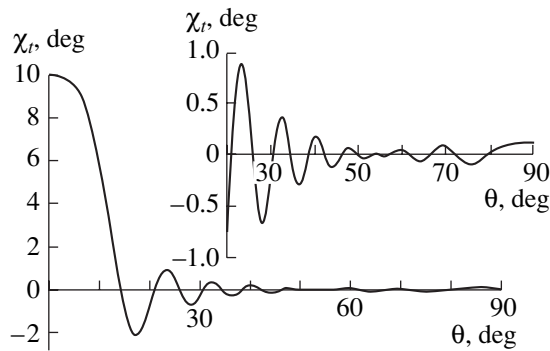


Fig. 4. Polarization azimuth χ_t of the light wave transmitted through the optically active crystalline plate normally to its surface as a function of angle θ of the deviation of the optic axis from the surface normal: $n_1 = n_2 = 1.54424$, $n_3 = 1.55335$, $\alpha_{11} = \alpha_{22} = -3.259 \times 10^{-5}$, $\alpha_{33} = 6.714 \times 10^{-5}$, $d = 500 \mu\text{m}$ (the optical parameters are equal to those of quartz, $\lambda = 0.589 \mu\text{m}$). In the inset: the same dependence in the range of angle θ from 20° to 90° .

as

$$J = T(1 + \cos 2\gamma_t \cos(2\beta_A - 2\chi_t))/2. \quad (26)$$

Thus, the use of the Berreman method and the package Mathematica-4.1 allows one to solve any problems of propagation of homogeneous plane waves through crystalline plates with arbitrary sets of optical properties such as birefringence, absorption, and optical activity. No limitations are imposed on the presence or absence of magnetic properties. Thus, it is a possible not only to obtain the numerical results by a comparatively simple and clear way, but also to derive the analytical expressions that describe various optical characteristics. It should be emphasized once again that the Berreman method is still not widely used in crystal optics.

SOME EXAMPLES OF SOLVING BOUNDARY PROBLEMS IN CRYSTAL OPTICS. DISCUSSION OF THE RESULTS

The use of all the above stated material allowed us to write an original program and calculate, with the aid of the built-in functions of the package Mathematica-4.1, the characteristics of the reflected and transmitted light for crystals of any class by setting the tensors ϵ and α in their general, including complex, forms, and by constructing the dependences of these characteristics on all the parameters of the media for which the calculations are made. Since the present study is aimed at the investigation of insufficiently studied optical properties of some concrete classes of crystals, we consider here only some purely illustrative examples. The detailed study of some interesting characteristics of light propagation in crystals will be considered later.

As a rule, crystal optics deals with plates whose thickness ranges from fractions of a millimeter to sev-

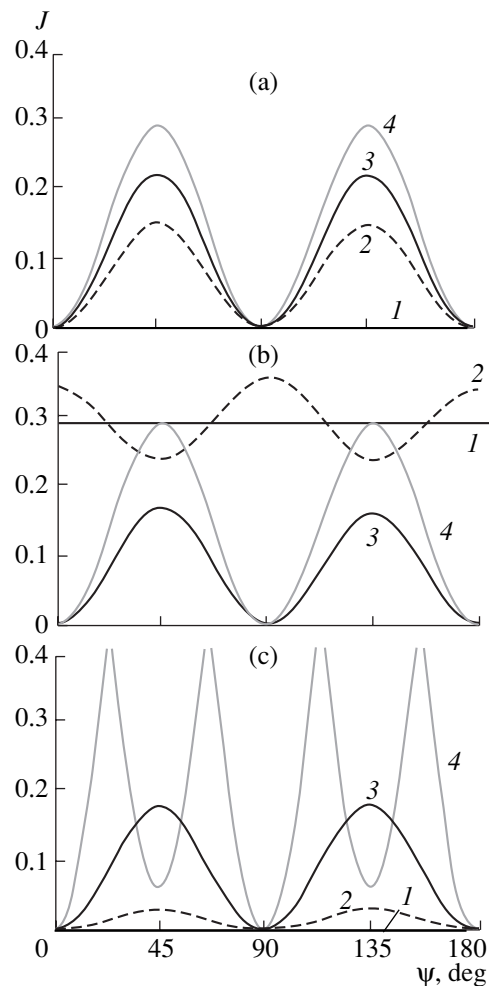


Fig. 5. Intensity of the light transmitted by a 1-mm-thick plate prepared from a uniaxial crystal normally to its surface placed between the crossed polarizer and analyzer as a function of the angle ψ of the plate rotation about the surface normal: $n_1 = n_2 = 1.5$, $n_3 = 1.51$; (1) $\theta = 0^\circ$, (2) $\theta = 5^\circ$, (3) $\theta = 20^\circ$, (4) $\theta = 90^\circ$; (a) optically inactive nonmagnetic crystal ($\alpha = 0$, $\mu = 1$), (b) optically active nonmagnetic crystal ($\alpha_{11} = \alpha_{22} = -10^{-5}$, $\alpha_{33} = 5 \times 10^{-5}$, $\mu = 1$); (c) optically inactive magnetic crystal ($\alpha = 0$, $\mu_{11} = \mu_{22} = 1.01$, $\mu_{33} = 1.03$).

eral millimeters. At such thicknesses and a fixed wavelength, it is rather difficult to establish the true run of the curves because of oscillations associated with multibeam interference. To avoid these oscillations, one has to take into account the range of possible wavelength variation. Otherwise, one can perform such calculations for thin plates, because all the features of these dependences are well preserved also at small plate thicknesses. This is illustrated by Fig. 2, which shows the dependence of the real parts of the reflection coefficients r_{pp} and r_{sp} on the azimuthal rotation angle ψ for two plates whose thicknesses differ by a factor of 500. It is clearly seen that the characteristic run of curves 1, 2 and 3, 4 is quite similar.

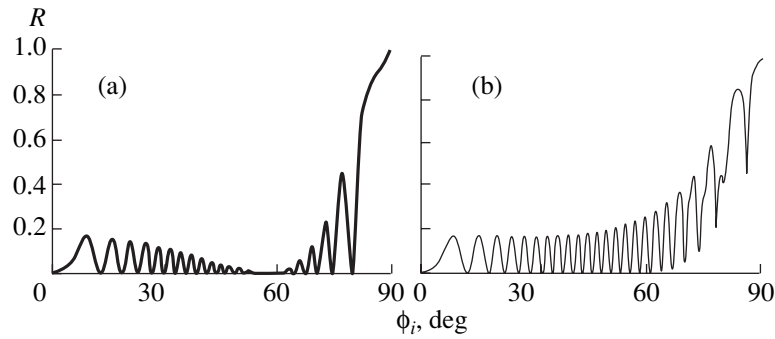


Fig. 6. Reflectivity R as a function of the angle of light incidence ϕ_i for a plate prepared from an optically active uniaxial crystal; (a) the incident light has p -polarization, (b) the incident light has right-hand circular polarization, $n_1 = n_2 = 1.55$, $n_3 = 1.56$, $\alpha_{11} = \alpha_{22} = -10 \times 10^{-5}$, $\alpha_{33} = 3 \times 10^{-5}$, $\varphi = \theta = \psi = 0$, $d = 20 \mu\text{m}$.

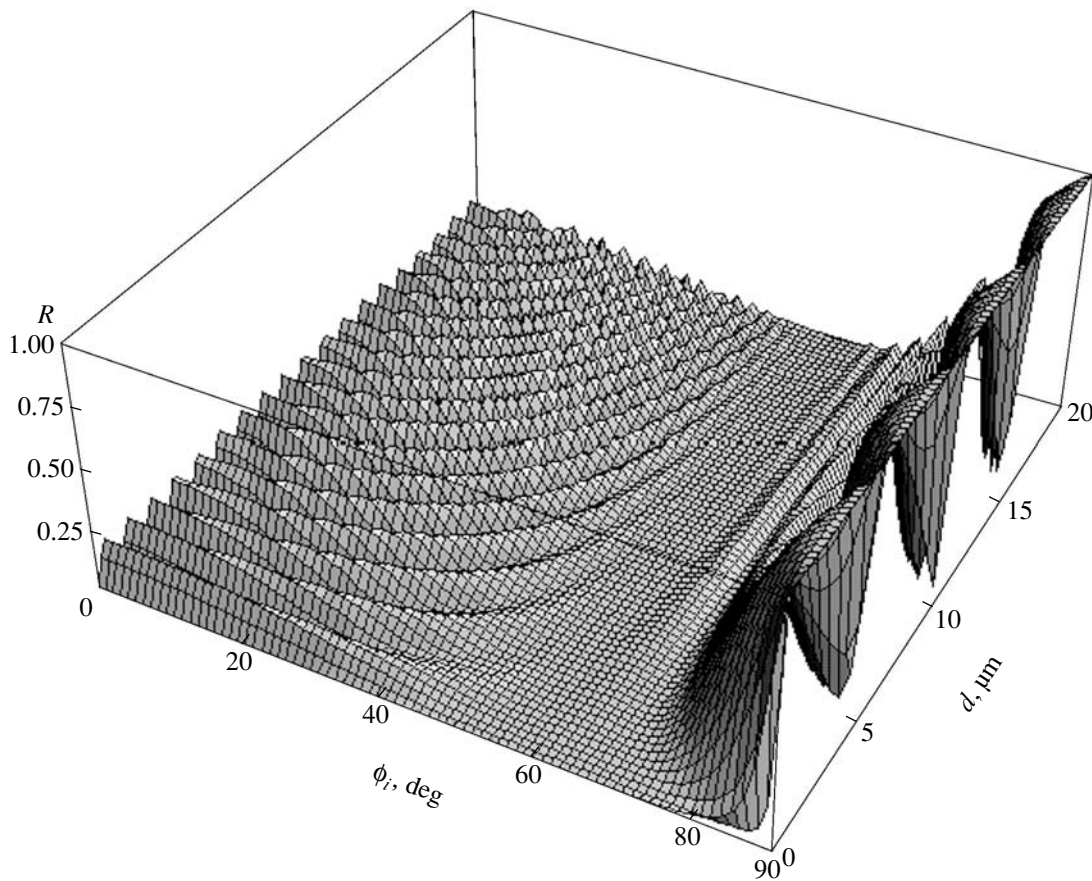


Fig. 7. Reflectivity R as a function of the angle of light incidence ϕ_i and thickness d of the plate prepared from an optically active uniaxial crystal. For the optical parameters see Fig. 6.

It should be indicated that all the calculations were made at $\lambda = 0.6328 \mu\text{m}$, $n_i = 1$, $n_t = 1$, and $\varphi = 0^\circ$ if not specified otherwise. These curves are also constructed using the package Mathematica-4.1.

Figure 3 shows reflectivity as a function of the angle of light incidence for the plates prepared from absorb-

ing biaxial (Fig. 3a) and isotropic (Fig. 3b) crystals. One can clearly see the considerable difference between the light reflection from the anisotropic and isotropic plates at small incidence angles: the R_{pp} and R_{ss} values in the isotropic plate are the same, whereas in the biaxial crystals, R_{pp} and R_{ss} values are different, which is a sign of crystal anisotropy.

Figure 4 shows the change in the polarization azimuth χ_t of the transmitted light as a function of the orientation angle of the optic axis θ for the normal incidence of p -polarized light onto the optically active plate. It is seen that, if the light propagates along the optical axis ($\theta = 0^\circ$), the angle χ_t corresponds to the rotation of the polarization plane. If the optical axis deviates from the normal, the angle χ_t first drastically decreases, then becomes zero, and, finally, increases again up to a certain value. This behavior is associated with the fact that the components α_{11} and α_{33} of the gyration tensor have different signs.

Figure 5 compares the effect of optical activity and magnetic properties on the intensity of the light transmitted by the plate of a uniaxial crystal located between the crossed polarizer and analyzer normally to its surface for some orientations of the optic axis. Figure 5a illustrates an increase in the intensity with an increase in the angle of the deviation of the optic axis from the surface normal of the plate, θ . It is clearly seen that if the light propagates along the optic axis ($\theta = 0^\circ$, lines 1) in an optically active crystal, the intensity of the transmitted light has a nonzero value (Fig. 5b). At small angles θ ($\theta = 5^\circ$, curves 2), one may notice the simultaneous effect of birefringence (because the intensity curve oscillates) and optical activity (because the intensity curve is above the abscissa in the whole range of the rotation angles of the specimen). In magnetic crystals (Fig. 5c), with an increase of the angle θ , the light intensity changes much more pronouncedly than the intensity in nonmagnetic crystals (Fig. 5a).

Figure 6 shows the influence of the type of polarization (circular or linear) of the incident light on the characteristics of the reflected light. For incident p -polarized light, the dependence of R on the incidence angle has the minimum in the vicinity of the Brewster angle (Fig. 6a), whereas for circularly polarized incident light no such minimum is observed, and the reflectivity R is much higher (Fig. 6b).

The possibilities of similar calculations and graphical constructions are illustrated by Fig. 7, which shows the dependence of reflectivity R on the angle of light incidence ϕ , and simultaneously on the plate thickness d for a plate prepared from an optically active uniaxial crystal. One can clearly see the region of the Brewster angle and a regular increase in the number of oscillations of the reflectivity curve R with an increase in the plate thickness.

Thus, it is shown that the combined use of the Berreman method and the package Mathematica-4.1 opens new vistas for solving the problems of crystal optics and studying the characteristics of light propagation in crystals with various optical properties. The depen-

dences considered above clearly demonstrate the universal nature of this approach, namely, the possibility of constructing any necessary dependence of the reflected and transmitted light with due regard for the optical activity and the magnetic properties and absorption in the plate and the substrate. Moreover, it is also possible to set the functional dependences of the optical properties of crystals, e.g., on the wavelength or the temperature, to set any polarization of the incident light, and to consider the dependence of the intensity and polarization of the light transmitted by the plate placed between the arbitrarily oriented polarizer and analyzer.

REFERENCES

1. F. I. Fedorov, *Optics of Anisotropic Media* (Akad. Nauk BSSR, Minsk, 1958).
2. L. M. Barkovskii, *Kristallografiya* **22** (1), 21 (1977) [*Sov. Phys. Crystallogr.* **22**, 10 (1977)].
3. B. V. Bokut', A. F. Konstantinova, and A. N. Serdyukov, *Kristallografiya* **18** (4), 812 (1972) [*Sov. Phys. Crystallogr.* **18**, 510 (1972)].
4. V. V. Filippov, *Kristallografiya* **28** (2), 234 (1983) [*Sov. Phys. Crystallogr.* **28**, 136 (1983)].
5. A. F. Konstantinova, A. Yu. Tronin, B. V. Nabatov, and E. A. Evdishchenko, *Kristallografiya* **44** (1), 149 (1999) [*Crystallogr. Rep.* **44**, 140 (1999)].
6. A. F. Konstantinova, B. V. Nabatov, A. Yu. Tronin, and E. A. Evdishchenko, *Poverkhnost*, No. 10, 65 (2000).
7. D. W. Berreman, *J. Opt. Soc. Am.* **62** (4), 502 (1972).
8. R. M. Azzam and N. M. Bashara, *Ellipsometry and Polarized Light* (North-Holland, Amsterdam, 1977; Mir, Moscow, 1981).
9. D. A. Yakovlev, *Opt. Spektrosk.* **84** (5), 829 (1998) [*Opt. Spectrosc.* **84**, 748 (1998)].
10. S. P. Palto, *Zh. Éksp. Teor. Fiz.* **119** (4), 638 (2001) [*JETP* **92**, 552 (2001)].
11. F. I. Fedorov, *Theory of Gyrotropy* (Nauka i Tekhnika, Minsk, 1976).
12. B. N. Grechushnikov, in *Modern Crystallography*, Vol. 4: *Physical Properties of Crystals*, Ed. by B. K. Vainshtein, A. A. Chernov, and L. A. Shuvalov (Nauka, Moscow, 1981; Springer-Verlag, Berlin, 1988).
13. A. Yariv and P. Yeh, *Optical Waves in Crystals: Propagation and Control of Laser Radiation* (Wiley, New York, 1984; Mir, Moscow, 1987).
14. Yu. I. Sirotin and M. P. Shaskolskaya, *Fundamentals of Crystal Physics* (Nauka, Moscow, 1975; Mir, Moscow, 1982).
15. M. Born and E. Wolf, *Principles of Optics* (Pergamon, Oxford, 1969; Nauka, Moscow, 1970).

Translated by L. Man

PHYSICAL PROPERTIES
OF CRYSTALS

High-Order Picosecond SRS
and Self-SRS Generation in Nd³⁺-doped CaMoO₄, SrMoO₄,
and SrWO₄ Laser Crystals

A. A. Kaminskiĭ*, S. N. Bagaev**, K. Ueda***,
K. Takaichi***, and H. J. Eichler ****

* Shubnikov Institute of Crystallography, Russian Academy of Sciences,
Leninskiĭ pr. 59, Moscow, 117333 Russia

e-mail: kaminalex@mail.ru

** Institute of Laser Physics, pr. Lavrent'eva 13/3, Novosibirsk, 630090 Russia

*** Institute for Laser Science, University of Electrocommunications, 182-8585 Tokyo, Japan

**** Optical Institute, Technical University of Berlin, D-10623 Berlin, Germany

Received January 30, 2002

Abstract—The results of a stimulated Raman scattering (SRS) spectroscopy study of Nd³⁺-doped CaMoO₄, SrMoO₄, and SrWO₄ crystals are presented. All the wavelengths of the Stokes and anti-Stokes generation observed in these crystals are identified. For the first time, the self-SRS conversion of the emission frequency of activator Nd³⁺-ions is attained in these lasing molybdates and tungstate with scheelite-type structures. © 2002 MAIK “Nauka/Interperiodica”.

The search for crystals doped with trivalent lanthanide ions for self-stimulated Raman scattering (self-SRS) lasers has been within the sphere of interest of many research groups for several years [1, 2]. These lasers provide emission in new spectral ranges and have a rather simple design, because their active media possess several functional properties. The crystals with high $\chi^{(3)}$ nonlinearity containing Nd³⁺ or Yb³⁺ ions [3–7], whose stimulated emission can be excited by the specially designed high-power AlGaAs and InGaAs semiconductor lasers [8], are most attractive for these purposes. According to [9–14], tetragonal molybdates and tungstates, already recognized as efficient lasing media [15], are also SRS-active crystals. Below, we present the results of the study of the Stokes and anti-Stokes generation and report the first promising self-SRS experiments for three Nd³⁺-doped lasing crystals—CaMoO₄, SrMoO₄, and SrWO₄—with scheelite-type structures.¹

In our SRS study of Nd³⁺-doped ($C_{\text{Nd}} = 0.5\text{--}1$ at. %) CaMoO₄, SrMoO₄, and SrWO₄ crystals, we used lasing elements in the shape of rods (5 mm in diameter and 10–15 mm in length) cut along the *a*-axis whose plane-parallel (~20°) end faces were coated with an antireflectory broad-band coating. For SRS spectroscopy, we also used CaMoO₄ samples with the same

orientation and dimensions as the Nd³⁺-doped ones. As in [9–12], the stationary SRS in these crystals ($\tau_p \gg T_2 = 1/\pi\Delta\nu_R$, where $T_2 = 2$ ps and $\Delta\nu_R$ are the time of phonon relaxation and the width of the corresponding line in the spectrum of spontaneous Raman scattering) was excited in a single-pass cavity-free experimental scheme by pumping with picosecond pulses of a Nd³⁺:Y₃Al₅O₁₂ laser emitted at $\lambda_{p1} = 1.06415$ μm with $\tau_{p1} \approx 110$ ps and $\lambda_{p2} = 0.53207$ μm (second harmonic) with $\tau_{p2} \approx 80$ ps at 300 K. The spectral composition of the components of parametric generation was studied with the aid of a CSMA spectrometry complex based on a ST-130 analyzer (Princeton Instruments) and a McPherson-218 grating monochromator with a cooled Si-CCD matrix (Hamamatsu S3923-1024Q). The spectra thus obtained are shown in Figs. 1a, 1b, and 2; the results of their analysis are summarized in the table.

For a body-centered tetragonal (sp. gr. $C_{4h}^6 - I_4/a$) unit cell of the CaMoO₄, SrMoO₄, and SrWO₄ crystals, the factor-group analysis predicts 36 ($3N_{\text{Z-rep}}$) vibrational modes described by the irreducible representations $\Gamma_N = 3A_g + 5B_g + 5E_g + 5A_u + 3B_u + 5E_u$ at $k = 0$. According to [16], the spectra of spontaneous Raman scattering should have $(3A_g + 5B_g + 5E_g)$ -vibrations with the acoustic modes ($A_u + E_u$) being the remaining vibrations (except for $3B_u$) observed in the IR absorption and reflection spectra. The identification of SRS-active frequencies $\omega_{\text{SRS}} \approx 879$ cm⁻¹ in the CaMoO₄ crys-

¹ These results were first discussed at the 198th meeting of the Moscow Seminar on Physics and Spectroscopy of Laser Crystals on January 31, 2002.

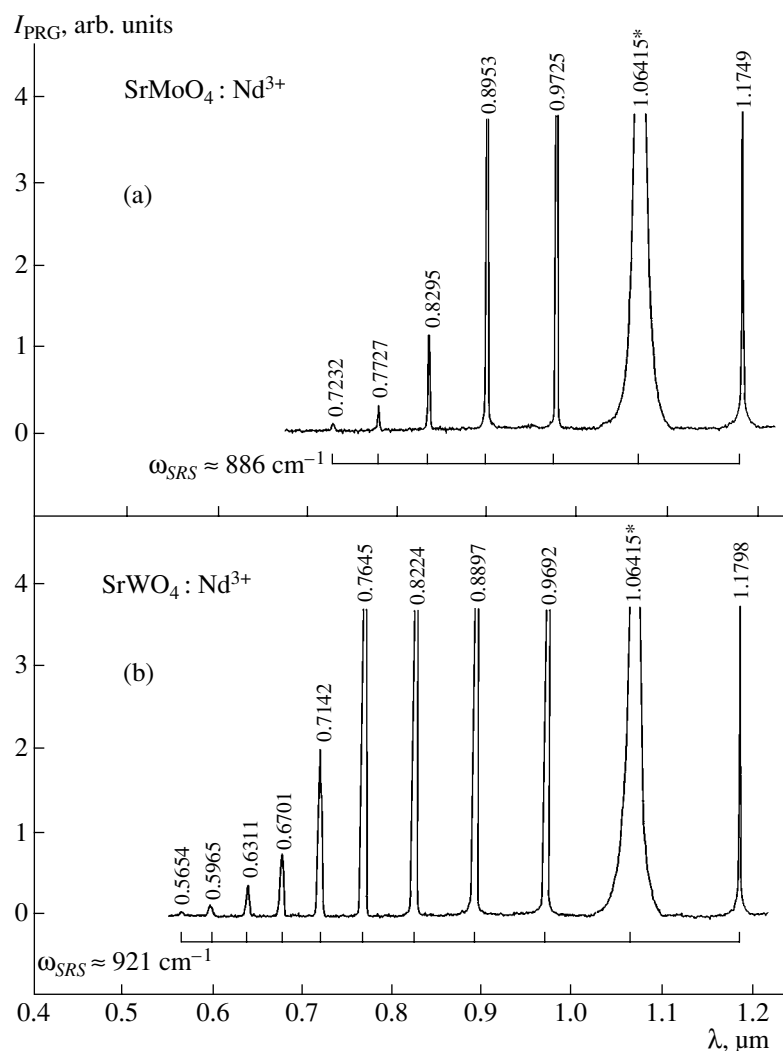


Fig. 1. Spectra of parametric Raman generation in Nd^{3+} -doped (a) SrMoO_4 and (b) SrWO_4 crystals under pumping with $\lambda_{p1} = 1.06415 \mu\text{m}$ (marked by an asterisk) at 300 K. Line wavelengths are given in μm ; their intensities, in arbitrary units without the correction for the spectral sensitivity of the detecting system based on the Si-CCD matrix. "Brackets" show the relation between the components of $\chi^{(3)}$ -generation and the SRS-active vibrational modes in the crystals.

tals, $\omega_{\text{SRS}} \approx 886 \text{ cm}^{-1}$ in the SrMoO_4 crystals, and $\omega_{\text{SRS}} \approx 921 \text{ cm}^{-1}$ in the SrWO_4 crystals was facilitated by the measurements of the spectra of spontaneous Raman scattering and IR absorption and reflection in these crystals reported in [17–19]. These results, and the results of our previous studies of parametric Raman generation in other lasing molybdates and tungstates with ordered and disordered scheelite-type structures [9–14], allowed us to conclude that the SRS-active frequencies revealed in the CaMoO_4 , SrMoO_4 , and SrWO_4 crystals belong to the internal totally symmetrical (stretching) optical vibrational modes $A_g(\nu_1)$ of their complex tetrahedral MoO_4^{2-} and WO_4^{2-} anions.

In the experiment on self-SRS conversion, the active elements prepared from Nd^{3+} -doped CaMoO_4 ,

SrMoO_4 , and SrWO_4 crystals were placed into a 30-mm laser cavity together with a passive Q-switch (1-mm-long plate prepared from Cr-doped $\text{Y}_3\text{Al}_5\text{O}_{12} : \text{Ca}$ garnet). The necessary Q-factor of the cavity at the wavelengths of stimulated emission and the first Stokes components was ensured by high reflection coefficients ($\sim 99\%$) of its plane and spherical ($R = 200 \text{ mm}$) mirrors. The source of stimulated-emission pumping was the beam of continuous radiation ($\lambda_p \approx 0.8 \mu\text{m}$) from a 1-W AlGaAs laser diode, which was corrected, focused, and directed onto the active element with the aid of the plane mirror. While the stimulated emission on π -transitions of the laser channel ${}^4F_{3/2} \rightarrow {}^4I_{11/2}$ of Nd^{3+} ions was excited at practically the same pumping power ($\sim 220 \text{ mW}$, initial transmission of the saturable filter $\sim 90\%$) for all the crystals, the SRS thresholds at

Spectral composition of the parametric Raman generation in the tetragonal CaMoO_4 , SrMoO_4 , and SrWO_4 crystals under picosecond pumping by an $\text{Nd}^{3+} : \text{Y}_3\text{Al}_5\text{O}_{12}$ laser in the $c(aa)c$ geometry at 300 K

Pump wavelength, μm	Characteristics of parametric Raman generation			SRS-active vibrational mode ω_{SRS} , cm^{-1}
	wavelength*, μm	line	identification	
$\text{SrMoO}_4 : \text{Nd}^{3+}$ (Fig. 1a)				
1.06415	0.7232	ASt_5	$\omega_{\text{p1}} + 5\omega_{\text{SRS}}$	~ 886
	0.7727	ASt_4	$\omega_{\text{p1}} + 4\omega_{\text{SRS}}$	~ 886
	0.8295	ASt_3	$\omega_{\text{p1}} + 3\omega_{\text{SRS}}$	~ 886
	0.8953	ASt_2	$\omega_{\text{p1}} + 2\omega_{\text{SRS}}$	~ 886
	0.9725	ASt_1	$\omega_{\text{p1}} + \omega_{\text{SRS}}$	~ 886
	1.06415	λ_{p}	ω_{p1}	
	1.1749	St_1	$\omega_{\text{p1}} - \omega_{\text{SRS}}$	~ 886
$\text{SrWO}_4 : \text{Nd}^{3+}$ (Fig. 1b)				
1.06415	0.5654	ASt_9	$\omega_{\text{p1}} + 9\omega_{\text{SRS}}$	~ 921
	0.5965	ASt_8	$\omega_{\text{p1}} + 8\omega_{\text{SRS}}$	~ 921
	0.6311	ASt_7	$\omega_{\text{p1}} + 7\omega_{\text{SRS}}$	~ 921
	0.6701	ASt_6	$\omega_{\text{p1}} + 6\omega_{\text{SRS}}$	~ 921
	0.7142	ASt_5	$\omega_{\text{p1}} + 5\omega_{\text{SRS}}$	~ 921
	0.7645	ASt_4	$\omega_{\text{p1}} + 4\omega_{\text{SRS}}$	~ 921
	0.8224	ASt_3	$\omega_{\text{p1}} + 3\omega_{\text{SRS}}$	~ 921
	0.8897	ASt_2	$\omega_{\text{p1}} + 2\omega_{\text{SRS}}$	~ 921
	0.9692	ASt_1	$\omega_{\text{p1}} + \omega_{\text{SRS}}$	~ 921
	1.06415	λ_{p1}	ω_{p1}	
	1.1798	St_1	$\omega_{\text{p1}} - \omega_{\text{SRS}}$	~ 921
CaMoO_4 and $\text{CaMoO}_4 : \text{Nd}^{3+}$ (Fig. 2)				
1.06415	0.6816	ASt_6	$\omega_{\text{p1}} + 6\omega_{\text{SRS}}$	~ 879
	0.7251	ASt_5	$\omega_{\text{p1}} + 5\omega_{\text{SRS}}$	~ 879
	0.7744	ASt_4	$\omega_{\text{p1}} + 4\omega_{\text{SRS}}$	~ 879
	0.8310	ASt_3	$\omega_{\text{p1}} + 3\omega_{\text{SRS}}$	~ 879
	0.8965	ASt_2	$\omega_{\text{p1}} + 2\omega_{\text{SRS}}$	~ 879
	0.9731	ASt_1	$\omega_{\text{p1}} + \omega_{\text{SRS}}$	~ 879
	1.06415	λ_{p}	ω_{p1}	–
	1.1740	St_1	$\omega_{\text{p1}} - \omega_{\text{SRS}}$	~ 879
0.53207	0.5083	ASt_1	$\omega_{\text{p2}} + \omega_{\text{SRS}}$	~ 879
	0.53207	λ_{p2}	ω_{p2}	–
	0.5582	St_1	$\omega_{\text{p2}} - \omega_{\text{SRS}}$	~ 879
	0.5870	St_2	$\omega_{\text{p2}} - 2\omega_{\text{SRS}}$	~ 879
	0.6189	St_3	$\omega_{\text{p2}} - 3\omega_{\text{SRS}}$	~ 879
	0.6545	St_4	$\omega_{\text{p2}} - 4\omega_{\text{SRS}}$	~ 879

* Measurement accuracy is $\pm 0.0003 \mu\text{m}$.

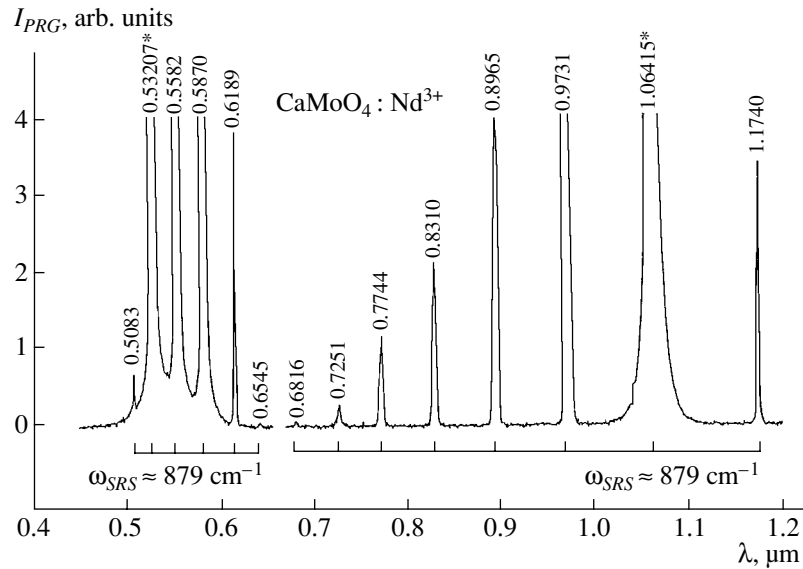


Fig. 2. Spectra of parametric Raman generation in CaMoO_4 under picosecond pumping with $\lambda_{p1} = 1.06415 \mu\text{m}$ and $\lambda_{p2} = 0.53207 \mu\text{m}$ at 300 K (for notation see Fig. 1).

the wavelengths of the first Stokes components in molybdates were higher by a factor of ~ 1.5 (about 480 mW). With an increase in the pump power absorbed in the lasing crystals from the threshold value up to the greatest accessible value (800 mW), the length of the stimulated-emission pulses and SRS decreased by a factor of 2, while their repetition rate increased by a factor of 2. Thus, at the pumping power $P_p \approx 750 \text{ mW}$, the lasing parameters of all the three crystals were almost equal, despite the different thresholds of the excitation of stimulated emission, namely, repetition rate $\sim 11 \text{ kHz}$, $\tau_{SI} \approx 35 \text{ ns}$, and $\tau_{SRS} \approx 20 \text{ ns}$. The total output power was about 3 mW; the ratio of the SRS and stimulated-emission contribution was about 1 : 5. At 300 K, the self-SRS lasers with $\text{CaMoO}_4 : \text{Nd}^{3+}$ emitted at $\lambda_{S1} \approx 1.166 \mu\text{m}$; with $\text{SrMoO}_4 : \text{Nd}^{3+}$, at $\lambda_{S1} \approx 1.167 \mu\text{m}$; and with $\text{SrWO}_4 : \text{Nd}^{3+}$, at $\lambda_{S1} \approx 1.156 \mu\text{m}$. The attained self-SRS conversion parameters can be substantially improved by optimizing the crystal characteristics (dimensions and concentration of Nd^{3+} -ions) and the scheme of semiconductor-laser pumping. In conclusion, we should like to emphasize that earlier, the stimulated-emission generation in the molybdates and tungstate under study was excited only under flashlight pumping.

ACKNOWLEDGMENTS

The authors note with gratitude that this study was performed in cooperation with the Joint Open Laboratory "Laser Crystals and Precision Laser Systems." They are grateful to R. Macdonald, D. Grebe, and J. Findeisen for their participation in the SRS experiments. The study was supported by the Russian Foun-

dation for Basic Research, project no. 00-02-16071, the International Association for Promotion of Cooperation of the Former Soviet Union (INTAS, project no. 99-01-366), and the Programs of the Ministry of Industry, Science, and Technologies of the Russian Federation.

REFERENCES

1. A. A. Kaminskiĭ, *Crystalline Lasers: Physical Processes and Operating Schemes* (CRC Press, Boca Raton, 1996).
2. A. A. Kaminskiĭ, *Raman Scattering—70 Years of Investigations* (Fiz. Inst. Ross. Akad. Nauk, Moscow, 1998), p. 206.
3. K. Andryunas, Yu. Vishchakas, V. Kabelka, *et al.*, *Pis'ma Zh. Éksp. Teor. Fiz.* **42** (8), 333 (1985) [*JETP Lett.* **42**, 410 (1985)].
4. A. A. Kaminskiĭ, N. S. Ustimenko, S. N. Bagaev, *et al.*, *Dokl. Akad. Nauk* **359** (2), 179 (1998) [*Dokl. Phys.* **43**, 148 (1998)].
5. A. S. Grabitchikov, A. N. Kuzmin, V. A. Lisnetskii, *et al.*, *Appl. Phys. Lett.* **75** (24), 3742 (1999).
6. A. A. Lagatsky, A. Abdolvand, and N. V. Kuleshov, *Opt. Lett.* **25** (9), 616 (2000).
7. W. Chen, Y. Inagawa, T. Omatsu, *et al.*, *Opt. Commun.* **194** (3), 401 (2001).
8. C. A. Wang and S. H. Groves, *IEEE J. Quantum Electron.* **28** (4), 942 (1992).
9. A. A. Kaminskii, S. N. Bagayev, K. Ueda, *et al.*, *Jpn. J. Appl. Phys.* **34** (11A), L1461 (1995).
10. A. A. Kaminskiĭ, S. N. Bagaev, D. Grebe, *et al.*, *Kvantovaya Élektron. (Moscow)* **23** (3), 199 (1996).
11. A. A. Kaminskiĭ, N. V. Klassen, B. S. Redkin, *et al.*, *Dokl. Akad. Nauk* **363** (1), 34 (1998) [*Dokl. Phys.* **43**, 659 (1998)].
12. A. A. Kaminskii, H. J. Eichler, K. Ueda, *et al.*, *Appl. Opt.* **38** (21), 4533 (1999).

13. A. A. Kaminskii, C. L. McCray, H. R. Lee, *et al.*, *Opt. Commun.* **183** (2), 277 (2000).
14. A. A. Kaminskii, S. N. Bagaev, K. Ueda, *et al.*, *Laser Phys.* **11** (10), 1142 (2001).
15. A. A. Kaminskii, *Laser Crystals, Their Physics and Properties* (Springer-Verlag, Berlin, 1990).
16. D. L. Rousseau, R. P. Bauman, and S. P. S. Porto, *J. Raman Spectrosc.* **10** (2), 253 (1981).
17. M. Liegeois-Duyckaerte and P. Tarte, *Spectrochim. Acta A* **28** (10), 2029 (1972).
18. P. Tarte and M. Liegeois-Duyckaerte, *Spectrochim. Acta A* **28** (10), 2037 (1972).
19. H. Kanamori, S. Hayashi, and Y. Ikeda, *J. Phys. Soc. Jpn.* **36** (2), 511 (1974).

Translated by A. Zolot'ko

PHYSICAL PROPERTIES OF CRYSTALS

New Family of $\text{LnBaMn}_2\text{O}_{6-\gamma}$ Manganites (Ln = Nd, Sm, and Gd)

I. O. Troyanchuk*, S. V. Trukhanov*, and G. Szymczak**

* *Institute of Solid-State and Semiconductor Physics, National Academy of Sciences,
ul. Brovki 17, Minsk, 220072 Belarus*

e-mail: troyan@iftf.bas-net.by

** *Institute of Physics, Academy of Sciences, ul. Lotnikov 32/46, PL-02-668, Warsaw, Poland*

Received January 4, 2002

Abstract—A new family of manganites, $\text{LnBaMn}_2\text{O}_{6-\gamma}$ (Ln = Nd, Sm, and Gd), is obtained by the method of topotactic reactions. In these compounds, rare-earth and barium ions are ordered, which results in a dramatic increase in the temperature of transition to the paramagnetic state. Thus, a $\text{SmBaMn}_2\text{O}_6$ compound with a disordered arrangement of Sm and Ba ions is a spin glass with the freezing temperature of magnetic moments $T_f = 40$ K, whereas in the state with an ordered Sm and Ba arrangement, the Curie temperature T_C , is ~ 280 K. Below T_C , a maximum in resistivity and magnetoresistance is observed. The possible models of magnetic ordering are discussed. © 2002 MAIK “Nauka/Interperiodica”.

INTRODUCTION

Manganites of the $\text{Ln}_{1-x}\text{D}_x\text{MnO}_3$ type (Ln is a rare-earth ion and D is an alkaline-earth ion) show a wide variety of magnetic and structural phase transformations with a dramatic change in the electric-transport properties. Therefore, they are convenient objects for studying the correlation between the magnetic and electric states. The important feature of manganites is their phase transformations provided by the orbital and charge states determining the type of magnetic ordering. Thus, the charge-ordered compounds are antiferromagnetic insulators, whereas the charge-disordered compounds are ferromagnetic metals [1]. An applied magnetic field causes a metamagnetic transition from the antiferromagnetic to the ferromagnetic state accompanied by a change in the conductance of many orders of magnitude [2–4].

It should be noted that the best studied manganites are those where Ln is replaced by alkaline-earth calcium and strontium ions [5–9]. This is explained by the possibility of growing high-quality single crystals with the given chemical composition by the floating-zone technique and the wide concentration range of the replacement of Ln by Ca and Sr which is, in turn, explained by the ionic radii of the considered elements. In the case of Ln replacement by calcium, a full series of solid solutions is formed if the synthesis proceeds in air, whereas if Ln is replaced by strontium, the complete series of solid solutions can be formed only under special conditions [10].

If Ln is substituted by barium, solid solutions are formed up to $x = 0.50$ in the synthesis in air [11]. In the range $0.20 \leq x \leq 0.50$, $\text{La}_{1-x}\text{Ba}_x\text{MnO}_3$ compounds are

metal ferromagnets with T_C up to ~ 350 K [12]. For the rare-earth ions, Ln = Pr and Nd, the temperature of magnetic ordering drops to ~ 160 K (Ln = Pr) [13, 14] and ~ 80 K (Ln = Nd) [11]. For the $\text{Sm}_{1-x}\text{Ba}_x\text{MnO}_3$ series, the replacement of Ln by barium ions leads to the concentrational phase transformation from the antiferromagnetic state ($x < 0.12$) to the spin-glass state ($x \geq 0.12$) without the transformation into the ferromagnetic phase. In this case, despite a great difference between the Ln and Ba ionic radii, the compounds with a high concentration of barium ions have a cubic structure [15], whereas the solid solutions where the rare-earth ions are replaced by calcium and strontium ions have an orthorhombically distorted unit cell.

It was reported [13] that the T_C of the $\text{Pr}_{0.50}\text{Ba}_{0.50}\text{MnO}_{3-\gamma}$ compound prepared under strongly reduction conditions is much higher than that of the same compound synthesized in air. For manganites, such a behavior of magnetic properties is very unusual, since it was established that the reduction of the $\text{La}_{1-x}\text{Ca}_x\text{MnO}_{3-\gamma}$ [16] and $\text{La}_{1-x}\text{Ba}_x\text{MnO}_{3-\gamma}$ series destroys the long-range order [17]. Moreover, it is known that the strongly reduced $\text{LnBaMn}_2\text{O}_5$ compounds become insulators with a magnetic-ordering temperature of ~ 120 K [17]. Therefore, we undertook a detailed study of the properties of the $\text{Ln}_{0.50}\text{Ba}_{0.50}\text{MnO}_{3-\gamma}$ compounds (Ln = Nd, Sm, and Gd) depending on the conditions of their synthesis. We established that the properties of these compounds are very sensitive to the crystallographic ordering of trivalent rare-earth ions and divalent barium ions in the A-sublattice of the perovskite-type ABO_3 structure.

EXPERIMENTAL

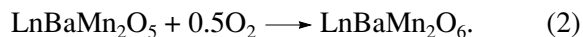
Ceramic $\text{LnBaMn}_2\text{O}_6$ samples (Ln = Nd, Sm, and Gd) were prepared using conventional ceramic technology. The samples of Ln_2O_3 and Mn_2O_3 oxides and BaCO_3 carbonate (of extra pure grade) were weighed in cationic proportion Ln : Ba : Mn = 0.50 : 0.50 : 1 and carefully mixed in an agate mortar with a small quantity of ethyl alcohol. Prior to weighing, the Ln_2O_3 was annealed for 2 h in air at a temperature of 1000°C to eliminate water and carbon dioxide. The mixtures of oxides and carbonates were pressed into pellets 1 cm in diameter and 1.5 cm in height, annealed for 2 h in air at 1100°C, and then ground. The synthesis was performed for 2 h in air at 1550°C. The samples were placed only on a platinum substrate. To obtain near stoichiometric compounds, the samples were held for 100 h in air at 900°C and then were cooled to room temperature at a rate of 100 deg/h.

The X-ray diffraction analysis of the reaction products was performed on a DRON-3 diffractometer (CrK_α -radiation) in the angular range $30^\circ \leq 2\theta \leq 100^\circ$ at room temperature. The oxygen content was determined by thermogravimetric analysis. According to our studies, the samples synthesized in air were stoichiometric with respect to oxygen. According to [18], the oxygen content in manganites with Ln replaced by calcium and strontium ions (up to $x \sim 0.50$) prepared in air was close to stoichiometric.

The reduced $\text{LnBaMn}_2\text{O}_6$ samples (Ln = Nd, Sm, and Gd) were obtained in the topotactic reactions. The samples were placed into the evacuated quartz ampoules together with a certain quantity of metallic tantalum (an oxygen getter). The quartz ampoules were held for 10 h at 900°C and then were cooled to room temperature at a rate of 100 deg/h. The equation of the reducing chemical reaction is



The oxygen content in the reduced samples was determined from the change in the mass by weighing the samples prior to and after the reduction. To decrease the relative error in the measurement of the oxygen content, we used a sample with a mass of 2–3 g. Under these conditions, the error did not exceed 0.3%. The reduced samples were reoxidized for 5 h in air at 900°C. The corresponding reaction is described by the equation



After oxidation, weighing the sample showed that the oxygen content increased in accordance with Eq. (2).

Magnetization was measured on a commercial OI-3001 vibrating magnetometer in the temperature range 4–350 K. The magnetic-transition temperature was determined as the temperature of the most sharp drop of magnetization (the minimum of the dM/dT derivative) in a low magnetic field. The electrical resistance was measured on $8 \times 2 \times 2\text{-mm}^3$ samples by the standard

four-probe method in the temperature range 77–350 K. The magnetoresistance was calculated by equation

$$MR(\%) = \{[\rho(H) - \rho(0)]/\rho(0)\} \times 100\%, \quad (3)$$

where $\rho(H)$ is the resistivity in a 9-kOe magnetic field and $\rho(0)$ is the resistivity in the zero magnetic field. The magnetic field was applied parallel to the electrical current in the sample.

RESULTS AND DISCUSSION

The unit-cell parameters of $\text{LnBaMn}_2\text{O}_{6-\gamma}$ samples (Ln = Nd, Sm, and Gd) prepared in air, reduced in quartz ampoules, and reannealed in air are indicated in Table 1. The samples obtained in air had a cubic unit cell, whereas the samples reduced in quartz ampoules had a tetragonally distorted unit-cell. With an increase in the atomic number of a rare-earth ion because of a decrease in its ionic radius, the unit-cell volume gradually decreased [19]. The reduced samples with a certain type of rare-earth ion had a much larger unit-cell volume, which is explained by the larger size of the manganese ion in the oxidized state. The nominal chemical formula of the reduced samples is $\text{LnBa}(\text{Mn}^{2+}\text{Mn}^{3+})\text{O}_{5 \pm 0.01}$. The X-ray diffraction patterns of $\text{NdBaMn}_2\text{O}_{6-\gamma}$ compounds ($\gamma = 0, 1$) (1) synthesized in air, (2) reduced in quartz ampoules, and (3) annealed in air after reduction are shown in Fig. 1. Similar X-ray diffraction patterns are also obtained from other samples with Sm- and Gd-ions. The c -parameter of the tetragonally distorted samples is doubled, which may be explained by the ordering of rare-earth and barium ions. The tetragonal distortion is partly removed by annealing in air at 900°C (Fig. 1c). Diffraction patterns of some samples annealed in air had a superstructure reflection indicating cationic ordering. It is worth noting that the volume per formula unit in the samples obtained in air and annealed after their reduction are approximately equal, although the volume in the second case is slightly smaller (Table 1). The tetragonal distortion is completely removed after annealing in air at 1300°C.

The temperature dependences of magnetization measured in a relatively low 100-Oe magnetic field after cooling the sample in a magnetic field (FC) and in a zero magnetic field (ZFC) are shown in Fig. 2. Prior to reduction, the temperature of magnetic ordering in the $\text{NdBaMn}_2\text{O}_6$ sample was about 90 K (Fig. 2a). A small temperature hysteresis (~ 3 K) near the temperature of magnetic ordering and a kink in the temperature dependence of magnetization that is still preserved in the fields up to 15 kOe indicate a first-order phase transition. The spontaneous magnetic moment per manganese ion is about $3\mu_B$, which is somewhat lower than the expected value of $3.50\mu_B$ under the assumption that $\mu(\text{Mn}^{2+}) = 4\mu_B$ and $\mu(\text{Mn}^{3+}) = 3\mu_B$. The reduced $\text{NdBa}(\text{Mn}^{3+}\text{Mn}^{2+})\text{O}_5$ sample is characterized by a much lower spontaneous magnetization (Fig. 3a), but the temperature of transition to the paramagnetic state

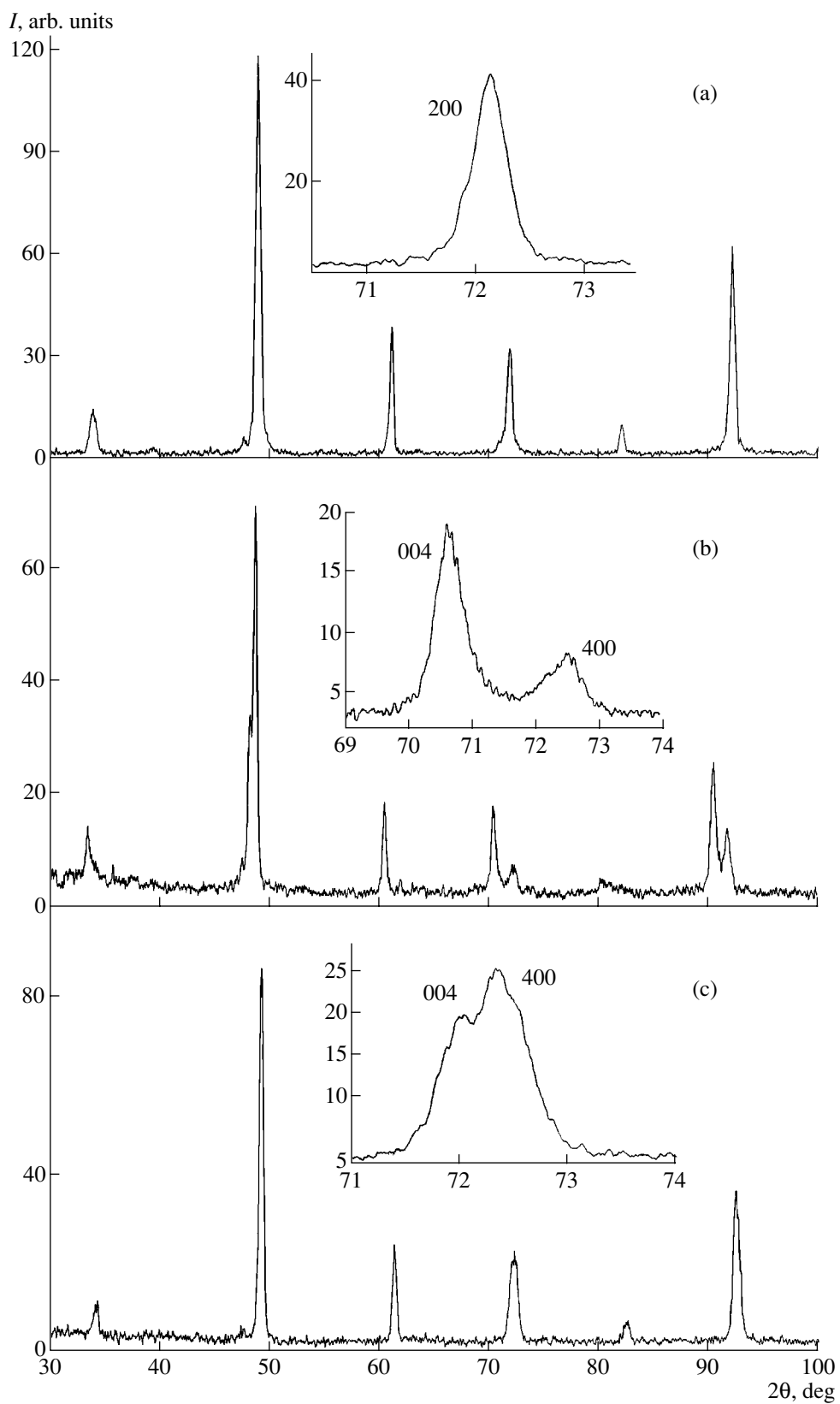


Fig. 1. X-ray diffraction patterns from the $\text{NdBaMn}_2\text{O}_{6-\gamma}$ sample (a) prepared in air ($\gamma = 0$), (b) reduced in a quartz ampoule ($\gamma = 1$), and (c) annealed in air after reduction ($\gamma = 0$). Insets show the 200 reflections for (a) and 004 + 400 reflections for (b) and (c).

Table 1. Unit-cell parameters (\AA) of $\text{LnBaMn}_2\text{O}_{6-\gamma}$ samples (A) prepared in air, (B) reduced in quartz ampoules, and (C) annealed in air after reduction

Chemical formula	Conditions of synthesis	Unit-cell symmetry	a , \AA	c , \AA	V , \AA^3
$\text{NdBaMn}_2\text{O}_6$	A	Cubic	3.896		59.16
$\text{NdBaMn}_2\text{O}_5$	B	Tetragonal	3.966	7.761	122.10
$\text{NdBaMn}_2\text{O}_6$	C	Tetragonal	3.899	7.756	117.94
$\text{SmBaMn}_2\text{O}_6$	A	Cubic	3.887		58.75
$\text{SmBaMn}_2\text{O}_5$	B	Tetragonal	3.951	7.727	120.62
$\text{SmBaMn}_2\text{O}_6$	C	Tetragonal	3.900	7.712	117.30
$\text{GdBaMn}_2\text{O}_6$	A	Cubic	3.879		58.39
$\text{GdBaMn}_2\text{O}_5$	B	Tetragonal	3.942	7.704	119.73
$\text{GdBaMn}_2\text{O}_6$	C	Tetragonal	3.901	7.651	116.47

Table 2. Type of magnetic state, critical temperature, and evaluated spontaneous magnetic moment per formula unit of $\text{LnBaMn}_2\text{O}_{6-\gamma}$ samples (A) prepared in air, (B) reduced in quartz ampoules, and (C) annealed in air after reduction. F is ferromagnet, FI is ferromagnetic insulator, SS is spin glass, F + P is inhomogeneous ferromagnet

Chemical formula	Conditions of synthesis	Magnetic state	T_C (K)	Spontaneous magnetic moment σ_c (μ_B per formula unit)
$\text{NdBaMn}_2\text{O}_6$	A	F	90	3.06
$\text{NdBaMn}_2\text{O}_5$	B	FI	130	0.23
$\text{NdBaMn}_2\text{O}_6$	C	F	320	2.94
$\text{SmBaMn}_2\text{O}_6$	A	SS	40	
$\text{SmBaMn}_2\text{O}_5$	B	FI	140	0.19
$\text{SmBaMn}_2\text{O}_6$	C	F + P	280	1.24
$\text{GdBaMn}_2\text{O}_6$	A	SS	40	
$\text{GdBaMn}_2\text{O}_5$	B	FI	145	0.92
$\text{GdBaMn}_2\text{O}_6$	C	F + P	250	0.28

increases up to 130 K. The *ZFC* and *FC* magnetization curves are essentially different (Fig. 2b), which is usually the case at high magnetic anisotropy. The transition to the paramagnetic state is rather steep, which is characteristic of magnetically uniform magnets. After annealing the reduced sample, both the spontaneous magnetization and Curie point drastically increase (up to 320 K) (Fig. 2c). The spontaneous magnetization is practically the same as for the sample prepared in air.

The $\text{SmBaMn}_2\text{O}_6$ sample prepared in air shows static magnetic properties typical of the spin-glass state (Fig. 3b). The *ZFC* magnetization curve (Fig. 2d) has a maximum at 40 K. Close to this temperature, the *ZFC* and *FC* curves diverge, and a spontaneous magnetization is recorded that cannot be saturated in fields up to 16 kOe (Fig. 3b). The curve $\sigma(H)$ is of the Langevin type characteristic of magnetic systems with clusters.

Long-range magnetic order arises in the reduced $\text{SmBaMn}_2\text{O}_5$ sample at a temperature close to 140 K

(Fig. 2e). This follows from the fact that the transition to the paramagnetic state is rather sharp. As in $\text{NdBaMn}_2\text{O}_5$, the spontaneous magnetization has a moderate value. It is difficult to evaluate the magnetic moment per manganese ion because of the pronounced contribution from rare-earth ions. Annealing in air leads to a dramatic rise in the critical temperature up to 280 K (Fig. 2f). However, the magnetization of this sample is much lower than for annealed $\text{NdBaMn}_2\text{O}_6$. Most probably, this can be explained by the existence of several magnetic phases, since the contribution from the samarium sublattice can hardly be that high. The properties of the $\text{GdBaMn}_2\text{O}_6$ sample annealed in air after reduction in the quartz ampoule are consistent with this assumption (Fig. 2i). Apparently, the $\text{GdBaMn}_2\text{O}_6$ sample prepared in air is also a spin glass with a T_f of about 40 K. A sharp rise in the (*FC*) magnetization with a lowering of the temperature is probably caused by the large contribution of the gadolinium

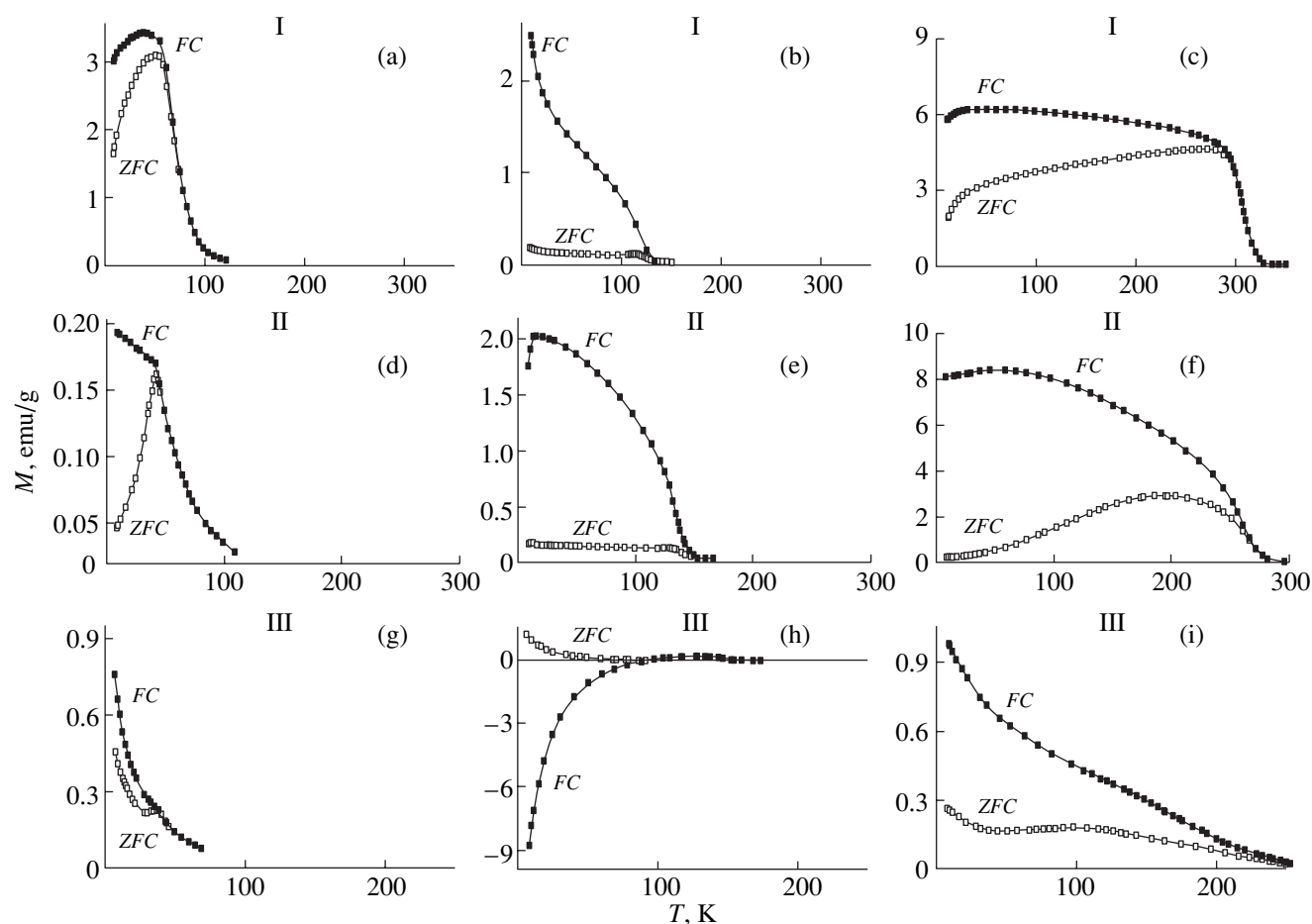


Fig. 2. Temperature dependences of magnetization in a 100 Oe external magnetic field (*ZFC*) after cooling in the zero field and (*FC*) after cooling in a magnetic field for (I) $\text{NdBaMn}_2\text{O}_{6-\gamma}$, (II) $\text{SmBaMn}_2\text{O}_{6-\gamma}$ and (III) $\text{GdBaMn}_2\text{O}_{6-\gamma}$ compounds (a, d, g) prepared in air ($\gamma = 0$), (b, e, h) reduced in quartz ampoule ($\gamma = 1$), and (c, f, i) annealed in air after reduction ($\gamma = 0$).

sublattice. It is well known that the magnetic moment of gadolinium is very high ($\mu(\text{Gd}^{3+}) = 7\mu_B$) [20]. The temperature of magnetic ordering in the reduced $\text{GdBaMn}_2\text{O}_5$ sample is 145 K (Fig. 2h). At a temperature of about 100 K, the compensation point is observed, which seems to be associated with the fact that with a lowering of the temperature, the contribution to magnetization from the gadolinium sublattice directed antiparallel to the magnetic moments of manganese ions gradually increases as in the case of rare-earth ions [20]. Although the *ZFC* and *FC* magnetization curves for the annealed sample diverge at a temperature of about 250 K, their smooth run is inconsistent with the cooperative process of magnetic ordering. A low value of spontaneous magnetization indicates an inhomogeneous magnetic state. One can assume that the magnetic properties of the $\text{GdBaMn}_2\text{O}_6$ sample annealed in air after reduction in the quartz ampoule are provided by ferromagnetic clusters with strong exchange interactions between manganese ions. Ferromagnetic clusters are incorporated in a paramagnetic matrix. This model does not contradict the experimen-

tal data. The results of the study of magnetic properties are listed in Table 2.

The temperature curves of electric conductance and magnetoresistance of the samples annealed in air after reduction are shown in Fig. 4. With a lowering of the temperature, the electric conductance of the $\text{NdBaMn}_2\text{O}_6$ and $\text{SmBaMn}_2\text{O}_6$ samples in a magnetically ordered state starts decreasing; however, the temperature of the resistivity maximum differs from the Curie point. In the vicinity of the Curie point, the maximum absolute value of magnetoresistance was observed, as in classical magnetic semiconductors. With a lowering of the temperature, a gradual increase in magnetoresistance was observed again, which is characteristic of polycrystalline samples of several conducting magnetic ceramics. This type of magnetoresistance is caused by the intergranular electric transport. The $\text{GdBaMn}_2\text{O}_6$ sample annealed in air after reduction shows a gradual increase in both resistivity and magnetoresistance, with a lowering of the temperature to 77 K (Fig. 4).

For the $\text{NdBaMn}_2\text{O}_6$ sample prepared in air, the classical behavior of electrical conductance and magne-

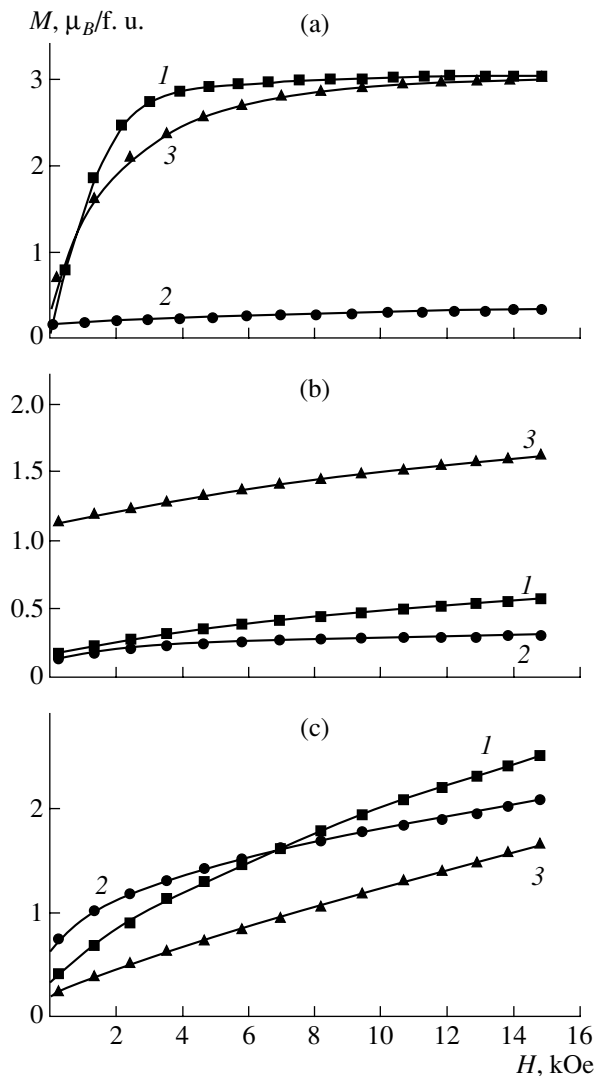


Fig. 3. Magnetization as a function of the applied magnetic field at 15 K for (a) $\text{NdBaMn}_2\text{O}_{6-\gamma}$, (b) $\text{SmBaMn}_2\text{O}_{6-\gamma}$, and (c) $\text{GdBaMn}_2\text{O}_{6-\gamma}$ compounds (1) prepared in air ($\gamma = 0$), (2) reduced in a quartz ampoule ($\gamma = 1$), and (3) annealed in air after reduction ($\gamma = 0$).

toresistance (typical of semiconductors) is observed, whereas $\text{SmBaMn}_2\text{O}_6$ and $\text{GdBaMn}_2\text{O}_6$ show neither the metal–insulator transition nor magnetoresistance, which is consistent with the magnetic data (Fig. 2d). The reduced $\text{LnBaMn}_2\text{O}_5$ samples are characterized by a high resistivity even at temperatures close to room temperature. It should be noted that the samples annealed in air at temperatures above 1300°C show magnetic and electric properties similar to those of the samples prepared in air.

We start our discussion with the nature of the magnetic state of the samples prepared in air. It is well known that the magnetic state of $\text{Ln}_{1-x}\text{D}_x\text{MnO}_3$ manga-

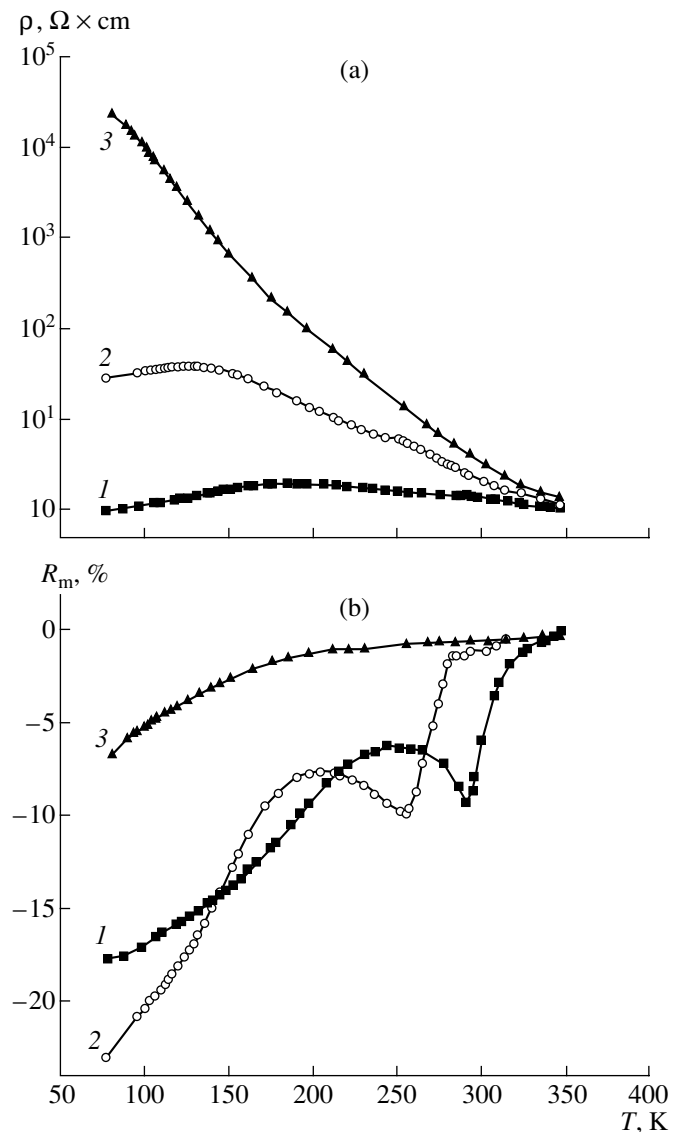


Fig. 4. Temperature dependences of (a) resistivity and (b) magnetoresistance in a 9 kOe external magnetic field for (1) $\text{NdBaMn}_2\text{O}_{6-\gamma}$, (2) $\text{SmBaMn}_2\text{O}_{6-\gamma}$ and (3) $\text{GdBaMn}_2\text{O}_{6-\gamma}$ compounds annealed in air after reduction ($\gamma = 0$).

nites ($D = \text{Ca}, \text{Sr}, \text{Ba}, \text{Pb}$) is determined by the ratio $\text{Mn}^{3+}/\text{Mn}^{4+}$ in the B -sublattice of the perovskite-like ABO_3 structure, the average ionic radii of alkaline-earth and rare-earth ions, and the variance between the cation sizes in the A -sublattice

$$\sigma^2 = \sum x_i r_i^2 - \langle r_A \rangle^2, \quad (4)$$

where x_i is the fractional occupancy of the perovskite-type A -sublattice by i -type cations with the radius r_i , and $\langle r_A \rangle$ is the average radius of the A -ions. This variance characterizes the difference between the radii of rare-earth and alkaline-earth ions [21]. The smaller the average ionic radius of the A -sublattice and the greater

the difference between the Ln and D radii, the lower the temperature of the magnetic ordering [22]. At a Mn^{3+}/Mn^{4+} ratio of manganese ions close to 1 : 1, an increase in the Mn^{4+} concentration results in the transition from the antiferromagnetic state to the ferromagnetic one [23]. The magnetic properties of the $Ln_{0.50}Ba_{0.50}MnO_3$ system are within the framework of this model. The compounds including relatively large ions such as La, Pr, and Nd are ferromagnetic metals, whereas compounds based on smaller ions such as Sm, Eu, Gd, and Tb show the properties of spin glasses with a semiconductor character of conductivity. The magnetic moment of $Nd_{0.50}Ba_{0.50}MnO_3$ seems to correspond to a two-phase state—the main ferromagnetic phase and small inclusions of the antiferromagnetic phase. It is precisely this explanation that is applied to the low magnetization values in comparison with their calculated value for the ferromagnetic ordering [24]. The spin-glass state arises because of a large difference in the Mn–O–Mn bond angles which, in turn, arise from the large difference between the ionic radii of Ln and D . One has to remember that the closer the Mn–O–Mn bond angle to 180° , the more pronounced the exchange interaction [25]. With a decrease in the Mn–O–Mn bond angle in the case of the orbitally disordered state, the sign of the exchange interaction can be changed from positive to negative. Since the Ln- and D -ions are randomly distributed over the A -sublattice, the local fluctuations in the Mn–O–Mn bond angle are lower than a certain critical value at which the ferromagnetic properties can yet exist, and, thus, the magnetic state of the spin-glass type is formed.

In the reduction of the $LnBaMn_2O_6$ to $LnBaMn_2O_5$, the Ln and Ba cations and oxygen vacancies are ordered in the A -sublattice as was observed for the $YBaMn_2O_5$ compound [26]. It is unambiguously established that the structure of this compound has planes predominantly occupied either by Ba- or Y-ions, alternating along the c -axis of the tetragonal unit cell. A similar crystal structure was also established in cobaltites $LnBaCo_2O_5$ [27].

The sharp transition to the paramagnetic state in the series of reduced samples indicates the existence of magnetic order. According to [28], the magnetic structure is determined by the antiparallel orientation of the magnetic moments of Mn^{3+} - and Mn^{2+} -ions. Unfortunately, the sample used in neutron diffraction studies [28] contained only 30% of the $YBaMn_2O_5$ phase, which considerably reduce the reliability of the results. At the antiparallel orientation of the magnetic moments of Mn^{3+} - and Mn^{2+} -ions, the magnetic moment per formula unit should be close to $1 \mu_B$; however, the magnetic measurements yielded a lower value (Fig. 3). Possibly, this is caused by the contribution made by rare-earth ions. In principle, a low ferromagnetic moment may arise from the Dzyaloshinski–Moriya antisymmetrical exchange, however, given the symmetrical consid-

erations and the relatively high magnetization it is hardly probable in these compounds.

We believe that the long-range order in the arrangement of Ln- and Ba-cations is preserved after annealing in air if the annealing temperature does not exceed $1300^\circ C$. It is also confirmed by the existence of the tetragonal distortions of the samples annealed in air after reduction in the quartz ampoule and the superstructure (0 0 3/2) reflection in their diffraction patterns. The long-range crystallographic order in the arrangement of cations in the A -sublattice gives rise to a translational symmetry in the Mn–O–Mn bond angles in the B -sublattice and, thus, to the formation of conditions under which ferromagnetism is possible. Note that the ordering of the Mn–O–Mn bonds results in a considerable increase in the temperature of magnetic ordering. Apparently, the bond angles in the samples oxidized after reduction (crystallographically ordered samples) vary only slightly with a decrease in radius of a rare-earth ion in contrast to the situation in the disordered $Ln_{1-x}Ba_xMnO_3$ with a perovskite structure. This assumption is confirmed by a slight decrease in the temperature of appearance of spontaneous magnetization with a decrease in the radius of the rare-earth ion.

There is no doubt that the compounds with large ionic radius of Ln are ferromagnetic, whereas with a decrease in the Ln radius, the inhomogeneous magnetic state is stabilized. We believe that the inhomogeneous magnetic state results from some structural characteristics of the ordered $LnBaMn_2O_6$ -type phases. To establish the details of the crystal and magnetic structures of these compounds, neutron diffraction studies are necessary.

ACKNOWLEDGMENTS

This study was supported by the Foundation for Basic Research of Belarus (project no. F00-223) and the Polish Science Committee (KBN, project no. PO3B 016-20)

REFERENCES

1. J. M. D. Coey, M. Viret, and S. von Molnar, *Adv. Phys.* **48**, 167 (1999).
2. Y. Tomioka, A. Asamitsu, Y. Moritomo, *et al.*, *Phys. Rev. Lett.* **74**, 5108 (1995).
3. M. Tokunaga, N. Miura, Y. Tomioka, and Y. Tokura, *Phys. Rev. B* **57**, 5259 (1998).
4. Y. Tokura and Y. Tomioka, *J. Magn. Magn. Mater.* **200**, 1 (1999).
5. G. H. Jonker and J. H. Van Santen, *Physica (Amsterdam)* **16**, 337 (1950).
6. G. Matsumoto, *J. Phys. Soc. Jpn.* **29**, 606 (1970).
7. G. Matsumoto, *J. Phys. Soc. Jpn.* **29**, 615 (1970).
8. X. Gang, E. J. McNiff, G. Q. Gong, *et al.*, *Phys. Rev. B* **54**, 6073 (1996).
9. A. Urushibara, Y. Moritomo, T. Arima, *et al.*, *Phys. Rev. B* **51**, 14 103 (1995).

10. K. Kikuchi, H. Chiba, M. Kikuchi, and Y. Syono, *J. Solid State Chem.* **146**, 1 (1999).
11. I. O. Troyanchuk, D. D. Khalyavin, S. V. Trukhanov, and H. Szymczak, *J. Phys.: Condens. Matter* **11**, 8707 (1999).
12. A. Barnabe, F. Millange, A. Maignan, *et al.*, *Chem. Mater.* **10**, 252 (1998).
13. I. O. Troyanchuk, S. V. Trukhanov, H. Szymczak, and K. Bärner, *J. Phys.: Condens. Matter* **12**, L155 (2000).
14. S. V. Trukhanov, I. O. Troyanchuk, I. M. Fita, *et al.*, *J. Magn. Magn. Mater.* **237**, 276 (2001).
15. I. O. Troyanchuk, S. V. Trukhanov, D. D. Khalyavin, and H. H. Szymczak, *J. Magn. Magn. Mater.* **208**, 217 (2000).
16. J. M. González-Calbet, E. Herrero, N. Rangavittal, *et al.*, *J. Solid State Chem.* **148**, 158 (1999).
17. V. Caignaert, F. Millange, B. Domenges, and B. Raveau, *Chem. Mater.* **11**, 930 (1999).
18. P. Shifer, A. P. Ramírez, W. Bao, *et al.*, *Phys. Rev. Lett.* **75**, 3336 (1995).
19. R. D. Shanon, *Acta Crystallogr., Sect. A: Cryst. Phys., Diffr., Theor. Gen. Crystallogr.* **32**, 751 (1976).
20. J. D. Cashion, A. H. Cooke, D. M. Martin, and M. R. Wells, *J. Appl. Phys.* **41**, 1193 (1970).
21. P. V. Vanitha, P. N. Santosh, R. S. Sing, *et al.*, *Phys. Rev. B* **59**, 13 539 (1999).
22. Lide M. Rodríguez-Martínez and J. Paul Attfield, *Phys. Rev. B* **58**, 2426 (1998).
23. H. Fujishiro, M. Ikebe, and Y. Konno, *J. Phys. Soc. Jpn.* **67**, 1799 (1998).
24. I. O. Troyanchuk, S. V. Trukhanov, H. Szymczak, *et al.*, *Zh. Éksp. Teor. Fiz.* **120**, 183 (2001) [*JETP* **93**, 161 (2001)].
25. E. E. Havinga, *Philips Rev. Rep.* **21**, 432 (1966).
26. T. P. Beales, M. Molgg, J. Jutson, and C. M. Friend, *Phys. Status Solidi A* **161**, 271 (1997).
27. E. Suard, F. Fauth, V. Caignaert, *et al.*, *Phys. Rev. B* **61**, R11 871 (2000).
28. J. A. Mcallister and J. P. Attfield, *J. Mater. Chem.* **8**, 1291 (1998).

Translated by T. Dmitrieva

PHYSICAL PROPERTIES
OF CRYSTALS

Manifestation of Nonequivalence of the Crystallographic {110} and {111} Planes and Charge-Transfer Mechanism in $Y_3Fe_5O_{12}$ Garnet Crystals

I. D. Lomako

*Institute of Solid-State and Semiconductor Physics, National Academy of Sciences of Belarus,
ul. Brovki 17, Minsk, 220072 Belarus*

e-mail: iftpanb@ift.basnet.minsk.by

Received September 24, 2001

Abstract—The nonequivalence of the crystallographic {110} and {111} planes in $Y_3Fe_5O_{12}$ (YIG) garnet crystals was revealed in the analysis of the crystal density as a function of the intensity ratio of coherent and incoherent X-ray scattering (K/nk). The samples were divided into two groups with different types of variation in their physical properties. For the first time, the quantitative correlation between the absorption coefficient α and K/nk with due account of the crystallographic orientation in the YIG crystals was established. It was found that the samples with the (111) orientation had minimum resistivity at 293 K because it is along this direction that the easy magnetization axis, domain boundaries, and dislocations were oriented. It was shown that the parameter K/nk can be used as a criterion for estimating the part of conduction electrons involved in charge transfer.
© 2002 MAIK “Nauka/Interperiodica”.

The main physical properties of $Y_3Fe_5O_{12}$ (YIG) single crystals such as optical absorption, specific Faraday rotation in the infrared (IR) range, and the width of the resonance absorption curve in the microwave range are strongly dependent on structural defects [1, 2]. The design of microwave and magneto-optical devices is closely related to the establishment of the unified mechanism underlying the variations in the physical properties associated with crystal growth and incorporation of noncontrolled impurities and structural defects. In spite of a very large number of publications on the electrical properties and nonstoichiometry of garnet-type crystals, none of them considered these problems with due regard for the crystallographic orientations of the samples [3–5].

The $Y_3Fe_5O_{12}$ garnet has a cubic unit cell containing eight $\{C_3\}[A_2](T_3)O_{12}$ formula units (the braces and square and round brackets indicate the positions of Y cations with the dodecahedral coordination and of Fe-ions octahedrally and tetrahedrally coordinated with oxygen ions, respectively). The crystal field in the dodecahedral positions (Y-ions) has orthorhombic symmetry with two axes being aligned in the $\langle 110 \rangle$ directions and the third axis aligned in one of the $\langle 100 \rangle$ directions [6]. The local symmetry is trigonal for the octahedral [A] positions and tetragonal for (T) positions occupied by Fe-ions and noncontrolled impurities.

The magnetic moments of Fe^{3+} -ions are antiparallel in the tetrahedral and octahedral sublattices and aligned along the $\langle 111 \rangle$ directions. For this direction, the magnetic moments of all the tetrahedral positions are mag-

netically equivalent; for two octahedral positions, they are not equivalent. Their nonequivalence manifests itself in the fact that the local C_3 -axis is parallel to the magnetization vector in the a_1 sublattice, whereas in the a_2 sublattice, the C_3 axis and the magnetization axis are directed along different space diagonals [7].

We continue the study of a series of YIG crystals by both increasing the number of samples and the range of techniques used [8–10]. All YIG crystals were grown from flux with the use of $PbO-PbF_2-B_2O_3$ or $BaO-B_2O_3$ solvents in both static and dynamic modes under the same conditions [8]. To study the anisotropy in the defect distribution in YIG, platelike 1.6–2.5-mm-thick samples were cut along the (110), (111), and (100) crystallographic planes. The transmission spectra were recorded on a Beckman spectrometer in unpolarized light in the 1000–2000 nm wavelength range at 293 K. The absorption coefficient α (at $\lambda = 1300$ nm) was calculated by the conventional formula taking into account the reflection coefficient and refractive index ($n = 2.3$) [9]. For the (110) and (111) orientations, we used specially chosen YIG plates of a high ($\alpha < 3$ cm $^{-1}$), medium ($3 < \alpha < 7.5$ cm $^{-1}$), and poor optical quality ($\alpha > 7.5$ cm $^{-1}$) (see table). The samples of group I were the high-quality plates and also some medium-quality ones (samples nos. 52 and 34), whereas the samples of group II were poor-quality plates and some medium-quality ones (samples nos. 50 and 32). The samples cut out from the same crystal but having different crystallographic orientations are indicated in the table and figures as nos. 40, 41, and 42. The samples were numbered

Classification of YIG samples into groups according to their optical quality with due regard for their absorption coefficients α and crystallographic orientations

Sample orientation	(110)		(111)		(100)		Nonoriented samples	
	α , cm ⁻¹	sample	α , cm ⁻¹	sample	α , cm ⁻¹	sample	α , cm ⁻¹	sample
Samples of group I	0.4	7	0.9	42	0.8	40		
	1.27	41	1.07	44	2.3	3		
Medium quality YIG samples	5.15	52	6.16	34			3.1	45
	6.91	50"					7.2	32
Samples of group II	13.2	50	10.2	46	23.5	VI-4		
	12.0	51	17.3	III-6				
			20.7	V-1				

according to the batches of plates of the same orientation or proceeding from their quality. Therefore, to facilitate the reading, we always indicate the specimen number in the figures. In Figs. 1–3, curves 1 and 2 correspond to (110)-oriented samples, curves 3 and 4, to (111)-oriented ones, and curve 5, to the (100) orientation.

In the samples under study, the relative content of Mn-ions and the weight ratio of the main ions (Y/Fe) were determined using neutron activation analysis. The mass of the samples ranged from 7 to 20 mg. The densities d were measured by the Archimedes method with an accuracy not lower than 0.3%. The mass of YIG samples ranged from 400 to 1100 mg. The quantitative data on the impurity content were obtained using the X-ray radiometric analysis using the Am²⁴¹ and Cd¹⁰⁹ excitation sources. The X-ray radiometric method was also used to determine the content of Y, Fe, Ba, Bi, and Pb and the intensity ratio of the coherent and incoherent scattering (K/nk). The analysis was performed on both sides of the plates with the averaging the results. The values of α , electrical resistivity (ρ), and K/nk were measured along the specified crystallographic directions at 293 K, so it was expected that the YIG samples studied would allow us to reveal the correlations associated with structural defects, nonstoichiometry, and the percentage of relatively free electrons.

The effect of nonstoichiometry and technological impurities (Ba, Mn, V) on the structural properties and absorption in the IR range was studied in our earlier study [10]. We also suggested the criterion for evaluating the quality of differently oriented plates from the batch under study in the form of the ratio of the total content of cations (Y + Fe) and the content of O anions (in our case, these quantities are expressed in wt %). Garnets possess a unique structure, which provides wide opportunities for introducing different ions with varying valence into the three nonequivalent cation

sublattices. The introduction of divalent ions (Ba, Ca, Pb) with large ionic radii into the dodecahedral sublattice provides the formation of vacancies at the cation sites of other positions. According to Kröger [11], each impurity atom gives rise to the formation of one vacancy. The final YIG faceting has only slowly growth-

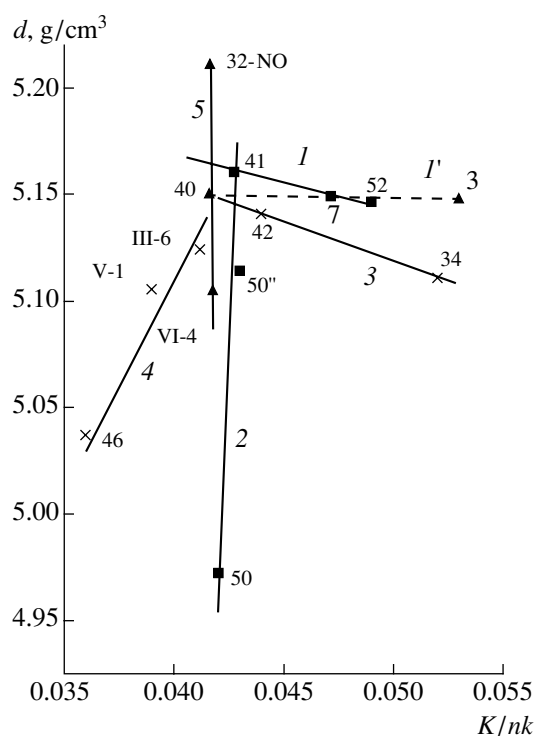


Fig. 1. Density of plates versus K/nk ratio for differently oriented YIG samples: (1) and (2), (110) orientation; (1') (dashed line), samples nos. 40 (110) orientation, 7 (110) orientation, 52 (110) orientation, and 3 (100) orientation; (3) and (4), (111) orientation; (5) (triangles), (100)-oriented samples and sample no. 32-NO.

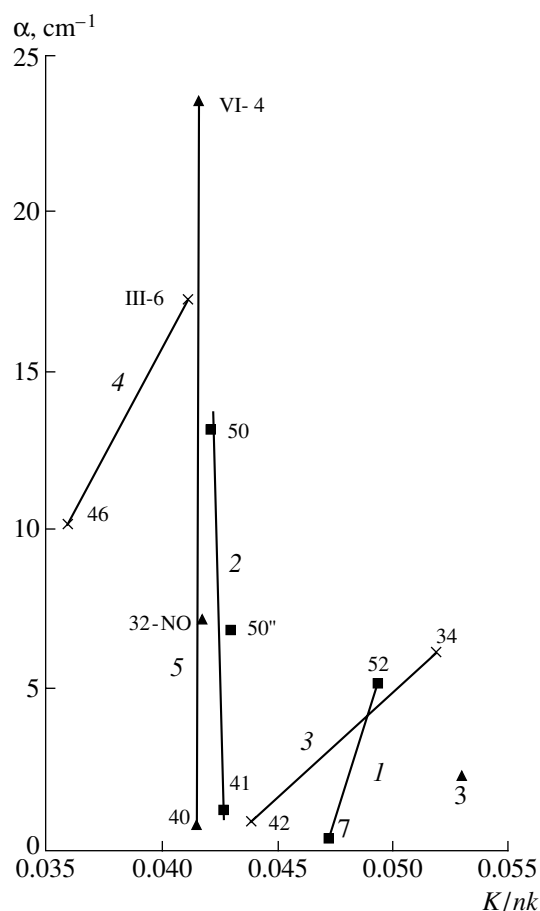


Fig. 2. Absorption coefficient α ($\lambda = 1300$ nm) versus K/nk ratio for differently oriented YIG samples: (1) and (2), (110) orientation; (3) and (4), (111) orientation; (5), (100)-oriented samples and sample no. 32-NO.

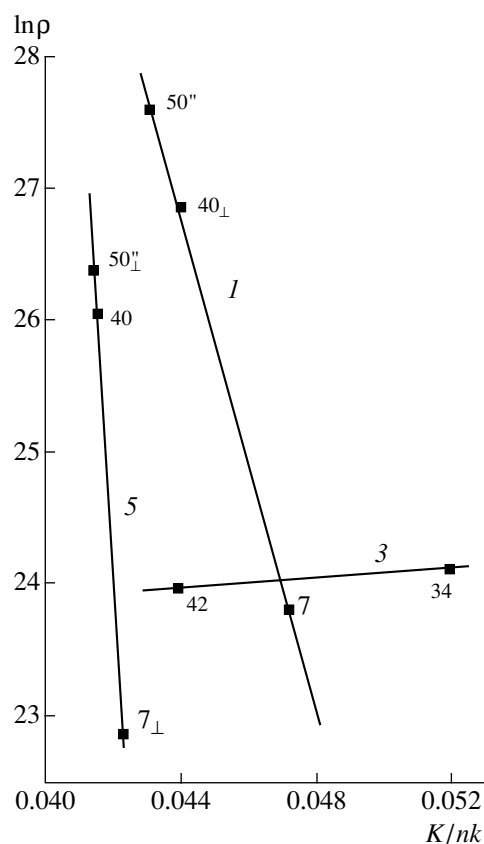


Fig. 3. Logarithm of electrical resistivity ρ at 293 K versus K/nk ratio for differently oriented YIG samples: (1) (110) orientation; (3) (111) orientation; (5) (100) orientation.

ing {110} faces. At the final growth stages (under conditions of low supersaturations), the difference in the growth rates of different faces and even of the faces of the same type differently located with respect to the feeding concentration flows becomes quite important. According to the conclusion made in [12], the growth rates for the {211} and {110} faces of YIG crystals are about twice as low as the growth rate of the (111) face.

The nonequivalence of the {110} and {111} planes in each group is clearly seen in Fig. 1, where the intensity ratio (K/nk) of coherent and incoherent X-ray scattering is plotted versus density d for YIG samples. The first group of samples with a density close to its theoretical value (5.17 g/cm^3) is characterized by a high transparency in the IR range and variations in the K/nk ratio over a wide range (Fig. 1, curve 1). Curve 1 corresponds to the (110)-oriented samples nos. 52, 7, and 41 (Fig. 1). The second group of (110)-oriented samples is represented by curve 2 in Fig. 1 (samples nos. 50, 50", and 41). The character of the curve is quite different: d varies over a wide range of values, whereas K/nk varies only slightly (0.042–0.043). Note that point 41

(sample no. 41) is located at the intersection of curves 1 and 2.

The K/nk ratio allows us to reveal the content of free electrons in each YIG sample taking into account the individual "ensemble" of impurity ions (Ba, Mn, Sm, Pb, V) with different valence, oxygen vacancies, and other structural defects. Most likely, the K/nk ratio characterizes the fraction of conduction electrons taking part in charge transfer, as was indicated by Sommerfeld [13].

The (111)-oriented samples are represented by curves 3 (samples nos. 34 and 42) and 4 (samples nos. III-6, V-1, and 46). The samples corresponding to curves 1 and 3 (group I) are characterized by high transparency in the IR range ($\alpha < 7 \text{ cm}^{-1}$).

The YIG samples of group II (curves 2 and 4, for which, usually, $\alpha > 7 \text{ cm}^{-1}$) are characterized by a looser structure and contain numerous impurities (see Table 1 from [10]). In [10], a similar type of implantation for a small amount of Ba ions and their effect on transparency was revealed in (110)- and (100)-oriented YIG samples. In the batch of samples studied, three

samples were cut from the same crystal: no. 40 (100), no. 41 (110), and no. 42 (111) and had the densities 5.15, 5.16, and 5.14 g/cm³, respectively. The (110) face growing at the minimum rate has a significant advantage in the uniform filling of the tetrahedral positions alternating with the dodecahedral ones and is characterized by the optimum d -value close to $d_{X\text{-ray}} = 5.17$ g/cm³. Sample no. 42 cut out parallel to (111) face growing at the maximum rate along the [111] direction in the garnet structure has the minimum density of the three plates cut out from the same crystal. Further analysis of the experimental results and the growth rates of the main crystal planes in YIG leads to the conclusion that the growth rate in the [100] direction is slightly higher than, or close to, the growth rate along the [110] direction, but is much lower than the growth rate along [111]. Among the YIG samples studied earlier, the minimum value, $\alpha = 0.034$ cm⁻¹, was obtained for the (100)-oriented plate [8]. This value is lower by about an order of magnitude than the value for (110)-oriented sample no. 7 from this batch possessing the highest transparency, $\alpha = 0.4$ cm⁻¹.

Figure 1 shows the data for (100)-oriented samples nos. 40 and VI-4 and for unoriented sample no. 32-NO with $d = 5.21$ g/cm³ and $K/nk = 0.0418$. Point 32-NO lies on the extension of curve 5. Point 3 ((100)-oriented sample no. 3) with coordinates $d = 5.147$ g/cm³ and $K/nk = 0.053$ is located separately and does not lie on any curve. At the same time, it can be joined to point 40 ((100)-oriented sample no. 40) corresponding to $d = 5.15$ g/cm³. Both samples are characterized by high transparencies, $\alpha = 2.3$ and 0.8 cm⁻¹, respectively, so that they can be related to group I. Taking into account the similar behavior of the (110)- and (100)-oriented YIG samples (for example, curves 2 and 5 in Fig. 1 and the aforementioned examples), we can suggest drawing curve I' through points 40, 7, 52, and 3 [samples nos. 40, (100); 7 and 52, (110); and 3, (100)]. For these samples, $d \approx (5.150 \pm 0.003)$ g/cm³ (dashed line in Fig. 1).

The nonequivalence of (110) and (111) planes in the garnet structure stems from the morphological and growth characteristics. The noncubic anisotropy of magnetic garnets grown from flux was first discussed in [14]. The (110) face, which has the minimum growth rate, has a morphological advantage in the successive filling of the tetrahedral positions alternating with dodecahedral positions occupied by Y- or Ba-ions. It is also characterized by the maximum thickness of an elementary layer ($EL \approx 4.37$ Å) [15]. For comparison, the thickness of an elementary layer on the (111) face is about 1.78 Å, which is less than that for the (110) face by a factor of 2.5. The thickness of the elementary layer is important since the stoichiometry in this layer remains unchanged; for the (100) face, the thickness of the elementary layer is 3.094 Å [16].

For the first time, we revealed the quantitative correlation between the absorption coefficient α and the K/nk ratio with due regard for the crystallographic ori-

entations of YIG samples (Fig. 2). Curve 1 describes samples nos. 7 and 52, and curve 2 describes samples nos. 41, 50, and 50 with the (110) orientation. Samples nos. 42 ($\alpha = 0.9$ cm⁻¹) and 34 (the latter is of medium quality) (see table). Two poor samples nos. 46 and III-6 from group II are described by curve 4. The samples cut out from the same crystal are presented by curves 5 (sample no. 40), 2 (sample no. 41), and 3 (sample no. 42) in Fig. 2. Curve 5 connects points VI-4, 40, and 32-NO characterizing sample no. VI-4 with the lowest transparency, one of the best samples with the (100) orientation (no. 40), and unoriented sample no. 32-NO with the coordinate $\alpha = 7/2$ cm⁻¹ that fits curve 5 well.

The analysis of data presented in Figs. 1 and 2 demonstrated that the points corresponding to the samples of group I are located on curves 1 and 3 and, partly, on curves 2 and 5, whereas the points characterizing the most transparent plates are located on the curves in the lower part in Fig. 2 and the upper part in Fig. 1. Curves 2 and 5 seem to form the boundary between the samples of the first and second groups and connect points corresponding to plates nos. 41 and 50 with the point of the extremum transparency; for the latter plate, the α value is maximal for the (110) orientation, and, similarly, for the (100) orientation, for samples nos. 40, 32-NO, and VI-4 ($\alpha = 23.5$ cm⁻¹).

To check the expediency of using the K/nk ratio as a characteristic of the number of conduction electrons taking part in charge transfer, we measured electrical resistivity at room temperature T_{room} for three differently oriented YIG samples with $\alpha < 7$ cm⁻¹ (mainly the samples from group I). The results are presented in Fig. 3, where the points corresponding to the (110)-, (111)-, and (100)-oriented samples are located on curves 1, 3, and 5, respectively. We assume that heat transfer proceeds along the crystallographic [111] directions to which the easy magnetization axis, dislocations, and domain walls are parallel. Therefore, the resistivity for the samples described by curve 3 is minimal.

The periodic chains of bonds (PCB-111) of the type O-3A-3D-3A-O, where O is a Fe-ion at the octahedral site, A is an anion (oxygen), and D is the Y-ion at the dodecahedral site are perpendicular to the (111) plane [15]. The easy magnetization axis, dislocations, and domain walls are parallel to these directions of YIG crystals. According to Blakemore [13], volume charges having cylindrical symmetry arise around the dislocations. The octahedral sublattice considerably distorts the generally non-cubic anisotropy in a garnet crystal [14]. Therefore, it is possible to state that PCB-111 contains numerous defects favoring charge transfer along these directions and providing the minimum resistivity of sample no. 42 ($\ln p = 23.95$) in comparison with resistivity of sample no. 40 with the (100) orientation ($\ln p = 26.05$). We believe that charge transfer in the (110)- and (100)-oriented plates takes place along PCB-001, which consist of T-2A-D-2A-T chains,

where T are the tetrahedral sites occupied by Fe-ions or those substituting them. These ions with a small radius create the minimum distortions in the garnet structure. Along the PCB-001 chains, the distortions should be less marked than along PCB-111. Hence, the numbers of defects and conduction electrons should also be less along this direction. That is why we observe the maximum resistivity in (110)- and (100)-oriented YIG samples.

As was shown earlier [8], divalent Ba-ions are inevitable technological impurities substituting Y-ions at the dodecahedral positions. The Ba-ions are characterized by stable valence and play the role of acceptor impurities in the YIG samples. On the contrary, Mn-ions can exhibit valences ranging from 2 to 4 and, in contrast to Y- and Ba-ions, they have magnetic moments, and, hence, they take an active part in charge transfer. Sample no. 7 with the (110) orientation has the maximum Mn content among all the samples of this batch and small content of Ba- and Pb-ions and shows the minimum resistivity among all the samples of group I. It seems that a small number of Mn-ions does not reduce the transparency in the IR range, because $\alpha = 0.4 \text{ cm}^{-1}$.

Note that changes $\Delta(K/nk) = 0.016$ are maximal for the (111)-oriented YIG plates of two groups. They are larger by a factor of 1.4 and 2.3 than those for (100)- and (110)-oriented plates. For the latter orientation, we have $\Delta(K/nk) = 0.007$. Note that $\Delta(K/nk)$ values for the three above orientations are inversely proportional to the thickness of the elementary layer; i.e., the minimum values of $\Delta(K/nk)$ for the (110) orientation correspond to the maximum thicknesses of the elementary layer, whereas at the (111) orientation, we arrive at the opposite limiting case.

For the samples with the minimum K/nk value, i.e., with the density of conduction electrons being low along the specified crystallographic direction, the electrical resistivity is maximal. The anisotropic character of K/nk variations for the three orientations is the most pronounced for samples nos. 40, 41, and 42 (see Figs. 1–3). For the (111)-oriented sample no. 42, the K/nk value is the largest, $K/nk = 0.0439$, while the $\ln p$ value is the lowest, $\ln p = 24$. For comparison, for (100)-oriented sample no. 40 and for (110)-oriented sample no. 50, we have $\ln p = 26$ and 27.59, respectively. The latter value of $\ln p$ is the highest for the batch of YIG single crystals under study.

Nonequivalence of crystallographic planes is caused by the distortions in the garnet structure arising during crystal growth from flux, the orthorhombic symmetry of the dodecahedral positions, and the nonequivalence of the two octahedral sublattices. The crystal grows in the shape of a dodecahedron inscribed into a sphere and is often faceted by the (110) planes. In the (110) plane, the short diagonal of the rhombus coincides with the [100] direction, whereas its long diagonal coincides with the [110] direction. In the course of growth, the

(211) faces can be formed, for which the [111] and [110] directions are mutually perpendicular [16].

If the plates are cut out along a specified crystallographic direction of the same crystal, the concentration inhomogeneity is observed [8]. Studying three differently oriented YIG samples cut out from the same crystal, we obtained close but not exactly coinciding values of α , lattice constants, and densities, whereas K/nk and electrical resistivity had essentially different values (Figs. 1–3). In other words, we observed obvious manifestations of anisotropy in growth and properties. The samples cut from different parts of different crystals, which were differently located with respect to the feeding concentration flows in the melt during growth, are characterized by nonstoichiometry and pronounced fluctuations in the impurity composition. For such samples, the {110} and {111} planes in YIG crystals were not equivalent.

Finally, we also managed to reveal the character of the variations in the density and the absorption coefficient with due account for structural defects in the plate with the aid of a single physical parameter K/nk , which, in our opinion, can be used as the criterion for estimating the relative density of conduction electrons in real crystals. We also revealed the nonequivalence of the main crystallographic planes {110} and {111}, which allows one to divide the samples of each orientation into two groups showing different behavior in their physical characteristics. In this paper, we also suggested the mechanism of charge transfer in YIG crystals via the PCB-111 and PCB-001 chains for (111)- and (110)-oriented YIG samples, respectively.

In the present series of experiments, we used 14 YIG plates of three different orientations. Obviously, it is insufficient to reveal all the variants of nonequivalence of crystallographic planes. General considerations allow us to conclude that the number of such variants should be not less than three at each orientation.

ACKNOWLEDGMENTS

The author is grateful to A.I. Komyak for stimulating discussions, N.A. Prytkova for the deposition of the indium contacts by the ultrasonic method, and A.I. Akimov for resistivity measurements of some YIG samples at $T = 293 \text{ K}$.

REFERENCES

1. D. L. Wood and J. P. Remeika, *J. Appl. Phys.* **38**, 1038 (1967).
2. A. A. Kaminskiĭ, E. A. Belokoneva, A. V. Butashin, *et al.*, *Izv. Akad. Nauk SSSR, Neorg. Mater.* **22**, 1061 (1986).
3. H. Donnerberg and C. R. A. Catlow, *J. Phys.: Condens. Matter* **5** (18), 2947 (1993).
4. R. Metselaar and P. K. Larsen, *J. Phys. Chem. Solids* **37**, 599 (1976).

5. R. Metselaar and H. Huyberts, *J. Solid State Chem.* **22**, 309 (1977).
6. L. R. Walker, *J. Appl. Phys.* **32**, S264 (1961).
7. P. Novak, J. Englich, H. Stepankova, *et al.*, *Phys. Rev. Lett.* **75** (3), 545 (1995).
8. I. D. Lomako, T. V. Smirnova, A. N. Igumentsev, and A. A. Mel'nikov, *Zh. Prikl. Spektrosk.* **63**, 667 (1996).
9. I. D. Lomako, A. G. Dutov, and A. N. Igumentsev, *Zh. Prikl. Spektrosk.* **67**, 217 (2000).
10. I. D. Lomako and A. G. Dutov, *Kristallografiya* **47** (1), 128 (2002) [*Crystallogr. Rep.* **47**, 120 (2002)].
11. F. A. Kröger, *The Chemistry of Imperfect Crystals* (Wiley, New York, 1964; Mir, Moscow, 1969).
12. A. N. Bobeck, *Bell Lab. Rec.* **48** (6/7), 163 (1970).
13. J. S. Blakemore, *Semiconductor Statistics* (Pergamon, Oxford, 1962; Mir, Moscow, 1964).
14. A. Rosencway and A. W. Tabor, *J. Appl. Phys.* **42**, 1643 (1971).
15. S. Sh. Gendelev and S. E. Semenov, *Izv. Akad. Nauk SSSR, Ser. Fiz.* **35**, 1220 (1971).
16. S. Sh. Gendelev and N. G. Shcherbak, *Kristallografiya* **10** (5), 708 (1965) [*Sov. Phys. Crystallogr.* **10**, 592 (1965)].

Translated by K. Kugel

PHYSICAL PROPERTIES
OF CRYSTALS

Localization of Plastic Deformation in Cu and Ni Single Crystals

V. I. Danilov, S. A. Barannikova, K. V. Gonchikov, and L. B. Zuev

*Institute of Strength Physics and Materials Science, Siberian Division, Russian Academy of Sciences,
Akademicheskii pr. 8, Tomsk, 634021 Russia*

e-mail: levzuev@mail.tomsknet.ru

Received November 15, 2001

Abstract—The patterns of plastic flow in fcc Cu and Ni single crystals oriented in a way to provide easy slip are studied. The main space–time characteristics of deformation localization at the stages of easy slip and linear strengthening in these single crystals are established. The relation between the orientation of the sites of deformation localization and the crystallography of the slip systems in the samples is studied. The velocity of the motion of the deformation-localization sites during sample tension is determined. © 2002 MAIK “Nauka/Interperiodica”.

INTRODUCTION

The characteristics and the specific features of plastic deformation cannot be studied without doing corresponding experiments on single-crystal samples, because these experiments provide the most exact determination of the main crystallographic elements of slip lines and bands and different stages of the deformation process and also the establishment of the relation between these stages and the distribution and motion of dislocations [1]. It is the experiments on Cu and Ni single crystals that laid the basis of the first theory of deformation strengthening [2].

Recent studies showed [3–8] that plastic deformation in the range from the yield stress to the complete fracture of the sample is necessarily accompanied by deformation localization on a macroscale. The experiments performed on both single crystals and polycrystals allowed not only the observation of deformation localization but also provided its systematization and establishment of the deformation types and the relation between the deformation type and deformation strengthening at the corresponding stage of flow. The ordered patterns of deformation localization are formed on the basis of the initial chaotic distribution of deformation sites [5–7] corresponding either to the initial or the transient parts of the stress–strain curves. The analysis of the general form and the quantitative parameters of the evolution of the patterns of plastic-flow localization showed its possible relation to the self-organization of the subsystem of defects in the deformed medium described in detail elsewhere [9–11]. This allowed us to suggest [3] and develop [4–8] an approach to the description of the evolution of the macroinhomogeneity of the plastic flow based on the representation of the localization zones in the form of auto-waves of plastic flow [12] characterized by the experi-

mentally determined wavelength λ and the velocity of the wave propagation V_{aw} .

The most interesting phenomena are observed in fcc single crystals at the stages of easy slip and linear strengthening, because fundamental data clarifying the nature of deformation strengthening in metal crystals are obtained from the analysis of the characteristic curves of plastic flow [2].

Earlier, this problem was studied mainly on single crystals of various doped alloys. This considerably reduced the generality of the theory thus developed, because it is well known that the micro- and macro-tails of plastic flow in alloys are essentially different from those in pure (undoped) metals [13, 14]. Thus, the stage of linear strengthening of solid solutions is considerably longer than this stage in metals. It is especially important that the propensity to slip localization is much more pronounced for alloys that are specially oriented for multiple slip. Under these conditions, the problem of the existence and possible forms of localization of plastic deformation in undoped Cu and Ni single crystals under tensile stresses becomes very important.

EXPERIMENTAL

The crystals used in our study were grown by the Bridgman technique from reagent-grade Cu and Ni (99.98%) on a Redmet-1 setup. The flat dumb-bell samples were cut out from homogenized single-crystal ingots on an electroerosion machine. The crystallographic orientation of the single crystals and the prepared samples was determined by the X-ray diffraction method.

The dimensions of the working part of single-crystal Cu samples were $30 \times 5 \times 3$ mm. The longitudinal axes

coincided with the $[\bar{1}39]$ direction, whereas the broad working surface was indexed as $(3\bar{2}1)$. Upon cutting out the samples, they were annealed for an hour at 1123 K and then were cooled in the furnace. The maximum value of the Schmid factor $m_1 = 0.49$ for the above orientation was possessed by the $(111)[\bar{1}01]$ slip system. The lines of this slip system should form an angle of $\varphi_1 = 44^\circ 26'$ on the working surface. The $(\bar{1}11)[101]$ and $(11\bar{1})[011]$ systems have Schmid factors $m_2 = 0.47$ and $m_2' = 0.41$, respectively, and, thus, are the secondary systems. Their slip lines on the working surface form the angles of $\varphi_2 = 90^\circ$ and $\varphi_2' = 40^\circ 30'$ with the sample axis. Under tension in the direction of the long axis and upon the attainment of the yield stress, these specimens are deformed via single slip along the $(111)[\bar{1}01]$ system.

The shape of the Ni samples was the same as the Cu, but the dimensions of the working surface were different, $30 \times 5 \times 1.3$ mm. The cut-out samples were annealed for 20 h in a neutral atmosphere at 1273 K and then were cooled in the furnace. The longitudinal axis of the samples coincided with the $[\bar{1}67]$ direction, whereas the working surface was indexed as $(0\bar{7}6)$. The Schmid factor of the primary $(111)[\bar{1}01]$ system was $m_1 = 0.46$, whereas these factors of the secondary $(111)[1\bar{1}0]$ and $(\bar{1}11)[101]$ systems were $m_2 = m_2' = 0.40$. The slip lines (or traces) of the primary slip system formed angles of $\varphi_1 = 48^\circ 28'$ with the sample axis on the working surface, whereas those of the secondary slip system, $\varphi_2 = 131^\circ 32'$ and $\varphi_2' = 119^\circ 9'$.

The main experimental procedure consisted in the successive restoration of the fields of the translation vectors of the points $\mathbf{r}(x, y)$ simultaneously on the whole sample surface (where x and y are the coordinates of the points on the surface) directly in the tension process [6] by the methods of double-exposure speckle interferometry [15] on an Instron-1185 testing machine at a rate of $5.5 \times 10^{-5} \text{ s}^{-1}$. These fields were recorded during loading with a time interval of 36 s (the increment in the total deformation $\delta\varepsilon_{tot} = 0.2\%$). The numerical differentiation of the set of $\mathbf{r}(x, y)$ values with respect to x and y provided the determination of the longitudinal ε_{xx} , shear ε_{xy} , and rotational ω_z components of the tensor of plastic distortion $\beta = \nabla\mathbf{r}(x, y)$ [16] at the points of the sample surface at a step of 1 mm. In what follows, we limit our consideration to local elongation $\varepsilon_{xx} = \partial u/\partial x$ of the samples (the u projection of \mathbf{r} onto the elongation axis x). The construction and analysis of the spatial $\varepsilon_{xx}(x, y)$ and spatial-temporal $\varepsilon_{xx}(x, t)$ patterns allow the determination of the zones of deformation localization and observation of their evolution with time. The slip traces in deformed samples were ana-

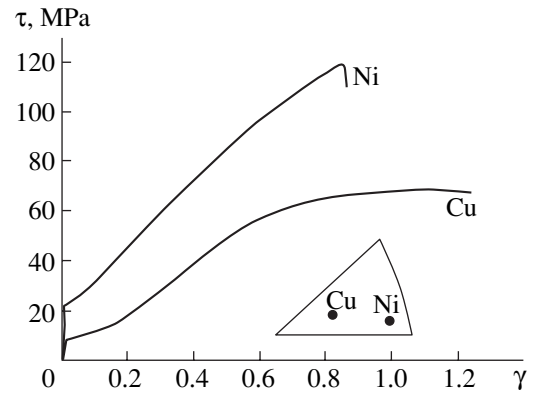


Fig. 1. Tension diagrams for Cu and Ni single-crystal samples. The orientations of the tension axes and the slip elements are indicated in the text.

lyzed in a Neophot-21 metallographic microscope. The tests were performed at 300 K.

EXPERIMENTAL RESULTS

The tension curves for the materials studied were constructed in the coordinates “reduced shear stress τ —reduced shear γ ” as was indicated in [13, 14] (Fig. 1). One can clearly see three stages that are characteristic of fcc single crystals—the stages of easy slip (I) and linear (II) and parabolic (III) strengthening [2, 13, 14]. We determined the following parameters of plastic flow: critical shear stress τ_0 , coefficients of deformation strengthening $\theta = d\tau/d\gamma$ at the stages of easy slip (θ_I) and linear strengthening (θ_{II}), and shear deformation corresponding to the beginning γ_{II} and end γ_{III} of the stage of easy slip. These data are listed in the table, which, for the sake of comparison, also contains the corresponding values taken from monograph [13]. Despite the qualitative differences, the deformation in Cu and Ni single crystals was consistent with generally accepted ideas, and, thus, the plastic flow is developed from the easy slip via linear strengthening to the parabolic stage.¹

Now, consider the patterns of slip traces on the observation plane of the samples. In a Cu single crystal, only the primary $(111)[\bar{1}01]$ system is active at the first stage (Fig. 2). Fine slip traces in this system form an angle of 40° with the sample axis. Then, prior to the completion of this stage, some short rough traces of the secondary $(\bar{1}11)[101]$ system appear at the crystal edges, which are inclined at an angle of 86° to the axis (Fig. 2). By this moment, the whole working plane of

¹ The value $\theta_I = 1.7 \times 10^{-4} G$ for Cu single crystals is minimal [2], with θ_I being essentially dependent on the orientation [13]. McLean points out [17] that θ_I for various orientations of fcc crystals ranges within 10^{-4} – $10^{-3} G$. According to Honeycombe [14], the $[139]$ -oriented Cu single crystals at 300 K have $\theta_I = 23$ – 41 MPa. At the same time, the coefficient θ_I is almost independent of orientation and is close to $4 \times 10^{-3} G$ at 300 K for all the fcc single crystals [12, 17].

Parameters of deformation strengthening in Cu and Ni single-crystal samples and their comparison with data [13]

Crystal	τ_0 , MPa	$\theta_I/G \times 10^4$	$\theta_I/G \times 10^4$ [13]	$\theta_{II}/G \times 10^3$	$\theta_{II}/G \times 10^3$ [13]	γ_{II}	γ_{III}
Cu	6.2	7.5	4	2.6	3	0.135	0.3
Ni	23	11	5	2	3	0.06	0.17

Note: For notation, see text.

the sample is uniformly filled with the slip traces of the primary system. The differences between the experimentally observed and the calculated angles (see above) seem to be caused by the insufficiently accurate determination of the sample orientation by the X-ray diffraction method. As earlier, at the stage of linear strengthening, one mainly observed the traces of the primary slip system.

In Ni single crystals, the traces of the $(111)\bar{1}01$ system also appear at the stage of easy slip. They form an angle of 49° with the sample axis (Fig. 2), which is within the error of the X-ray diffraction method used to determine the sample orientation. At the same stage, traces of the secondary $(\bar{1}11)[101]$ system also appear, which form an angle of 122° with the tension axis. However, the number of the latter traces is less than the number of the traces of the primary system within the whole deformation process. These traces often intersect the traces of the primary system and become bent

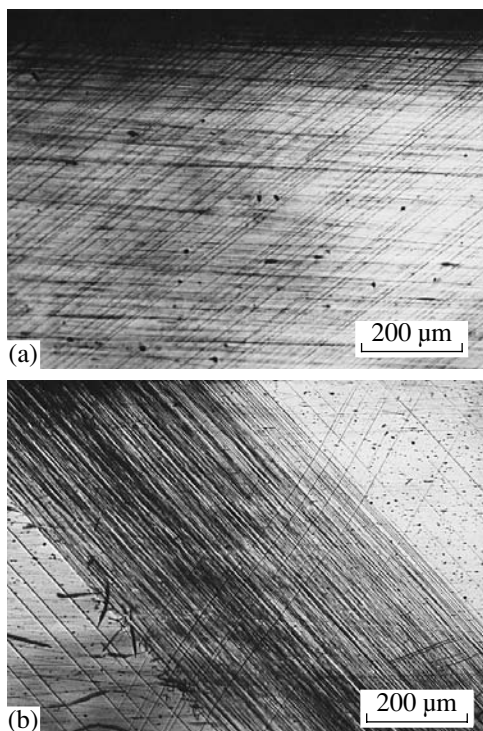


Fig. 2. Slip traces on the working surface of a single-crystal sample; (a) Cu, $\gamma_{tot} = 0.075$ and (b) Ni, $\gamma_{tot} = 0.055$. The completion of the easy-slip stage.

(Fig. 2). Also, at the first stage, one can often observe the surface regions where there are no slip traces at all. With further tension of the sample and the transition to the stage of linear strengthening, the densities of the traces of primary slip and the primary and secondary systems increase, and they become curved and rough. At the stage of linear strengthening, the traces of the primary and secondary slip systems fill the whole working field. The traces of the $(11\bar{1})[101]$ system on the working surface of the samples were never observed at all; they were recorded only at the sample "heads."

Thus, the analysis of the shape of the plastic-flow curves and the orientations of the slip traces showed no essential differences from those observed for Cu and Ni single crystals [13, 14] and, thus, these data are indicated here only to prove the accuracy of the experimental method used. Completely new results were obtained in the studies of the plastic-deformation distribution over the samples at different stages of flow. The measurements of the local elongation made by the speckle-interferometry method showed that deformation is macroscopically localized at all stages of the plastic flow.

Figure 3 shows the arrangement of the sites of deformation localization ϵ_{xx} characteristic of the easy-slip stage. In Cu single crystals, it is a combination of three or four equidistant zones ($\lambda = 4.0 \pm 0.5$ mm) more than 1.5 mm in width. The map of isolines of local elongations for this case (Fig. 3) shows that these zones are inclined to the longitudinal axis of the sample at an angle of $\varphi = 50^\circ$ – 55° . It seems that this fact is provided by the action of only one primary slip system, whose traces, as was indicated above, are inclined by an angle of $\varphi_1 = 40^\circ$ to the $[\bar{1}39]$ axis.

The pattern of local elongation in a Ni sample at the easy-slip stage is shown in Fig. 4. Two local ϵ_{xx} maxima move toward one another; the map of isolines of local elongations (Fig. 4) shows that, at the very beginning of the easy-slip stage, the slope of one deformation site is $\varphi_1 = 50^\circ$, whereas that of the other one is $\varphi_1' = 54^\circ$. In other words, these sites are almost parallel. Later, these angles increase approaching 90° . We should like to repeat once again that the traces of the primary slip system $(111)\bar{1}01$ in Ni form an angle of $\varphi_1 = 49^\circ$ with the direction of the tension axis $[\bar{1}67]$. A situation with two moving zones of deformation localization in Ni is very

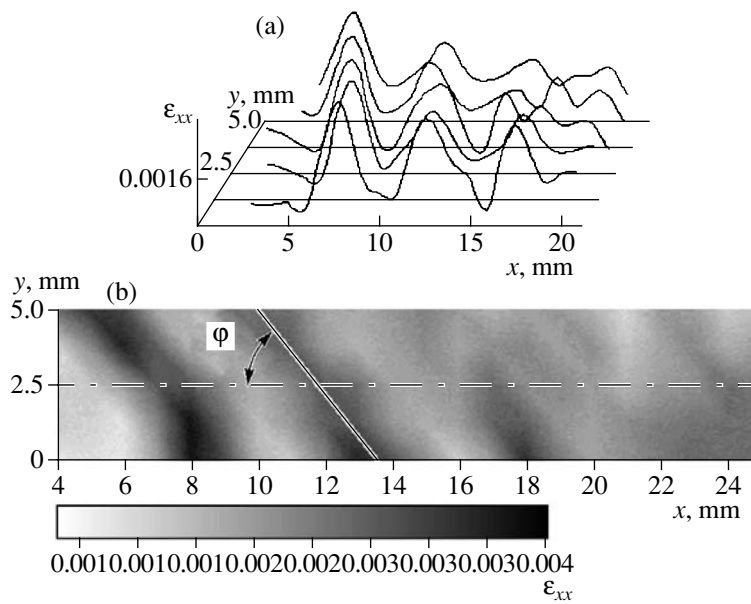


Fig. 3. Arrangement of moving deformation sites at the stage of easy slip in (a) a Cu single crystal and (b) isolines of local elongation corresponding to this case; $\gamma_{tot} = 0.03$, $\phi = 53^\circ$ is the angle of the inclination of the zones of deformation localization to the tension axis.

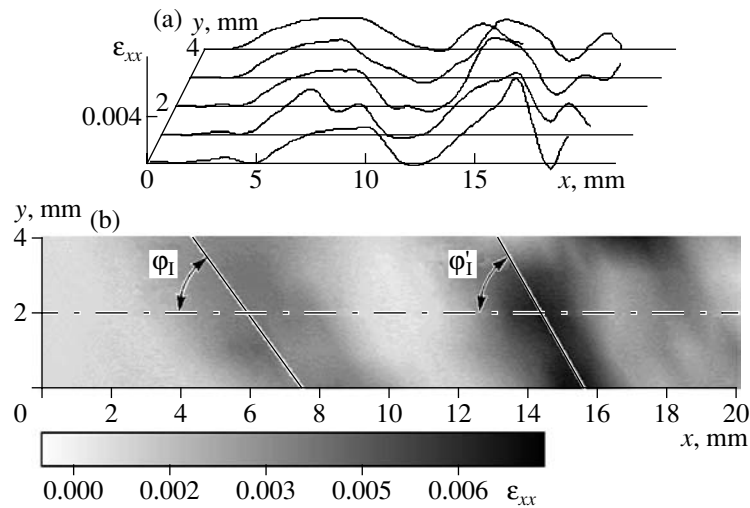


Fig. 4. Arrangement of moving sites of deformation localization at the stage of easy slip in (a) an Ni single crystal and (b) isolines of local elongation, $\gamma_{tot} = 0.03$.

often encountered. However, we also observed the motion of a single deformation front oriented approximately along the traces of the primary slip system.

The patterns of local-deformation distribution at the stage of the linear strengthening in both materials are the mobile sequences of equidistant sites of plastic flow similar to those described for the easy slip in Cu single crystals. There also exist four moving sites of deformation localization. In Ni, the distance between the localization zones is $\lambda \approx 3.5$ mm, in Cu, 4.5 mm (Fig. 5).

DISCUSSION

The data obtained show that the phenomenon of the localization of plastic flow is of a general nature and is readily seen in both Cu and Ni single crystals at the stages of easy slip and linear strengthening, which until now has gone unnoticed.² Nevertheless, it is clear that the real pattern of deformation distribution in single crystals is *a priori* inconsistent with the assumption that

² At the parabolic stage of strengthening in Cu and Ni single crystals, the sites of localized plasticity form a stationary periodic system similar to that described, e.g., in [3–5].

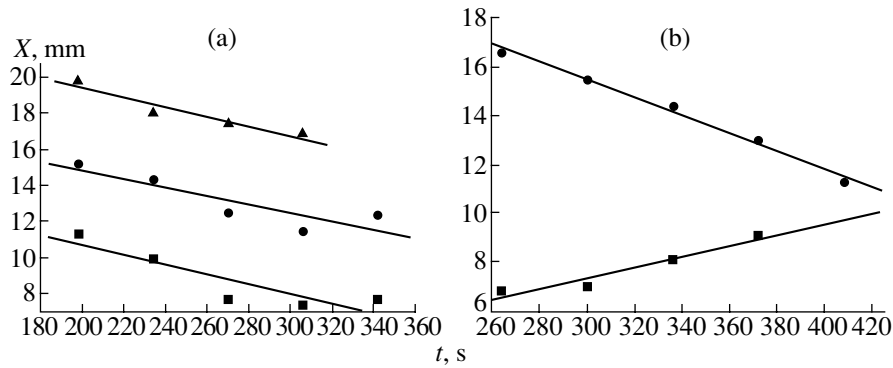


Fig. 5. Determination of the motion velocity of sites of deformation localization at the stage of easy slip in (a) Cu and (b) Ni single crystals.

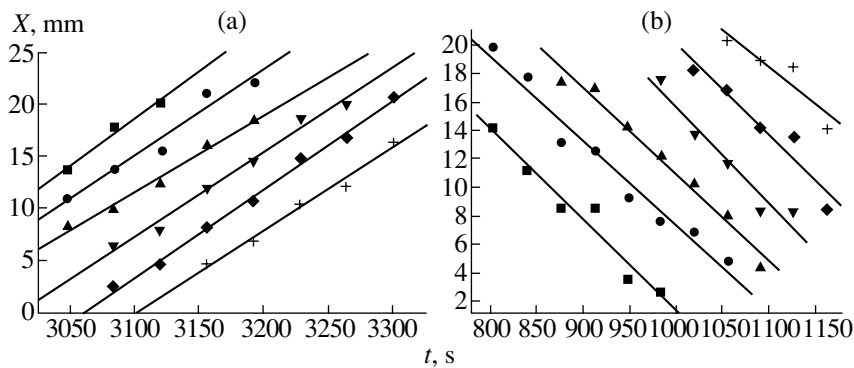


Fig. 6. Spatial-temporal arrangement of the sites of deformation localization at the stage of the linear strengthening in (a) Cu and (b) Ni single crystals.

dislocation-induced shear is uniformly distributed in the bulk of a deformed crystal [18]. Plastic flow is localized in certain active zones of the sample regularly distributed along its length. In this case, the zones between these sites show no deformation, whereas the active zones (at least at the stages of easy slip and linear strengthening) move along the sample axis. In this motion, some parts of the sample participate in plastic flow only successively, one after another, and not simultaneously. Such cycles of the participation in plastic flow are repeated several times within one stage of the process.

The most interesting feature of the localization of plastic deformation at the stages of easy slip and linear strengthening is the mutually correlated motion of the sites of plastic flow along the tension axis. This phenomenon was first observed in undoped single crystals, although it is studied in detail [6–8] in doped single crystals and polycrystals of some metals and alloys.

At the stage of easy slip of the deformation process in Cu and Ni, the sites of deformation localization move synchronously. Figure 6 shows the positions of the X maxima of localization of the component ε_{xx} on the tension axis as a function of time t . The velocity of their motion V_{av} was determined from the slope of the

dependence $X(t)$ [4–6]. It was established that, at the stage of easy slip, the zones of deformation localization in Cu single crystals move with a velocity of 2.6×10^{-5} m/s, whereas in Ni single crystals, with velocities of $+3.6 \times 10^{-5}$ m/s and -2.2×10^{-5} m/s. The signs + and – indicate the opposite directions of the motion of the zones of deformation localization in Ni. The orders of magnitude of the velocities (10^{-5} m/s) are close to those recorded earlier at the stages of easy slip in single crystals of the Cu–Ni–Sn alloy [4], chromium–nickel austenite [8], and manganese austenite ([012] orientation) [19], but they are much higher than the analogous values obtained in NiTi single crystals [5, 6] and manganese austenite with the tension axis parallel to the [377] direction [19]. This qualitative difference seems to be caused by the fact that deformation in the NiTi intermetallic compound is attained via the martensite $B2 \rightarrow B19'$ transformation [20] and in the [377]-oriented single crystals of the Hatfield steel, by twinning [21], whereas the deformation in all the other materials is associated with dislocation-induced slip.

We should like to emphasize the fact that, in single crystals of the Cu–Ni–Sn alloy and doped γ -Fe, the patterns of deformation localization at the stage of easy slip are in the form of moving individual deformation

fronts similar to the Lüders bands observed, e.g., in α -Fe polycrystals [14, 17]. This situation is also characteristic of Ni single crystals, where the deformation front passes one time each unit volume and where one or two fronts moving in the opposite directions can be considered as Lüders bands. The stage of easy slip is completed when two deformation sites meet, and, in the case of deformation caused by the motion of an individual front, it is completed simultaneously with the completion of the front's motion.

However, the configuration of several successively moving deformation sites that is usual in Cu single crystals (Fig. 3) is closer to the situation characteristic of the stage of linear strengthening (see below). In this case, the periods of active deformation in each zone of the sample regularly alternate with almost the same periods of absence of any deformation.

At the stage of linear strengthening, the mobile equidistant systems of the plastic-flow sites (the "waves") are formed in Cu and Ni single crystals. The velocities of the motion of these sites are somewhat higher than at the stage of easy slip and are equal to 8×10^{-5} m/s in Cu and 6×10^{-5} m/s in Ni (Fig. 6). An increase in the velocity of the deformation-site motion at the stage of linear strengthening with respect to that at the stage of easy slip was also observed earlier in the tension experiments on single crystals of the Cu–Ni–Sn alloy and also on the chromium–nickel and high-manganese austenites. It was shown [7, 22] that at the linear stage the velocities of the motion of deformation sites V_{aw} are inversely proportional to the coefficient of deformation strengthening $\theta^* = G^{-1}\theta_{II}$ normalized to the shear modulus G . It follows from Fig. 7 that our data can be described by a linear dependence of the form

$$V_{aw} = V_0 + \Omega/\theta^*, \quad (1)$$

whose plot was constructed with the use of known data on the velocities of the waves in other (doped) single crystals [3–8]. In the above equation, $V_0 = 3.6 \times 10^{-5}$ m/s and $\Omega = 2.5 \times 10^{-7}$ m/s are the constants, whereas the correlation coefficient is ~ 0.74 . The result obtained confirms the similar character of the wave processes observed at the stage of linear strengthening in all the single crystals.

Consider a possible nature of the dependence $V_{aw} \sim 1/\theta^*$ at the stage of linear strengthening. Based on the fact that the velocity of the motion of the site of localized deformation is proportional to the path of the head dislocations of a planar pileup, we assume that $dV_{aw}/d\theta^* \sim l(\theta^*)$ (where l is the length of the slip line at this stage). The explicit form of the function $l(\theta^*)$ can be determined from the following consideration. According to [2], $l = \Lambda/(\gamma - \gamma_1)$ with the constant Λ being dependent only on the material studied, whereas deformation γ_1 corresponds to the beginning of the

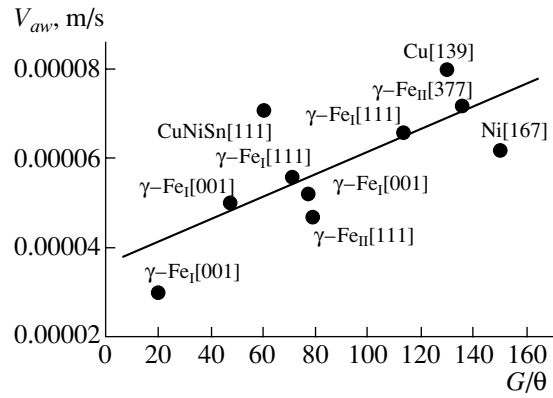


Fig. 7. Generalized dependence of the velocity of the deformation autowaves on the coefficient of deformation strengthening.

stage of linear strengthening. As was shown in [2], we have at the stage of linear strengthening

$$\theta^* \approx \sqrt{nb/3\Lambda}, \quad (2)$$

where n is the number of dislocations with the Burgers vector b in the planar pileup [2, 13]. Determining Λ from (2) and assuming that Λ and θ^* vary with the change of the material, we have

$$dV_{aw} \sim \frac{nb}{\gamma - \gamma_1} \frac{d\theta^*}{\theta^{*2}}. \quad (3)$$

Since $\gamma - \gamma_1$ and n only weakly depend on the material [13], it follows from (3) that $V_{aw} \sim 1/\theta^*$.

CONCLUSION

Thus, the study of plastic deformation in undoped single crystals of fcc metals confirmed the statement made in [3–8] that there exist new types of waves associated with the self-organization processes. These waves are generated during the quasi-static deformation of solids. Since these waves were observed earlier in doped single crystals and polycrystals of various alloys [6–8, 22, 23], then, with due regard for the new data, the wave (autowave) nature of plastic deformation can be recognized as universal for the processes of plastic flow in all the materials. It should be emphasized that the wavelike approach allows the detection of considerable differences in the deformation of various materials. Thus, the deformation localization (the wave patterns) at the stage of easy slip in Cu and Ni single crystals are different with all the other parameters of the process being practically the same. This difference can be caused by different properties of the active media [12] generating different types of the autowave processes in single crystals.

Another aspect of the problem is that, while analyzing microscopically different types of dislocation ensembles formed at different stages of plastic flow, it is necessary to take into account from which part of the

sample volume the microsample was cut out. In this case, the total deformation of the sample may no longer serve as an adequate description of the process. Thus, the analysis of this statement showed [23] that the deformation structures in localized deformation sites develop much faster than in the regions between these sites. This seems to be very important especially for the interpretation of the transmission electron microscopy (TEM) data for thin foils. In this case, the analysis of the dependence of the densities of various dislocations on the total deformation without allowance for the character of deformation localization at each stage of the process can give somewhat erroneous results.

REFERENCES

1. E. Schmid and W. Boas, *Kristallplastizität, mit besonderer Berücksichtigung der Metalle* (J. Springer, Berlin, 1935; Gos. Ob"edinennoe Nauchno-Tekhnicheskoe Izd. NKTP SSSR, Moscow, 1938).
2. A. Seeger, in *Dislocations and Mechanical Properties of Crystals: Proceedings of the International Conference, 1956* (Wiley, New York 1957; Inostrannaya Literatura, Moscow, 1960).
3. L. B. Zuev, *Metallofiz. Novejšie Tekhnol.* **16**, 31 (1994).
4. L. B. Zuev, V. I. Danilov, and N. V. Kartashova, *Pis'ma Zh. Éksp. Teor. Fiz.* **60**, 538 (1994) [*JETP Lett.* **60**, 553 (1994)].
5. L. B. Zuev and V. I. Danilov, *Fiz. Tverd. Tela* (St. Petersburg) **39**, 1399 (1997) [*Phys. Solid State* **39**, 1241 (1997)].
6. L. B. Zuev and V. I. Danilov, *Philos. Mag. A* **79**, 43 (1999).
7. L. B. Zuev, V. I. Danilov, S. A. Barannikova, *et al.*, *Kristallografiya* **46**, 99 (2001) [*Crystallogr. Rep.* **46**, 92 (2001)].
8. L. B. Zuev, V. I. Danilov, and S. A. Barannikova, *Int. J. Plast.* **17**, 47 (2001).
9. Y. Estrin and P. L. Kubin, *Acta Metall.* **34**, 2455 (1986).
10. E. C. Aifantis, *Int. J. Plast.* **3**, 211 (1987).
11. G. A. Malygin, *Usp. Fiz. Nauk* **169**, 979 (1999).
12. V. A. Vasil'ev, Yu. M. Romanovskii, and V. G. Yakhno, *Autowave Processes* (Nauka, Moscow, 1987).
13. R. Berner and H. Kronmüller, *Plastische Verformung von Einkristallen, in Moderne Probleme der Metallphysik*, Ed. by A. Seeger (Springer-Verlag, Berlin, 1965; Mir, Moscow, 1969).
14. R. W. K. Honeycombe, *The Plastic Deformation of Metals* (Arnold, London, 1968; Mir, Moscow, 1972).
15. R. Jones and C. M. Wykes, *Holographic and Speckle Interferometry* (Cambridge Univ. Press, Cambridge, 1983; Mir, Moscow, 1986).
16. A. Kadic and D. G. B. Edelen, *A Gauge Theory of Dislocations and Disclinations* (Springer-Verlag, Berlin, 1983; Mir, Moscow, 1986).
17. D. McLean, *Mechanical Properties of Metals* (Wiley, New York, 1963; Metallurgiya, Moscow, 1965).
18. J. Diehl, *Z. Metallkd.* **47**, 411 (1956).
19. S. A. Barannikova, *Zh. Tekh. Fiz.* **70** (10), 138 (2000) [*Tech. Phys.* **45**, 1368 (2000)].
20. V. S. Boiko, R. I. Garber, and A. M. Kosevich, *Reversible Plasticity in Crystals* (Nauka, Moscow, 1991).
21. A. A. Urusovskaya, in *Modern Crystallography*, Vol. 4: *Physical Properties of Crystals*, Ed. by B. K. Vainshtein, A. A. Chernov, and L. A. Shuvalov (Nauka, Moscow, 1981; Springer-Verlag, Berlin, 1988).
22. L. B. Zuev, *Ann. Phys.* **10**, 965 (2001).
23. T. M. Poletika, V. I. Danilov, and L. B. Zuev, *Fiz. Met. Metalloved.* **91**, 5 (2001).

Translated by L. Man

**SURFACE, THIN FILMS,
AND NANOMATERIALS**

On Two-Dimensional Ferroelectricity in Layered Polymer Films on Substrates

S. A. Pikin

*Shubnikov Institute of Crystallography, Russian Academy of Sciences,
Leninskii pr. 59, Moscow, 117333 Russia*

e-mail: pikin@ns.crys.ras.ru

Received February 14, 2002

Abstract—A simple model for describing structural phase transitions in thin ferroelectric copolymer films on solid substrates obtained by the Langmuir–Blodgett method has been suggested. It is shown that the polymer–substrate interaction and surface tension considerably influence these transitions and, in particular, can induce additional low-temperature first- and second-order phase transitions depending on the material parameters and the film thickness. The main dimensionless parameter and its critical value, which control the formation of the additional order in very thin films, are determined. © 2002 MAIK “Nauka/Interperiodica”.

INTRODUCTION

Recently, the existence of a ferroelectric phase transition in thin films of arbitrary copolymers of vinylidene fluoride and trifluorethylene were reported for the cases where the film thickness did not exceed several monomolecular layers [1–4]. Two first-order phase transitions were observed in these almost two-dimensional films—a high-temperature transition at the temperature close to that of the phase transition in a bulk copolymer sample and a low-temperature phase transition, which seemed to be provided only by surface properties of the film. This phenomenon is rather interesting in terms of fundamental and applied science. The physical reasons of this phenomenon are not quite clear. Thus, the two-dimensional ferroelectricity observed in these experiments was explained only by the properties of the copolymer thin film, whereas the effect of the substrate supporting this film was ignored [1–4]. However, taking into account the method used for film preparation—layer-by-layer application of the polymer by the Langmuir–Blodgett method providing the formation of the layer structure (i.e., the introduction of an additional order into the molecular system), one can expect that the substrate should also play an important role. As in the case of smectic liquid crystals, this additional order can be described by the order parameter $\psi(\mathbf{r})$ decreasing relatively rapidly with the distance of the point of observation from the substrate along the surface normal (the z -axis) and includes the periodic dependence $\exp(i\mathbf{k}\mathbf{r})$, where the component k_z of the wave vector \mathbf{k} is close to the reciprocal thickness of a molecular layer. This layer consists of a fragment of both the main polymer chain and also the side chains characterized by the constant electric dipole moments \mathbf{p} , which form crystalline grains with the macro-

scopic polarization \mathbf{P} in the ferroelectric phase of the copolymer.

In a conventional disordered film, these crystalline regions are oriented in a random way, but in artificially synthesized layer films, these regions can also have the above-mentioned additional order, whose character is strongly dependent on the copolymer–substrate interaction. The maximum value of the order-parameter amplitude, $|\psi|$, on the substrate equals ψ_0 . In the absence of any surface effects, this order parameter equals zero in the whole film. Thus, one can assume that the macroscopic polarization \mathbf{P} interacts with this order parameter of the structure so that, in the simplest case, \mathbf{P} depends on the coordinate z only slightly, whereas $\psi(\mathbf{r})$ rapidly varies in the vicinity of the substrate–copolymer interface. It should be indicated that, unlike the situation in freely suspended films of chiral smectics of type C , where polarization is the consequence of the inclination of the chiral molecules [15], the polarization \mathbf{P} in the materials under study is, in fact, the inherent order parameter. The experiments also revealed some changes in thin crystalline films and their “metallic” properties [6, 7]. Below, we shall show that the unusual ferroelectric behavior of very thin polymer Langmuir–Blodgett films in which the small depth of the structural modulation imitates the two-dimensional order in a thin subsurface layer can be interpreted in terms of a rather simple model.

MODEL OF SURFACE-INDUCED PHASE TRANSITION

The structure of a polymer ferroelectric Langmuir–Blodgett film has not been studied in detail as yet. However, there is no doubt that this structure is similar to that of a smectic and that, similar to all the Langmuir–Blodgett films, it is obviously of a defective nature.

Since the macroscopic polarization \mathbf{P} exists in the local regions, the smectic order can promote an increase in the component P_z even in the absence of an electric field. The experimental data [1] indicate that the maximum value of P_z corresponds to 50% polarization, with all the dipoles being normal to the film surface. The surface tension of the film dependent on the interaction between the dipole moments of the polymer chains and the substrate should considerably influence the film structure. Since the data for constructing a microscopic model of the surface tension are rather limited, we suggest a simple phenomenological model that describes the interaction of a polarized copolymer with the substrate, which induces an additional positional ordering of the chains in the vicinity of the film surface with the density distribution

$$\Psi = \psi_0 \exp(-\lambda z + i\mathbf{k}\mathbf{r}), \quad (1)$$

where $\psi = \psi_0 \exp(-\lambda z)$ is the amplitude of the density wave, ψ_0 is the amplitude at the interface, the positive parameter λ determines the rate of decrease in the density with the distance from the substrate, and \mathbf{k} is the wave vector of the subsurface structure, which describes the local order of the polymer chains in the crystal.

In this case, the effect produced by the surface can be taken into account by introducing the following term into the free-energy density:

$$\frac{c}{2} P_z \left(\Psi^* \frac{d\Psi}{dz} + \Psi \frac{d\Psi^*}{dz} \right) = -c\lambda P_z \psi_0^2 \exp(-2\lambda z). \quad (2)$$

This term is invariant in the whole crystal structure. In the simplest approximation, there is no need to consider the dependence of the component P_z on the coordinate z , because the copolymer is also polarized in the film bulk also at $\Psi = 0$; in other words, it is possible to assume that the characteristic scale of considerable variations in P_z essentially exceeds the scale of λ^{-1} . Integrating Eq. (2) over the volume, we arrive at a negative contribution to the energy equal to $-cP_z\psi_0^2/2$ at a certain polarization orientation on the surface dependent on the sign of the phenomenological constant c characterizing the interaction between the substrate and the polarized copolymer.

In the general case, the solution $\psi = \psi_0 \exp(-\lambda z)$ can be obtained by minimizing the total free energy

$$F = \int_0^L \left[\tau P_z^2 + \frac{1}{2} P_z^4 + a|\psi|^2 + |\psi|^4 + \frac{d\Psi}{dz} \frac{d\Psi^*}{dz} + \frac{c}{2} P_z \left(\Psi^* \frac{d\Psi}{dz} + \Psi \frac{d\Psi^*}{dz} \right) \right] dz, \quad (3)$$

where the quantity cP_z in square brackets in the integrand is positive, L is the film thickness, the temperature-dependent parameter τ describes the formation of

the inherent ferroelectricity, a is the positive parameter corresponding to the absence of inherent smectic order, and the coefficients before P_z^4 , $|\psi|^4$, and $|d\Psi/dz|^2$ are omitted under the assumption that the quantities P_z , ψ , and z are renormalized so as to simplify further computations. The local crystal structure and the vector \mathbf{k} in Eqs. (1) and (3) are not specified, and the allowance for the concrete value of the component k_z results only in the renormalization of the coefficient a . It should be emphasized that an additional proper structural transition is impossible because of the positiveness of the parameter a .

Equation (3) shows that solution (1) is correct if the term $|\psi|^4$ is small in comparison with the term $a|\psi|^2$ and, therefore, can be considered as a certain correction. In the case where $|\psi|^4$ considerably exceeds $a|\psi|^2$, the amplitude $\psi(z)$ is determined from the equation

$$2\psi^3 = \frac{d^2\Psi}{dz^2} \quad (4)$$

with the solution

$$\psi = \frac{1}{z + A}. \quad (5)$$

Solution (5) minimizes the free energy so that the value of $\psi(0) \equiv \psi_0$ is equal to $1/A$. Equations (1) and (5) are very useful for the qualitative consideration of possible phase transitions in the vicinity of the interface, where polarization $P_z(T)$ increases with a decrease in the temperature T .

As usual, the possible appearance of the inherent polarization P_z is associated with the reversal of the sign of the parameter τ , whereas its modulus $|\tau|$ is assumed to be small. Substituting Eq. (1) into Eq. (3) and minimizing F with respect to the parameter λ , we arrive at

$$\lambda^2 = a + \frac{1}{2} \psi_0^2, \quad (6)$$

which is approximately correct if the value of ψ_0^2 is less than that of the parameter a . The further substitution of Eq. (6) into Eq. (3) and minimization of F with respect to ψ_0^2 determines the quantity

$$\psi_0^2 = \frac{1}{9} (c^2 P_z^2 - 12a) + \sqrt{\frac{1}{81} (c^2 P_z^2 - 12a)^2 + \frac{4a}{9} (c^2 P_z^2 - 4a)}. \quad (7)$$

Using Eqs. (3) and (7), we obtain the free energy $F(P_z, \tau)$. To determine the conditions for the occurrence of the phase transition from the state $\{\psi_0^2 = 0, P_z^2 = -\tau\}$

to the state $\{\psi_0^2 \neq 0, P_z^2 \neq 0\}$, we have to consider the following two equations:

$$\frac{\partial F(P_z, \tau)}{\partial P_z} = 0, \quad F(P_z, \tau) = -\frac{1}{2}\tau^2 L. \quad (8)$$

Introducing the new variables (y, t) and the parameter α with the aid of the equations

$$\tau = -\frac{a}{c^2}t, \quad P_z = \frac{\sqrt{a}}{c}y, \quad \alpha = \frac{4\sqrt{a}}{c^4}L \quad (9)$$

and applying Eq. (9), we can rewrite Eq. (8) in the form

$$t = \frac{16 - 3y^2 + 12\alpha y^3}{1 + 12\alpha y} \quad (10)$$

$$= y^2 - \frac{1}{\alpha y} \left[\frac{1}{9}(y^2 - 12) + \sqrt{\frac{1}{81}(y^2 - 12)^2 + \frac{4}{9}(y^2 - 4)} \right].$$

The solutions of Eq. (10) describe second-order phase transitions if $\alpha \geq 1/8$; then, at the phase-transition point $t_c = 4$, the following relationships are satisfied: $y_c^2 = t_c = 4$ and $\psi_0^2 = 0$. However, if $\alpha < 1/8$, first-order phase transitions occur; then, the "transition temperature" t^* is approximately equal to

$$t^* \approx 4[1 - (1 - 8\alpha)^2], \quad (11)$$

if the value of $(1 - 8\alpha)$ is small. The corresponding jumps in the order parameters at the transition point are

$$y^{*2} \approx 4 + \frac{16}{3}(1 - 8\alpha), \quad P_z^* \approx \frac{2\sqrt{a}}{c} \sqrt{1 + \frac{4}{3}(1 - 8\alpha)}, \quad (12)$$

$$\psi_0^{*2} \approx \frac{4a}{3}(1 - 8\alpha).$$

If $t \geq t^*$, i.e., at temperatures lower than the temperature of the first-order phase transition, where $t = t^* + \Delta t$, $y = y^* + \Delta y$, and $\psi_0^2 = \psi_0^{*2} + \Delta\psi_0^2$, Eqs. (10) yield

$$\Delta y \approx -\frac{2}{7}(1 - 8\alpha) + \sqrt{\frac{4}{49}(1 - 8\alpha)^2 + \frac{18}{77}\Delta t}, \quad (13)$$

$$\Delta\psi_0^2 \approx a\Delta y.$$

The above expressions show that above the point t^* , polarization $P_z(t)$ increases relatively rapidly and is approximately proportional to $\sqrt{\Delta t}$.

Now, consider the case of power law (5) for the spatial distribution $\psi(z)$. The corresponding calculation of the energy F and the minimization of $F(P_z, \psi_0)$ allow one to determine the characteristics of the first-order phase transition at the point

$$\tau^* = \frac{1}{2} \left(\frac{c^3}{24L} \right)^2, \quad (14)$$

namely, the jumps in the order parameter

$$\psi_0^* = \frac{c^4}{48L}, \quad P_z^* = \frac{c^3}{24L}. \quad (15)$$

It should be emphasized that this is the phase transformation from the state with $\psi_0 = P_z = 0$ to the state with finite values of ψ_0 and P_z . In fact, in this case, there is only one phase transition at the point $\tau^* > 0$, and the situation can exist only under the condition that the value of ψ_0^* is much larger than the value of \sqrt{a} , i.e., if $\alpha \ll 1/8$.

CONCLUSION

Thus, the dimensionless parameter of the interaction between the substrate and the polarized copolymer, $1/\alpha$, can effectively control both the number and the character of phase transitions in the films under consideration. In particular, the parameter α is proportional to the film thickness L , which signifies that the film thickness plays an important role in the phase transformation. Thus, for rather thick films, the low-temperature transformation is a second-order phase transition. In this case, the existence of finite spontaneous polarization in the film bulk and the orienting effect of the substrate provide the formation of an additional order in the crystal, e.g., smectic order in the copolymer, whereas an increase in the film thickness results in a relative decrease in the thermodynamic contribution due to this additional order. In the latter case, the corresponding contribution to the specific temperature dependence of the dielectric permittivity should also decrease, which was confirmed experimentally [8]. At small film thicknesses ($\alpha < 1/8$), the appearance of smectic order indicates the occurrence of a first-order phase transition with jumps in the order parameters and temperature of the smectic transition being the higher, the thinner the film thickness [see Eqs. (11) and (12)]. It should be emphasized that unless the parameter α is higher than, or approximately equal to, $1/8$, the temperatures of both phase transitions are only slightly dependent on the film thickness—the high-temperature transition occurs at $\tau = 0$, whereas the low-temperature transition, at $\tau \approx -4a/c^2$. It seems that it is this situation that was observed experimentally in [1]. Finally, if the film thicknesses are too small ($\alpha \ll 1/8$), smectic order and spontaneous polarization should appear simultaneously, with the jumps in the order parameters being quite pronounced and the transition temperature higher than in the bulk film [see Eqs. (14) and (15)].

Of course, as in a conventional bulk copolymer, the high-temperature transformation can be a first-order phase transition, which is unimportant in this case. The suggested model is useful, because it allows one to calculate all the characteristics of phase transitions and determine the main dimensionless parameter α and its critical value. In the low-temperature phase, where the

order parameters P_z and ψ_0 induce one another, the temperature behavior of polarization is unusual—it additionally increases with a decrease in the “temperature” τ (below the point $\tau^* = \tau(t^*) < 0$).

It should also be emphasized that the energy of surface cohesion described by Eq. (2) also plays an important part in repolarization processes, because the interface gives an additional contribution to the stabilization of the polarized state. In this case, an oriented electric field stabilizes this state, whereas the field of the opposite sign should overcome a surface energy barrier to reorient the polarization in the film bulk. Thus, in extremely thin films, a certain bistability threshold exists or, in other words, there is a certain critical field above which the copolymer is repolarized and remains in this new state even after the field is switched off. A similar effect in ferroelectric liquid crystals was studied both theoretically and experimentally with due regard for the possible rotation of polar molecules and the effect of surface tension [9, 10]. In this case, the coercive field can be rather intense and depends mainly on the properties of the interface and not on the film thickness. In thick films, only those volume effects related to nucleation as a switching mechanism are important, which are characterized by a less intense coercive field, because, in this case, the energy contribution of the interface is relatively small. With a decrease in the film thickness, the interface starts playing a more important role, whereas the volume effects become less important, because with an increase in the film thickness, the coercive field should be less intense. With a decrease in the film thickness, i.e., with an increase in the above surface factor, the hysteresis loops should become asymmetrical. All these effects, including an increase in spontaneous polarization with a decrease in the temperature below the point of the low-temperature phase transition $T \approx 20^\circ\text{C}$, were observed experimentally [1, 2]. However, these

phenomena are not necessarily associated with “two-dimensional ferroelectricity” proper and can be explained by the reasons considered above.

ACKNOWLEDGMENTS

The author is grateful to V.M. Fridkin, K.A. Verkhovskaya, and L.M. Blinov for discussion of the experimental data. This study was supported by the Russian Foundation for Basic Research, project no. 00-02-17801.

REFERENCES

1. L. M. Blinov, V. M. Fridkin, S. P. Palto, *et al.*, *Usp. Fiz. Nauk* **170** (3), 247 (2000).
2. S. P. Palto, A. M. Lotonov, K. A. Verkhovskaya, *et al.*, *Zh. Éksp. Teor. Fiz.* **117**, 342 (2000) [*JETP* **90**, 301 (2000)].
3. S. Palto, L. Blinov, A. Bune, *et al.*, *Ferroelectr. Lett. Sect.* **19**, 65 (1995).
4. A. V. Bune, V. M. Fridkin, S. Ducharme, *et al.*, *Nature* **391**, 874 (1998).
5. E. I. Demikhov, S. A. Pikin, and E. S. Pikina, *Phys. Rev. E* **52**, 6250 (1995).
6. J. Choi, P. A. Dowben, A. V. Bune, *et al.*, *Phys. Lett. A* **249**, 505 (1999).
7. J. Choi, P. A. Dowben, C. N. Borca, *et al.*, *Phys. Rev. B* **59**, 1819 (1998).
8. T. Furukawa and G. E. Johnson, *J. Appl. Phys.* **52**, 940 (1981).
9. S. A. Pikin, *Ferroelectrics* **117**, 197 (1991).
10. S. A. Pikin, L. M. Blinov, L. A. Beresnev, *et al.*, *Ferroelectrics* **178**, 111 (1996).

Translated by L. Man

**SURFACE, THIN FILMS,
AND NANOMATERIALS**

Reconstruction of the Surface Layer Density Profile by the X-ray Reflectometry Method

V. A. Bushuev*, A. A. Lomov, and A. G. Sutyryn***

* *Physics Department, Moscow State University,
Vorob'evy gory, Moscow, 119899 Russia*

e-mail: vab@surfsite.phys.msu.su

** *Shubnikov Institute of Crystallography, Russian Academy of Sciences,
Leninskii pr. 59, Moscow, 117992 Russia*

e-mail: a.lomov@ns.crys.ras.ru

Received July 2, 2001

Abstract—The method for reconstructing the profile of the material density distribution arbitrarily varying over the depth of the subsurface layer of the specimen from X-ray reflectometry data is suggested. For the first time, the recurrent relationships for the derivatives of the specular reflection coefficient with respect to the parameters of the subsurface layer are obtained, which reduce the volume of the necessary computations by one to two orders of magnitude. The class of functions for which such density-profile reconstruction can be made within a 5% error is characterized. The method is tested on thin tungsten and carbon films on silicon substrates and thin films of porous silicon films with p^+ -type conductivity. © 2002 MAIK “Nauka/Interperiodica”.

INTRODUCTION

The recent development of high technologies imposes additional requirements for the surfaces of various materials (semiconductor substrates, optoelectronic devices, multilayer structure and superlattices, porous materials, organic films and membranes, etc.) [1]. This, in turn, stimulated the development of the already existing methods [2, 3] and the creation of new efficient techniques for studying various surfaces [4–7].

X-ray methods are traditionally used for the efficient nondestructive characterization of crystals and thin subsurface layers [4, 7]. One of these methods is high-resolution X-ray reflectometry (HRXR) [7–9] characterized by relative simplicity, high speed (especially if synchrotron radiation is used), no necessity to perform vacuum studies, etc. The high angular collimation of the primary beam in combination with the precision angular analysis of the X-ray radiation scattered by the specimen in the HRXR method allows one not only to determine the root-mean-square height of the surface roughness, but also to reconstruct the surface morphology [10, 11]. The analysis of the scattering indicatrix [12–14] and the construction of the two-dimensional distribution of the X-ray intensity scattered by the specimen in the vicinity of the direction of specular reflection [7, 15, 16] are considerably more informative than integrated specular-reflection curves.

The development of thin-film technologies posed the problem not only of film thickness and density but also of roughness height and correlation length on the surface and at the interfaces. In most cases, the applica-

tion of the HRXR method to homogeneous films provides the reconstruction of these parameters from the specular-reflection and diffuse-scattering data [17]. However, such determinations are usually based on *a priori* data obtained, e.g., from growth conditions. In some instances, if the density variations are rather weak [18, 19] and the parameters of multilayer structures are close to their technological values [20] or else if certain values and forms of the electron-density distribution are known [21], one can reconstruct the density profile practically unambiguously.

At the same time, for locally inhomogeneous films and multilayer structures with the density arbitrarily varying both over the depth and along the surface, the problem of the reconstruction of these parameters from X-ray reflectometry data has not been solved as yet. This is explained, on the one hand, by the fact that the use of the adequate complicated structure model can considerably increase the number of necessary parameters and often results in the loss of their physical meaning and, on the other hand, by the increasing complexity of the specimen morphology, which results in the fact that the type of density inhomogeneities and their location in the specimen depth are not always known *a priori*. Also, in volume-inhomogeneous films (e.g., in porous materials), a considerable part of the radiation is scattered diffusely, and neglect of this scattering channel in the consideration of the specular reflection can often lead to erroneous results.

The present article is dedicated to the development of a general approach to processing HRXR curves that

provides the determination of the density profile averaged over the surface characterized by arbitrary density variations over the depth in the subsurface layer of the specimen. The reconstruction of the density profile is reduced to the minimization of the functional χ^2 based on the well-known recurrent formulas suggested by Parratt. We obtained here, for the first time, the recurrent formulas for the derivatives of the specular-reflection coefficient in terms of the sublayer density in the subsurface region, which reduces the volume of computations by one to two orders of magnitude. The method is tested on a number of model objects and is used in the reflectometry studies of thin tungsten and carbon films on silicon substrates and thin porous silicon films. The results obtained are compared with the atomic-force microscopy data.

THEORY

Consider a subsurface layer of thickness L in which the relative density $\rho(z) = \chi(z)/\chi_0$ differs from the substrate density, where $\chi(z)$ and χ_0 are the material polarizabilities in the layer and substrate, respectively, and the z -axis directed inside the material is normal to the surface. Depending on the required accuracy, the layer can be divided into N homogeneous sublayers with smooth boundaries. The middle sections of the layers pass through the points z_n whose distribution along the z -axis can be chosen, e.g., from the data known *a priori*. In the absence of such data, the layer thicknesses are assumed to be the same. The parameters of this model are the relative densities $\rho(z)$ at these points that are constant within each sublayer, $v_n = \rho(z_n) = \chi_n/\chi_0$, where χ_n is the polarizability of the n th sublayer; the layers are numbered in the direction from the substrate ($n = 0$) to the vacuum ($n = N + 1$).

The solution of the problem of density-profile reconstruction $\rho(z)$ is sought in the form of such a set of values of the parameters $\{v\} = (v_1, v_2, \dots, v_N)$ that would determine the angular distribution of the intensities of X-ray specular reflection, which is the closest to the experimentally measured one. To determine the parameter v_n , one has to minimize the functional $\chi^2(\{v\})$ in the form [22]

$$\chi^2 = \frac{1}{m-N} \sum_{i=1}^m (I_i^e - I_i^t)^2 / s_i^2, \quad (1)$$

where m is the number of the points on the experimental curves, I_i^e and I_i^t are the measured and calculated intensities, and s_i are the errors in the measurements of the i th point of the experimental curve. We have to solve the following set of N nonlinear equations:

$$\partial \chi^2 / \partial v_k = 0, \quad k = 1, 2, \dots, N. \quad (2)$$

This set of equations can be solved in terms of the sought parameters by the method of successive approximations using the following iterative procedure [22]:

$$v_k^{j+1} = v_k^j - G_{kl}^{-1}(\{v^j\}) X_l(\{v^j\}), \quad (3)$$

where j is the successive number of the iteration,

$$X_k = \sum_{i=1}^m \frac{I_i^t - I_i^e}{s_i^2} \frac{\partial I_i^t}{\partial v_k}, \quad (4)$$

$$G_{kl} = \sum_{i=1}^m \frac{1}{s_i^2} \frac{\partial I_i^t}{\partial v_k} \frac{\partial I_i^t}{\partial v_l}. \quad (5)$$

It should be noted that Eq. (1) includes the statistical errors at each point of the measured curve. If the number of such points is large, the random quantity in Eq. (1) tends to its average theoretical limit $\langle \chi^2 \rangle = 1$. It is the use of the procedure described by Eqs. (1)–(5) that allows one to restore most adequately the deformation and amorphization profiles of the crystal structure from X-ray diffraction data obtained in the wide range of scanning angles in the vicinity of the Bragg angle [23].

In order to calculate I^t in Eq. (1), introduce the partial amplitude coefficients of specular reflection $R_n = E_n^r / E_n^i$, where E_n^r and E_n^i are the amplitudes of the reflected and incident waves in the n th layer, respectively. Then, the intensity of specular reflection from the whole system of N layers is determined as $I^t = |R(\theta)|^2$, where $R(\theta) = R_{N+1}$, θ is the grazing angle of the X-ray radiation with respect to the specimen surface. The amplitude reflection coefficient R is calculated by the recurrent Parratt relationship [24] as

$$R_{n+1} = (r_n + R_n g_n) / A_n, \quad (6)$$

where $n = 0, 1, \dots, N$,

$$r_n = (s_{n+1} - s_n) / (s_{n+1} + s_n), \quad A_n = 1 + r_n R_n g_n, \quad (7)$$

$$s_n = (\sin^2 \theta + \chi_0 v_n)^{1/2}, \quad g_n = \exp(4\pi i s_n d_n / \lambda). \quad (8)$$

Here, r_n is the Fresnel coefficient of reflection from the interface between the media with the polarizabilities χ_{n+1} and χ_n , d_n is the thickness of the n th layer, and λ is the wavelength of the X-ray radiation. The recurrent procedure described by Eq. (6) is performed under the boundary conditions $R_0 = 0$, $v_0 = 1$ (substrate), and $\chi_{N+1} = 0$ (vacuum).

The equations of the iteration procedure (3)–(5) include the matrix of the intensity derivatives with respect to the sought parameters, v_k ,

$$\frac{\partial I_i^t}{\partial v_k} = \frac{\partial R}{\partial v_k} R^* + R \frac{\partial R^*}{\partial v_k}, \quad (9)$$

where $R = R(\theta_i)$; θ_i is the grazing angle corresponding to the i th point of the experimental reflection curve.

The calculation of $m \times N$ elements of matrix (9) is the most time-consuming stage of each iteration described by Eqs. (3)–(5). Therefore, we suggest here calculating the derivatives $\partial R/\partial v_k$ analytically, which would allow one to essentially reduce the time necessary for the calculation of derivatives (9). With this aim, we have to differentiate Eq. (6) with respect to the k th parameter. As a result, we arrive at the following important recurrent relationship for calculating the derivatives of the amplitude reflection coefficients R_n :

$$\frac{\partial R_{n+1}}{\partial v_k} = B_n \frac{\partial R_n}{\partial v_k} + C_{n,k}, \quad (10)$$

where $k = 1, 2, \dots, n$,

$$B_n = g_n(1 - r_n^2)/A_n^2, \quad (11)$$

$$C_{n,k} = [(1 - R_n^2 g_n^2) \partial r_n / \partial v_k + R_n(1 - r_n^2) \partial g_n / \partial v_k] / A_n^2. \quad (12)$$

The quantities $C_{n,k}$ include the derivatives of the Fresnel reflection coefficients r_n and the phase factors g_n with respect to the parameter v_k that can readily be calculated by analytical formulas. It should be indicated that the r_n values described by Eq. (7) depend only on the parameters v_n and v_{n+1} , whereas g_n in Eq. (8) depends only on v_n . Therefore, at a fixed value of k , all the quantities $C_{n,k}$ (except for $C_{k-1,k}$ and $C_{k,k}$) are zeroes, which considerably simplifies the problem. With due regard for the equality $R_0 = 0$, the boundary condition for the recurrent procedure described by Eq. (10) has the form $\partial R_0/\partial v_k = 0$.

Now, consider the suggested recurrent procedure at the given k in more detail. In accordance with Eq. (10), we can write the formulas for the derivatives of interest for each n th sublayer in the form

$$\frac{\partial R_1}{\partial v_k} = \frac{\partial R_2}{\partial v_k} = \dots = \frac{\partial R_{k-1}}{\partial v_k} = 0, \quad (13)$$

$$\frac{\partial R_k}{\partial v_k} = C_{k-1,k}, \quad \frac{\partial R_{k+1}}{\partial v_k} = B_k \frac{\partial R_k}{\partial v_k} + C_{k,k}, \quad (14)$$

$$\frac{\partial R_{k+2}}{\partial v_k} = B_{k+1} \frac{\partial R_{k+1}}{\partial v_k}, \quad \dots, \quad \frac{\partial R_{N+1}}{\partial v_k} = B_N \frac{\partial R_N}{\partial v_k}. \quad (15)$$

It follows from Eq. (13) that the real calculations should be performed only at values $n = k - 1, \dots, N$, i.e., only beginning with the derivatives described by Eq. (14). Moreover, according to Eq. (15), the derivatives of R_n in the neighboring layers beginning with $n = k + 1$ differ only in their coefficients B_n . Therefore, the computations by Eqs. (13)–(15) with respect to n can be reduced analytically to the following compact equation for the derivative of the reflection coefficient with

respect to the k th parameter for the whole system of n layers:

$$\partial R/\partial v_k = (B_k C_{k-1,k} + C_{k,k}) P_k, \quad P_k = \prod_{n=k+1}^N B_n. \quad (16)$$

The coefficients P_k in Eqs. (16) can be conveniently calculated in the reverse order, i.e., at k values $k = N, N - 1, \dots, 1$, by calculating the products $P_{k-1} = P_k B_k$. The comparison of the last relationship with the definition of P_k , Eqs. (16), leads to the boundary condition $P_N = 1$. Using the recurrent relationship obtained for P_{k-1} with a decreasing index k , we can successively determine both P_k values and the sought derivatives of the coefficients R in Eqs. (16) and then substitute these values into Eq. (9).

Thus, the use of Eqs. (16) considerably reduces the computation time. Indeed, in the numerical differentiation of the intensities I^t , one has to use individual recurrent procedure (6) for each k , which requires the performance of N^2 operations described by Eqs. (6)–(8). The application of the approach suggested in this article to the calculation of matrix (9) requires only N operations, including the calculation of the quantities described by Eqs. (6)–(8) with the use of Eqs. (11), (12), and (16). It should also be noted that the above reduction of the computer time is not associated with the use of any approximations in the fitting procedure.

TEST OF THE METHOD ON MODEL STRUCTURES

To determine the reliability of the density profile reconstruction, $\rho(z)$, we tested the above iteration method on a number of model profiles. First, using recurrent Eq. (6), we solved the direct problem of the determination of the specular-reflection coefficient $R(\theta)$ for the known model profile $\rho(z)$, and then, calculated the reflection intensity $I(\theta) = I_0 |R(\theta)|^2 G(\theta)$ corresponding to this profile, where I_0 is the intensity of the X-ray beam transmitted by the collimator slits. $G(\theta)$ is the geometrical factor taking into account the change in the fraction of the primary beam participating in reflection depending on the grazing angle. The function $G(\theta)$ is determined by the beam shape and width and the specimen's dimensions [25]. This function was calculated with the invocation of the corresponding experimental parameters. The intensity values $I(\theta)$ thus obtained were considered as the measured ones and were used in the iteration procedure of minimizing functional (1). Then, different classes of density profiles restored within an accuracy of up to 4 to 5% were thoroughly analyzed.

Figures 1 and 2 show the reconstructed density profiles for various model films on silicon substrates and the corresponding specular-reflection curves for the $\text{CuK}\alpha$ radiation. It is seen from Fig. 1 that a depth-homogeneous film on the substrate with smooth transi-

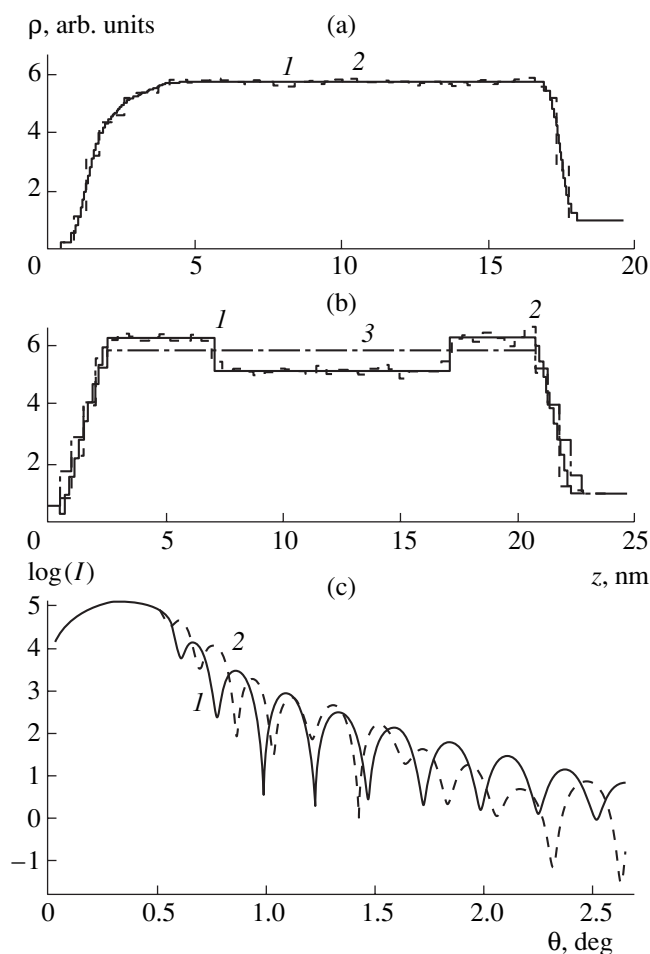


Fig. 1. (a, b) Model (solid curves 1) and reconstructed (dashed curves 2) density profiles $\rho(z)$ from (a) homogeneous and (b) weakly inhomogeneous films. Dashed-and-dotted curve 3 shows the initial approximation; (c) specular-reflection curves 1 and 2 calculated for the model profiles 1 shown in (a) and (b), respectively.

tion layers on both interfaces is reconstructed within an accuracy of about 4% (Fig. 1a, curves 1 and 2). If the film is depth-inhomogeneous (e.g., a layer with a pronounced boundary and a lower density in the bulk), its density profile is restored with an accuracy of 5% (Fig. 1b). The specular-reflection curves for the initial model density profiles (Figs. 1a–1b, curves 1) are shown in Fig. 1c. With an increase in the number of profile “anomalies,” the degree of its inhomogeneity, and the film thickness, the accuracy of the profile restoration usually decreases (5 and 6% for profiles 2 in Figs. 2a and 2b, respectively).

Curves 3 in Figs. 1b and 2a, 2b illustrate one of the numerous initial approximations used in the iteration procedure. Despite the fact that these curves have no anomalies (homogeneous and linear profiles), the final results turned out to be very close to the model profiles.

Thus, the analysis of the inverse problem solution performed shows that the processing of specular-reflec-

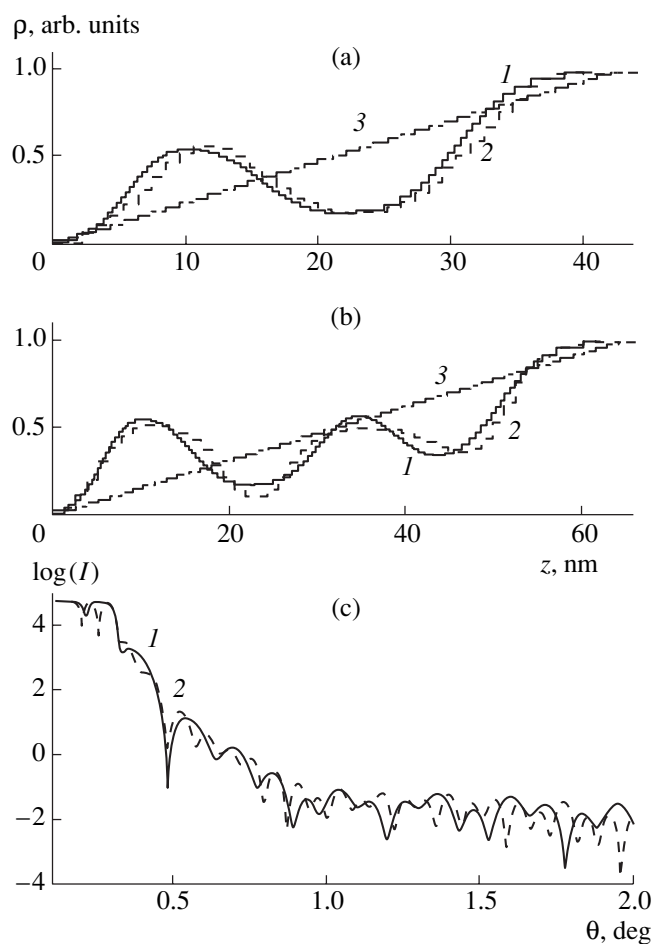


Fig. 2. (a, b) (1) Model and (2) reconstructed density profiles of (a) moderately and (b) pronouncedly inhomogeneous films; specular-reflection curves 1 and 2 correspond to the model profiles shown in (c); curve 3 (a, b) shows the initial approximation.

tion curves allows one to reconstruct smooth density profiles (i.e., profiles smoothly varying over the depth) with a sufficient accuracy. Thus, if $\text{CuK}\alpha$ radiation is used, the relative change in the density in 1 nm-thick layers should not exceed 30%.

If, according to the preliminary data, the film has N_t transitional layers corresponding to the Gaussian distribution of the interlayer roughness, their parameters (thicknesses l_k of the transitional layers, location in the depth t_k , and jumps in the density $\Delta\rho_k$ between the adjacent homogeneous layers) can become the parameters to be determined by minimizing the functional χ^2 . The densities of the individual sublayers stop being independent and are now determined by the following equation:

$$v_i = \sum_{k=1}^{N_t} \Delta\rho_k / [1 + \exp\{-1.67(z_i - t_k)/l_k\}], \quad (17)$$

where z_i is the coordinate of the i th sublayer. If the thicknesses l_k are equal to the root-mean-square heights of the interlayer roughness, the terms in Eq. (17) describe quite well the dependence of the material density on the layer depth averaged along the corresponding interlayer boundaries [26].

EXPERIMENTAL

To analyze the possibilities provided by the approach suggested for reconstruction of the density profile in real structures, we performed a comparative study of the density distribution both in continuous films with strongly different densities (tungsten, carbon) and porous (silicon) films with nanoscale gradient-density changes.

Approximately 20-nm-thick tungsten and carbon films were obtained on standard silicon substrates by the magnetron sputtering method. Porous silicon layers [25, 27, 28] were deposited onto standard (111)-oriented p -type single-crystal wafers (KDB-10). Then, the subsurface region of the substrate was doped with boron atoms (thermal diffusion) up to a boron concentration $\sim 4 \times 10^{20} \text{ cm}^{-3}$. As a result, a p^+ -type layer was formed in the vicinity of the surface. The films of porous silicon were obtained by 150-s-long anodizing in an electrolyte (the mixture of the fluoric acid HF and ethyl alcohol $\text{C}_2\text{H}_5\text{OH}$ in the proportions 1 : 2 and 1 : 1 for specimens 1 and 2, respectively) at a current density of 10 mA/cm^2 at room temperature [25]. The longitudinal dimension of the region coated with a porous silicon film was 15 mm.

The X-ray reflectometry curves were measured on a triple-crystal TRS-1 diffractometer connected with a MATEX controller. The radiation source was a 1.1-kW X-ray tube with a copper anode. The beam of the characteristic $\text{CuK}_{\alpha 1}$ radiation was shaped by a threefold-reflection monochromator Si(111) and the exit slits of the collimator. The vertical and horizontal dimensions of the exit slits during recording HRXR curves were 2 mm and $20 \mu\text{m}$, respectively. The intensity of the primary beam at the collimator exit was $I_0 = 10^5 \text{ pulse/s}$. A horizontal slit with an angular width of $160''$ was placed before the X-ray detector. Specular reflection intensities were recorded in the $\theta/2\theta$ scanning mode. To exclude diffuse scattering (whose contribution increases with an increase in the angle θ), the scattering indicatrix was measured in the vicinity of the specular-reflection peak of interest in the θ -scanning mode at fixed positions of the specimen.

RESULTS AND DISCUSSION

The experimental specular-reflection curve from the specimen coated with a tungsten film is shown by dots in Fig. 3a. The corresponding reconstructed density profiles are shown in Fig. 3b. The density distribution at the film–surface interface is described by the model

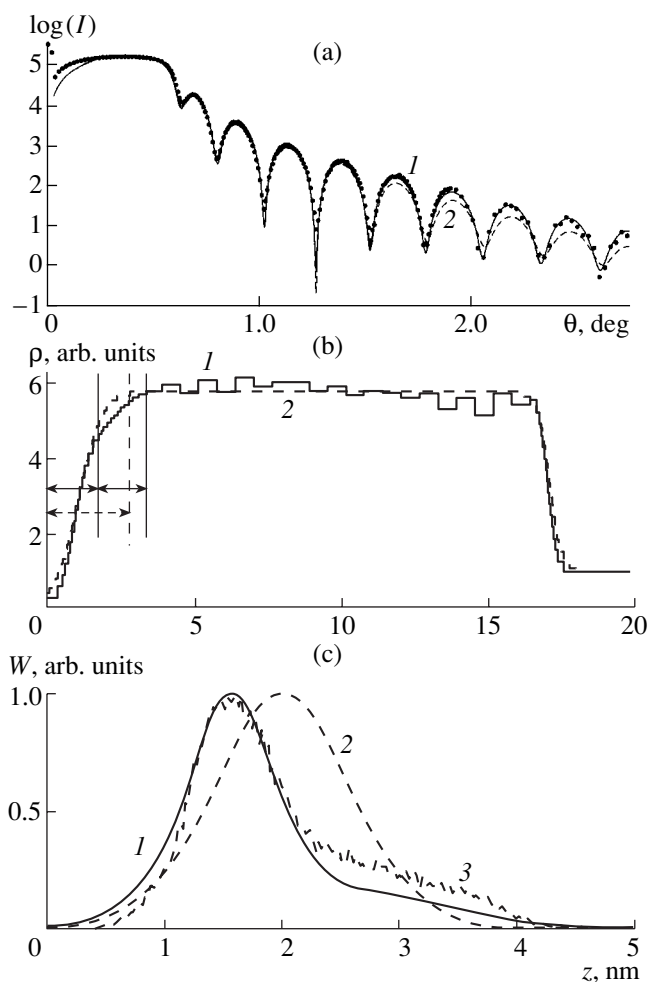


Fig. 3. (a, b) (1, 2) Experimental (dots) and theoretical specular-reflection curves from a tungsten/silicon structure. Curve 1 shows the density profile reconstructed for a structure with one (dashed curve 2) and two (solid curve 1) transitional layers on the surface; (c) the probability density function for roughness heights at the vacuum–film interface calculated based on the specular-reflection data from the specimen with (1) two and (2) one transitional layers and (3) based on atomic-force microscopy data.

with one transitional layer of form (17). It should be noted that the agreement between the theory and the experiment is better for the model with two layers of form (17) at the vacuum–film interface and with varying density in the film bulk (solid curve 1 in Fig. 3b) than for a homogeneous film with only one transitional layer at this interface (Fig. 3b, dashed line 2). This is seen from the comparison of experimental (dots) and reflection curves 1 and 2 in Fig. 3a calculated based on profiles 1 and 2 in Fig. 3b (reconstruction quality $\chi^2 = 8$ and 73, respectively).

Thus, we obtained the homogeneous density distribution (within an accuracy of 4%) for a (16.1 ± 0.2) -nm-thick tungsten film (Fig. 3b), which corresponds to the technological data of specimen preparation. Moreover, we also determined the thicknesses of the

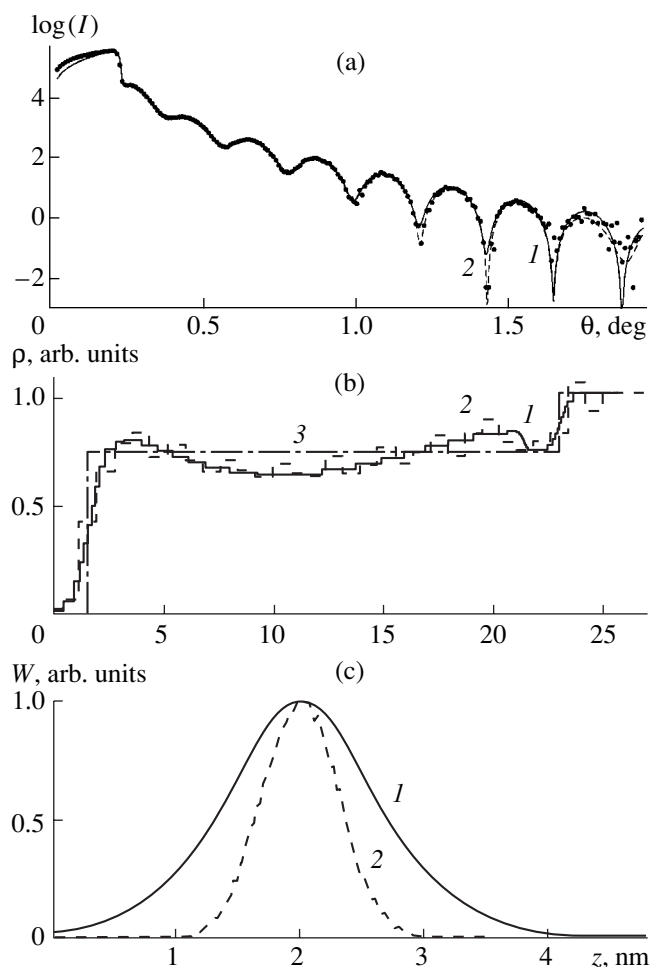


Fig. 4. (a) Specular-reflection curves from a carbon film on the silicon substrate; (b) the corresponding density profiles calculated for the models with (1) five transitional layers, (2) different densities of the sublayers, and (3) in the initial approximation; (c) functions $W(z)$ obtained from (1) the specular-reflection and (2) atomic-force microscopy data.

transition layers at the vacuum–film (~ 2.7 nm) and the film–substrate (~ 1 nm) interfaces.

Figure 4a shows the experimental (dots) and calculated (1 and 2) specular-reflection curves for a carbon film. The analysis of the reconstructed density profile of a (20 ± 0.5) -nm-thick carbon film (according to the technological data) shows that, in this case, the film is somewhat inhomogeneous—the film density is slightly lower in the center than at the periphery (Fig. 4b, solid line 1). In addition to the inhomogeneity of the film proper, we also observed a decrease in the density at the film–substrate interface, which seems to be associated with the presence of a thin native silicon oxide layer at this interface. The density of the latter (2.0 ± 0.3) -nm-thick layer was 1.9 g/cm^3 , which is lower by 10% than the density of the native silicon oxide layer. It seems that this decrease in the density is associated with carbon atoms incorporated into the film during its deposi-

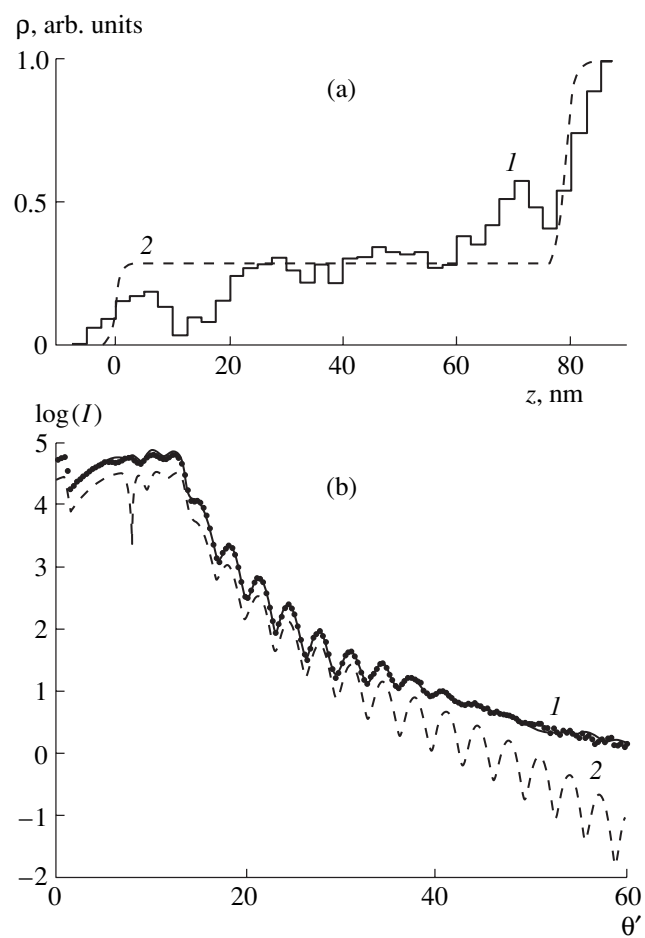


Fig. 5. Density profiles of a porous silicon film calculated in the models of (1) sublayers with different independent densities and (2) a homogeneous film with smooth transitional layers (a); (b) specular-reflection curves 1 and 2 correspond to profiles 1 and 2, respectively; the dotted line indicates the experimental data, the specular reflection intensities of curve 2 are multiplied by 0.5.

tion. In the case of a tungsten film, this layer is not seen because of the considerable absorption of the X rays by this layer and its small contribution to scattering in comparison with the contribution to scattering from tungsten. All the specific features (transitional layers) of the density distribution in carbon film are well described by the model with five transitional layers of form (17) (Fig. 4b, curve 1) and are reproduced in the modeling of the density profile by a set of sublayers with individual (independent) densities (Fig. 4b, dashed curve 2). Corresponding specular-reflection curves 1 and 2 in Fig. 4a almost coincide ($\chi^2 = 11$ and 16, respectively). According to the reflectometry data, the average thickness of the carbon film, 21.5 ± 0.3 nm, is somewhat higher than the thickness that could be expected from the sputtering conditions.

The derivative of the density profile $\rho(z)$ with respect to depth z at the vacuum–film interface in the

region of the transition layers yields the probability density function of roughness heights of the film, $W(z)$ (Figs. 3c, 4c, solid curves 1). The data for tungsten and carbon films are confirmed by independent measurements of the distribution of roughness heights obtained by the method of atomic force microscopy [29]. According to the atomic-force microscopy data, the function $W(z)$ for a tungsten film has two peaks—the main one and the additional weak one (Fig. 3a, curve 3). It is seen that both methods yield almost the same value of the main peak, which corresponds to the root-mean-square height of the roughness. Moreover, X-ray reflectometry also allows one to record the additional peak with parameters close to those obtained by atomic-force microscopy. At the same time, the widths of the function $W(z)$ for a carbon film obtained by the two methods are essentially different (Fig. 4c, curves 1 and 2), which seems to be associated with the impurities adsorbed on the film surface. In the case of a dense tungsten film, scattering from these impurities only slightly affects the roughness parameters obtained, whereas the density of the impurities adsorbed on the carbon film is rather close to the film density and, thus, can considerably change the roughness parameters “seen” by HRXR.

On the whole, the HRXR curves from both porous silicon specimens are described sufficiently well if a porous layer is modeled by a homogeneous film with a transition layer of form (17) (Figs. 5, 6). However, in order to reveal possible inhomogeneity along the film depth, we have to use a multilayer model with the unknown densities of individual sublayers to be determined. The corresponding density profiles are shown in Figs. 5a and 6a (solid curves 1). It is seen that the more thorough minimization of functional χ^2 (1) than that in the model of a homogeneous film with a smaller number of parameters allowed us to detect the inhomogeneity of the porous films studied.

In addition to a slow increase in the density with the specimen depth, we also observed a noticeable density modulation along the z -axis (Figs. 5a and 6a). The angular range of the measurements for the first specimen was 60° , whereas the increased diffuse background for the second specimen reduced the range of the angular intensity measurements to 40° . Therefore, the smaller number of the experimental points for the second specimen made its density profile less accurate. Thus, the HRXR curve for specimen 2 is also well modeled if another density profile is chosen (Fig. 6a, profile 2). Nevertheless, profile 1 seems to be more probable, because it reflects the general tendency of an increase in density over the depth for both specimens prepared under similar conditions. The comparison of profiles 1 in Figs. 5a and 6a shows that, with a decrease in the alcohol concentration in the electrolyte, the degree of porosity also decreases and the film becomes more homogeneous, while its thickness remains almost constant.

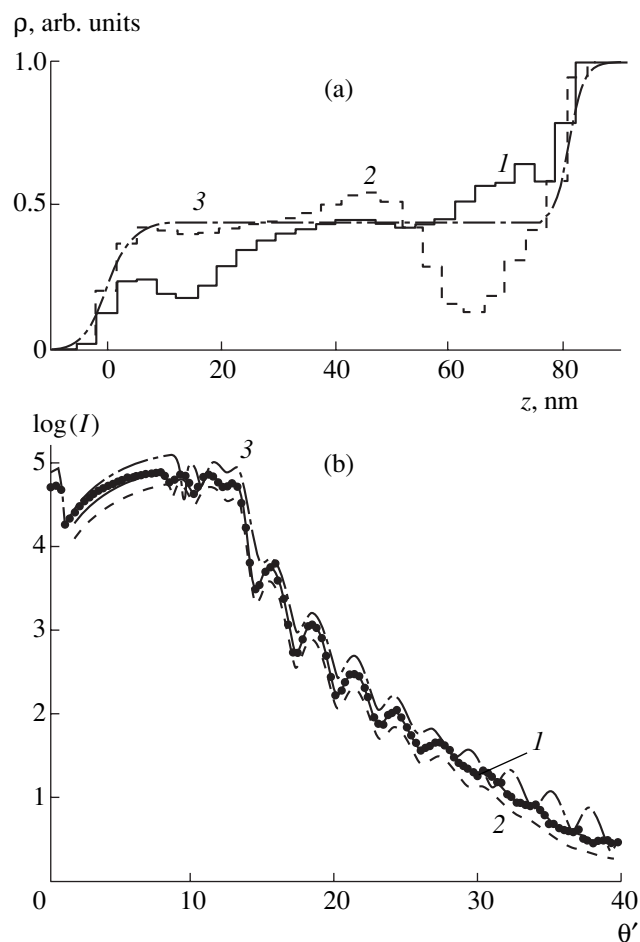


Fig. 6. (a) (1, 2) Density profiles for specimen 2 in the model of sublayers with different independent densities and of (3) a homogeneous film with smooth transitional layers (dash and dot curve 3); (b) The specimens with density profiles 1 and 2 yield almost indistinguishable specular-reflection curves (fitting quality $\chi^2 = 4$ and $\chi^2 = 5$, respectively); curves 2 and 3 are multiplied by $2/3$ and 1.5 , respectively.

CONCLUSION

Thus, we suggested a method for solving the inverse problem of the density-profile reconstruction in the subsurface region of the specimen from the specular-reflection intensities. We also tested the suggested method on model objects and real specimens. It is shown that the method allows one to reconstruct within an error of $\leq 5\%$ a density profile distribution that varies rather arbitrarily with depth. The class of functions that allow one to reconstruct the density profiles is characterized. For the first time, the recurrent relationships for the derivatives of the amplitude specular-reflection coefficients are obtained by minimizing the functional χ^2 , which considerably (by a factor of N) reduces the volume of calculations.

The studies show that, depending on the value of the $\chi(z)/\chi_0$ ratio in continuous films, one can extract information on the characteristics of transitional layers and the thin intermediate layer formed at the film–substrate

interface in these films. The measurements of a carbon film on the silicon substrate provided the detection of a native oxide layer and the reliable determination of its thickness (2.0 ± 0.3 nm) and density (1.9 g/cm³). Thus, the suggested approach can be used as one more method of studying thin films. It should also be noted that the insufficient intensities at large grazing angles in a standard X-ray reflectometry experiment make the detection of a native-oxide film and the determination of its parameters a rather complicated and time-consuming problem.

The suggested method is also rather sensitive to the statistical characteristics of the surface. The comparison of the data obtained on root-mean-square heights of the surface roughness for carbon and tungsten films with the corresponding atomic force microscopy-based data showed quite satisfactory results. Finally, it should also be indicated that, in some instances, the analysis of structures with pores of nanodimensions did not allow a unique reconstruction of the density profiles for two reasons; first, because of the insufficient angular range of recording the specular-reflection curves and, second, because of the assumption that the diffuse-scattering contribution was small. This assumption is invalid for scattering from structures with local inhomogeneities in the bulk, because diffuse scattering from pores is more intense than diffuse scattering from interlayer roughness. The latter problem is beyond the scope of the present study and is the subject of our next article.

ACKNOWLEDGMENTS

This study was supported by the Ministry of Industry, Science and Technologies of the Russian Federation, subprogram Physics of Solid Nanostructures, project no. 98-3009.

REFERENCES

1. I. Brodie and J. J. Muray, *The Physics of Microfabrication* (Plenum, New York, 1982; Mir, Moscow, 1985).
2. V. I. Nefedov and V. T. Cherepin, *Physical Methods for Research of Surface Layers of Solids* (Nauka, Moscow, 1983).
3. É. V. Suvorov, *Physical Principles of Modern Methods for Research of Real Structures of Crystals* (Nauchn. Tsentr Chernogolovki Ross. Akad. Nauk, Chernogolovka, 1999).
4. A. M. Afanas'ev, A. P. Aleksandrov, and R. M. Imamov, *X-ray Diffraction Diagnostics of Submicron Layers* (Nauka, Moscow, 1989).
5. M. A. Andreeva and R. N. Kuz'min, *Mössbauer and X-ray Optics of Surface* (Obshchenatsional'naya Akademiya Znaniĭ, Moscow, 1996).
6. I. A. Vartanyants, J. A. Pitney, J. L. Libbert, and I. K. Robinson, *Phys. Rev. B* **55** (19), 13 193 (1997).
7. V. Holy, U. Pietsch, and T. Baumbach, *High-Resolution X-ray Scattering from Thin Films and Multilayers* (Springer-Verlag, Berlin, 1999).

8. A. V. Andreev, *Usp. Fiz. Nauk* **145** (1), 113 (1985) [*Sov. Phys. Usp.* **28**, 70 (1985)].
9. M. A. Andreeva, S. F. Borisova, and S. A. Stepanov, *Poverkhnost*, No. 4, 5 (1985).
10. S. K. Sinha, E. B. Sirota, S. Garoff, and H. B. Stanley, *Phys. Rev. B* **38** (4), 2297 (1988).
11. T. Salditt, T. H. Metzger, Ch. Brandt, *et al.*, *Phys. Rev. B* **51** (9), 5617 (1995).
12. A. V. Vinogradov, N. N. Zorev, I. V. Kozhevnikov, *et al.*, *Zh. Éksp. Teor. Fiz.* **94** (8), 203 (1988) [*Sov. Phys. JETP* **67**, 1631 (1988)].
13. V. E. Asadchikov, A. Yu. Karabekov, V. V. Klechkovskaya, *et al.*, *Kristallografiya* **43** (1), 119 (1998) [*Crystallogr. Rep.* **43**, 110 (1998)].
14. V. E. Asadchikov, A. Duparre, S. Jakobs, *et al.*, *Appl. Opt.* **38** (4), 684 (1999).
15. X. Jiang, T. H. Metzger, and J. Peisl, *Appl. Phys. Lett.* **61** (8), 904 (1992).
16. M. Rauscher, T. Salditt, and H. Spohn, *Phys. Rev. B* **52** (23), 16 855 (1995).
17. W. Plotz, V. Holy, W. V. D. Hoogenhof, and K. Lischka, *J. Phys. C* **4** (9), 1565 (1994).
18. M. K. Sanyal, J. K. Basu, A. Datta, and S. Banerjee, *Europhys. Lett.* **36** (4), 265 (1996).
19. M. K. Sanyal, S. Hazra, J. K. Basu, and A. Datta, *Phys. Rev. B* **58** (8), R4258 (1998).
20. D. E. Savage, N. Schimke, Y.-H. Phang, and M. G. Lagally, *J. Appl. Phys.* **71** (7), 3283 (1992).
21. I. V. Kozhevnikov, V. E. Asadchikov, and I. N. Bukreeva, in *Proceedings of the III National Conference on X-ray, Synchrotron, Neutron, and Electron Radiation, 2001* (Inst. Kristallografii Ross. Akad. Nauk, Moscow, 2001), p. 318.
22. W. T. Eadie, D. Dryard, F. E. James, M. Roos, and B. Saboulet, *Statistical Methods in Experimental Physics* (North-Holland, Amsterdam, 1971; Atomizdat, Moscow, 1976).
23. A. M. Afanas'ev, M. A. Chuev, R. M. Imamov, *et al.*, *Kristallografiya* **42** (3), 514 (1997) [*Crystallogr. Rep.* **42**, 467 (1997)].
24. L. G. Parratt, *Phys. Rev.* **95** (2), 359 (1954).
25. V. A. Bushuev, A. A. Lomov, A. G. Sutyurin, and V. A. Karavanskiĭ, *Perspekt. Mater.*, No. 4, 25 (2000).
26. L. A. Smirnov and S. B. Anokhin, *Opt. Spektrosk.* **48** (3), 574 (1980) [*Opt. Spectrosc.* **48**, 315 (1980)].
27. V. A. Karavanskiĭ, A. A. Lomov, E. V. Rakova, *et al.*, *Poverkhnost*, No. 12, 32 (1999).
28. A. A. Lomov, V. A. Bushuev, and V. A. Karavanskiĭ, *Kristallografiya* **45** (5), 915 (2000) [*Crystallogr. Rep.* **45**, 842 (2000)].
29. A. A. Lomov, A. G. Sutyurin, and V. A. Bushuev, in *Proceedings of IX National Conference on Crystal Growth, 2000* (Inst. Kristallografii Ross. Akad. Nauk, Moscow, 2000), p. 397.

Translated by L. Man

CRYSTAL
GROWTH

Kinetics of Hydrothermal Crystallization of Quartz in Na_2CO_3 Solutions

V. N. Rumyantsev

*Institute of Lithosphere of Marginal Seas, Russian Academy of Sciences,
Staromonetnyĭ per. 22, Moscow, 109180 Russia*

Received May 15, 2000

Abstract—The kinetics of crystallization of the $\{0001\}c$, $\{01\bar{1}1\}r$, and $\{10\bar{1}1\}R$ faces of quartz in 0.5 M Na_2CO_3 (M is molarity) aqueous solutions has been studied in the temperature range 200–450°C. It is established that the dependence of the crystal growth rate on temperature in the $\log V-1/T$, K coordinates is of a parabolic nature. It is most probable that the nonlinearity of this dependence is associated with a deficiency in the solution of silica monomers, taking part in the elementary event of quartz crystallization. The causes of a jumpwise decrease in the activation energy of the growth of the c , r , and R faces at $t > 280-325^\circ\text{C}$ are considered. © 2002 MAIK “Nauka/Interperiodica”.

INTRODUCTION

Despite the wide use of Na_2CO_3 aqueous solutions as mineralizers in the hydrothermal growth of quartz ($\alpha\text{-SiO}_2$), the kinetics of quartz crystallization in this solution is studied insufficiently in comparison with the kinetics of quartz growth in NaOH [1–3] and is limited to the temperature range 330–400°C [2]. Laudise, who studied the crystallization kinetics of the pinacoidal faces $\{0001\}$ and the positive $\{\bar{1}\bar{1}20\}$ (+ x) and negative $\{11\bar{2}0\}$ (– x) faces of the trigonal prisms of quartz, also considered the temperature dependence of the growth rates of the c , + x , and – x faces in other alkali solutions (NaOH, KOH, NaHCO_3 , and KHCO_3) [2]. The experiments were performed in 0.5 M aqueous solutions with a constant coefficient of autoclave filling (0.75). It was established that the temperature dependences of the rate of quartz crystallization in the NaOH and KOH solutions differ from the crystallization rate in the solutions of sodium and potassium carbonate and bicarbonate, where growth rate V linearly depends on the temperature in the $\log V-1/T$, K coordinates, whereas in the NaOH and KOH aqueous solutions, this dependence is parabolic.

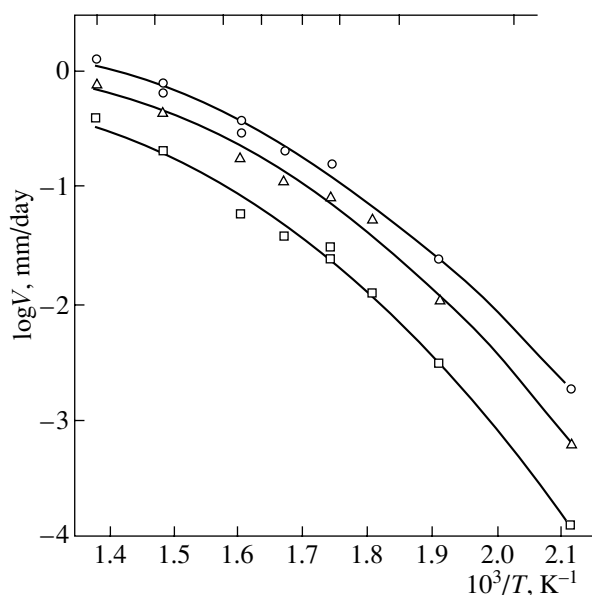
Our study of the crystallization kinetics of the pinacoidal faces and the faces of the small $\{01\bar{1}1\}r$ and large $\{10\bar{1}1\}R$ rhombohedra in a 0.5 M NaOH aqueous solution performed in the temperature range 250–450°C [3] confirmed the data [2] on the parabolic dependence of the growth rates of various quartz faces in this solution.

Dissolution of quartz in a Na_2CO_3 aqueous solution is determined by the presence of chemically active hydroxyl ions formed as a result of hydrolysis [4, 5].

Then, the forms of silica presence in the Na_2CO_3 and NaOH aqueous solutions and the mechanisms of hydrothermal crystallization of quartz in these solutions should be identical. The character of the temperature dependence of quartz growth in these solutions should also be similar. The aim of our study was to verify experimentally this assumption and to continue studying the role of the adsorbed-water film on the quartz surface detected from the data on the kinetics of quartz dissolution and crystallization in aqueous solutions of various electrolytes [3, 6, 7].

EXPERIMENTAL RESULTS AND DISCUSSION

The kinetic studies were performed in 0.35-l laboratory autoclaves made of 1Kh18N9T steel. Heating was performed in two-section electric furnaces that maintained the necessary temperature mode due to the variation of resistivity. The method is described in detail elsewhere [8]. We used the standard $6.5 \times 1.0 \times 0.2$ -cm seeding plates and a constant amount of the charge (60 g). The seeds were located at fixed sites in the reaction chamber. The experiments were performed under conditions which excluded the stratification and spontaneous formation of quartz in the system and the precipitation of mineralizer (Na_2CO_3) from the solution. To exclude the effect of the solution density on the crystallization rate of quartz in homogeneous solutions (usually taking place at $t > 300^\circ\text{C}$ [1, 8]), the coefficient of autoclave filling (and, thus, the solution density) were maintained constant ($F = 0.75$). To preserve the homogeneity of the solution at 200–300°C, the process was performed at higher filling coefficients under the isobaric conditions (500 bar). We used 0.5 M solutions. The experiment duration in the stationary mode ranged



Kinetics of quartz crystallization in 0.5 M Na_2CO_3 solution:
 ○ the pinacoidal faces, Δ the faces of the small rhombohedron, \square the faces of the large rhombohedron.

from 2.5 to 45.5 days depending on the crystallization temperature. The growth rate was always estimated on the same side of the seed.

The results of the experimental study of the dependence of the crystallization rate of quartz (the pinacoidal faces and the faces of small and large rhombohedra) in the 0.5 M Na_2CO_3 aqueous solution in the tempera-

ture range 200–450°C with a temperature difference of 20°C are shown in the figure. The dependence of the logarithm of the crystallization rate of all the faces on the reciprocal temperature has an obvious nonlinear character. The mathematical treatment of the results obtained indicates that all the experimental points on the c , r , and R faces are best described by the following parabolas:

$$\log V_c = -3.0842x^2 + 6.9872x - 3.7208 \quad (1)$$

$$(R^2 = 0.996),$$

$$\log V_r = -3.922x^2 + 9.5909x - 5.9446 \quad (2)$$

$$(R^2 = 0.993),$$

$$\log V_R = -3.933x^2 + 9.0693x - 5.5033 \quad (3)$$

$$(R^2 = 0.993),$$

where $x = 1000/T$ and R^2 is the correlation coefficient.

At the same time, the curves had almost linear segments in the temperature ranges $t_1 = 200\text{--}325^\circ\text{C}$ and $t_2 = 325\text{--}450^\circ\text{C}$ for the pinacoidal faces, and $t_1 = 200\text{--}300^\circ\text{C}$ and $t_2 = 300\text{--}450^\circ\text{C}$ for the faces of small and $t_1 = 200\text{--}280^\circ\text{C}$ and $t_2 = 280\text{--}450^\circ\text{C}$ for the faces of large rhombohedra. These linear segments are described by the equations

$$\log V_c(t_1) = -4.8028x + 7.4662 \quad (R^2 = 0.987), \quad (4)$$

$$\log V_c(t_2) = -2.6828x + 3.8122 \quad (R^2 = 0.980), \quad (5)$$

$$\log V_r(t_1) = -5.9324x + 9.3468 \quad (R^2 = 0.993), \quad (6)$$

$$\log V_r(t_2) = -2.7781x + 3.7243 \quad (R^2 = 0.994), \quad (7)$$

$$\log V_R(t_1) = -6.6481x + 10.132 \quad (R^2 = 0.998), \quad (8)$$

$$\log V_R(t_2) = -3.3876x + 4.2734 \quad (R^2 = 0.982). \quad (9)$$

Thus, the deviation of the temperature dependence of the growth rates of various quartz faces in the aqueous Na_2CO_3 solution from the linear dependence can be revealed only if one studies a sufficiently large temperature range. This explains the fact that nonlinearity of this dependence was not revealed in the kinetic experiments performed in the range 330–400°C [2].

The activation energies for the c , r , and R faces of quartz calculated on the rectilinear segments of the activation-energy curves of these faces are indicated in the table. For comparison, the table also lists the activation energies of the same faces in a 0.5 M NaOH aqueous solution [3]. The activation energy of growth of the pinacoidal face and the faces of small and large rhombohedra in 0.5 M Na_2CO_3 and 0.5 M NaOH aqueous solutions in the temperature ranges from (200–250) to (280–325°C) and from (280–325) to 450°C are essentially different. The high activation energies at $t < 280\text{--}$

Activation energy of growth (E) of various quartz faces in 0.5 M Na_2CO_3 and 0.5 M NaOH aqueous solutions

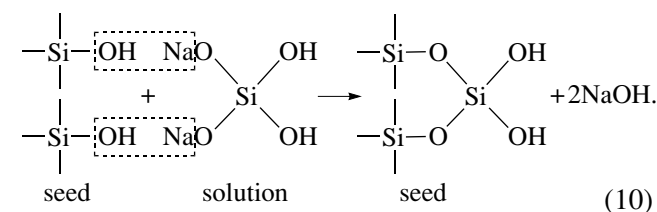
Face	Temperature range, °C	Solution	E , kJ/mol
Pinacoid	325–450	Na_2CO_3	51.5
	200–325	Na_2CO_3	92.1
Small rhombohedron	300–450	Na_2CO_3	53.2
	200–300	Na_2CO_3	113.4
Large rhombohedron	280–450	Na_2CO_3	64.9
	200–280	Na_2CO_3	127.3
Pinacoid	325–450	NaOH	59.0
	250–325	NaOH	96.7
Small rhombohedron	325–450	NaOH	71.6
	250–325	NaOH	121.4
Large rhombohedron	300–450	NaOH	88.7
	250–300	NaOH	153.2

325°C (exceeding 80 kJ/mol (20 kcal/mol)) indicate that crystallization proceeds in the kinetic mode, i.e., under conditions where the growth rate is limited by the kinetics of the processes at the crystal–mother solution interface. The jumpwise change from the kinetic to the diffusion mode of the process was revealed in the studies of the kinetics of quartz growth in NaOH [6, 7] aqueous solution at 275–300°C. Thus, there are grounds to believe that the kinetic difficulties in the crystallization of the *c*, *r*, and *R* faces of quartz at $t < 280$ –325°C are associated with the formation of a polymolecular layer of adsorbed water molecules on the chemisorbed hydroxyl coating (of monomolecular thickness as on the surfaces of other minerals [9]). The layer is formed by the mechanism of hydrogen bonding.

The high activation energy of dissolution and crystallization of quartz (and, thus, the low rates of these processes in the presence of physically adsorbed water molecules) can be explained as follows. The long-range forces acting on the quartz surface and on the surfaces of other minerals at distances of 1500–2000 Å [10] and even the polymolecular layer of physically adsorbed water molecules with the thickness in the above-indicated range cannot be an insurmountable hindrance for the dissolution and crystallization processes. However, such a layer considerably hinders the diffusion of the particles detached from the solid during its dissolution or the particles of the feeding substance flowing to the seed surface during crystallization. With an increase in the temperature and the gradual destruction of the layer of physically adsorbed water molecules, the decelerating effect of the layer becomes weaker, whereas the rates of dissolution and crystallization increase. It can be assumed that here the Palit rule [11], well-known in organic chemistry, is valid, i.e.; if the active center participating in the reaction is blocked by a hydrogen bond or some other interaction of this center with the solvent, the reaction rate in this solvent decreases [12].

As is seen from the tabulated data, the temperature of the jumpwise change in the activation energy of crystallization of various faces in the Na₂CO₃ solution corresponding to the moment of dehydration of quartz surface changes as $c(325^\circ\text{C}) > r(300^\circ\text{C}) > R(280^\circ\text{C})$ and shows the different adsorption activity of hydroxyl-coated (0001), (01 $\bar{1}$ 1), and (10 $\bar{1}$ 1) surfaces. The correlation of the above series with a decrease in the growth rates of the same faces allows one to state that the adsorption activity of various quartz faces and their ability to be crystallized vary in a similar way. This can be considered as an additional argument in favor of the concept [3] according to which the hydroxyl groups chemisorbed on the quartz surface and the polymolecular layer of physically adsorbed water molecules in the water film perform different functions. The oxygen

atoms of OH-groups can participate in donor–acceptor interactions, whereas the hydroxyl groups play the role of active centers of quartz crystallization,



The layer of physically adsorbed water molecules hinders the diffusion of silicate particles to the growing surface of the crystal and, thus, also limits the crystallization rate.

CONCLUSIONS

The general signs of the kinetics of crystallization of all the quartz faces (except those of a slowly growing hexagonal prism [3]) in Na₂CO₃ and NaOH aqueous solutions at 200–450°C are the deviation of the temperature dependence of the growth rate from the linear one in the $\log V-1/T$, K coordinates and the jumpwise decrease of the activation energy of crystallization at $t > 280$ –325°C.

These characteristics are associated with (1) dehydration of the quartz surface and the destruction of the layer of physically adsorbed water molecules in the water film at $t \sim 300^\circ\text{C}$ (occurring by the mechanism of hydrogen bonding) and (2) an increase in the fraction of polymer silica groupings in the aqueous alkali solution with an increase in the temperature, which leads to a deficiency in silicon monomers participating in elementary events of quartz crystallization.

The adsorption activity of the quartz surface coated with hydroxyl groups (with respect to the polar water molecules) changes in the sequence $c(325^\circ\text{C}) > r(300^\circ\text{C}) > R(280^\circ\text{C})$ (the approximate dehydration temperature of the surface is indicated in parentheses) and correlates with the propensity of these faces to crystallization. In turn, this indicates that hydroxyl groups chemisorbed on the quartz surface play not only the role of centers of physical adsorption but also the role of active centers of chemical crystallization of quartz.

ACKNOWLEDGMENTS

The author is grateful to V.A. Klipov for supplying material for the experiments.

REFERENCES

1. R. A. Laudise, J. Am. Chem. Soc. **81** (3), 562 (1959).
2. A. A. Chernov and V. A. Kuznetsov, Kristallografiya **14** (5), 879 (1969) [Sov. Phys. Crystallogr. **14**, 753 (1969)].

3. V. N. Rumyantsev, in *Proceedings of the International Conference "Crystals: Growth, Properties, Real Structure, and Applications," Aleksandrov, 1999*, Vol. 1, p. 16.
4. A. G. Volosov, I. L. Khodakovskii, and B. N. Ryzhenko, *Geokhimiya*, No. 5, 575 (1972).
5. V. N. Rumyantsev, *Zh. Neorg. Khim.* **40** (1), 42 (1995).
6. V. N. Rumyantsev, *Izv. Akad. Nauk SSSR, Neorg. Mater.* **10** (2), 321 (1974).
7. V. N. Rumyantsev, *Neorg. Mater.* **28** (7), 1420 (1992).
8. V. N. Rumyantsev, *Kristallografiya* **37** (2), 500 (1992) [*Sov. Phys. Crystallogr.* **37**, 259 (1992)].
9. T. G. Petrov, E. B. Treĭvus, Yu. O. Punin, and A. P. Kasatkin, *Crystal Growth from Solutions* (Nedra, Leningrad, 1983).
10. G. I. Distler, in *Crystal Growth* (Nauka, Moscow, 1968), Vol. 8, p. 108.
11. S. R. Palit, *J. Org. Chem.* **12** (6), 752 (1947).
12. E. S. Amis, *Solvent Effects on Reaction Rates and Mechanisms* (Academic, New York, 1966; Mir, Moscow, 1968).

Translated by L. Man

CRYSTAL
GROWTH

Hydrothermal Synthesis and Ionic Conductivity of CdF₂ and Low-Temperature Modifications of PbF₂ and PbSnF₄

O. K. Nikol'skaya, L. N. Demianets, and N. I. Sorokin

Shubnikov Institute of Crystallography, Russian Academy of Sciences,

Leninskiĭ pr. 59, Moscow, 117333 Russia

e-mail: demianets@mail.ru

Received October 16, 2001

Abstract—Single crystals of CdF₂ and low-temperature modifications of PbF₂ and PbSnF₄ are synthesized from high-temperature hydrothermal solutions in the MF₂–M'F₂–HF (KF, NH₄F)–(Pb)–H₂O systems, where M = Cd and Pb and M' = Sn. Ionic conductivity of the synthesized phases showed pronounced anisotropy of fluoride-ion transport. Conductivity of α -PbF₂ measured along two directions equals $\sigma_{\parallel a} = 1.4 \times 10^{-3}$ Sm/cm and $\sigma_{\parallel c} = 2.3 \times 10^{-4}$ Sm/cm. © 2002 MAIK "Nauka/Interperiodica".

INTRODUCTION

Inorganic fluorides are studied by many scientists because of their high fluoride-ion conductivity. Simple Pb and Cd fluorides and Pb–Sn tetrafluoride are known as fluoride-ion conductors at 300 to 600°C, i.e., at temperatures lower by several hundred degrees centigrade than their melting points [1–9]. Although the chemical compositions of these compounds are rather simple, the growth of single crystals of some polymorphous modifications is still a serious problem because of several phase transitions undergone by these compounds in a narrow temperature range.

The data on the structure and stability regions of various modifications of fluorides under study are rather contradictory [10–14]. Most of the experimental data on ionic conductivity were measured on polycrystal samples obtained by solid-phase synthesis, sedimentation from solutions, and crystallization from melts. Since the structural data indicate the anisotropy of the electrophysical properties of the low-temperature modifications of Pb difluoride and (Pb,Sn) tetrafluoride, their detailed studies should be performed on single crystals of these modifications.

The analysis of the known data on the synthesis, structure, and polymorphism of PbF₂ and PbSnF₄ led to the conclusion that the optimum method of obtaining single crystals of their low-temperature modifications should be hydrothermal synthesis. A finely crystalline powder or very small crystals (0.1–0.3 mm) of CdF₂, PbF₂, and PbSnF₄ can be obtained by deposition from low-temperature solutions. In [12], large CdF₂ and PbF₂ crystals were grown by the method of directed crystallization from melts; however, because of high melting points, only the β -PbF₂ phase was crystallized, whereas the α -modification was formed only as an impurity. Unfortunately, tin–lead tetrafluoride cannot be synthe-

sized from melt because, below the melting point (~399°C), PbSnF₄ undergoes a number of phase transitions [10, 11]. The experiments performed in [14] showed that PbSnF₄ single crystals can be grown by the method of hydrothermal synthesis.

The present study was aimed at the synthesis of single crystals of low-temperature PbF₂ and PbSnF₄ modifications by the hydrothermal method and measurements of conductivity of the grown crystals.

EXPERIMENTAL

Single crystals were obtained by hydrothermal synthesis under conditions of a direct vertical temperature gradient. The experiments were performed either in 40-cm³ silver-lined steel autoclaves or in 170-cm³ autoclaves with the use of copper ampules or Teflon cans. The temperature in the dissolution zone varied from 170 to 450°C; the vertical temperature gradient ranged from 1.9 to 2 deg/cm. The pressure was determined from the pressure–volume–temperature (PVT) dependences for water and aqueous solutions with the fill coefficient varying within 0.65–0.80 depending on the solvent (HF, NH₄F, and KF solutions) concentration. Single crystals of CdF₂ fluoride were synthesized in the CdF₂–HF(NH₄F)–H₂O system, those of PbF₂, in the PbF₂–KF(NH₄F)–H₂O system, and those of PbSnF₄, in the PbF₂–SnF₂–HF(KF)–H₂O system.

The final products of crystallization were analyzed by X-ray phase analysis (Rigaku D-max III-C automated diffractometer), X-ray diffraction analysis (single crystal SYNTEX-2 diffractometer), the methods of optical (optical binocular microscope, ZRQ-3 goniometer) and electron (JXA-8600S) microscopy, and differential thermal analysis (DTA) (Sinku Rico TA 7000).

Table 1. Experimental data on the synthesis of fluorides under hydrothermal conditions

Starting materials	Solvent concentration	t_{gr} , °C	Characteristics of grown crystals
CdF ₂	2% HF	280	CdF ₂ , octahedral crystals with 1- to 2-mm-long octahedron edges
CdF ₂	10% NH ₄ F	280	CdF ₂ , finely crystalline powder
*PbF ₂	10% NH ₄ F	450	α-PbF ₂ , thin (100)-platelike crystals (75–65%); β-PbF ₂ , finely crystalline powder (25–35%)
*PbF ₂	6% NH ₄ F	450	α-PbF ₂ , thin (100)-platelike crystals (65–50%); β-PbF ₂ , finely crystalline powder (35–50%)
PbF ₂	10% NH ₄ F	280	α-PbF ₂ , 0.1- to 2-mm-long prismatic crystals with the β-PbF ₂ , {120}, {010}, and {012} main simple forms
PbF ₂	6% NH ₄ F	280	α-PbF ₂ , 0.1- to 0.2-mm-long needlelike crystals
*PbF ₂	10% KF	450	α-PbF ₂ , 0.2- to 0.3-mm-long isometric crystals (10%); β-PbF ₂ , finely crystalline powder (90%)
PbF ₂	10% KF	280	α-PbF ₂ , elongated prismatic crystals with 5-mm-long edges and well-developed {100} and {010} faces
PbF ₂	20% KF	270	α-PbF ₂ , elongated prismatic crystals with up to 10-mm-long edges and well-developed {100}, {010}, and {012} faces
PbF ₂ (crystals)	20% KF	280	α-PbF ₂ , up to 17-mm-long crystals with prismatic habits and well-developed {100}, {010}, and {012} faces
PbF ₂ + SnCl ₂ · H ₂ O	10% NH ₄ F	180	PbFCl, finely crystalline powder (80%); PbF ₂ , thin platelike crystals up to 5 mm in size (20%)
PbF ₂ + SnF ₂ (1 : 1)	20% KF	270	K ₂ SnF ₆ · 6H ₂ O, up to 5-mm-large crystals with dipyramidal habits; β-PbF ₂ , up to 10-mm-long crystals with prismatic habits
PbF ₂ + SnF ₂ (1 : 1)	20% KF	380	α-PbF ₂ , thin 10 × 3 × 0.2 mm ³ -large platelets (40–50%); SnF ₂ , finely crystalline powder
**PbF ₂ + SnF ₂ (1 : 1)	0.2% HF	180	α'-PbSnF ₄ , up to ~0.1-mm-long platelike crystals (40–45%); β-PbF ₂ , finely crystalline powder (5–10%); α-PbF ₂ , finely crystalline powder (25%); SnF ₂ , finely crystalline powder (25%)
PbF ₂ + SnF ₂ + Pb (1 : 1.2 : 0.2)	0.2% HF	180	α'-PbSnF ₄ , 5 × 5 × 0.02-mm-large (100)-platelike crystals
PbF ₂ + SnF ₂ + Pb	2% HF	200	α'-PbSnF ₄ , 10 × 10 × 0.02-mm-large (100)-platelike crystals

Bulk resistance was determined using electrochemical C|PbF₂(PbSnF₄)|C cells. Temperature measurements were made in an experimental setup that allowed one to measure electric conductivity in the range 293–700 K with an accuracy in temperature maintenance of ±1 K. The impedance was measured in a ~0.1-Pa vacuum by a TESLA BM507 impedancemeter in the frequency range from 5 Hz to 500 kHz. The preliminary studies showed that the contribution of electron conductivity to the total electrical conductivity of PbF₂ and α'-PbSnF₄ crystals can be ignored. Conductivity was calculated by the formula $\sigma = (h/S)R_v^{-1}$, where R_v is the bulk resistance of the specimen associated with the anionic transport, h is the specimen thickness, and S is the surface area of the specimen. The

measurements were made on α-PbF₂ single crystals (along and normally to the c -axis), α'-PbSnF₄ single crystals (along the c -axis), and polycrystal ceramics.

RESULTS AND DISCUSSION

Growth of single crystals. The results of the experiments on hydrothermal synthesis of inorganic fluorides are shown in Table 1. Most of the experiments were made in Teflon-lined autoclaves at temperatures below ~280°C. The experiments performed in copper- and platinum-lined autoclaves are marked with one and two asterisks, respectively. The X-ray diffraction and DTA data obtained for the specimens are indicated in Table 2.

Table 2. Unit-cell parameters and the first phase transitions observed in the heating of the synthesized fluoride crystals

Compound	Unit-cell parameters at 25°C				Sp. gr.	First phase transition observed during heating
	<i>a</i> , Å	<i>b</i> , Å	<i>c</i> , Å	γ , deg		
CdF ₂	5.391				<i>Fm</i> 3 <i>m</i>	
PbF ₂	7.652	6.439	3.899		<i>Pc</i> <i>nm</i>	α -PbF ₂ $\xrightarrow{349^\circ\text{C}}$ β -PbF ₂
α' -PbSnF ₄	4.191	4.193	22.962	91.73	<i>P</i> 2 ₁ / <i>n</i>	α' -PbSnF ₄ $\xrightarrow{82^\circ\text{C}}$ β -PbSnF ₄

Single crystals of CdF₂ were obtained in the CdF₂–HF–H₂O system at the optimum HF concentration equal to ~2 wt %. Colorless crystals were obtained for the first time in the form of transparent {111} octahedra with well-shaped faces (Fig. 1). X-ray diffraction analysis of the crystals confirmed that they belong to the fluorite structure type.

Single crystals of PbF₂ were synthesized in the PbF₂–NH₄F–H₂O and PbF₂–KF–H₂O systems; the optimum KF solvent had a concentration of ~20 wt % and the optimum crystallization temperatures ranged within 270–280°C. According to the data of X-ray phase analysis, these crystals were identified with the low-temperature α -PbF₂ modification (Fig. 2, Table 2). With an increase in the solvent temperature and concentration, *C_R*, the crystal habit changed from a needle-like habit (elongation in the direction of the *c*-axis) to a habit flattened along the *a*-axis and somewhat elongated along the *c*-axis (Fig. 3). At low growth temperatures, the main faces were two pinacoidal {010} and {100} and two prismatic {012} and {120} ones. With an increase in the growth temperature, the {120} faces disappeared and the {100} faces were developed. The

analysis of the growth morphology of the face surfaces led to the conclusion that the (100) face of α -PbF₂ crystals was a singular one and grew by the layer-by-layer mechanism (steps repeating the face configuration, flattening of crystals). It is possible that the dislocation mechanism could be switched on in the course of crystal growth (the formation of growth hillocks). The (120) faces grew by the normal growth mechanism. The {012} faces seem to be singular but showed a more pronounced tendency to the transition to the rough atomic state of the surface and normal growth mechanism, which was indicated by the presence of growth hillocks and the higher growth rate of these faces in comparison with the growth rate of the (100) face. The DTA data proved the occurrence of the α -PbF₂ \rightarrow β -PbF₂ phase transition at a temperature of 349 ± 5°C.

Single-phase PbSnF₄ crystals were synthesized only in the PbF₂–SnF₂–HF–H₂O system with added lead to prevent tin oxidation. In KF solutions with a finely crystalline PbF₂ and SnF₂ mixture as a starting nutrient, pyramidal K₂SnF₄ · 6H₂O crystals were formed at temperatures below 300°C. According to the data of X-ray diffraction analysis, PbSnF₄ crystals grown from the

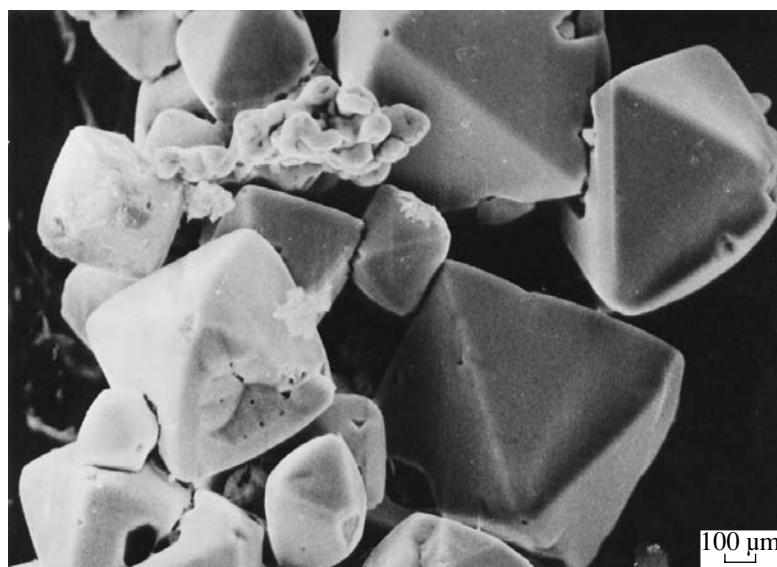
**Fig. 1.** Single crystals of CdF₂ synthesized in the CdF₂–HF–H₂O system.

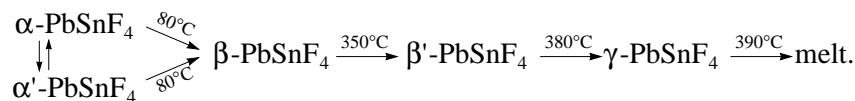


Fig. 2. Single crystals of α -PbF₂ synthesized in the PbF₂-KF-H₂O system.

HF solutions are the α' -modification of PbSnF₄ crystals and have the shape of thin platelets of the square habit (Fig. 4) with unit-cell parameters corresponding to those indicated in [10] for tetrafluoride obtained by deposition from solution.

Fluoride polymorphism. Among all fluorides studied in our works, only CdF₂ has one modification with the fluorite structure type. There are two modifications of PbF₂ (α and β), whereas, according to various data, PbSnF₄ has from three to five polymorphous modifications (Table 3). The known data on the phase-transition temperatures and the structural characteristics of these phases are inconsistent, which seems to be caused by

different methods of their synthesis and different treatment of the synthesized crystals (cooling, keeping in a certain atmosphere, annealing, etc.). As a result, the synthesized Pb_xSn_{1-x}F₄ solid solutions ($0.5 < x < 0.75$) or the mixture of the phases $\alpha + \alpha'$, $\alpha' + \beta$, $\alpha + \beta$, and $\beta + \beta'$ were often mistakenly identified with pure α -, β -, and γ -modifications. The polymorphism scheme indicated in [10] seems to be the most adequate, because the phase transition temperatures in [10] were reliably determined from the differential calorimetric analysis data for crystals synthesized at different temperatures (20 and 250°C). It has the form



At room temperature, at least two modifications, α and α' , can coexist (the reversible transition between these phases occurs at $t < 80^\circ\text{C}$). Also, these phases have similar structures and activation energies of conductivity; the conductivity of α' -PbSnF₄ is somewhat higher than the conductivity of the α -phase. With an increase in the temperature, three phase transitions successively take place in the solid phase, $\beta \rightarrow \beta' \rightarrow \gamma$ -PbSnF₄.

The DTA data indicated several thermal effects, of which only the first one could be reliably interpreted (at $81 \pm 1^\circ\text{C}$), because the DTA measurements were made in air. This effect corresponds to the phase transition $\alpha' \rightarrow \beta$ which proceeds at a high rate. The reverse transformation proceeds very slowly, is characterized by a considerable hysteresis, and cannot be recorded on the cooling curve. At heating above 250°C , the crystal

changes its color because of the interaction with CO₂ and H₂O vapors. Despite the changes occurring in the crystal, the transition $\beta' \rightarrow \gamma$ is still quite pronounced at $399\text{--}400^\circ\text{C}$. Heating of the crystal up to 420°C in air did not lead to its melting.

Ionic conductivity. Ionic conductivity of PbF₂ and SnF₂ was discussed elsewhere [5, 9–14]. Most of the data analyzed were obtained on polycrystal specimens.

The bulk α -PbF₂ single crystals up to several millimeters in size allowed us to make electrophysical measurements along the crystallographic a - and c -axes.

Figure 4 shows the temperature curves of ion conductivity for α -PbF₂ single crystals along the crystallographic a - and c -axes in the temperature range 300–450 K (i.e., below the temperature of the polymorphous transformation into the β' -phase). The α -PbF₂ crystals showed anisotropy of conductivity. The ratio of the

Table 3. Stability ranges and unit-cell parameters of different polymorphous modifications of PbSnF₄ crystals

Modification	Stability ranges, °C	System	Unit-cell parameters				Z	Sp. gr.	Reference
			a, Å	b, Å	c, Å	γ, deg			
α	<80	Monoclinic	4.204	4.205	11.414	91.56	8	P2/n	[10]
			6.021	5.840	22.875				[13]
α'	80–85	Monoclinic orthorhombic	4.191	4.193	22.83	91.9		P2 ₁ /n Aba2 = C2ca	[10]
			22.84	5.850	6.021				[3]
α''	<80	Orthorhombic	6.010	5.886	11.388		4	C222 Cmma	[1]*
			6.00	5.79	11.41		4		[12]**
β	80–350	Tetragonal	4.216		11.407		1	P4/n P4/nm	[10]
	80–355		4.22		5.70				[12]
	<260–290		4.219		11.415				[1]***
β'	350–380	Tetragonal	4.215		11.744		2	P4/nm	[2]
	60–390		16.83		23.063				[1]
	350–380		5.969		51.51				36
γ	355–380	Cubic	5.91				2		[12]
γ'	<420		6.05						[1]

* The phase is identified by the author as α-PbSnF₄.

** The phase is identified by the author as α'-PbSnF₄.

*** The existence range of α-PbSnF₄ is indicated.

conductivities along the *a*- and *c*-axes, $\sigma_{\parallel a}/\sigma_{\parallel c}$, varies from 3.1 at 300 K to 6.3 at 400 K. The activation energy of the ionic transport determined in conductometric measurements was 0.36 eV along the *a*-axis and 0.31 eV along the *c*-axis, which is in good accord with the migration energy of fluoride-ion vacancies (0.33–0.38 eV) in polycrystal line α-PbF₂ specimens [6, 9]. Thus, the results obtained indicate the vacancy nature of ionic conductivity in α-PbF₂ single crystals.

The absolute ionic conductivity of hydrothermally grown α-PbF₂ crystals turned out to be much higher than for ceramic specimens obtained by solid-phase synthesis, $\sigma_{\parallel a} = 1.4 \times 10^{-3}$ Sm/cm, $\sigma_{\parallel c} = 2.3 \times 10^{-4}$ Sm/cm, and $\sigma_{\text{cer}} = (1-2.5) \times 10^{-6}$ Sm/cm at 400 K [5–9]. We assumed that the high ionic conductivity of hydrothermally grown α-PbF₂ crystals in comparison with the conductivity of crystals grown by other methods can be explained by the partial replacement of Pb²⁺ by K⁺ ions from the KF solution. Thus, the formation of *V_F* vacancies might be associated with this replacement. However, X-ray microanalysis revealed no potassium atoms in the crystals studied and, therefore, the cause of the high conductivity of hydrothermally-grown α-PbF₂ single crystals can be established only upon some additional experiments.

Because of the perfect cleavage and platelike habit of α'-PbSnF₄ single crystals, their conductivity was measured only along the *c*-axis (Fig. 5). Therefore, we

had to make electrophysical measurements also on 1 to 3-mm-thick ceramic tablets α'-PbSnF₄ 5 mm in diameter. The inert electrodes were prepared from the DAG-580 graphite paste applied to opposite sides of the specimens.

It is seen from Fig. 5 that in the vicinity of the phase transition temperature $T_{\alpha-\beta} = 354$ K, the temperature dependence of ionic conductivity of ceramic specimens is nonlinear. On the contrary, the temperature dependence of conductivity along the *c*-axis of single crystals shows no anomalies. The activation energy of conductivity in the α'-PbSnF₄ single crystals equals 0.30 eV.

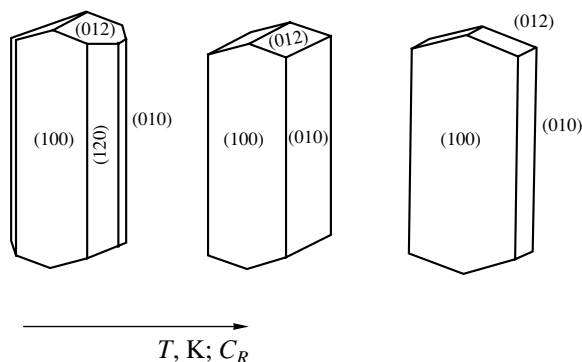


Fig. 3. Changes in the habit of α-PbF₂ crystals grown at different temperatures and concentrations of the solvent.

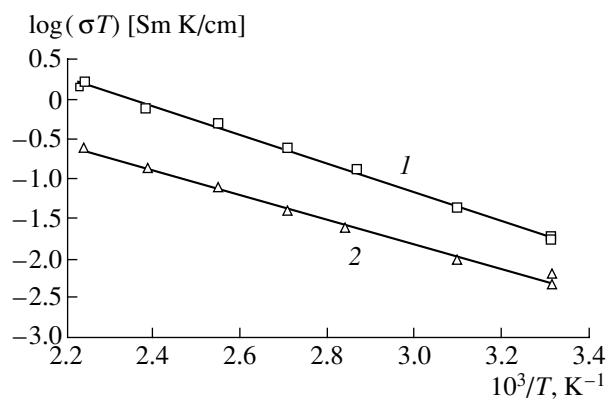


Fig. 4. Temperature curves of ionic conductivity of α -PbF₂ single crystals along the (1) *a*- and (2) *c*-axes.

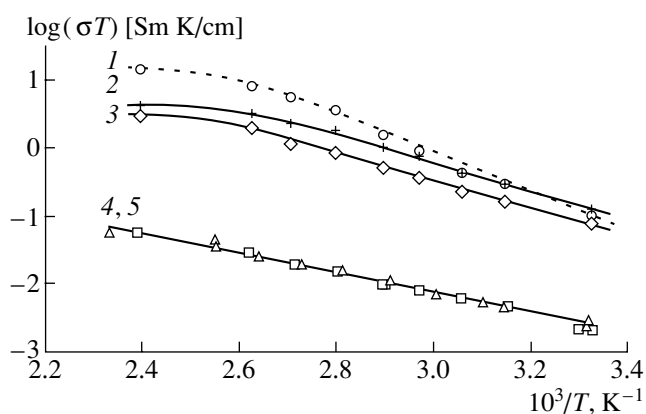


Fig. 5. Temperature dependences of ionic conductivity in α' -PbSnF₄: (1, 2, 3) ceramic specimens, (4, 5) single crystals.

The electrophysical measurements made on single crystals and ceramic specimens indicate the pronounced anisotropy of the ionic transport in PbSnF₄: the $\sigma_{cer}/\sigma_{||c}$ ratio equals 50 at 300 K (α' -phase) and 250 at 417 K (β -phase). Thus, PbSnF₄ crystals can be considered as two-dimensional superionic conductors with fast transport of fluoride ions in the crystallographic planes normal to the *c*-axis.

CONCLUSION

Single crystals of CdF₂ difluoride and low-temperature modifications of PbF₂ and PbSnF₄ fluorides were synthesized by the method of direct temperature gradi-

ent under hydrothermal conditions. The conditions for the monophasic crystallization of CdF₂, PbF₂, and PbSnF₄ from F-containing solutions are determined.

The conductivity of hydrothermally grown α -PbF₂ crystals is measured at temperatures up to 420 K. It is established that the transport of fluoride ions is highly anisotropic (the $\sigma_{||a}/\sigma_{||c}$ ratio is 3.1 at 300 K and 6.3 at 400 K). Electrophysical studies of single crystals of the low-temperature α' -PbSnF₄ modification also showed pronounced anisotropy of fluoride-ion transport and much higher conductivity in α' -PbSnF₄ single crystals in comparison with the conductivity of the ceramic. The PbSnF₄ tetrafluoride can be considered as a two-dimensional superionic conductor in which fast fluoride-ion transport proceeds in the crystallographic planes normal to the *c*-axis.

REFERENCES

1. S. Vilminot, G. Perez, W. Granier, and L. Cot, *Solid State Ionics* **2**, 91 (1981).
2. S. Vilminot, G. Perez, W. Granier, and L. Cot, *Solid State Ionics* **2**, 87 (1981).
3. J. M. Reau, C. Lucat, J. Portier, *et al.*, *Mater. Res. Bull.* **13**, 877 (1978).
4. A. M. Vakulenko and E. A. Ukshe, *Élektrokimiya* **28**, 1257 (1992).
5. J. H. Kennedy, R. Miles, and J. Hunter, *J. Electrochem. Soc.* **120**, 1441 (1973).
6. C. C. Liang and A. V. Joshi, *J. Electrochem. Soc.* **122**, 466 (1975).
7. I. V. Murin, A. V. Glumov, and O. V. Glumov, *Élektrokimiya* **15**, 1119 (1979).
8. J. Oberschmidt and D. Lazarus, *Phys. Rev. B* **21**, 2952 (1980).
9. N. I. Sorokin, P. P. Fedorov, and B. P. Sobolev, *Neorg. Mater.* **33**, 5 (1997).
10. G. Perez, S. Villinot, W. Granier, *et al.*, *Mater. Res. Bull.* **15**, 587 (1980).
11. G. Perez, J. Pannetier, G. Denes, and J. Lucas, *Mater. Res. Bull.* **14**, 627 (1979).
12. Y. Ito, T. Mukoyama, H. Funatomi, *et al.*, *Solid State Ionics* **64**, 301 (1994).
13. S. V. Chernov, A. Z. Moskvin, and I. V. Murin, *Solid State Ionics* **47**, 71 (1991).
14. O. K. Nikol'skaya, L. N. Dem'yanets, N. P. Kuznetsova, and A. S. Antsyshkina, *Izv. Akad. Nauk, Neorg. Mater.* **32**, 1392 (1996).

Translated by L. Man

OBITUARIES

Anatoliĭ Georgievich Luchaninov (March 14, 1948–December 27, 2001)



On the night of December 27, 2001, Anatoliĭ Georgievich Luchaninov suddenly died in the middle of his creative work, having completed his doctoral dissertation. He left life while writing his last article. While in a coma, he still continued citing the formulas from this article.

Luchaninov was one of those rare physicists of our time who luckily combined two gifts—he was both an outstanding experimenter and an exceptional theoretician.

Upon graduating from the Physics Faculty, Rostov-on-Don University, in 1971, he started working at the plant *Avrora*, where he successfully combined his work in industry with research. His first publication (co-authored with V.Z. Borodin and A.I. Sogr) was published in 1971.

In the late 1970s, he paid attention to the gap existing in studies of the symmetry aspects of the physics of ferroelectrics and related materials. Luchaninov man-

aged to show, first theoretically and then also experimentally, that a piezoelectric ceramic depolarized by a crystal field in such a way that its macroscopic polarization is zero possesses a considerable piezoelectric effect but does not possess any pyroelectric effect (an analogue of quartz). These studies formed the basis for his candidate dissertation in physics and mathematics (1987) entitled *Piezoelectric Effect in Electrically Depolarized Polycrystalline Ferroelectrics*, written under the guidance of L.A. Shuvalov and A.V. Shil'nikov. Continuing working as a main researcher in industry, Luchaninov actively continued the research along these chosen lines and published his articles in the most prestigious Soviet and foreign scientific journals.

In October 1999, he started working on his doctorate at the Department of Physics, Volgograd Academy of Architecture and Construction (advisers Shil'nikov and Shuvalov). On December 20, 2001, he presented the results of his doctoral dissertation entitled *Piezoelectric Effect in Nonpolar Ferroelectric Materials* at a

departmental meeting. Developing the results of his candidate dissertation, Luchaninov showed, in particular, that the theoretical model in which piezoelectric ceramic is considered as a system consisting of crystallites with identical properties cannot be used for the qualitative description of experimental data. For the analysis of the effective characteristics of polarized and electrically depolarized piezoelectric ceramics, he suggested using a more adequate model in which, in accordance with the experimental data, one has also to take into account (1) the domain structure of crystallites, (2) the irreversible displacement of 90° -domain boundaries, and (3) the rearrangement of the domain structure under the action of the polarizing field. Using this model, Luchaninov calculated the pyroelectric, dielectric, piezoelectric, elastic, and inelastic constants of the BaTiO_3 ceramic as functions of the degree of specimen polarization and obtained good agreement between the predicted and experimental results. To be able to predict the values of these constants for an arbitrary piezoelectric ceramic, he constructed a system of nonlinear equations based on the solution of the problem of pyro-

electrically active inclusions in a transversely isotropic pyroelectrically active medium. These equations are, in fact, the most general formulation of the method of effective medium and rigorously take into account the piezoelectric interactions in the material.

Luchaninov published about 70 articles, had 10 invention certificates, and delivered about 20 papers to various international and national scientific conferences.

Luchaninov not only successfully worked in industry and was a gifted scientist. He also knew and loved literature, especially classical Russian authors.

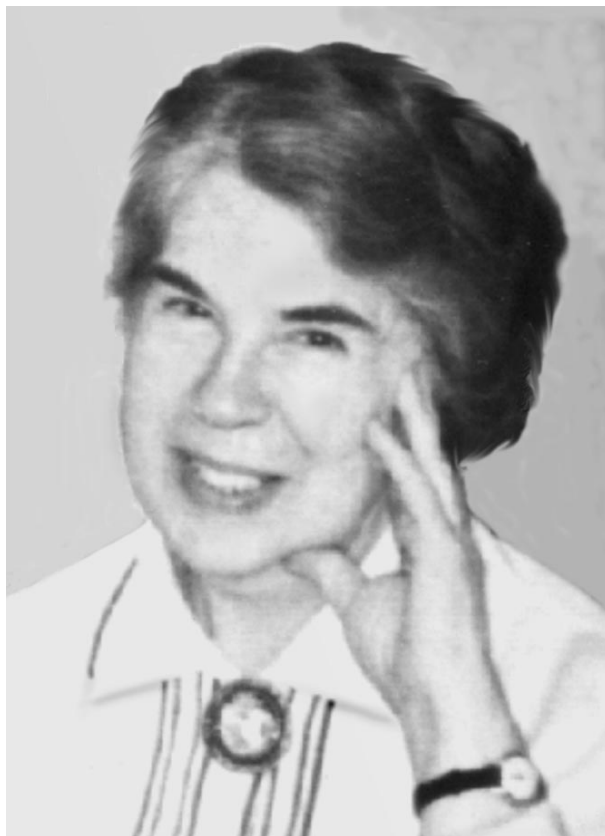
Luchaninov was a wonderful modest person. He was always surrounded by many friends and was always ready to help them. He was also a wonderful family man—a son, husband, father, and grandfather.

Luchaninov's death is an irreplaceable loss to science and industry. Many people who knew him well will always keep his noble image in their memory.

Translated by L. Man

OBITUARIES

Marina Aleksandrovna Chernysheva
(December 14, 1911–January 31, 2002)



On January 31, 2002, Marina Aleksandrovna Chernysheva, the oldest scientist at the Institute of Crystallography of the Russian Academy of Sciences, died in the ninety-first year of her life. A gifted scientist, an industrious, kind, and charming person, she belonged to the cohort of founders of the Institute of Crystallography. She started her research in a team guided by Aleksei Vasil'evich Shubnikov in 1942. According to her own words, she was charmed with the magic beauty of crystals and devoted her scientific life to crystals. These studies not only gave her deep satisfaction as a researcher, but also enormous an esthetic pleasure.

Chernysheva was a brilliant experimenter and was very demanding in her research; she was an unsurpassed expert on the application of various optical methods to the studies of crystals. At the same time, she took an active part in the design and development of

new devices and instruments necessary for planned experiments.

Some outstanding scientific achievements are closely associated with her name. At the beginning of her scientific carrier, Chernysheva participated in the tests of highly durable composition materials—the first glass-reinforced plastics in this country—created at the Institute of Crystallography in the 1940s to 1950s by the outstanding architect A.K. Burov.

In her dissertation on twinning in Seignette salt, she used the polarization–optical method and, for the first time, managed to visualize ferroelectric domains and investigate and interpret their physical nature. This result received world recognition, and entered the golden foundation of science as an important discovery in the physics of ferroelectrics.

She applied the unique method of high-speed filming in polarized light to the study of the distribution and

evolution of stresses in crystals in the process of their plastic deformation under conditions of forbidden glide, and achieved remarkable results on nucleation and the development of fault formation.

Chernysheva made a considerable contribution to the growth of lasing crystals, which was formulated and solved at the Institute of Crystallography in the 1960s. She was among the designers of a unique conoscope for studying and measuring stresses in large crystals. For the creation of this device, Chernysheva was awarded the Vavilov prize. This device was successfully used in experiments on stress relaxation in corundum crystals during annealing. The latter studies, performed in cooperation with outstanding scientists of the Institute of Crystallography such as M.V. Klassen-Neklyudova, V.L. Indenbom, and A.A. Urusovskaya, considerably improved crystal quality and the elements used in the first ruby lasers.

Up to the last days of her life, Chernysheva kept a clear mind and interest in life, whose main component was always work and science. Only recently, she completed and published a book about her father Academician A.A. Chernyshev, an outstanding physicist in the field of electricity who was one of the founders of this science in this country. She was interested in all aspects of scientific life at the Institute of Crystallography and

continued active studies with a number of its laboratories. She was always a benevolent adviser to all her colleagues. Those who come to her always found understanding and support from her side.

Chernysheva was an all-round educated person, she loved and knew literature and music, played piano, and was a serious painter. She was a natural carrier of the cultural and moral values of the Russian intelligentsia, disinterestedly devoted to life and work in her native country.

Despite all the historical catastrophes of the 20th century and the severe tests that befell her generation, Chernysheva and all those cultural and moral values safely reached the 21st century. We should like to believe that the "thread connecting our days" will never be torn, and the succession of new generations will not waste the best tradition of the Russian intelligentsia of whom Marina Aleksandrovna Chernysheva was a shining example.

The memory of this remarkable woman shall always be in the grateful hearts of all those who were happy to be friendly with her, work with her, and meet her on their paths through life.

Translated by L. Man

Erratum: “Triple-Crystal X-ray Spectroscopy of Diffuse Scattering from Tracks”

[*Crystallogr. Rep.* 46 (5) (2001), pp. 717–721].

V. N. Peregudov and É. M. Pashaev

We regret the error made in the article.

The correct formula for q_z has an additional term and should be written as

$$q_z = k_0[\Delta\theta \cos(\theta_B - \psi) - 2\alpha \sin\theta_B \sin\psi]. \quad (6)$$

The second term in this formula may be essential in the analysis of asymmetric diffraction schemes. The authors are grateful to S.S. Fanchenko, who showed interest in their article and drew their attention to the incompleteness of Eq. (6) in the article.

Translated by L. Man